CHARLES UNIVERSITY IN PRAGUE

FACULTY OF SCIENCE

ELEMENTAL AND ISOTOPIC STUDY OF DIFFERENTIATED METEORITES AND IMPLICATIONS FOR THE ORIGIN AND EVOLUTION OF THEIR PARENT BODIES

Patricie Halodová

Dissertation thesis

Supervisors: Doc. RNDr. Jan Košler, Ph.D.

prom. geolog Petr Jakeš, Ph.D.

Prague, 2011

Acknowledgments

I would like to thank both my supervisors, Jan Košler (University of Bergen, Bergen, Norway) and deceased Petr Jakeš (Charles University, Prague, Czech Republic) for their exceedingly helpful guidance and patience, and for suggestions during preparation of this thesis and related publications. Martin J. Whitehouse (Laboratory for Isotope Geology, Swedish Museum of Natural History, Sweden) is thanked for help with SIMS analysis. This study was funded by Charles University, Faculty of Science, and Czech Geological Survey. I am very grateful to my colleague and husband Jakub Haloda (Czech Geological Survey) for his support and help during my work on this thesis. Special thanks belong to my parents Libuška Týcová and František Týc for their encouragement.

I declare that this disertation thesis is original work and has not been used for obtaining the same or another academical degree. All literature and other sources of information and data are properly referenced and listed in the References section.

Prague, 15 March 2011 Patricie Halodová

ABSTRACT

ELEMENTAL AND ISOTOPIC STUDY OF DIFFERENTIATED METEORITES AND IMPLICATIONS FOR THE ORIGIN AND EVOLUTION OF THEIR PARENT BODIES

Iron meteorites are differentiated meteorites composed largely of Fe–Ni alloys. The metallic phase of many iron meteorites shows a texture called the Widmanstätten pattern, which develops as a two-phase intergrowth of kamacite (α-bcc, ferrite) and taenite (γ-fcc, austenite), and forms by nucleation and growth of kamacite from taenite during slow cooling of the parent body.

Selected iron meteorites – octahedrites of different structural and chemical groups (Canyon Diablo, Toluca, Bohumilitz, Horh Uul, Alt Biela, Nelson County, Gibeon and Joe Wright Mountain) were studied with intention to evaluate the scale and extent of Fe isotopic heterogeneities in iron meteorites and to find the possible link between the isotopic variations and thermal histories of the respective meteorite parent bodies. The Fe isotopic compositions of kamacite and taenite in the studied meteorites, obtained by three independent analytical techniques with different spatial resolution capabilities (laser ablation and solution MC ICP-MS and SIMS) show significant variations of up to ~4.5‰ in δ^{56}Fe. The taenite is isotopically heavier compared to kamacite in all studied meteorites. There is no correlation between the Fe isotope composition of the taenite-kamacite pairs and the bulk Ni content of the studied meteorites (thus no obvious relation to the width of taenite lamellae). The results indicate that there is no relationship between samples of the same chemical group IA (Bohumilitz, Canyon Diablo, and Toluca) and iron isotopic composition of their Fe-Ni phases. There is also no similarity in Fe isotopic composition amongst magmatic or non-magmatic members.

The SIMS data indicate that the taenite lamellae are not homogeneous in their isotopic composition. This suggests that spatial resolution has a significant effect of the measured Fe isotopic composition and that the bulk Fe isotope analysis of taenite by solution MC ICP-MS may not record the maximum isotopic variability for the kamacite-taenite pairs. The previously recorded differences in the bulk iron isotope composition are real and can in part be due to the variable amount of taenite analyzed during bulk sampling of the meteorites. The small scale isotopic heterogeneities within the meteorite samples can explain the apparent differences in Fe isotopic composition previously reported for meteoritic irons in the literature.

The new laser ablation MC ICP-MS data from the studied iron meteorite samples revealed a systematic correlation between the kamacite–taenite Fe isotopic offset $\Delta^{56}Fe_{taen-kam}$ and the meteorite cooling rates (5–500 °C/My) determined using metallographic methods based on Ni diffusion in taenite. This correlation is interpreted as resulting from Fe isotopic fractionation driven by diffusion between kamacite and taenite lamellae and variable cooling rates of the studied meteorites. Data presented in this study suggest that the differences in Fe isotopic composition between different iron meteorite groups reflect variations in their respective cooling histories and provide us with new insights into the evolution of iron meteorite parent bodies during the early phases of Solar system evolution.

Two articles on elemental and isotope geochemistry, and magnetic properties of meteorites are also part of this thesis. These articles comprise the results which were obtained and published during my PhD study and are enclosed as supplementary material in the appendix.

ABSTRAKT

PRVKOVÉ A IZOTOPICKÉ STUDIUM DIFERENCOVANÝCH METEORITŮ A JEHO VÝZNAM PRO PŮVOD A VÝVOJ JEJICH MATEŘSKÝCH TĚLES

Železné meteority patří do skupiny diferencovaných meteoritů a jsou tvořeny převážně Fe-Ni slitinami. Ve většině železných meteoritů můžeme na řezu pozorovat strukturu tzv. Widmanstättenových obrazců – dvoufázové prorostlice kamacitu (α-bcc, ferrit) a taenitu (γ-fcc, austenit), které vznikly odmíšením kamacitu z taenitu během chladnutí mateřských těles železných meteoritů.

Vybrané vzorky železných meteoritů - oktaedritů (Canyon Diablo, Toluca, Bohumilitz, Horh Uul, Alt Biela, Nelson County, Gibeon and Joe Wright Mountain) náležící k různým strukturním a chemickým skupinám, byly podrobeny detailnímu studiu. Cílem tohoto studia bylo stanovení rozsahu variability izotopického složení Fe železných meteoritů a nalezení možných vztahů mezi rozdíly v izotopickém složení a termálním vývojem mateřských těles železných meteoritů. Izotopické složení Fe kamacitu a taenitu ve studovaných vzorcích bylo stanoveno pomocí tří nezávislých analytických metod (LA MC ICP-MS, MC ICP-MS z roztoku a SIMS). Byly zjištěny značné rozdíly ve složení, s rozpětím ~4.5‰ pro δ^{56}Fe. Ve všech studovaných meteoritech je taenit izotopicky těžší než kamacit. Nebyla však zjištěna žádná korelace mezi izotopickým složením Fe v párech kamacit-taenit a celkovým obsahem Ni v meteoritech. Dále nebyl nalezen žádný vztah mezi vzorky pocházejícími ze stejné chemické skupiny IA (Bohumilitz, Canyon Diablo a Toluca) a jejich izotopickým složením Fe v Fe-Ni slitinách. Rovněž nebyly zjištěny podobnosti izotopického složení Fe v meteoritech magmatických a „ne-magmatických“ skupin.

Výsledky analýzy izotopického složení Fe pomocí SIMS odhalily značnou izotopickou nehomogenitu taenitových lamel. Tato zjištění mají zásadní význam pro případné další analýzy a dokazují, že hodnoty izotopického složení Fe v taenitu závisí na postorovém rozlišení analytické metody a naznačují, že analýza taenitu pomocí MC ICP-MS z roztoku neodráží maximální možnou izotopickou variabilitu párů taenit-kamacit. Dříve popsané rozdíly v celkovém izotopickém složení železných meteoritů mohou být částečně způsobeny přítomností variabilního obsahu taenitových lamel ve vzorku celkové horniny.

Nové výsledky měření studovaných železných meteoritů pomocí metody LA MC ICP-MS ukazují systematickou korelaci mezi rozdílem izotopického složení kamacit-taenitových párů $\Delta^{56}Fe_{taen\text{-}kam}$ meteoritů a jejich rychlostech chladnutí (5–500 °C/Ma), stanovenou s použitím metalografických metod, založených na difuzi Ni v taenitu. Tato korelace je vysvětlována jako důsledek izotopické frakcionace Fe způsobený difuzí izotopů železa v taenitových a kamacitových lamelách při různých rychlostech chladnutí studovaných meteoritů. Získané výsledky naznačují, že rozdíly v izotopickém složení Fe mezi různými skupinami meteoritů odráží rozdílnost termálních vývojů mateřských těles a mohou přinést nové informace o vzniku těchto těles v raných fázích vývoje Sluneční soustavy.

Součástí dizertace jsou dvě již publikované práce zabývající se studiem geochemických, izotopických a magnetických vlastností vybraných meteoritů. Tyto publikace shrnují výsledky získané během mého doktorského studia a jsou připojeny v příloze dizertační práce.

CONTENTS:

1. INTRODUCTION

1.1. Iron meteorites

Iron meteorites are differentiated meteorites that are thought to be cores of asteroids that melted and differentiated early in their history. They consist mainly of iron-nickel metal with small amounts of sulphide and carbide minerals. Though iron meteorites constitute only about 5 percent of observed meteorite falls, they are relatively easy to distinguish from terrestrial rock and survive longer in soil compared to stony meteorites; thus, they are found more often than stony or stony iron meteorites. Iron meteorites play a vital role in our efforts to understand differentiation of the Solar System´s first solid bodies. Their textures and chemistry tell us much about the thermal history of their parent bodies and from the cooling rates of their central cores, estimates of the sizes of their original parent bodies can be made. The cooling rates of meteorites were a function of their depth of burial. Contrary to traditional views about their origin, iron meteorites may have been derived originally from bodies as large as 1000 km or more in size. Most iron meteorites come directly or indirectly from bodies that accreted before the chondrites, possibly at 1–2 AU (astronomical units) rather than in the asteroid belt. Many of these bodies may have been disrupted by impacts before they cooled slowly (Bottke et al., 2006).

Iron meteorites are composed largely of Fe–Ni alloys, and most contain only minor accessory minerals of Co, P, S, and C. These accessory minerals often occur in rounded nodules that consist of the iron-sulfide troilite (FeS) or graphite, often surrounded by the iron-phosphide schreibersite $(Fe,Ni)_3P$ and the iron-carbide cohenite $(Fe,Ni)_3C$. The Ni content varies from a minimum of 5 up to 60 wt % although the vast majority of irons have between 5 and 12 wt % Ni (Buchwald, 1975). The metallic phase of many iron meteorites shows a texture called the Widmanstätten pattern, which develops as a two-phase intergrowth of kamacite (α-bcc, ferrite) and taenite (γ-fcc, austenite), and forms by nucleation and growth of kamacite from taenite during slow cooling of the parent body. The conventional explanation of Widmanstätten pattern formation, which is only partly correct (see Goldstein et al., 2009 for details), is based on the binary Fe–Ni equilibrium phase diagram (Fig. 1) published by Yang et al. (1996). A meteorite of a given Fe–Ni content cools from the one-phase taenite (γ) region into the two-phase $\alpha+\gamma$ region, where kamacite (α) nucleates and grows as the meteorite continues to cool.

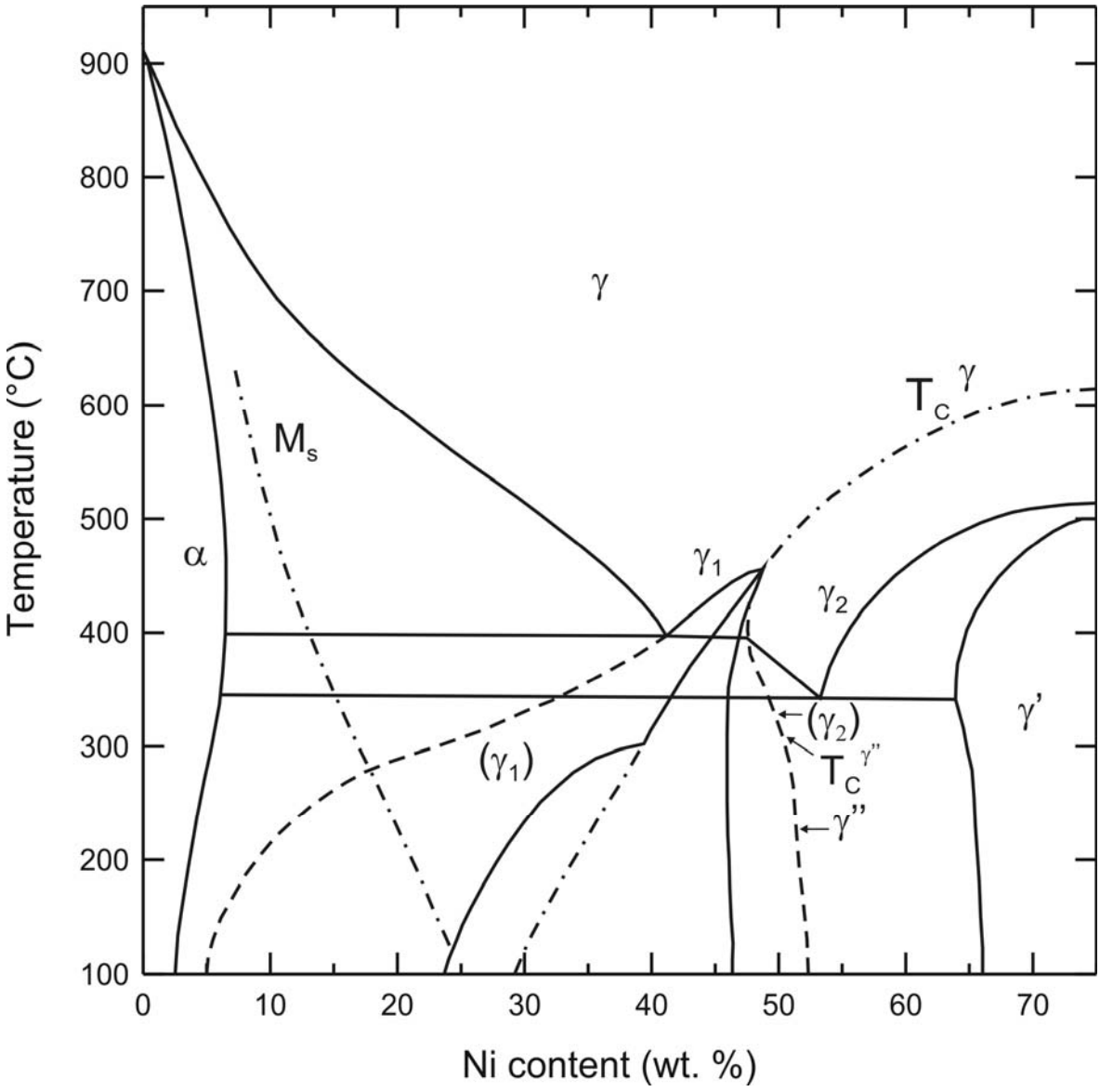

Figure 1. *Fe–Ni binary phase diagram (Yang et al., 1996). On this diagram, α is a low-Ni bcc phase, γ represents a high-Ni fcc phase, γ_1 represents a low-Ni paramagnetic fcc phase, γ_2 represents a high-Ni ferromagnetic fcc phase, γ' is ordered Ni_3Fe, γ'' is ordered FeNi–tetrataenite, and M_S represents the martensitic transformation starting temperature. T_C^{γ} is the Curie temperature of the γ phase. $T_C^{\gamma''}$ is the ordering temperature of FeNi, γ''.*

Depending on the bulk Ni content, nucleation of α-FeNi occurs between 500 and 800 °C. Kamacite nucleates on the close packed octahedral {111} planes of taenite, forming a Widmanstätten pattern (Fig. 2). In three dimensions, kamacite grows as two-dimensional plates into the surrounding taenite. As cooling continues, kamacite grows at the expense of taenite and the Ni content of both kamacite and taenite increases. Most of

the original γ-FeNi undergoes complex decomposition reactions at temperatures below 400 °C (Yang et al., 1997a).

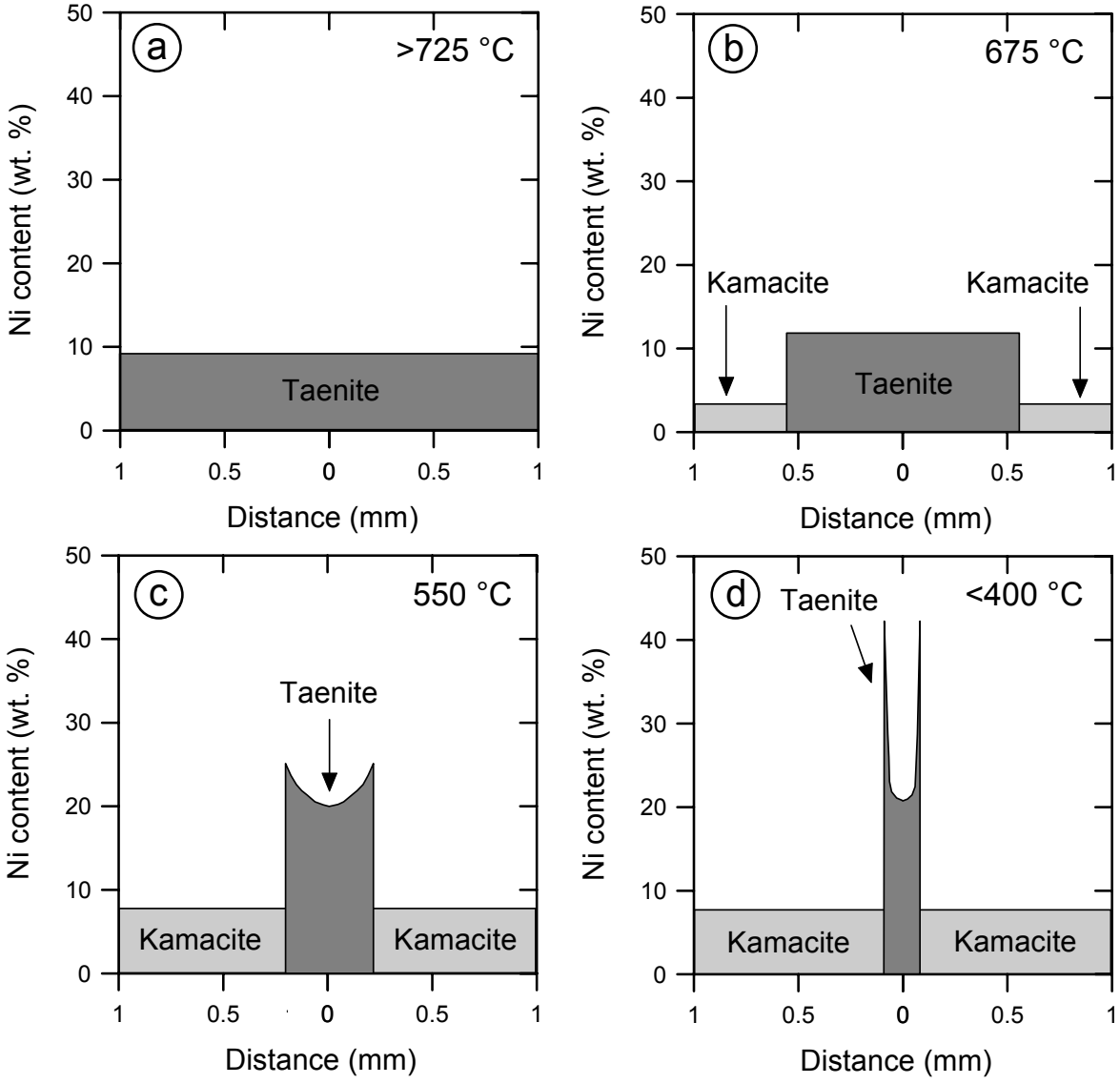

Figure 2. *This scheme shows stages in evolution of the Widmanstätten structure, for the cooling rate 2 ºC/My. (a) Initially, above ~700 °C, the iron meteorite is composed of pure taenite with homogeneous distribution of Ni. (b) Following temperature decrease bellow 700 °C, the metal enters kamacite/taenite stability field and thin kamacite plates begin to form on either side of the taenite. (c) The temperature has reached ~ 550 °C and the kamacite has continued to grow at the expense of the taenite. Diffusion begins to get sluggish at this temperature and taenite fails to accept the Ni into the interior. Instead, Ni builds up on the kamacite/taenite margins creating a Ni gradient across the taenite plate. By temperature ~450 °C (d), the characteristic M-shape trace appears with high Ni concentration at the margins of the taenite. Modified after Norton, 2002.*

1.2. Classification of iron meteorites

There are two classifications of iron meteorites based upon either structural or chemical criteria.

The nature and scale of kamacite has led to a structural classification of iron meteorites (for details see Buchwald, 1975). The width of the kamacite plates depends upon the bulk Ni content (Table 1). Hexahedrites (H) are one-phase kamacite (Fig. 3) with Ni of 5 – 6.5 wt. %. Upon etching, hexahedrites do not display any Widmanstätten pattern, but they often exhibit fine, parallel lines called "Neumann lines". These lines represent a shock-induced, structural deformation of the kamacite plates, and they suggest an impact history for the hexahedrite parent body. Octahedrites (O) have macroscopically visible Widmanstätten patterns with kamacite widths of 0.2 – 3 mm and Ni concentrations of 6 to ~12 wt. % (Table 1, Fig. 3) that are generally inversely related to the kamacite width. The width of the kamacite lamellae allows classification into 5 structural groups: the coarsest, coarse, medium, fine and finest octahedrites. Plessitic octahedrites are transitional between octahedrites and ataxites. Ataxites (D) have microscopic Widmanstätten patterns where kamacite is similarly oriented and <0.2 mm in width and Ni contents of ~10 to >20 wt. %.

Structural classification of iron meteorites

Group	Symbol	Kamacite band width (mm)	Ni (wt. %)
Hexahedrite	H	>50	4.5-6.5
Octahedrites	O		
coarsest	Ogg	3.3-50.0	6.5-7.2
coarse	Og	1.3-3.3	6.5-7.2
medium	Om	0.5-1.3	7.4-10.3
fine	Of	0.2-0.5	7.8-12.7
finest	Off	<0.2	7.8-12.7
plessitic	Opl	<0.2	kamacite spindles
Ataxite	D	no structure	>16.0

Table 1. *Structural classification of iron meteorites. This table shows a structural division of the irons into nine groups based upon their kamacite band width and their Ni content (Norton, 2002).*

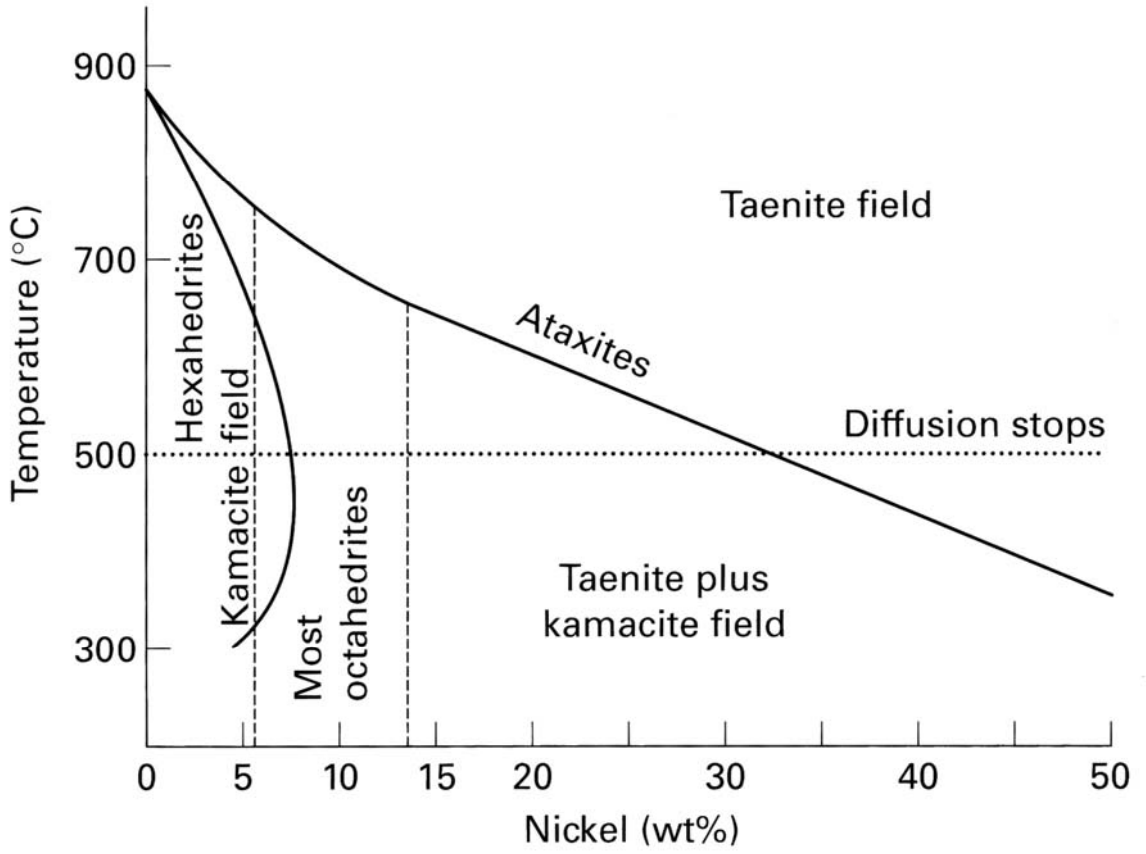

Figure 3. *The Fe-Ni stability phase diagram which predicts three stability fields of kamacite, taenite and kamacite+taenite for various temperatures and Ni compositions. Appropriate fields for hexahedrites, octahedrites and ataxites are also plotted, (after Norton, 2002).*

Whereas the subdivision into hexahedrites, octahedrites, and ataxites is purely descriptive, a genetically more significant classification is based on the trace element content of the metal phase.

The chemical classification uses nickel and trace elements Ga, Ge and Ir compositions of the meteorites. Other trace elements used to resolve groups are Sb, As, Co, Cu, Au, Tl, and W. On plots of log(E) vs. log(Ni), where E denotes one of the trace elements, approximately 85% of iron meteorites belong to one of 14 clusters or chemical groups (Table 2.). About 15% of the irons do not fit these groups and are labelled as ungrouped (for details see review of Mittlefehldt et al., 1998).

Chemical classification of iron meteorites

Group	Number	Ni (wt. %)	Structural groups
IAB	110	6-60	Og, D
IC	11	6-7	Ogg, Og
IIAB	78	5.3-6.5	H, Ogg
IIC	8	9.3-11.5	Opl
IID	21	9.6-11.1	Om, Of
IIE	17	7.2-9.5	Og-Off
IIF	6	11-14	Opl, D
IIG	6	4.1-4.9	H
IIIAB	220	7.1-10.6	Om
IIICD	12	12-23	Of-D
IIIE	14	8.1-9.6	Og
IIIF	8	6.8-8.5	Og, Om
IVA	61	7.5-12	Of
IVB	14	16-18	D
Ungrouped	110	6-35	Ogg-D

***Table 2**. Chemical classification of iron meteorites based upon properties of 14 groups of iron meteorites and the ungrouped irons (Goldstein et al., 2009).*

Gallium and germanium are the most useful elements to classify meteoritic irons (Fig. 4) because the concentration range within most groups only varies by a factor of less than 2.5, whereas the total range between all groups varies by a factors of 10^{3-4}. The ability of this classification to reveal correlations between numerous meteorite properties, including mineralogical, chemical and isotopic parameters, shows that the members of each group are closely related and formed together in one parent body (Buchwald, 1975; Scott and Wasson, 1975; Haack and McCoy, 2004).

Comparison of the chemical trends within groups and their mineralogical composition suggests that there are two very different group types:

1. groups IIAB, IID, IIIAB, IVA, IVB, and possibly the smaller groups such as IC and IIIF, which are largely free of silicates have compositional trends that can be explained by chemical fractionation during solidification of molten iron

2. groups IAB, IIICD, and IIE, with more abundant silicates show large compositional variability and only weak chemical trends (Scott,1972).

In the first type, the chemical variations are largely consistent with the process of fractional crystallization and can be modelled using experimentally determined solid

metal/liquid metal partition coefficients, whereas in the second type, the trace element distribution cannot be explained by fractional crystallization alone (Chabot and Jones, 2003; Chabot and Haack, 2006).These two types of iron meteorite groups are referred to as ‘‘magmatic’’ and ‘‘non-magmatic’’(Wasson, 1985).

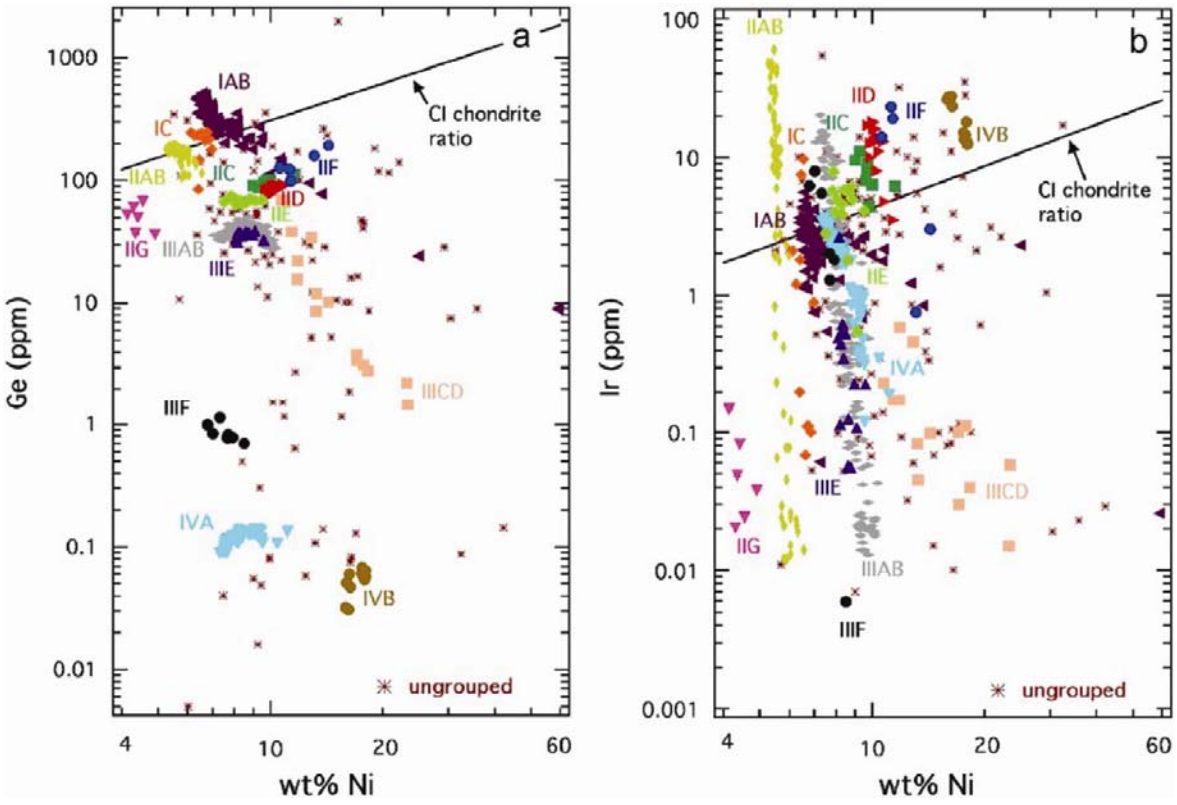

Figure 4. *Logarithmic plots of (a) Ge vs. Ni and (b) Ir vs. Ni of bulk compositions of all iron meteorites (Goldstein et al., 2009). The meteorite chemical groups are shown in different colors and symbols.*

Fractionally crystallized iron meteorite groups are widely thought to be derived from the cores of asteroids that melted, whereas the silicate-bearing groups may come from bodies that were not heated sufficiently for metallic cores to have formed (Haack and McCoy, 2004). In this case, a group of iron meteorites from the core of a single differentiated body should have cooled at almost identical rates because of the high thermal conductivity of metal compared with silicate mantle and crust materials. However, there is evidence in several fractionally crystallized groups for diverse cooling rates so these irons could not have cooled in an insulated metallic core. At least one group, IVA,

appears to have formed in a metallic body that crystallized and cooled with virtually no silicate mantle (Goldstein et al., 2009).

1.3. Cooling rates of iron meteorites

Knowing the cooling rate of iron meteorites is important because it can help to constrain the nature of the heat source responsible for differentiation of planetesimals (decay of short-lived nuclides ^{26}Al and ^{60}Fe, collisions between planetesimals, electromagnetic induction) as well as the size of asteroids present in the inner part of the early solar system (2–100 km; Chabot and Haack, 2006).

The formation of the Widmanstätten pattern in iron meteorites is controlled initially by nucleation and then by kamacite growth in the surrounding taenite during the temperature decrease. To determine the cooling rate of an individual meteorite in any of the chemical groups, the appropriate formation mechanism for the Widmanstätten pattern must be first established (for details and references see Goldstein et al., 2009), using the bulk Ni and P content, so that an appropriate cooling rate simulation can be applied.

Experiments have been performed to nucleate and grow intragranular α – kamacite as a function of cooling time and temperature in Fe–Ni–P alloys (Narayan and Goldstein, 1984a,b). These authors observed that growth kinetics is dictated by the bulk diffusion of Ni in taenite and equilibrium partitioning of Ni and P between kamacite and taenite that takes place at the α/γ interface. A numerical model to simulate growth of the kamacite crystal was developed based on these observations. The numerical model used to simulate Ni redistribution and kamacite growth of experimental alloys is identical to the model used to simulate the formation of Widmanstätten pattern in iron meteorites. Although the numerical model used for Widmanstätten pattern growth extrapolates Ni distributions for a process that takes millions of years, it has been validated based on its successful application to experimental alloys.

The metallographic cooling rate model simulates growth of the Widmanstätten pattern and distribution of Ni content in kamacite and taenite phases during their growth. The model considers five major factors:

1. mechanism for Widmanstätten pattern formation
2. kamacite nucleation temperature
3. effect of impingement

4. Fe–Ni and Fe–Ni–P phase relations
5. interdiffusion coefficients.

Numerical models have been developed which simulate diffusion controlled kamacite growth in taenite (Widmanstätten pattern development) in the Fe–Ni–P phase system. A constant cooling rate is usually assumed for the temperature range in which the Widmanstätten pattern forms. The model includes the applicable nucleation mechanisms (II, III, and V; Yang and Goldstein, 2005) for the formation of Widmanstätten pattern and the kamacite nucleation temperature for the bulk Ni and P content of a specific iron meteorite. The model also includes the equilibrium tie lines in the Fe–Ni and Fe–Ni–P phase diagrams and the binary and ternary diffusion coefficients as a function of temperature and composition. The output of the computer model is the Ni profile in kamacite and taenite for a specific cooling rate and bulk meteorite Ni and P contents (Goldstein et al., 2009).

1.3.1. Metallographic cooling rate methods

A variety of metallographic methods have been used to determine the cooling rates of the Widmanstätten pattern in iron meteorites. The taenite profile matching and the taenite central Ni content methods are the most accurate. In the taenite profile-matching method, the Ni content vs. distance profile in taenite is computed for several cooling rates from the cooling rate model as a function of bulk Ni and P content and half- width of the taenite lamella.. The calculated Ni composition profile in taenite (Ni vs. distance) is then plotted and compared with Ni composition profiles measured for a given meteorite using the electron probe microanalysis - EMPA (Goldstein and Ogilvie, 1965). For each taenite band the orientation of the kamacite plates must be measured in order to obtain accurate distances traversed by the EPMA. In the taenite central Ni content method, the Ni content in the center of a taenite lamella is computed for several cooling rates from the cooling rate model as a function of bulk Ni and P content and taenite half-width. The calculated central Ni content is then plotted vs. the half-width of the taenite for several cooling rates (Wood, 1964). Ni contents in the center of taenite phases of various half-widths are measured for a given meteorite with the EPMA. The data are plotted on the same graph as the computer simulated iso-cooling curves of central Ni content vs. taenite half-width. The measured data should fall along one of the computed iso-cooling rate curves (Wood, 1964). A

variation of this cooling rate method was developed by Rasmussen (1981), who measured the local bulk Ni and bulk P contents for each taenite lamella.

Other metallographic cooling rate methods (kamacite bandwidth, taenite maximum Ni, and kamacite central Ni content) have been developed, although they have limited applicability. The kamacite bandwidth method of Short and Goldstein (1967) relates the width of the kamacite to the cooling rate. The method cannot be employed since the effects of impingement are not considered and a constant amount of undercooling before nucleation of the Widmanstätten pattern is assumed (Saikumar and Goldstein, 1988). The taenite maximum Ni method of Short and Goldstein (1967) relates the maximum Ni content in the taenite next to the kamacite/taenite boundary measured with the EPMA with the cooling rate.

Yang et al. (1997b) proposed an empirical cooling rate indicator for meteoritic metal based on the size of the high-Ni particles, island phase, in the cloudy zone of taenite. Since the inverse relationship between high-Ni particle size (island phase size) and metallographic cooling rate holds not only for iron meteorites but also for metal in stony-irons, and stony meteorites, the scale of the cloudy taenite microstructure provides a valuable guide to relative cooling rates of metal-bearing meteorites at 350–200 °C.

To establish whether there is any variation of cooling rate within a given chemical group, it is important to minimize the uncertainty in the cooling rate measurement of each meteorite and to evaluate the inaccuracy. To establish cooling rate trends in chemical groups, careful attention must be paid to determining uncertainties in the measurement of each individual cooling rate. At this time it is not possible to determine if cooling rates vary within a chemical group, unless the individual cooling rates vary by more than a factor of 2 (Yang and Goldstein, 2006; Yang et al., 2007b; Yang et al., 2008). Table 3 summarizes the measured cooling rate data for individual chemical groups.

The highest quality cooling rate measurements have been obtained for groups IIIAB and IVA, particularly studies in which the orientation of kamacite/taenite interfaces have been measured (Yang and Goldstein, 2006; Yang et al., 2007b; Yang et al. 2008). Cooling rates vary from 56 to 338 °C/Myr for the IIIA irons and from 100 to 6600 °C/Myr for the IVA irons. In both cases, the cooling rate ranges exceed those expected for samples from a core enclosed by a silicate mantle, as such samples should have indistinguishable cooling rates.

Group	Cooling rate variation (°C/Myr)	Authors	Method
IAB	2-3	Goldstein and Short, 1967	1
	63-980	Rasmussen, 1989	1
	25-70	Herpfer et al., 1994	2
IIICD	87-480	Rasmussen, 1989	1
IIAB	0.8-10	Randich and Goldstein, 1978	3
IIIAB	1.0-10	Goldstein and Short, 1967	1
	21-185	Rasmussen, 1989	2
	56-338	Yang and Goldstein, 2006	2
IVA	7-90	Goldstein and Short, 1967	1
	2-96	Rasmussen, 1982	2
	19-3400	Rasmussen et al., 1995	2
	100-6600	Yang et al., 2008	2
IVB	2-25	Goldstein and Short, 1967	1
	110-450	Rasmussen et al., 1984	1
	1400-17000	Rasmussen, 1989	1

1. Kamacite bandwidth method (Goldstein and Short, 1967)
2. Taenite central Ni content method (includes effects of P on phase diagram and on diffusion coefficients for Ni in taenite
3. Phosphide growth simulation

Table 3. *Cooling rate variations in iron meteorite chemical groups (Goldstein et al., 2009).*

1.3.2. Alternative approach

In the last two decades, metallographic cooling rate determinations have undergone a number of refinements, yet still there exist substantial variations in cooling rates of individual iron meteorite groups. Other independent methods of cooling rate determination would be beneficial. Recent work of Dauphas (2007) shows the potential use of Fe and Ni isotopes to test the validity of the parameters and assumptions that are used in modelling the formation of Widmanstätten pattern. The main virtue of Fe and Ni isotopes is that they provide a direct test that only involves determination of an additional parameter, β. If this value is known for Fe and Ni, then isotopic fractionation can be calculated in a straightforward way from modelling the concentration profiles. Possible inaccuracies in the assumptions and parameters used in the simulations could be also tested using Fe and Ni isotopes.

1.4. Iron isotopes

Naturally occurring iron consists of four isotopes: 5.845% of ^{54}Fe, 91.754% of ^{56}Fe, 2.119% of ^{57}Fe and 0.282% of ^{58}Fe. In the last decade, advances in mass spectrometry

have allowed the detection and quantification of minute, naturally occurring variations in the ratios of the stable isotopes of iron.

The isotope geochemistry of Fe has drawn considerable attention in recent years (see Taylor and Konhauser, 2011 for review). Iron is by far an element of central importance in geosciences and life sciences, the most abundant transition element in the universe and dominant constituent of the Earth`s core. Fe isotopic studies are becoming extremely useful for tracing the geochemical processes, such as low-temperature sedimentation, redox cycling of iron in anoxic environments, bacterial reduction of Fe, hydrothermal fluid-rock interactions or high-temperature vaporisation and condensation, subduction of isotopically variable oceanic crust or crystal fractionation of magmas within the mantle. The calculated Fe isotopic fractionation factors suggest that Fe isotopic shifts will occur during important geological processes (Polyakov and Mineev, 2000). The isotopic variations of elements such as H, C, N, O or S in nature have been extensively studied in the past and a large number of analytical data for various geological materials is now available. The interest in stable isotope measurements of transition metals (such as Fe, Ni, Cu or Zn) has increased and the field of Fe isotope geochemistry has become very attractive. This course of study is still being developed, with particular attention to fractionation mechanisms. The natural mass-dependent isotopic variations in the isotopic composition of Fe are small and span the range of ~ 4 per mil (‰) in $^{56}Fe/^{54}Fe$ ratios (Anbar, 2004; Beard and Johnson, 2004a). The resolution of these small natural isotope variations requires precise and accurate isotopic analyses.

Isotopic analysis of Fe is conducted using two main types of instrumental techniques: thermal ionization spectrometry (TIMS) and multi-collector inductively coupled plasma mass spectrometry (MC ICP-MS). TIMS technique is time-consuming, requires the use of double-spike method and suffers from the low ionization efficiency of Fe (see Fantle and Bullen, 2009 for details). In contrast, MC ICP-MS offers a number of advantages applicable to isotope studies of Fe and yields high ionization efficiency in the Ar plasma source. Instrumental mass bias corrections are made using sample-standard bracketing or by measuring the known isotopic composition of another element, such as Cr, that is added as internal standard to the sample. Precisions better than ~ 0.03‰ (95% confidence interval) for $\delta^{56}Fe$ have been obtained by high-mass resolution MC ICP-MS (e.g. Dauphas et al., 2009). Furthermore, when combined with in-situ laser ablation analysis, the technique can provide useful information on small-scale Fe isotopic variations from a wide range of natural samples (Košler et al., 2005; Horn et al., 2006).

1.5. Fe isotopic variations in meteorites

Various extraterrestrial samples have been extensively studied in respect to their iron isotope composition. Iron is one of the most abundant rock-forming elements in the solar system, the most abundant element in planetary cores and a major constituent of the silicate portions of planets occurring in meteorites in metallic form, as well as in silicates and sulphides. The Fe isotopic variations measured in extraterrestrial samples were most likely produced by mass-dependent processes and it appears that the solar nebula was well homogenized with respect to Fe isotopes (Zhu et al., 2001a). Figure 5 summarizes the variation in Fe isotopic composition of various solar system materials.

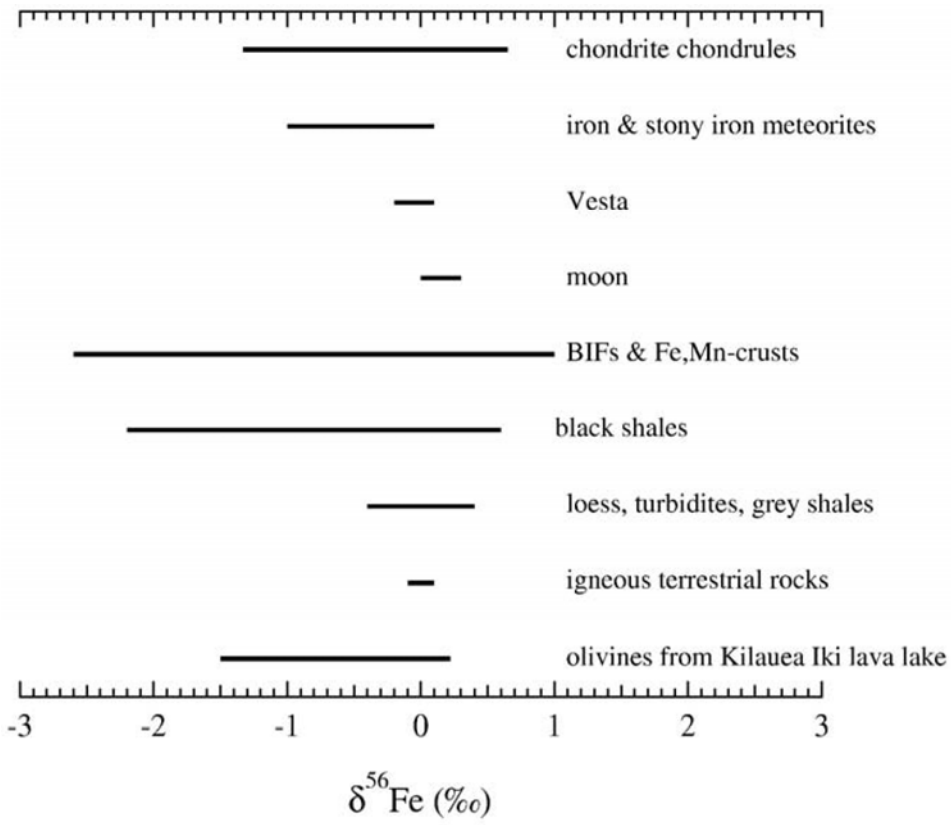

***Figure 5**. Compilation of Fe isotope compositions of various solar system materials (Hezel et al., 2010).*

Chondritic meteorites, and individual chondrules and CAIs in particular, define a spread of $^{56}Fe/^{54}Fe$ ratios of ~ 2.5 ‰ (Alexander and Wang, 2001; Zhu et al., 2001b; Kehm et al., 2003; Mullane et al., 2005; Poitrasson et al., 2005; Needham et al., 2009). Bulk

chondrites fall within a restricted isotopic range of <0.2‰ δ^{56}Fe, and chondrules define a larger range of >1‰ (-0.84‰ to 0.21‰ relative to the IRMM-14 Fe standard, Institute of Reference Materials JRC Reference Laboratory for Isotopic Measurements $^{56}Fe/^{54}Fe$ = 15.69786, $^{57}Fe/^{54}Fe$ = 0.36257). Fe isotope compositions do not vary systematically with the very large differences in total Fe concentration or oxidation state, of the H, L, and LL chondrite classes. Similarly, the Fe isotope compositions of chondrules do not appear to be determined by the H, L or LL classification of their host chondrite. This may support an origin of the three ordinary chondrite groups from variable accretion of identical Fe bearing precursors. The mean Fe isotope composition of bulk ordinary chondrites was found to be -0.06‰ (±0.12‰ 2σ; Needham et al., 2009); this is isotopically lighter than the terrestrial mean composition and all other published non-chondritic meteorite suites e.g. lunar and Martian samples, eucrites, pallasites, and irons. Ordinary chondrites, though the most common meteorites found on Earth today, were probably not the sole building blocks of the terrestrial planets (Needham et al., 2009). The Fe budget of many chondrules is dominated by their opaque phases. Hence, the bulk Fe isotope composition of these chondrules is dominated by the Fe isotope composition of their opaque phases. The variable Fe isotope compositions of chondrules are the result of elemental exchange between the still molten or at least hot chondrule and the surrounding nebula gas. This variation could be subsequently overprinted and shifted by a metasomatic event of the parent body (Theis et al, 2008; Needham et al., 2009).

The existence of subtle differences in the Fe isotope composition among inner solar system from the bulk-meteorite to the planetary scale ~ 0.3‰ in $\delta^{57}Fe/^{54}Fe$ were reported (Poitrasson et al., 2004, 2005), see Figure 6. The results of Poitrasson et al., 2009 suggest that significant iron isotope fractionation is unlikely during equilibration of molten core-forming materials in a deep magma ocean and cannot explain the determined heavier Fe isotope composition of the Moon relative to the Earth, that is isotopically heavier than Mars, Vesta and chondrite parent bodies. This issue of core–mantle isotope fractionation is central to understanding the variable Fe isotope signatures observed between chondrites, iron meteorites and the silicate portions of planets that were either interpreted in terms of contrasted planetary accretion processes (i.e. runaway growth versus giant impact, Poitrasson et al., 2004, 2005, 2007) or core–mantle differentiation (Schoenberg and von Blanckenburg, 2006; Williams et al., 2006). Processes of core formation in the early stages of terrestrial planet histories are not completely understood.

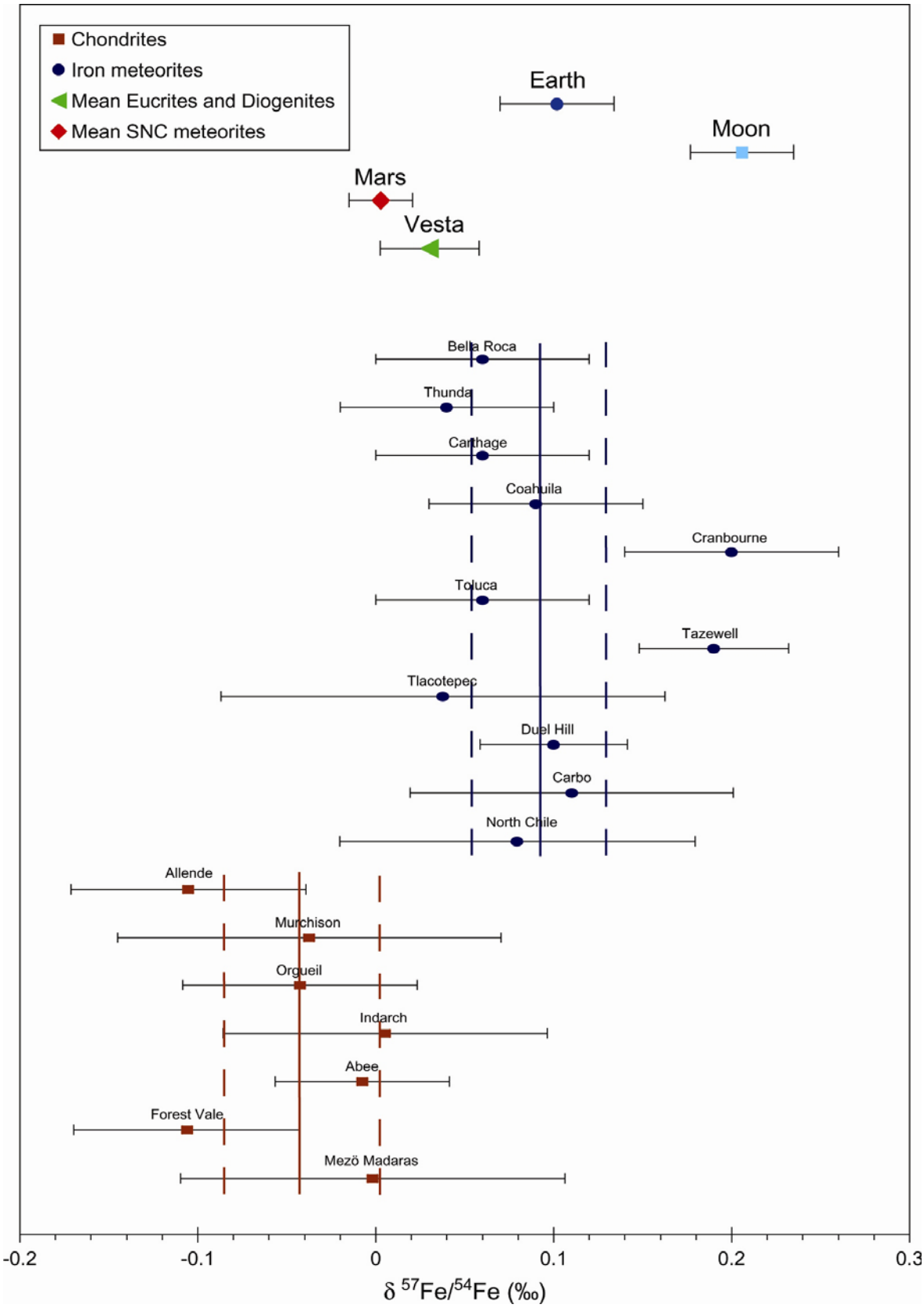

Figure 6. *Iron isotope composition of bulk chondrites and iron meteorites. Individual sample uncertainties are 2 standard errors. The mean values (solid lines) and their two standard error envelopes (dashed lines) for the two meteorite groups are shown (Poitrasson et al., 2005).*

Large isotopic variations (up to 0.5‰ in $\delta^{56}Fe$) were observed among pallasite bulk metal and olivine separates, where significant high-temperature inter-mineral isotopic fractionation during iron metal segregation occurs (Weyer et al., 2005), and between individual minerals – taenite and kamacite – that form the iron meteorites (up to 0.3‰ in $\delta^{57}Fe$) but no clear explanation of this phenomenon was provided (Poitrasson et al., 2005). This observation was therefore calling into question the significance of previously reported bulk iron meteorite data with an average bulk-rock $\delta^{56}Fe$ of –0.03±0.04‰ (2 sigma) (Beard and Johnson, 2004b; Kehm et al., 2003) where the metallic and non-metalic phases in iron meteorites were not separated and the analyzed metal samples represent mixtures of phases.

Recently, several groups have reported Fe and Ni isotope variations in adjacent taenite and kamacite in some iron meteorites (Košler et al., 2005; Horn et al. 2006; Cook et al. 2006), however, different isotopic compositions have been reported for the same iron meteorite by different researchers (e.g. Toluca, Poitrasson et al., 2005; Horn et al., 2006). This may be attributed to different sampling strategies used, however, no simple explanation of this phenomenon has been provided.

2. GOALS OF THE THESIS

In this study the extent of Fe isotopic fractionation in iron meteorites on the inter- and intra-mineral scale will be assessed using different approaches to sample preparation and analysis. The scale and extent of Fe isotopic heterogeneities in the iron meteorites and the link of isotopic variations to thermal histories of the meteorite parent bodies will be evaluated. The major objectives of the thesis are:

1. To select suitable set of iron meteorites of different structural and chemical groups and characterize the samples and their elemental compositions by electron microbeam techniques. Thorough description of internal structure of the meteorite samples together with microchemical characterization of mineral phases present is crucial prior to their sampling for isotopic analysis.

2. To evaluate the scale and extent of Fe isotopic heterogeneities in the iron meteorites by acquiring Fe isotopic data of kamacite and taenite coexisting in iron meteorites, using independent analytical techniques with variable spatial resolution capabilities (laser ablation and solution MC ICP-MS and SIMS).

3. To compare the results obtained using these methods and to compare the measured Fe isotopic composition of taenite-kamacite pairs from different chemical and structural groups of iron meteorites (find the possible relationship between the magmatic and non-magmatic groups).

4. To discuss the potential mechanisms of Fe isotopic fractionation in iron meteorites.

5. To examine the possible relation between Fe isotopic fractionation in iron meteorites and meteorite cooling histories which could provide us with additional information for deciphering more complete thermal histories of iron meteorites and their planetary parent bodies.

This thesis consists of a general text and two published articles that deal with geochemistry, isotopic studies, and magnetic properties of specific meteorites. These

articles summarize the results which were obtained and published during my PhD study and are enclosed at the end of this thesis as a supplementary material.

3. SAMPLES AND SAMPLE PREPARATION

For the purpose of this study eight iron meteorites from the octahedrite group, exhibiting well-developed Widmanstätten pattern of kamacite-taenite intergrowths were selected. The samples were loaned from the Department of Geochemistry at Charles University and from Naturhistorisches Museum in Vienna, Austria. The selected samples cover a wide range in Ni and trace element contents, representing members of different chemical groups and structural subgroups (Fig. 7). The chosen samples include both magmatic and non-magmatic iron meteorites, thus they are expected to originate from different iron meteorite parent bodies. The list of all samples with their principal characteristics is given in Table 4. To minimize the potential effect of alteration on the Fe isotopic composition (Poitrasson et al, 2004), sampling the vicinity of fusion crust was avoided and only fresh sample interiors were chosen for the analysis.

Name	Group	Structure	Ni wt%	Ga μg/g	Ge μg/g	Ir μg/g	Likely origin
Alt Biela	IID	Om	10.04	75	84	16	fractional crystallization of core
Joe Wright Mountain	IIIAB	Om	9.3	20.1	35.5	0.015	fractional crystallization of core
Gibeon	IVA	Of	7.59	2.18	0.11	2.51	fractional crystallization of core
Nelson County	IIIF	Ogg	7.02	6.33	0.84	6.25	fractional crystallization of core
Bohumilitz	IAB	Og	7.22	77.6	264	2.04	impact melting?
Canyon Diablo	IAB	Og	7.01	81.8	327	2.32	impact melting?
Toluca	IAB	Og	8.03	72.1	237	2.41	impact melting?
Horh Uul	IIIAB	Om	9.77	27.5	46.3	0.236	fractional crystallization of core

Table 4. *Characterization and trace element composition of analyzed iron meteorites. All compositional data were taken from Koblitz (2003).*

Alt Biela

A mass of about 4kg was said to have fallen at the beginning of nineteenth century, it was found in 1898 in the Ostrava region, Czech Republic. This octahedrite was later described by Buchwald (1975) and analysed for trace elements by INAA and classified as a member of IID group by Kracher et al. (1980). The Widmanstätten pattern with 0.7 mm kamacite bandwidths is visible on the polished surface. The meteorite contains inclusions of schreibersite.

Joe Wright Mountain

A mass of 43 kg was found in Arkansas, USA in 1884. The meteorite was analyzed by Scott et al. (1973) and further described by Buchwald (1975).This medium-grained octahedrite with 0.9 mm kamacite bandwidths and low Ir concentration contains cohenite and rare inclusions of troilite.

Gibeon

Large masses were reported near the East bank of the Great Fish River, Great Namaland, Namibia in 1836. At least 81 masses totalling about 21,400 kg have now been recovered. Detailed description of the recovered meteorite fragments can be found in Buchwald (1975). Due to high abundance of the samples in repositories, numerous analyses and experimental studies have been performed on this meteorite (see Koblitz, 2003 for more information). This meteorite contains nodules of recrystallized troilite, daubreelite ($FeCr_2S_4$) particles in kamacite, and rare silica inclusions.

Nelson County

A mass of 73 kg was found in 1856 in Kentucky, USA. The meteorite was classified by Scott and Wasson (1976) and further described by Buchwald (1975) as a sample exhibiting signs of pre-terrestrial cold deformation. The meteorite is a coarsest octahedrite with etched section displaying a very irregular kamacite lamellae that range from 1-10 mm in width. Nelson County is the most thoroughly deformed (pre-terrestrial, cold-worked) iron meteorite known. All structural elements - kamacite, plessite, taenite, and troilite - are heavily kneaded and sheared. The kamacite has Neumann lines that are bent and faulted. The taenite and plessite fields are sheared and torn apart as is the schreibersite. This is indicative of a violent, plastic deformation event.

Bohumilitz

A mass of about 52kg was found near Bohumilitz Castle, Czech Republic, in 1829. A second mass of 962g was found near Bohumilitz in 1899, and a third mass of 5850g was found in 1925 at Vyškovice. Classification and analysis was done by Wasson (1970). The meteorite is heavily weathered, but the fresh interior shows kamacite lamellae of 1.9 mm in width. Besides silicate inclusions, it contains inclusions of graphite, troilite and schreibersite.

Canyon Diablo

Numerous masses of total weight over 30 tons and ranging from minute fragments to pieces of over 500 kg have been found in 1891 in the vicinity of a crater-like stucture known as "Meteor Crater" 10 miles SE of Canyon Diablo, Arizona, USA. Comprehensive description, transported masses, and history of the find were done by Buchwald (1975). This iron meteorite has been subject of many studies, for references see Koblitz (2003). The meteorite contains inclusions of carbides (cohenite, haxonite and moissanite), schreibersite, troilite and graphite.

Toluca

Numerous masses, more than 3000 kg, were found near the village of Xiquipilco, Mexico, and were being forged into agricultural equipment in 1776. Due to high abundance of the samples in repositories, many analyses and experimental studies have been performed on this meteorite (see Koblitz, 2003 for more information). This coarse-grained octahedrite contains silicate inclusions and inclusions of troilite, schreibersite, graphite and carbides (haxonite and cohenite).

Horh Uul

A 44 kg specimen was found on the foothills of the Horh Mountains and the meteorite was then purchased by a private collector. Mineralogy and classification can be found in Russell et al. (2004). The meteorite is moderately weathered. The fresh interior shows the Widmanstätten pattern with 0.8 mm kamacite bandwidths. It has a low sulphide content, irregular inclusions of shreibersite and very low shock stage.

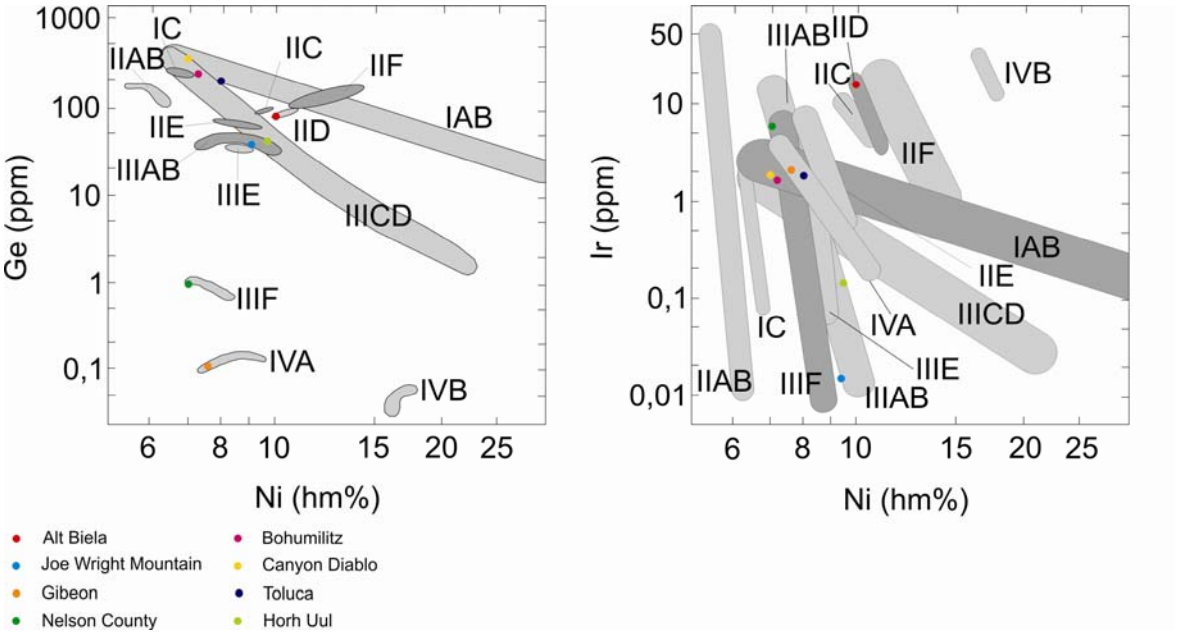

***Figure 7**. Plots of Ge vs. Ni and Ir vs. Ni showing the fields for the iron meteorite groups. The compositions of studied samples are marked by colour dots.*

Synthetic Fe-Ni alloys

In order to test the effect of variable Ni content, such as observed in kamacite and taenite phases in iron meteorites, on the measured Fe isotopic ratios, we have prepared and analyzed synthetic Fe-Ni alloys with variable Ni contents – pure Fe starting material, Fe-Ni (10 wt. %), and Fe-Ni (30 wt. %). The alloys were produced by melting Fe-metal (99.998% purity, supplied by the Koch-Light Laboratory, U.K.) and Ni-metal (99.98% purity, supplied by the Research Institute for Metals, Czech Republic) mixture in electrical arc furnace in Ar atmosphere at Department of Condensed Matter Physics, Faculty of Mathematics and Physics, Charles University, Prague. The experimental charges were then quenched in water-cooled crucibles, mounted in epoxy blocks, polished and checked for composition and Fe/Ni homogeneity using EDS, WDS and backscattered electron techniques. These alloys were then used for testing the matrix effects and for calibration of the instruments (see Košler et al., 2005 and Košler et al., 2006 for details).

The samples and standards were mounted in 1 inch epoxy resin blocks, except for large meteorite slabs that were analyzed in their original form. They were all polished using diamond polishing paste to achieve flat and smooth surface suitable for electron microbeam, laser ablation MC ICP-MS and SIMS analysis. Samples of meteorites (0.8-1.0 g) with well developed taenite lamellae designated for solution MC ICP-MS were placed

in flasks containing 150 ml of 0.2 N HCl at laboratory temperature. They were kept in this solution for two months until the kamacite was completely dissolved, leaving only skeletal taenite lamellae (see Rasmussen et al., 1988 for details of the etching technique). For SIMS analysis, representative chips of meteorite samples Toluca, Horh Uul and Bohumilitz, IRMM-014 reference standard and three synthetic Fe-Ni alloys were cast in epoxy. The mount was polished using diamond polishing paste and coated with thin gold layer (2-5 nm) before analysis.

4. ANALYTICAL METHODS

4.1. Electron probe microanalysis

The characterization of the sample elemental compositions was done using backscattered electron (BSE) images and quantitative X-ray wavelength dispersive spectral analysis on a CamScan 3200 scanning electron microscope fitted with MICROSPEC 3PC X-ray wavelength dispersive system at the Czech Geological Survey. The analyses of taenite and kamacite were performed using accelerating voltage of 20 kV, 22 nA beam current, 10 μm beam size and ZAF correction procedures. The counting times were 20 s for Fe and Ni and 30 s for Co and P. Pure metal standards for Fe, Ni and Co were used for calibration. In addition, a synthetic GaP standard was used to calibrate P measurements. Details of analytical conditions, standards and detection limits of measured elements for both instruments are presented in Table 5. Relative uncertainties are calculated to be <1% at the >10 wt. % level, <12% at the ~1 wt. % level and >20% at the <0.5 wt. % level.

MICROSPEC 3PC X-ray wavelength dispersive system

Element	Standard (mineral name)	Element wt%	Crystal	X-ray line	CT-P-STD	CT-B-STD	CT-P-SMP	CT-B-SMP	Detection limit (ppm)
Fe	Pure Iron	99.998	LIF	Kα	20	10	20	10	213
Ni	Pure Nickel	99.980	LIF	Kα	20	10	20	10	255
Co	Pure Cobalt	99.990	LIF	Kα	30	10	30	10	286
P	Galium Phosphide	30.760	PET	Kα	30	10	30	10	186

CT-P-STD = counting time on the peak (standard)
CT-B-STD= counting time on the background (standard)
CT-P-SMP = counting time on the peak (sample)
CT-B-SMP= counting time on the background (sample)

***Table 5**. Details of analytical conditions, used standards and detection limits of measured elements for MICROSPEC 3PC X-ray wavelength dispersive system.*

4.2. Laser ablation and solution MC ICP-MS

Iron isotopic analyses of iron meteorite samples were performed on a Finnigan Neptune high-mass resolution MC ICP-MS coupled to a New Wave UP-213 UV Nd:YAG laser at the University of Bergen.

4.2.1. Laser ablation

The samples were placed in a 35 cm^3 ablation cell mounted on the motorized stage of the microscope. The sample cell was flushed with He gas (99.9999% purity, 0.9 l/min)

which was mixed with Ar (0.7 l/min) at the back end of the ICP torch before entering the plasma. The laser was fired at 10 Hz repetition rate using energy density of 0.5-2 J cm^{-2} and laser beam diameter of 20-60 μm, subject to the width of the lamellae. The ablation rate was measured by moving the focus of the optical microscope between sample surface and the bottom of the laser crater, and it varied between 0.1 and 0.3 μm per laser pulse, subject to the energy density used for ablation. To suppress the laser-induced isotopic fractionation of Fe and to improve the reproducibility of Fe isotopic measurements, the analyses were obtained from linear rasters of the laser beam (raster speed 10μm/s) within the adjacent kamacite and taenite lamellae exposed on the polished sample surface, see Figure 8. (Košler et al., 2005). During rastering, the sample was moved under stationary laser beam at speed of 10 μm s^{-1} and typically 2-3 raster passes over the same area of the sample were performed during single analysis.

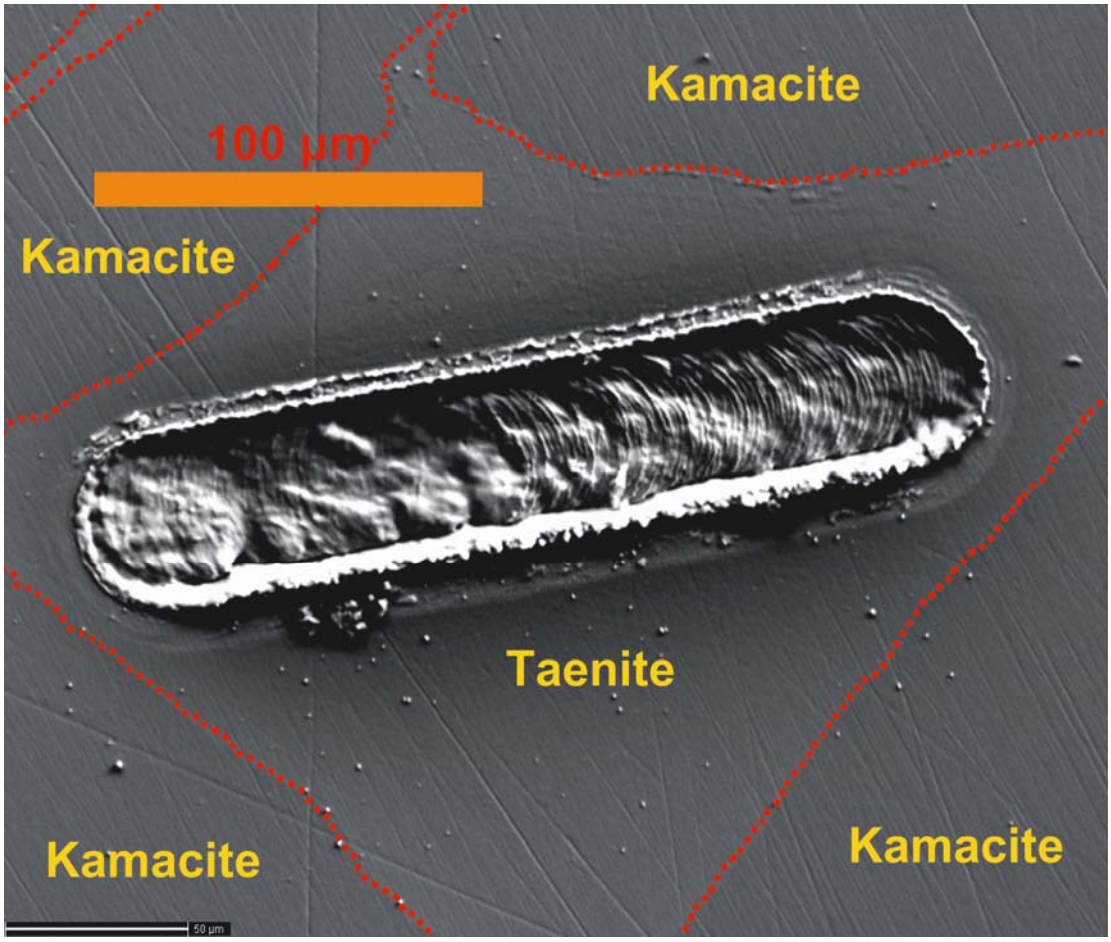

Figure 8. *Secondary electron image (SEI) of the iron meteorite sample surface showing the laser raster track in the analyzed taenite.*

4.2.2. MC ICP-MS analytical conditions

The ICP source of MC ICP-MS was operated at hot plasma conditions at 1350 W. The mass resolving power of 6450 (5,95% definition - Weyer and Schwieters, 2003) was achieved by employing narrow entrance and exit slits in combination with tuning of high mass resolution ion lenses of the Neptune MC ICP-MS. The peak intensities of Fe isotopic signals were measured in the centre of the ca. 15 milli-a.m.u. (atomic mass units) wide plateau on the lower mass side of the Fe peaks (Fig. 9).

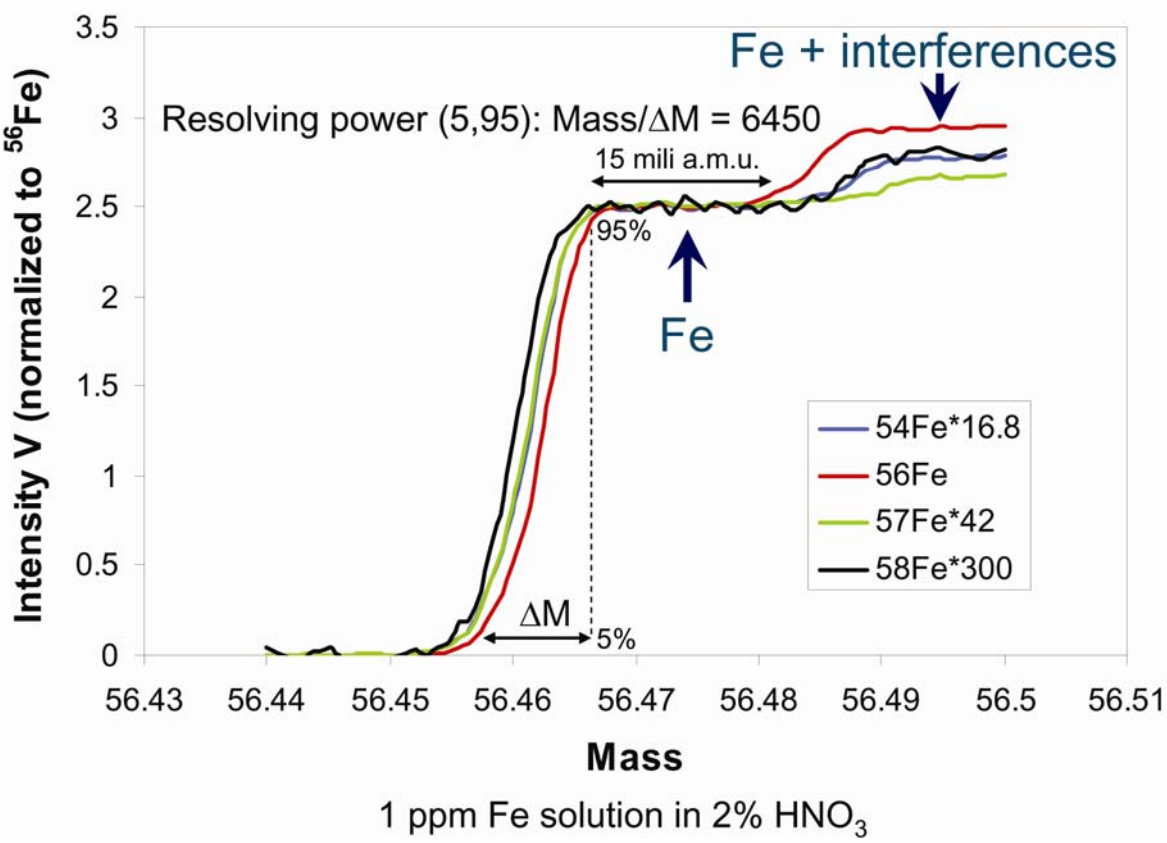

***Figure 9**. Mass scan performed in the Neptune´s high mass resolution mode showing all Fe isotopes, the center of the plateau and a peak consisting of Fe and polyatomic interferences are marked with arrows. Fe isotope ratios can be measured interference-free on the plateau. Signal intensities are normalized to 56Fe.*

Data were acquired in a static mode using six detectors from an array of nine faraday cups - the four Fe isotopes with masses 54, 56, 57 and 58 were measured and the contributions of Cr and Ni were monitored using masses 53 and 60, respectively. Figure 10 shows the analytical settings of the MC ICP-MS instrument. Typically, a single analysis consisted of measurement of the instrument baseline, 120 isotopic ratios obtained during

40 s of gas blank measurement, followed by 200 s of acquisition corresponding to the laser ablation sampling. All Fe isotopic values are reported relative to the IRMM-014 iron isotope standard (which is -0.09 and -0.11‰ relative to bulk Earth for $\delta^{56}Fe$ and $\delta^{57}Fe$, respectively; Beard and Johnson, 2004b). Uncertainties reported in this work are 2σ standard errors of multiple measurements made on each sample and include the uncertainties of standard measurements used for bracketing.

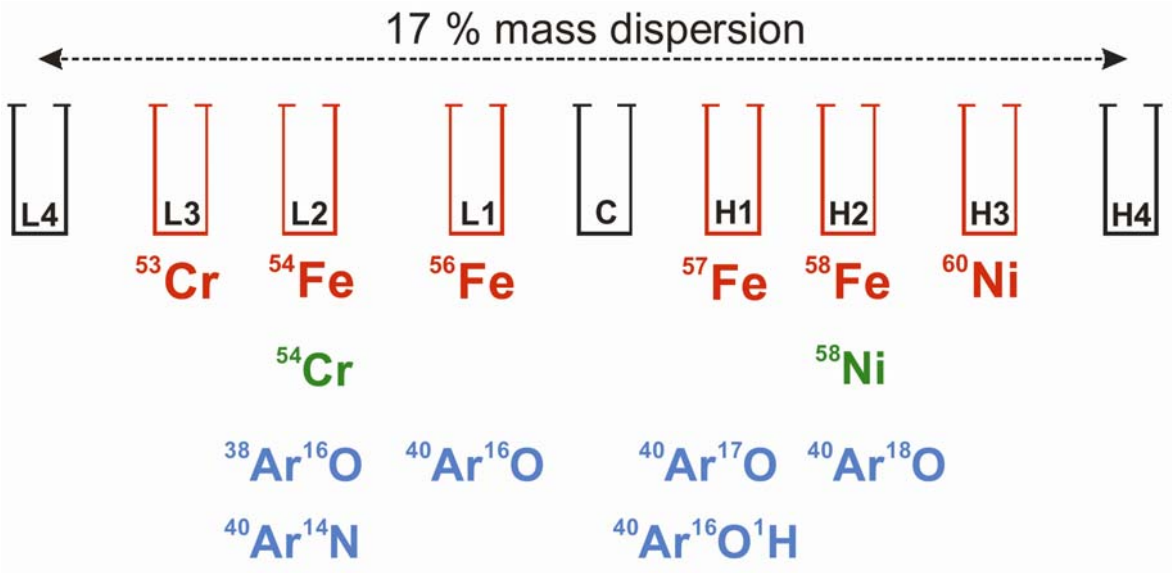

Figure 10. *Detector configuration used for the Fe high mass resolution simultaneous measurements. All major mono- and polyatomic interferences are marked.*

4.2.3. Isobaric interference

ICP-MS analyses of Fe suffer from isobaric interference with molecular species present in the ICP argon gas (mainly $^{40}Ar^{14}N^{+}$, $^{40}Ar^{16}O^{+}$, $^{40}Ar^{16}O^{1}H^{+}$, $^{40}Ar^{18}O^{+}$). The technique for dealing with the interferences used in this study closely followed the procedure for high mass resolution analysis of Fe isotopes described in Weyer and Schwieters (2003). The cup positioning and mass calibration were checked frequently using 1 ppm Fe solution in 2% HNO_3 to ensure that intensities of Fe isotopic signals were measured in the centre of the ca. 15 milli-amu plateau on the lower mass side of the Fe peaks, thus avoiding the interfering molecular ions. A mass resolving power of 6450 (5,95% definition) was routinely achieved by employing a narrow entrance slit in combination with tuning of high mass resolution ion lenses of the Neptune MC ICP-MS.

The atomic isobaric interferences of Cr on ^{54}Fe, Ni on ^{58}Fe can also affect the isotopic measurements of Fe in Cr-, and Ni-rich metal samples. Although the amount of Cr present in the studied samples was very small, all iron meteorite analyses were corrected for the ^{54}Cr interference on ^{54}Fe using the measured intensity of the ^{53}Cr and the natural Cr isotopic composition. The interference of ^{58}Ni on the minor ^{58}Fe isotope was too large (up to 100% of the ^{58}Fe intensity) and it could not be corrected for without a significant loss in precision and accuracy of the corrected ^{58}Fe/^{54}Fe ratios. As a result, the δ^{58}Fe values will not be reported here.

4.2.4. Instrumental mass bias

The measured isotopic ratios were corrected for mass discrimination from measurements of the IRMM-014 isotopic reference material (Institute of Reference Materials JRC Reference Laboratory for Isotopic Measurements ^{56}Fe/^{54}Fe = 15.69786, ^{57}Fe/^{54}Fe = 0.36257) before and after each analysis (standard-sample-standard bracketing; Beard et al., 2003). Based on the repeated measurements of IRMM-014, the variations in the mass bias during a single day were less than 0.5‰ per amu (2 standard deviations). The Fe isotopic data are further reported using the conventional delta notation:

$$\delta^{56}Fe = \left[\frac{\left(\frac{^{56}Fe}{^{54}Fe} \right)_{SAMPLE}}{\left(\frac{^{56}Fe}{^{54}Fe} \right)_{STANDARD}} - 1 \right] \times 1000 \quad (1)$$

and

$$\delta^{57}Fe = \left[\frac{\left(\frac{^{57}Fe}{^{54}Fe} \right)_{SAMPLE}}{\left(\frac{^{57}Fe}{^{54}Fe} \right)_{STANDARD}} - 1 \right] \times 1000 \quad (2)$$

where ^{x}Fe/^{54}Fe$_{sample}$ and ^{x}Fe/^{54}Fe$_{standard}$ refer to the isotopic ratios for sample and IRMM-014 standard, respectively.

4.2.5. Precision and reproducibility

The internal precision of individual laser analyses (120 ratios collected over 200 s of ablation) was better than 0.15 and 0.20‰ (2σ) for $\delta^{56}Fe$ and $\delta^{57}Fe$, respectively. The long term reproducibility of Fe isotopic measurements (IRMM-014 over a period of 4 months) was 0.16 and 0.21‰ (2σ) and the corresponding mean values for $\delta^{56}Fe$ and $\delta^{57}Fe$ were -0.02 and 0.06‰, respectively.

4.2.6 Solution MC ICP-MS

To complement the laser ablation MC ICP-MS in-situ analyses by bulk kamacite and taenite data, the isotopic composition of Toluca, Horh Uul and Bohumilitz meteorites was subsequently measured by solution MC ICP-MS. Samples of meteorites (0.8-1.0 g) with well developed taenite lamellae were placed in flasks containing 150 ml of 0.2 N HCl at laboratory temperature. They were kept in this solution for two months until the kamacite was completely dissolved, leaving only skeletal taenite lamellae. One lamella of taenite residue from each sample was used for the analysis. It was dissolved in 1.5 ml of 50 % aqua regia, dried down and re-dissolved in 2.5 ml of 8N HCl. An aliquot of the kamacite 0.2 N HCl solution was also dried down and re-dissolved in 8N HCl. The kamacite and taenite HCl solutions (0.5 ml each) were then purified using the chromatographic separation (Strelow, 1980). The $^{56}Fe/^{54}Fe$ and $^{57}Fe/^{54}Fe$ isotopic ratios were determined using the Finnigan Neptune high-mass resolution MC ICP-MS using standard-sample-standard bracketing with solution of IRMM-014 isotopic reference material before and after each analysis.

4.3. SIMS analysis

The secondary ion mass spectrometry (SIMS) was used for direct in situ measurement of isotopic composition of Fe in selected micrometer sized areas of three meteorite samples - Horh Uul, Toluca and Bohumilitz. Compared to LA MC ICP-MS, the SIMS is capable of achieving a better spatial resolution that is required to further resolve isotopic variations within the taenite lamellae. In addition, the SIMS analyses were also used to verify the results obtained by LA MC ICP-MS. The analyses were performed at the Swedish Museum of Natural History, Stockholm (NordSIM facility) using a Cameca IMS1270 ion microprobe. The technique followed the procedure described in Whitehouse and Fedo (2007).

4.3.1. Primary ion beam

An O_2^- primary ion beam was used with incident energy of 13 kV. The primary column mass aperture of 150 μm was used to produce elliptical, sputtering craters with flat bottom and long axes of ca. 18 μm (150 μm aperture) and corresponding ion beam currents of ca. 6 nA.

4.3.2 Secondary ion beam

Positive secondary ions were extracted at 10 kV, using an energy window of 60 eV. The secondary ion optics was operated in the "circular" mode in order to accomodate the ion beam in the restricted height of the multicollector exit slits.

4.3.3. Detector configuration

The detector configuration was set to accommodate simultaneous Faraday cup measurements of ^{54}Fe and ^{56}Fe both in the meteorites and in the standards. Since the iron meteorites contain small amounts of Cr, it is necessary to monitor and correct for a possible ^{54}Cr isobaric interference. An additional low mass detector was used to measure ^{52}Cr, and the correction for a possible isobaric interference on ^{54}Fe was set up. No other significant direct interferences were expected so the instrument was operated at the lowest mass resolution (500 μm exit slit). Full analytical details including instrument operating parameters and data reduction information are given in Whitehouse and Fedo (2007).

4.3.4. Matrix effect

In order to correct the data for instrumental mass discrimination and matrix effects that may result from matrix differences between IRMM-014 reference material (Fe metal) and meteorites (Fe-Ni alloy), two Fe-Ni synthetic alloys with different Ni contents were analyzed repeatedly during the session. Quantitative SEM-WDS measurements of the analyzed phases, as well as the reference material, were done adjacent to the points of analysis (Table 6).

Alloy	Ni (wt. %)	δ^{56}Fe (‰)	±2σ
$FeNi_{10}$	8.65	-1.62	0.36
$FeNi_{10}$	7.96	-1.31	0.38
$FeNi_{10}$	8.04	-1.13	0.36
$FeNi_{10}$	8.31	-0.54	0.37
$FeNi_{10}$	8.26	-1.41	0.36
$FeNi_{10}$	8.35	-1.68	0.37
$FeNi_{10}$	8.58	-1.55	0.36
$FeNi_{10}$	9.27	-0.97	0.36
$FeNi_{30}$	26.31	-3.20	0.37
$FeNi_{30}$	25.66	-2.15	0.37
$FeNi_{30}$	27.09	-3.29	0.37
$FeNi_{30}$	26.26	-2.96	0.37
$FeNi_{30}$	26.47	-3.11	0.37
$FeNi_{30}$	28.37	-3.29	0.37

Table 6*. The results of EMP and SIMS analyses of the synthetic Fe-Ni alloys.*

There was a systematic negative correlation between Ni contents and measured δ^{56}Fe values of these synthetic alloys (Fig. 11). Such matrix dependence can be described by linear equation obtained from regression of experimental data and published value δ^{56}Fe for pure Fe standard (Košler et al., 2005) as a function of Ni content in wt. %:

$$\delta^{56}Fe(‰) = -0.117107 \cdot Ni \ \ (wt.\%); \ \ R^2 = 0.963665 \tag{3}$$

Since the Ni content of analyzed areas within the meteorite samples varied significantly, all measured SIMS data were corrected for this matrix effect following an equation:

$$\delta^{56}Fe(‰)_{corrected} = \left[\delta^{56}Fe(‰)\right]_{measured} + 0.117107 \cdot Ni \ \ (wt.\%) \tag{4}$$

All data are reported relative to the reference material IRMM-014.

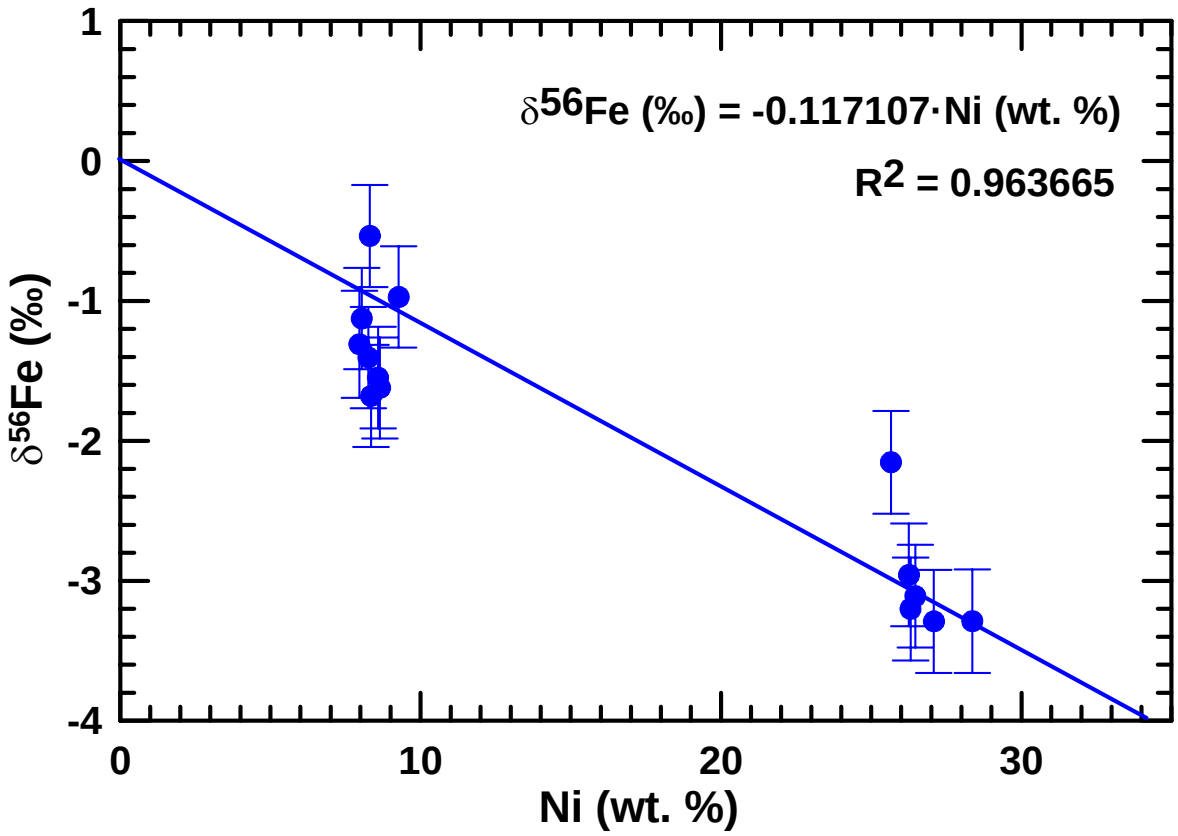

Figure 11. *Linear regression model based upon the SIMS analyses of synthetic Fe-Ni alloys used for correction on matrix effect.*

5. RESULTS

5.1. Laser ablation and solution MC ICP-MS analyses

The analysis of inter-mineral variation in the Fe isotopic composition of the studied iron meteorites showed that iron meteorite interiors exhibit much greater Fe isotopic variations than bulk irons. The laser ablation MC ICP-MS analyses show distinct $\delta^{56}Fe/^{54}Fe$ and $\delta^{57}Fe/^{54}Fe$ values for coexisting FeNi phases kamacite (Ni-poor) and taenite (Ni-rich) in all studied meteorites. Data are also reported for cohenite $(FeNi)_3C$, that was measured in the Joe Wright Mountain meteorite. Table 7. summarizes Fe isotopic data for the studied iron meteorites. Measured isotopic ratios show raw data, which were corrected for instrument mass bias and residual laser-induced isotopic fractionation using external calibration to synthetic IRMM-014 standard.

The Fe isotopic composition of studied phases from different meteorite chemical groups shows significant variation of up to ~ 3.6‰ in $\delta^{56}Fe$ (Fig. 12), with data plotting along the mass dependent isotopic fractionation line in the three isotope plot ($\delta^{56}Fe$ vs. $\delta^{57}Fe$; Fig. 13).

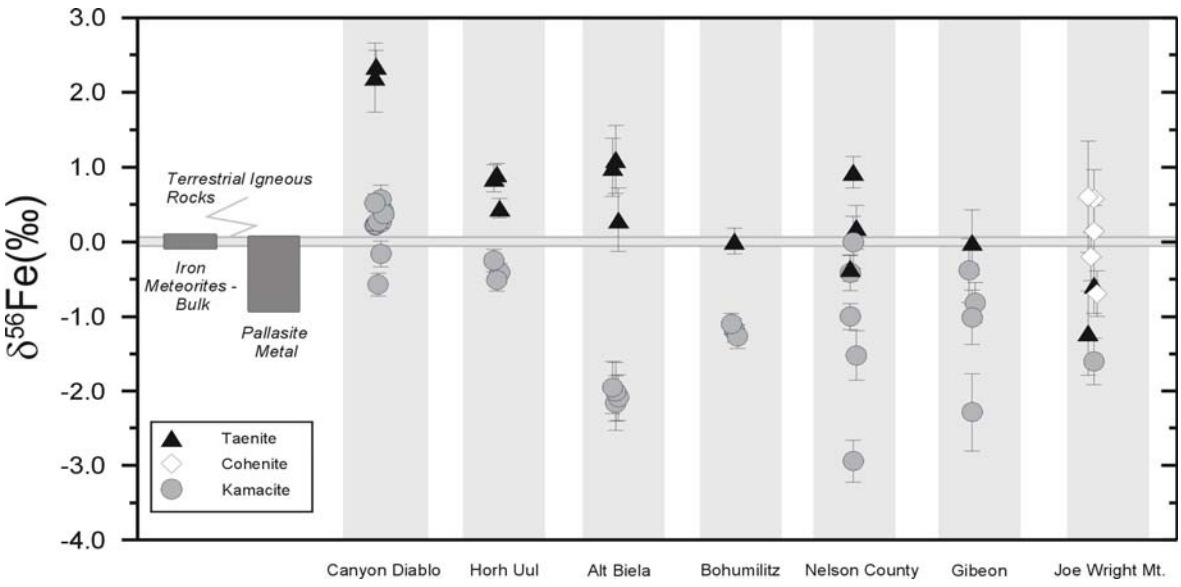

Figure 12. *Fe isotopic composition of analyzed iron meteorites compared to the composition of terrestrial igneous rocks, pallasites, and bulk iron meteorites (Hezel et al., 2010). Uncertainties are 2σ.*

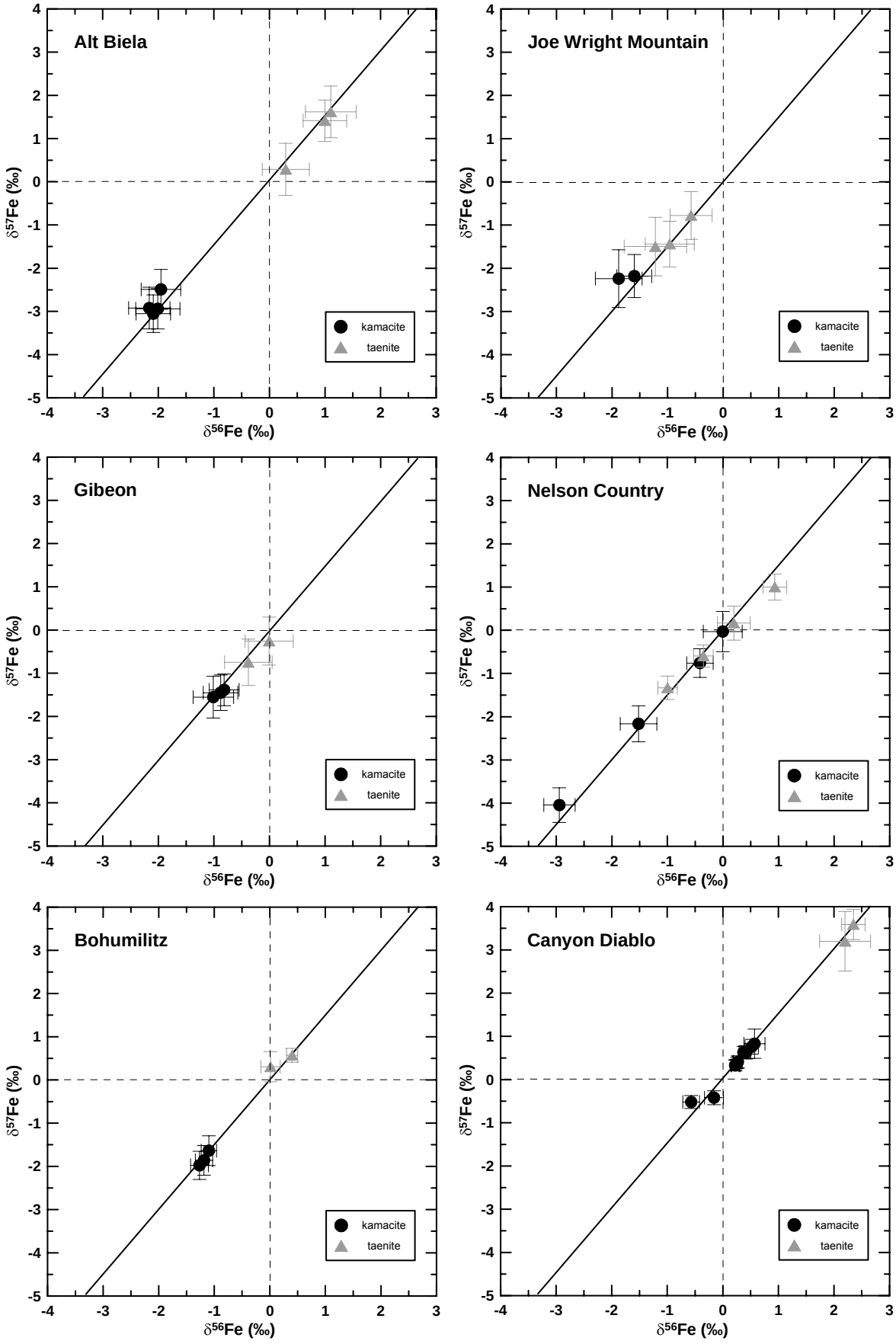
Alt Biela
Joe Wright Mountain
Gibeon
Nelson Country
Bohumilitz
Canyon Diablo
kamacite
taenite
δ57Fe (‰)
δ56Fe (‰)

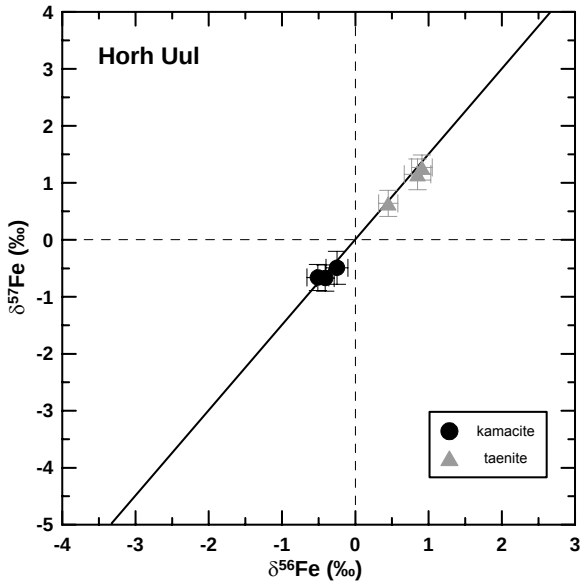

***Figure 13**. Three isotope plots ($\delta^{5}Fe$–$\delta^{56}Fe$) for individual iron meteorites analyzed by laser ablation MC ICP-MS showing the variability in taenite (triangles) and kamacite (circles) isotopic compositions along the mass dependent isotopic fractionation line (full lines). Error bars correspond to 2σ uncertainties.*

The composition of Fe in taenite is isotopically heavier compared to kamacite in all studied meteorites. Cohenite from Joe Wright Mountain meteorite appears to be isotopically heavier than the coexisting taenite. For kamacite, the $\delta^{56}Fe$ values range from -2.94 ± 0.28‰ to +0.57 ± 0.19‰ (variation of ~ 3.5‰ in $\delta^{56}Fe$) and the $\delta^{57}Fe$ values range from -4.04 ± 0.4‰ to +0.83 ± 0.34‰ (variation of ~ 4.9‰ in $\delta^{57}Fe$). Taenite $\delta^{56}Fe$ values range from -1.22 ± 0.56‰ to +2.35 ± 0.21‰ (variation of ~ 3.6‰ in $\delta^{56}Fe$) and the $\delta^{57}Fe$ values vary from -1.50 ± 0.68‰ to +3.59 ± 0.35‰ (variation of ~ 5.1‰ in $\delta^{57}Fe$). Cohenite $\delta^{56}Fe$ values range from -0.69 ± 0.31‰ to +0.60 ± 0.75‰ (variation of ~ 1.3‰ in $\delta^{56}Fe$) and $\delta^{57}Fe$ values are in the range of -0.99 ± 0.37‰ to +0.81 ± 0.96‰ (variation of ~ 1.8‰ in $\delta^{57}Fe$).

The Alt Biela meteorite has the largest variation in $\delta^{56}Fe$, between -2.16 and +1.10‰. The Gibeon meteorite has the smallest range, between -1.01 and -0.01‰ in $\delta^{56}Fe$. The heaviest kamacite was recorded in the Nelson County meteorite, having the $\delta^{56}Fe$ of -2.94 ± 0.28‰, however this sample exhibits the most scattered Fe isotopic composition. The lightest taenites were measured in the Canyon Diablo meteorite.

The relative difference $\Delta^{56}Fe_{taen\text{-}kam}$ in isotopic composition of the taenite-kamacite pairs can be expressed using the conventional notation:

$$\Delta^{56}Fe_{taen-kam}(‰) = \delta^{56}Fe_{taenite} - \delta^{56}Fe_{kamacite} \quad (5)$$

The presented $\Delta^{56}Fe_{taen\text{-}kam}$ values are calculated from the averages of kamacite and taenite compositions of individual meteorites (see Table 7). The extent of variation in the Fe isotopic composition differs significantly for individual meteorite samples and such variations in iron meteorites have not been previously described.

There is no correlation between the isotopic composition of the taenite-kamacite pairs and the bulk Ni content of the studied meteorites (thus no obvious relation to the width of taenite lamellae), see Fig. 14. The results indicate that there is no relationship between samples of the same chemical group IA (Bohumilitz, Canyon Diablo, and Toluca) and iron isotopic composition of their Fe-Ni phases. There is also no relation between the isotopic composition and supposed origin of meteorites (no similarity amongst magmatic or non-magmatic members).

Results of bulk kamacite and taenite MC ICP-MS solution analysis of Horh Uul, Toluca and Bohumilitz meteorites are listed in Table 8. The overall variation of the Fe isotopic composition obtained by solution analysis is 0.4‰ in $\delta^{56}Fe$ and the data plot along the mass dependent fractionation line in the three isotope plot on Fig. 15. Consistent with the in-situ isotopic measurements, the composition of Fe in taenite is isotopically heavier compared to the kamacite for Horh Uul and Toluca meteorites, while for Bohumilitz the fractionation between taenite and kamacite cannot be resolved outside the analytical uncertainties obtained from the solution analysis.

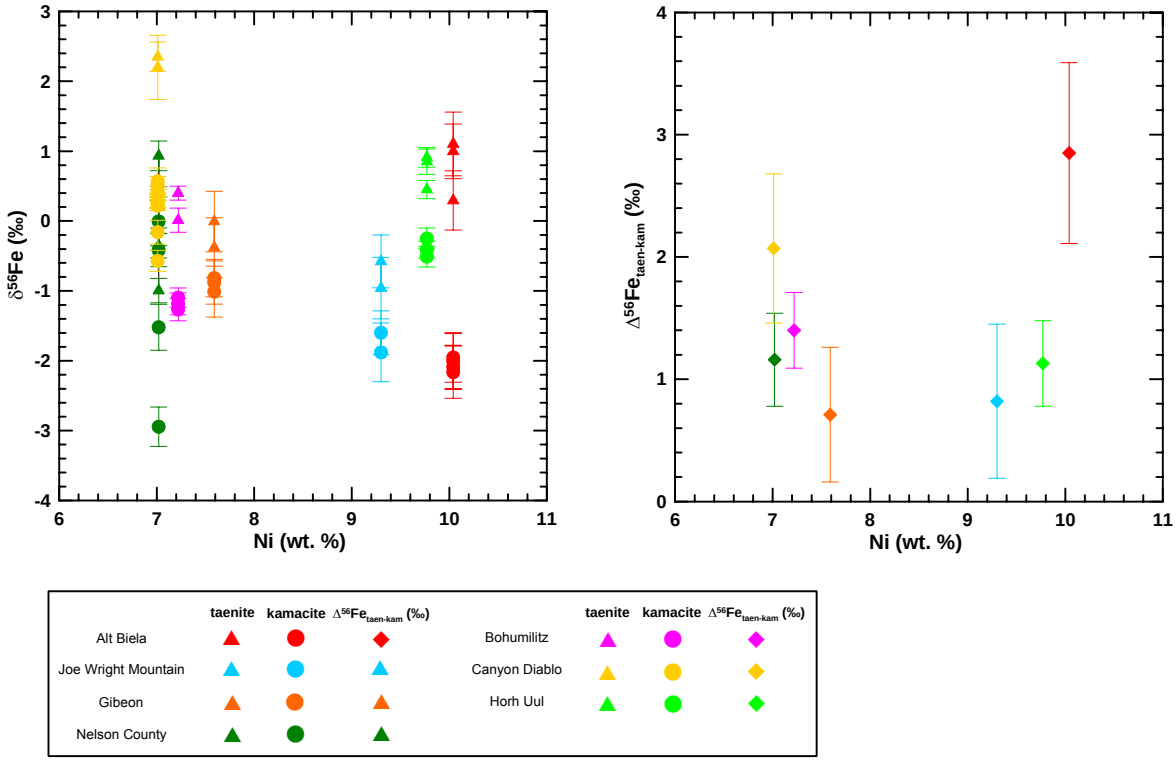

Figure 14. *Plots of $\delta^{56}Fe$ vs. Ni and $\Delta^{56}Fe_{taen\text{-}kam}$ vs. Ni for individual iron meteorites show that there is no obvious correlation between the Fe isotopic composition of the samples and their Ni content.*

Sample	Mineral phase	Measured isotopic ratios				Corrected isotopic ratios				Per mil relative to IRMM-014					
		$^{56}Fe/^{54}Fe$	±2σ	$^{57}Fe/^{54}Fe$	±2σ	$^{56}Fe/^{54}Fe$	±2σ	$^{57}Fe/^{54}Fe$	±2σ	δ56Fe	±2σ	δ57Fe	±2σ	Mean $\Delta^{56}Fe_{taen-kam}$	±2σ
Alt Biela	Kamacite	17.20137	0.00223	0.40394	0.00007	15.66721	0.36166	0.00279	0.00008	- 1.95	0.36	- 2.49	0.46	2.85	0.74
	Kamacite	17.21259	0.00243	0.40412	0.00006	15.66631	0.36150	0.00312	0.00008	- 2.01	0.40	- 2.94	0.46		
	Kamacite	17.18080	0.00180	0.40321	0.00007	15.66505	0.36146	0.00244	0.00008	- 2.09	0.31	- 3.05	0.43		
	Kamacite	17.18162	0.00275	0.40325	0.00008	15.66390	0.36151	0.00291	0.00009	- 2.16	0.37	- 2.92	0.48		
	Taenite	17.19460	0.00224	0.40378	0.00006	15.71352	0.36308	0.00308	0.00009	1.00	0.39	1.41	0.48		
	Taenite	17.23313	0.00332	0.40492	0.00010	15.71518	0.36315	0.00359	0.00011	1.10	0.46	1.62	0.60		
	Taenite	17.20707	0.00289	0.40413	0.00010	15.70247	0.36267	0.00333	0.00011	0.29	0.42	0.29	0.60		
Joe Wright Mountain	Kamacite	17.07156	0.00233	0.40036	0.00008	15.67276	0.36178	0.00246	0.00009	- 1.60	0.31	- 2.18	0.50	0.82	0.63
	Kamacite	17.15526	0.00150	0.40284	0.00006	15.66834	0.36175	0.00331	0.00012	- 1.88	0.42	- 2.24	0.67		
	Taenite	17.12296	0.00281	0.40186	0.00009	15.68880	0.36228	0.00296	0.00010	- 0.58	0.38	- 0.78	0.55		
	Taenite	17.14565	0.00136	0.40247	0.00003	15.68276	0.36204	0.00348	0.00010	- 0.96	0.44	- 1.44	0.53		
	Taenite	17.14050	0.00462	0.40237	0.00012	15.67872	0.36202	0.00442	0.00012	- 1.22	0.56	- 1.50	0.68		
	Cohenite	17.05144	0.00248	0.39968	0.00009	15.70007	0.36261	0.00270	0.00010	0.14	0.34	0.11	0.57		
	Cohenite	17.11737	0.00603	0.40176	0.00017	15.70736	0.36286	0.00585	0.00017	0.60	0.75	0.81	0.96		
	Cohenite	17.13583	0.00179	0.40220	0.00007	15.69472	0.36245	0.00251	0.00009	- 0.20	0.32	- 0.33	0.52		
	Cohenite	17.17009	0.00177	0.40323	0.00007	15.70692	0.36280	0.00304	0.00010	0.58	0.39	0.65	0.55		
	Cohenite	17.11332	0.00214	0.40158	0.00005	15.68702	0.36221	0.00240	0.00007	- 0.69	0.31	- 0.99	0.37		
Gibeon	Kamacite	17.22807	0.00274	0.40454	0.00008	15.68199	0.36200	0.00286	0.00009	- 1.01	0.36	- 1.55	0.48	0.71	0.55
	Kamacite	17.19591	0.00114	0.40359	0.00003	15.68406	0.36204	0.00243	0.00007	- 0.88	0.31	- 1.45	0.41		
	Kamacite	17.16033	0.00161	0.40251	0.00005	15.68505	0.36206	0.00211	0.00007	- 0.82	0.27	- 1.38	0.37		
	Taenite	17.16902	0.00304	0.40280	0.00009	15.69189	0.36229	0.00336	0.00010	- 0.38	0.43	- 0.75	0.54		
	Taenite	17.17422	0.00343	0.40297	0.00010	15.69774	0.36247	0.00341	0.00010	- 0.01	0.43	- 0.26	0.56		
Nelson County	Kamacite	16.86097	0.00109	0.39369	0.00004	15.69135	0.36229	0.00187	0.00006	- 0.41	0.24	- 0.76	0.33	1.16	0.38
	Kamacite	16.87241	0.00134	0.39403	0.00005	15.65163	0.36110	0.00221	0.00007	- 2.94	0.28	- 4.04	0.40		
	Kamacite	16.91441	0.00199	0.39532	0.00006	15.67399	0.36178	0.00258	0.00008	- 1.52	0.33	- 2.16	0.42		
	Kamacite	17.00072	0.00179	0.39799	0.00006	15.69779	0.36256	0.00275	0.00008	- 0.00	0.35	- 0.03	0.46		
	Taenite	16.86615	0.00108	0.39387	0.00004	15.68221	0.36208	0.00138	0.00005	- 1.00	0.18	- 1.33	0.27		
	Taenite	16.91628	0.00116	0.39539	0.00004	15.69233	0.36235	0.00138	0.00005	- 0.35	0.18	- 0.59	0.26		
	Taenite	16.94433	0.00145	0.39625	0.00005	15.71250	0.36293	0.00167	0.00005	0.93	0.21	1.00	0.30		
	Taenite	16.96986	0.00183	0.39703	0.00006	15.70092	0.36263	0.00232	0.00007	0.20	0.30	0.17	0.39		
Bohumilitz	Kamacite	16.50733	0.00107	0.38266	0.00006	15.67925	0.36189	0.00122	0.00006	- 1.19	0.16	- 1.86	0.34	1.40	0.31
	Kamacite	16.50475	0.00092	0.38266	0.00005	15.68065	0.36197	0.00108	0.00006	- 1.10	0.14	- 1.64	0.35		
	Kamacite	16.51161	0.00102	0.38272	0.00005	15.67798	0.36185	0.00126	0.00006	- 1.27	0.16	- 1.98	0.33		
	Taenite	16.51492	0.00036	0.38319	0.00001	15.70410	0.36277	0.00079	0.00003	0.40	0.10	0.57	0.16		
	Taenite	16.51740	0.00104	0.38315	0.00005	15.69806	0.36268	0.00136	0.00006	0.01	0.17	0.31	0.35		

***Table 7**. Fe isotopic composition of iron meteorites measured by laser ablation MC ICP-MS.*

Sample	Mineral phase	Measured isotopic ratios				Corrected isotopic ratios				Per mil relative to IRMM-014					
		$^{56}Fe/^{54}Fe$	±2σ	$^{57}Fe/^{54}Fe$	±2σ	$^{56}Fe/^{54}Fe$	±2σ	$^{57}Fe/^{54}Fe$	±2σ	δ56Fe	±2σ	δ57Fe	±2σ	Mean $\Delta^{56}Fe_{taen-kam}$	±2σ
Canyon Diablo	Kamacite	16.70790	0.00050	0.39754	0.00002	15.70120	0.36268	0.00120	0.00004	0.22	0.07	0.33	0.12	2.07	0.61
	Kamacite	16.70830	0.00060	0.39756	0.00002	15.70150	0.36269	0.00120	0.00005	0.23	0.08	0.33	0.13		
	Kamacite	16.71020	0.00060	0.39764	0.00003	15.70450	0.36280	0.00130	0.00006	0.42	0.08	0.63	0.15		
	Kamacite	16.71060	0.00080	0.39763	0.00003	15.70600	0.36284	0.00180	0.00006	0.52	0.12	0.76	0.17		
	Kamacite	16.70890	0.00060	0.39760	0.00002	15.70360	0.36280	0.00130	0.00005	0.37	0.08	0.63	0.14		
	Kamacite	16.70340	0.00060	0.39739	0.00002	15.70190	0.36271	0.00120	0.00005	0.26	0.08	0.39	0.13		
	Kamacite	16.70590	0.00060	0.39748	0.00002	15.70210	0.36271	0.00120	0.00005	0.27	0.08	0.41	0.14		
	Kamacite	16.69880	0.00140	0.39726	0.00006	15.70690	0.36287	0.00290	0.00012	0.57	0.19	0.83	0.34		
	Kamacite	16.83230	0.00120	0.40009	0.00003	15.69530	0.36242	0.00270	0.00006	- 0.16	0.17	- 0.42	0.16		
	Kamacite	16.82370	0.00110	0.40005	0.00003	15.68900	0.36238	0.00240	0.00006	- 0.57	0.15	- 0.52	0.15		
	Taenite	16.70930	0.00120	0.39758	0.00013	15.73240	0.36373	0.00720	0.00025	2.20	0.46	3.20	0.69		
	Taenite	16.73130	0.00110	0.39844	0.00006	15.73470	0.36387	0.00330	0.00013	2.35	0.21	3.59	0.35		
Horh Uul	Kamacite	16.32880	0.00080	0.38382	0.00004	15.69390	0.36239	0.00230	0.00010	- 0.25	0.15	- 0.49	0.29	1.13	0.35
	Kamacite	16.33290	0.00090	0.38390	0.00003	15.68980	0.36233	0.00240	0.00008	- 0.51	0.15	- 0.66	0.23		
	Kamacite	16.34450	0.00080	0.38408	0.00004	15.69140	0.36232	0.00190	0.00008	- 0.41	0.12	- 0.67	0.23		
	Taenite	16.34980	0.00120	0.38447	0.00004	15.71120	0.36298	0.00290	0.00010	0.85	0.18	1.15	0.27		
	Taenite	16.36080	0.00080	0.38474	0.00003	15.71220	0.36303	0.00210	0.00008	0.91	0.14	1.27	0.22		
	Taenite	16.36610	0.00070	0.38472	0.00003	15.70500	0.36280	0.00210	0.00008	0.45	0.13	0.64	0.23		

Table 7 (continuing). *Fe isotopic composition of iron meteorites measured by laser ablation MC ICP-MS.*

Sample	Mineral phase	Per mil relative to IRMM-014			
		δ56Fe	±2σ	δ57Fe	±2σ
Horh Uul	kamacite	0.36	0.08	0.49	0.16
	taenite	0.51	0.08	0.77	0.17
Toluca	kamacite	0.11	0.08	0.15	0.17
	taenite	0.28	0.08	0.30	0.18
Bohumilitz	kamacite	0.11	0.08	0.24	0.18
	taenite	0.09	0.07	0.12	0.19

***Table 8**. Fe isotopic composition of iron meteorites measured by solution MC ICP-MS.*

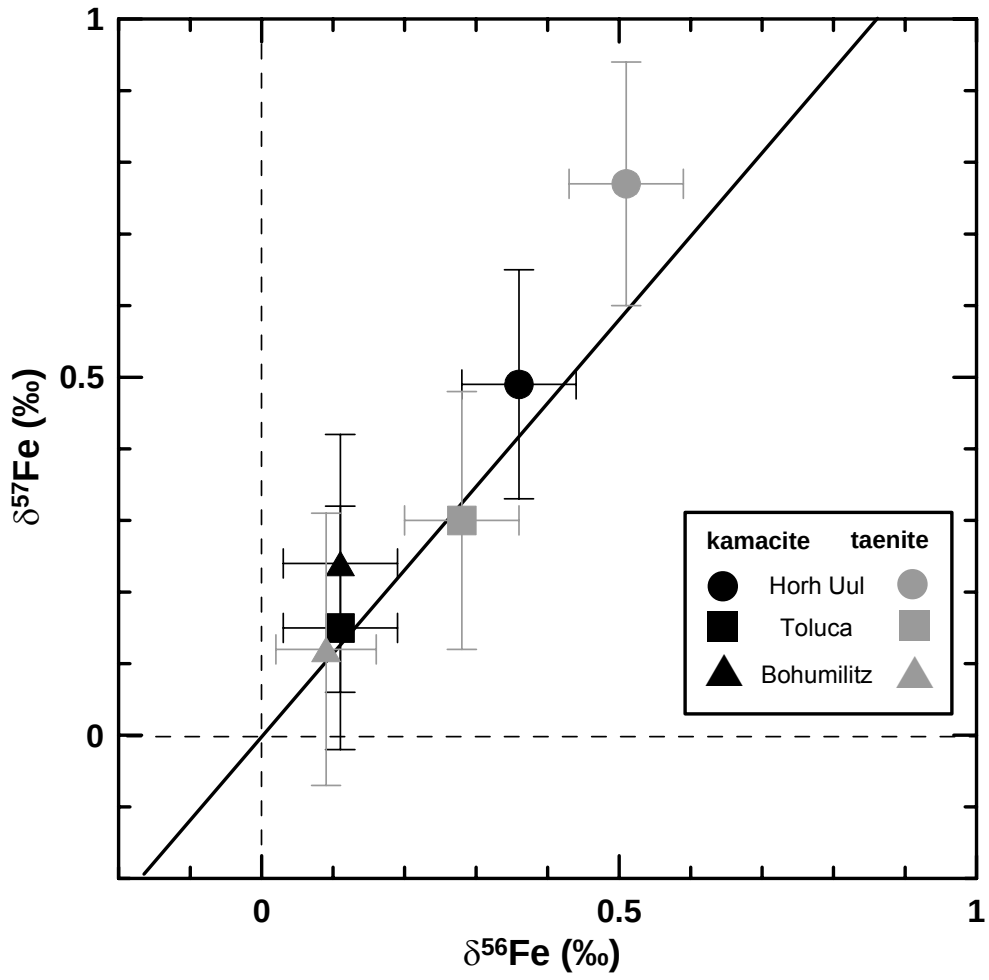

***Figure 15**. Three isotope plot ($\delta^{5}Fe$–$\delta^{56}Fe$) for iron meteorites Horh Uul, Toluca and Bohumilitz analyzed by solution MC ICP-MS. Error bars correspond to 2σ uncertainties.*

5.2. SIMS analyses

In order to verify the laser ablation MC ICP-MS data by an independent in-situ method, SIMS analyses were carried out on the Horh Uul, Toluca and Bohumilitz samples for which solution MC ICP-MS data were also obtained.

The spatial resolution of this method (spot size 20 μm in diameter) made it possible to conduct a traverse across the taenite lamella and adjacent kamacite in the Horh Uul meteorite. The composition and homogeneity of the analyzed taenite lamella were well established in order to exclude domains that contain plessite and other phases (Fig. 16).

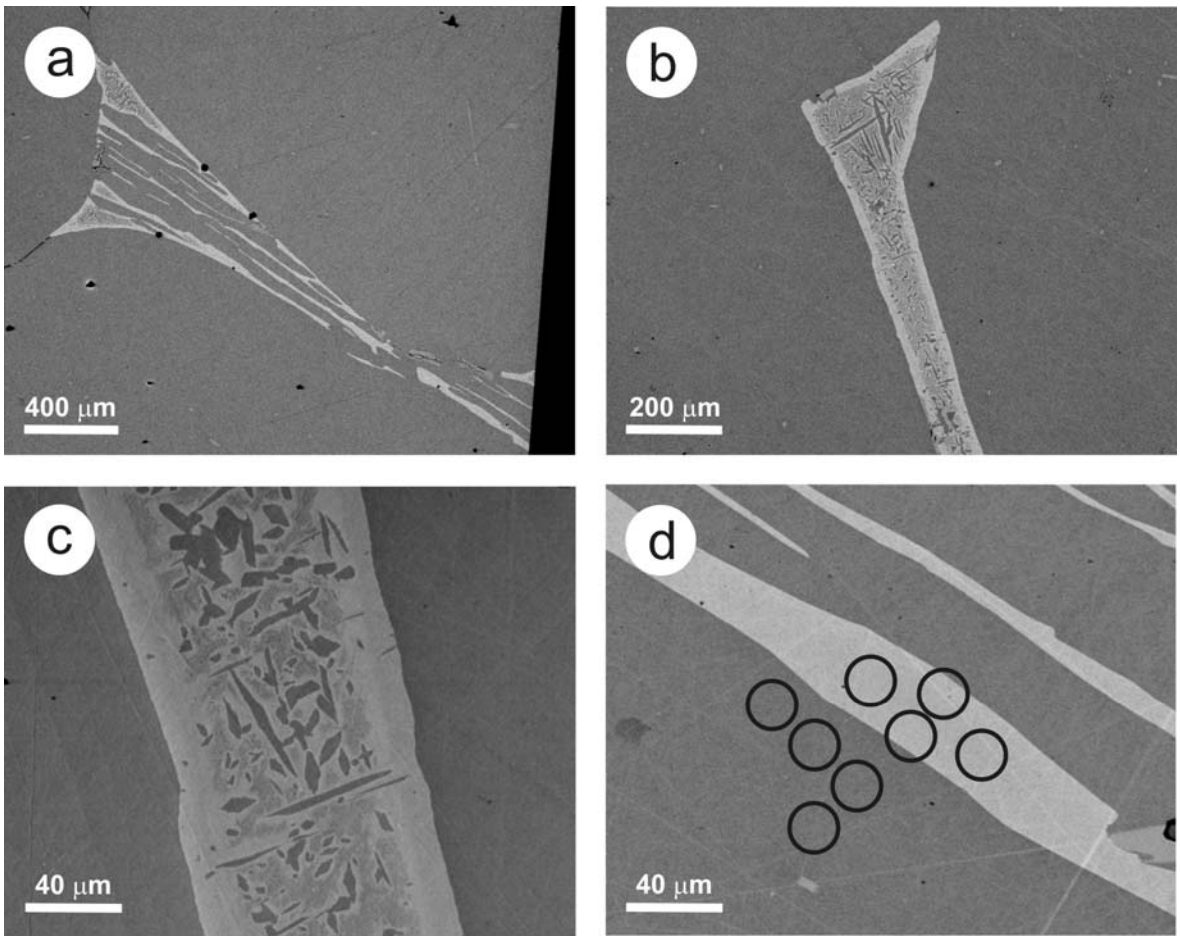

Figure 16. *Backscattered electron images of taenite lamellae in the Toluca meteorite (a-c). The taenite is inhomogeneous and contains abundant plessite (fine-grained intergrowths of kamacite and taenite). (d) Homogeneous taenite lamella that was analyzed by SIMS; black circles represent the locations of SIMS analyses and the size of points corresponds to the diameter of SIMS primary ion beam.*

Unfortunately, it was not possible to conduct similar analytical traverse across the Toluca and Bohumilitz samples, since they did not contain sufficiently wide taenite lamellae. However, several representative analyses of taenite and adjacent kamacite were acquired for these two meteorites.

The SIMS results are listed in Table 9 and the isotopic variations in δ^{56}Fe obtained from the traverse across the Horh Uul meteorite are shown in Fig. 17.

Sample	Mineral phase	Ni (wt%)	Per mil relative to IRMM-014	
			δ56Fe	± ‰ (1σ)
Toluca	kamacite	5.71	-0.28	0.35
	kamacite	5.62	-0.19	0.35
	kamacite	5.15	-0.52	0.45
	kamacite	5.52	-0.12	0.35
	taenite*	18.57	0.16	0.37
	taenite**	26.55	2.36	0.35
	taenite**	24.71	2.19	0.35
	taenite*	21.66	-0.07	0.36
Horh Uul	kamacite	5.76	-0.22	0.35
	kamacite	5.68	-0.38	0.35
	kamacite	5.65	-0.38	0.35
	kamacite	5.70	0.14	0.35
	kamacite	5.88	-0.07	0.35
	taenite**	38.53	2.06	0.42
	taenite*	19.42	-0.01	0.37
	taenite*	16.94	-0.51	0.37
	taenite*	16.74	-0.07	0.36
	taenite*	17.41	0.36	0.37
	taenite*	21.04	0.17	0.38
	taenite**	36.73	3.50	0.42
Bohumilitz	kamacite	5.86	-1.31	0.35
	kamacite	5.64	-1.11	0.35
	kamacite	5.50	-1.24	0.35
	taenite**	29.22	1.96	0.35
	taenite*	19.15	-0.55	0.35
	taenite**	24.26	1.67	0.38

*central part of taenite lamella

** rim of taenite lamella

Table 9*. Fe isotopic composition of selected iron meteorites measured by SIMS.*

Similarly to the laser ablation and solution MC ICP-MS analysis, the Fe isotopic composition of taenite analyzed by SIMS is heavier compared to the adjacent kamacite for all samples, with the overall variation of ~4.5‰ in δ^{56}Fe. Moreover, the isotopic composition of taenite varies across the lamella and there is a close relation between the

degree of Fe isotopic fractionation and the Ni content (Fig. 17). The isotopic differences between the taenite-kamacite pairs $\Delta^{56}Fe_{taen\text{-}kam}$ vary from 0.97 ± 1.02‰ to 2.25 ± 0.86‰.

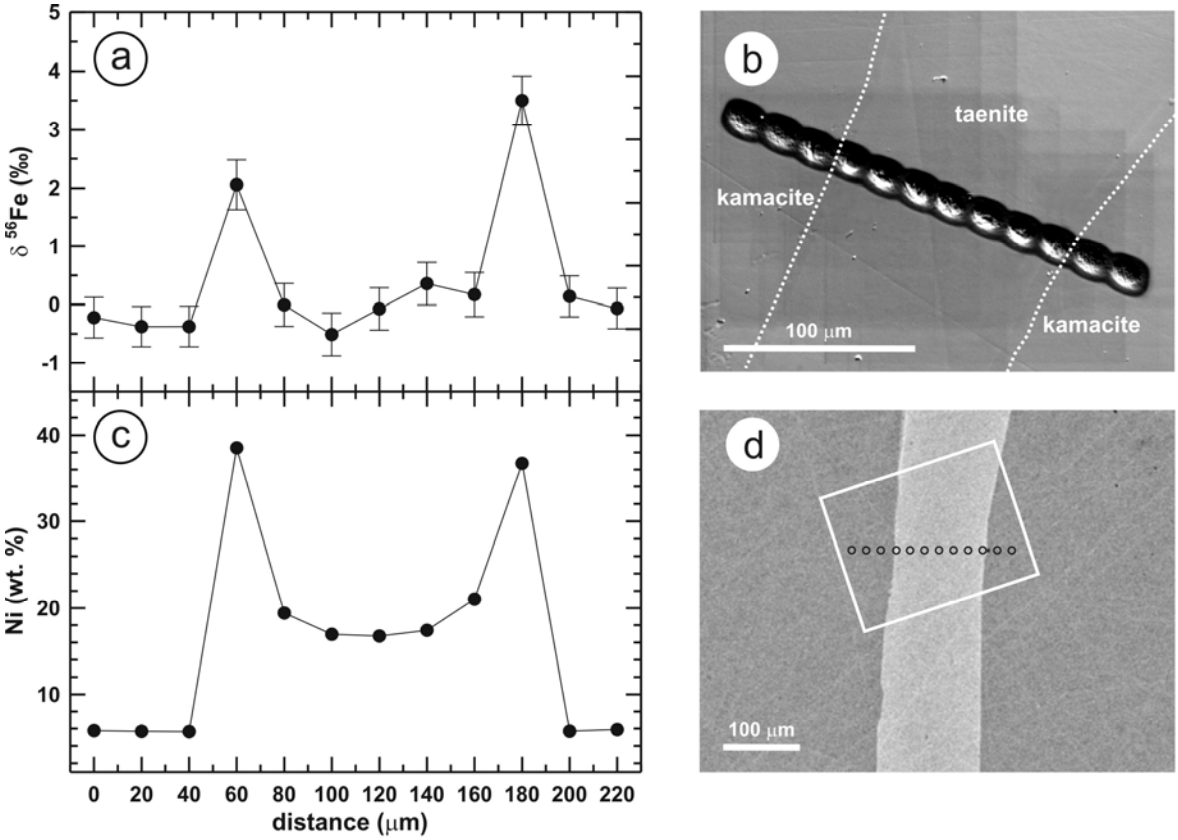

Figure 17. *(a) Fe isotopic traverse obtained by SIMS across the kamacite-taenite-kamacite assemblage in the Horh Uul meteorite. (b) Secondary electron image of the sample documenting the measured traverse in (a). (c) Ni concentration profile across the same area as (a,b) showing the typical M-shaped diffusion profile. (d) Backscattered electron image showing the studied taenite lamella with the locations analyzed by electron microprobe. The step of the SIMS and EMP measurements was 20 μm, corresponding to the diameter of the SIMS primary ion beam.*

6. DISCUSSION

6.1. Effects of spatial resolution

The range of Fe isotopic compositions observed for iron meteorites in this study overlaps with the narrow band of Fe isotopic values reported for planetary samples from the inner solar system (Poitrasson et al., 2004; Poitrasson et al., 2005; Schoenberg and von Blanckenburg, 2006). This study attempts to determine Fe isotopic variations on a small (mineral) scale in samples that have previously appeared homogeneous on the bulk sample scale (Zhu et al., 2001b; Kehm et al., 2003). Here, using different analytical techniques, the range of isotopic variations on the scale of individual mineral phases has been found to be larger compared to the values previously reported by Poitrasson et al. (2005) and Horn et al. (2006).

The larger extent of Fe isotopic intra- and inter-mineral variations for the coexisting kamacite and taenite in the individual meteorites compared to the previously reported values can be explained by differences in the sampling strategies. Conventional Fe-isotope determinations obtained by micro drilling from kamacite and taenite in the iron meteorites Toluca and Cranbourne by Poitrasson et al. (2005) show significant differences in their δ^{56}Fe values, with taenite being consistently 0.1–0.3‰ heavier than kamacite. As shown in this study for in-situ measurements, the Fe isotopic composition in a single meteorite sample is strongly dependent on the spatial resolution and location of analyses. Sampling by micro-drilling of kamacite and taenite can result in insufficient phase purity of the samples. This may be the case for meteorites with finely intergrown lamellae of kamacite and taenite or with plessite present within the taenite lamellae.

The results of SIMS analyses suggest that the taenite lamellae are not homogeneous in the Fe isotopic composition (see Fig. 17). During laser ablation of the taenite, the kamacite matrix may be also partly sampled, especially when the laser penetrates into thin taenite lamellae. To avoid analysis of mixed phases, we exclusively selected well characterized samples with sufficiently wide and homogeneous taenite lamellae. The ablation of linear patterns produced by rastering a circular laser beam with diameter of ~ 20 μm reduces the penetration depth of the laser and minimizes the chances of kamacite encounter. Since the taenite is isotopically inhomogeneous, the laser ablation results are

expected to show larger variation in Fe isotopic composition compared to solution analyses of micro-drilled or bulk samples.

Data for kamacite-taenite pairs of Toluca presented by Horn et al. (2006) show small Fe isotopic variations; unfortunately this work does not discuss the microchemical and phase compositions of the analysed meteorite mineral phases in detail. Yet, Horn et al. (2006) noted that taenite results showed a larger variability than those of kamacite, but this is explained due to the fact that kamacite matrix was ‘‘tapped’’ while deepening the laser crater into the small taenite grain (they used UV-femtosecond laser ablation, spot analysis with the laser beam diameter of 35 μm). The authors also mentioned a possibility that during cooling of the meteorite parent body, a disequilibrium effect or diffusion-caused zonation known especially for Co and Ni in taenite can also produce Fe-isotopic zonation. The individual analyses of taenite also had reduced precision due to a relatively short acquisition time, and also due to a possible kamacite ablation. Significant amount of finely intergrown phase mixtures and a common presence of plessite (enclosed in taenite lamellae) in all meteorites in the present study (Fig. 16) required the microchemical characterization of all taenite lamellae prior to their sampling for isotopic analysis.

To illustrate the effects of spatial resolution on the measured Fe isotopic composition, this work compares the results of kamacite and taenite analysis in the Horh Uul meteorite by different analytical techniques (Fig. 18).

The SIMS results show a wide range of Fe isotopic variation across the taenite lamella of the Horh Uul meteorite (up to ~ 4.1‰ in δ^{56}Fe). The Fe isotopic traverse conducted across this lamella shows that the highest δ^{56}Fe values are restricted to narrow zones in the lamella close to the taenite-kamacite interface (Fig. 17), while the acquired δ^{56}Fe values for the central part of lamella are similar to δ^{56}Fe values of the adjacent kamacite. The calculated average δ^{56}Fe values for taenite 0.79 ± 0.98‰ and for kamacite -0.18 ± 0.77‰ from these analyses are in good agreement with laser ablation MC ICP-MS data (Table 7, Figs. 12, 13). This suggests that spatial resolution has a significant effect on the measured Fe isotopic composition and that the bulk Fe isotope analysis of taenite by solution MC ICP-MS may not record the maximum isotopic variability for the kamacite-taenite pairs. In summary, the previously recorded differences in the iron isotopic composition are real and can in part be due to the variable amount of taenite analyzed during bulk sampling of the meteorite.

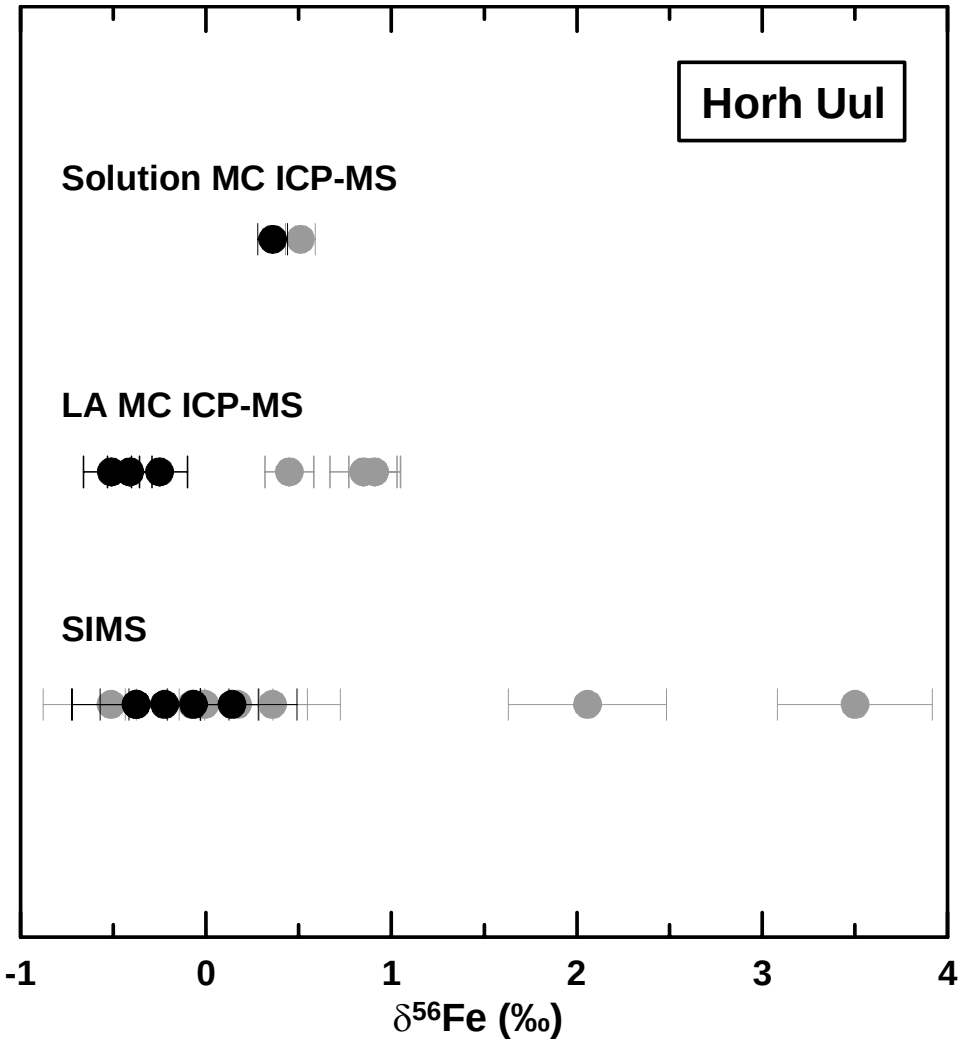

***Figure 18**. Isotopic composition of the Horh Uul meteorite (expressed as δ^{56}Fe) obtained by three different analytical techniques (solution and laser ablation MC ICP-MS and SIMS) with different spatial resolution. The figure illustrates that poor spatial resolution can result in apparently low isotopic fractionation. Black symbols correspond to kamacite, grey symbols correspond to taenite. Error bars are 2σ for solution and laser ablation MC ICP-MS analyses, while for SIMS the uncertainties are shown as 1σ.*

The solution MC ICP-MS analyses of kamacite and taenite lamellae in the Horh Uul and Bohumilitz meteorites show smaller variations in Fe isotopic composition compared to the laser ablation MC ICP-MS data. For Toluca, the kamacite and taenite δ^{56}Fe values obtained by solution MC ICP-MS analysis are in a good agreement with the data published by Poitrasson et al. (2005) and Horn et al. (2006). The SIMS data, however, show a wider range of δ^{56}Fe values for both phases. This is expected given the superior spatial resolution of this in-situ analytical technique.

6.2. Fe isotopic fractionation in irons

It has been previously demonstrated that non-biotic processes can fractionate Fe isotopes by several permil even at high temperatures. Several studies (Zhu et al., 2002; Beard and Johnson, 2004b; Poitrasson et al., 2005; Cohen et al., 2006) reported on inter-mineral isotopic fractionation in terrestrial igneous and metamorphic rocks and in pallasites as a result of high-temperature isotopic equilibration. Metal-silicate fractionation in pallasites took place during an early stage of planetary formation and differentiation. Pallasites are supposed to have formed at the transition zone between the reduced core and the oxidized mantle of their parent bodies (Mittlefehldt et al., 1998 and references therein). It can be anticipated that redox reactions represent an important factor in controlling the metal-silicate Fe isotopic fractionation in pallasitic meteorites. In principle, iron isotope fractionation could occur during metal-silicate partitioning, at equilibrium conditions given the contrasting redox state of native Fe (0 valence) and mantle silicates (mostly +2). Change in the redox state of Fe is known to be a key factor responsible for iron isotopic fractionation between condensed phases (e.g. Polyakov and Mineev, 2000). However, this isotopic fractionation should be minimized by the very high temperature conditions prevailing during core formation. As for other stable isotopes, Polyakov and Mineev (2000) have shown that the magnitude of equilibrium Fe isotopic fractionation is essentially inversely proportional to the square of the temperature.

Since the iron meteorites are mostly composed of reduced phases, the redox processes are an unlikely cause of the observed Fe isotopic variations. The parent bodies of the iron meteorites underwent melting and metal segregation within a few million years after the formation of the solar system, apparently independent of their initial composition, size and time of crystallization (Horan et al., 1998; Walter and Trønnes, 2004; Qin et al., 2008). Despite the different crystallization and cooling histories of the metallic cores represented by different chemical groups of iron meteorites, the similarity of mean Fe isotopic compositions between the groups suggests that the bulk-rock isotopic composition of these cores was homogenous prior to the metal segregation and crystallization.

Results of this study show that the extent of isotopic fractionation between kamacite and taenite in individual meteorites varies up to ~ 4.5‰ in δ^{56}Fe and the measured variations in δ^{56}Fe and δ^{57}Fe resulted from a mass dependent isotopic fractionation. The preferential enrichment of isotopically heavier Fe in taenite is consistent with its predominantly face-centered cubic (*fcc*) structure with stronger Fe–Fe and Fe–Ni

bonds compared to the predominantly body-centered cubic (*bcc*) structure of kamacite (Fig. 19).

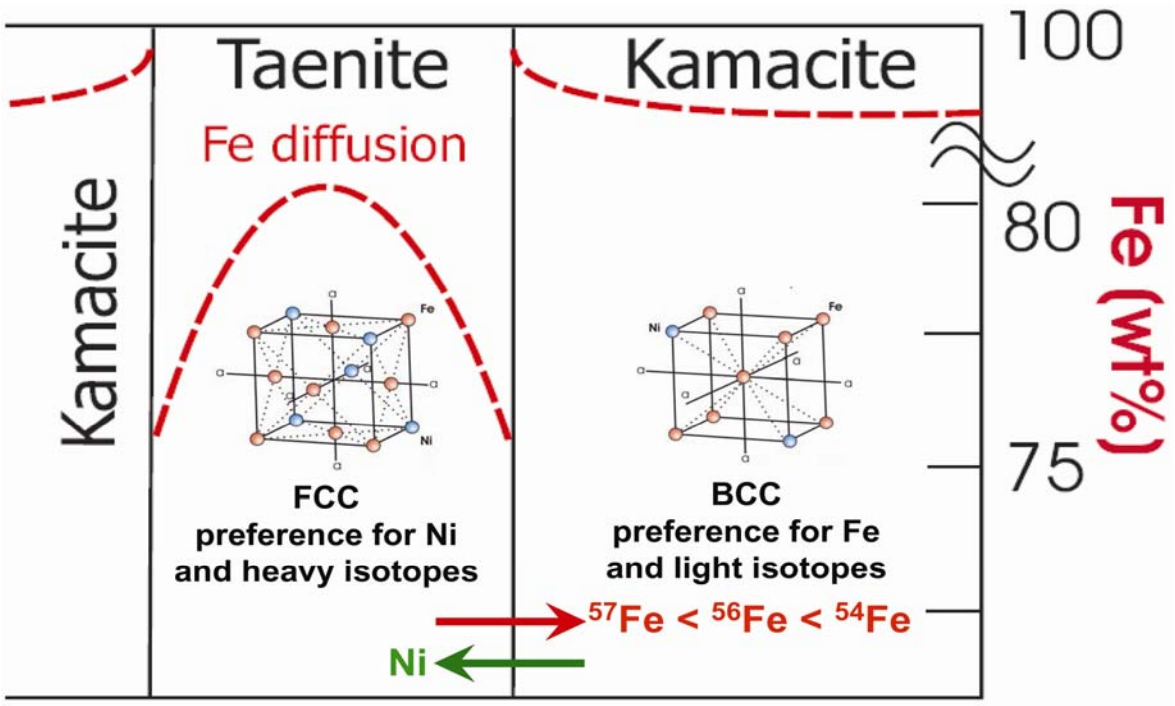

Figure 19. *Qualitative plot of Fe isotopic fractionation between FeNi phases as a result of their diverse structure. The rate of cooling has an influence on the shape of diffusion profile.*

The Mössbauer spectroscopic data for the meteoritic Fe–Ni alloys that could be used to predict the Fe isotopic fractionation between kamacite and taenite are not available but equilibrium isotopic fractionation of ~ 0.7‰ δ^{57}Fe at 750 °C (typical kamacite–taenite unmixing temperature) can be expected from the analogy with Fe metal (Polyakov and Mineev, 2000). Since the observed isotopic fractionation is significantly larger, it is likely to result from a kinetic, rather than from an equilibrium process.

The kinetic fractionation could take place during the initial kamacite exsolution at ~ 750 °C (for octahedrites with Ni content of 7–10 wt. %; Yang et al., 1996). This explanation is not likely because isotopic fractionation during kamacite exsolution would probably result in Fe isotopic variation that is significantly smaller that the variation observed in this study. More likely, kinetic fractionation could take place during the subsolidus diffusive exchange of Fe between kamacite and taenite in response to cooling, at temperatures ranging from the kamacite-taenite eutectic to, or even below the effective closure temperature for Fe elemental diffusion (~ 450 °C). At low temperatures, the

differences in diffusion rates of heavy and light isotopes are expected to be large (Polyakov and Mineev, 2000), precluding formation of chemically and isotopically homogenous metal phases.

6.3. The effect of meteorite cooling rate on Fe isotopic fractionation

The observations made of Fe isotopic fractionation between taenite and kamacite suggest that differences in diffusivities played an important role in producing the isotopic fractionation. During formation of the Widmanstätten pattern, growth of kamacite is mainly limited by Ni diffusion in taenite. Because light isotopes diffuse faster than heavy ones, it can be expected that the center of taenite will have light Ni and heavy Fe isotopic compositions relative to adjacent kamacite. However, at 500 °C, it is not possible to rule out the possibility that equilibrium fractionation contributed to the overall isotopic fractionation that was measured (e.g., Polyakov and Mineev 2000; Poitrasson et al. 2005; Williams et al. 2006; Horn et al., 2006). There is no constraint on what the equilibrium fractionation between taenite and kamacite might have been at the temperatures relevant to the formation of the Widmanstätten pattern.

Differences in the diffusion rates of Fe isotopes in kamacite and taenite may produce the observed Fe isotopic variations (up to ~ 4.5‰ $^{56}Fe/^{54}Fe$) in iron meteorites. Isotopic fractionation due to difference in diffusivities of Fe and Ni isotopes was modeled for the Toluca (IAB) meteorite by Dauphas (2007). He demonstrated for a range of cooling rates that the growth of kamacite out of taenite during the formation of Widmanstätten patterns can result in isotopic fractionation. The cooling rates of metal phases in iron and stony-iron meteorites have traditionally been measured using metallographic techniques that are dependent on number of assumptions and physical and chemical parameters (Wood, 1964; Dean and Goldstein, 1986; Saikumar and Goldstein, 1988; Herpfer et al., 1994; Yang et al., 1997; Hopfe and Goldstein, 2001). The possibility to determine the meteorite cooling rates by an independent approach (e.g. isotopic fractionation of Fe or Ni) would therefore be of great importance.

The laser ablation MC ICP-MS data obtained for iron meteorites in this study show a systematic correlation between the taenite-kamacite Fe isotopic offset $\Delta^{56}Fe_{taen\text{-}kam}$ and the meteorite cooling rates (5–500 °C/My) determined by metallographic methods based

on the Ni diffusion in taenite (Fig. 20). The relation between the measured $\Delta^{56}Fe_{taen\text{-}kam}$ and the calculated cooling rates can be expressed by a logaritmic function:

$$\Delta^{56}Fe_{taen-kam}(‰) = -0.57756 \cdot \ln[\text{cooling rate}(K)] + 3.79199; R^2 = 0.9782 \quad (6)$$

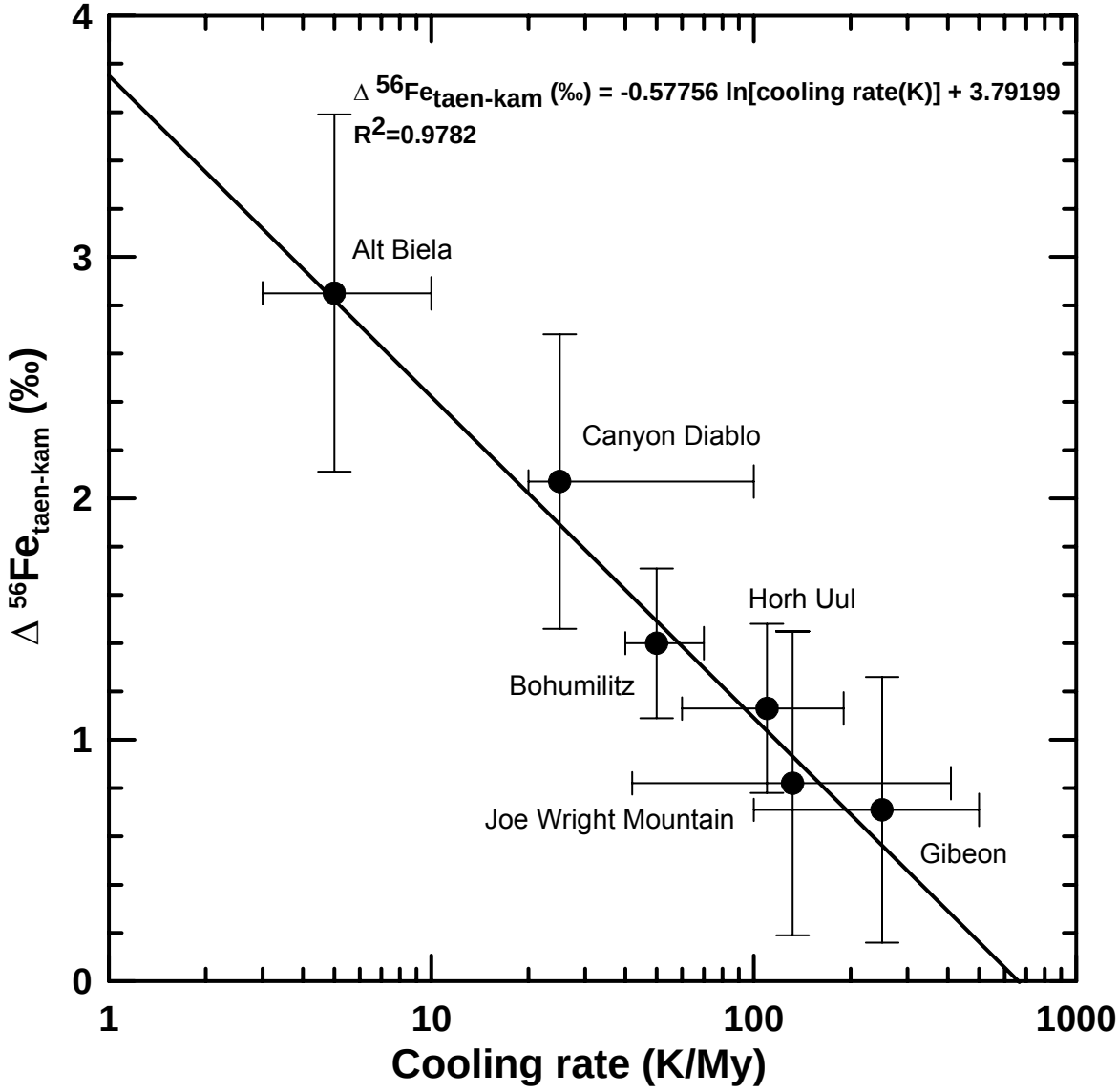

Figure 20. *Correlation plot for $\Delta^{56}Fe_{taen\text{-}kam}$ and cooling rates estimated for the analyzed iron meteorites. The cooling rates for individual meteorites were taken from Yang et al., 1997 (range for IID group used for Alt Biela); Hopfe and Goldstein, 2001 (Canyon Diablo); Yang et al., 1997 (Gibeon); Herpfer et al., 1994 (average value and range for IAB group used for Bohumilitz); Yang and Goldstein, 2006 (average value and range for IIIAB used for Joe Wright Mt.). Cooling rate for Horh Uul (~110K/My) was estimated using the method of Yang and Goldstein, 2006.*

This correlation can be interpreted as resulting from Fe isotopic fractionation driven by diffusion between kamacite and taenite lamellae and variable cooling rates of the studied meteorites. According to the theoretical model of Dauphas (2007), kinetic isotopic fractionation during slow cooling would produce heavier taenite composition compared to the fast cooling.

Isotopic diffusion of Fe can thus provide us with additional information for deciphering more complete thermal histories of iron meteorites and their planetary parent bodies. The conventional interpretation of individual iron meteorite groups is that their members represent fragments of a single parent body, or perhaps of several closely-related bodies (Scott and Wasson, 1975). If all members of an iron meteorite group share the same cooling rate and display identical rates of Fe isotopic fractionation, they are presumed to be pieces of a single metallic core. Metal conducts heat rapidly relative to the cooling rates and accordingly, all parts of the metallic core should always be at the same temperature and should cool at the same rate. However, for the cooling rates to differ, the meteorites must either come from several cores in differently sized bodies of from several masses buried at different depths in the poorly conducting silicate mantle of a single body. In the later scenario, the Fe isotopic composition would differ significantly for individual meteorite samples within a particular chemical group. Subsequent events such as impact-related melting may also be recognizable by Fe isotopic scatter.

6.4. Cooling histories of magmatic and non-magmatic iron meteorites

The differences ($\Delta^{56}Fe_{taen\text{-}kam}$) between the iron isotopic composition of coexisting taenite and kamacite pairs in the studied samples could have resulted from combination of several factors: burial depth, degree of parent-body differentiation, initial composition, cooling rate and disruptive impact processes occurring at the early stages of solar system history. Schoenberg and von Blanckenburg (2006) observed small differences in the bulk sample $\delta^{56}Fe$ values for magmatic and non-magmatic iron meteorites; these were interpreted as resulting from sample heterogeneities due to large crystal sizes. Data presented in this study suggest that the differences in Fe isotopic composition between different iron meteorite groups reflect variations in their respective cooling histories (Fig. 20).

6.4.1. Magmatic iron meteorites

The Horh Uul and Joe Wright Mountain meteorites (magmatic group IIIAB) have been interpreted to represent a core of relatively small differentiated asteroid that was most likely disrupted by a single impact event ~ 650 Ma ago (Voshage and Feldmann, 1979). This disruption may be partly responsible for the scattered isotopic record of the Joe Wright Mountain meteorite (see Table 7; Figs. 12, 13). Regardless the scattered isotopic composition, these two IIIAB group members exhibit comparable taenite-kamacite pairs differences $\Delta^{56}Fe_{taen\text{-}kam}$.

It has been suggested that the Gibeon meteorite (magmatic group IVA) formed in the core of a small differentiated asteroid that was partly disrupted by a major impact shortly after its formation (Haack et al., 1996; Horan et al., 1998). The asteroid was subsequently re-accreted and after thermal equilibration of hot and cold fragments it underwent a relatively rapid cooling (Rasmussen et al., 1995). This thermal history is possibly recorded by its Fe isotopic composition, resulting in small Fe isotopic fractionation ($\Delta^{56}Fe_{taen\text{-}kam} = 0.71 \pm 0.55‰$).

The calculated cooling rates for IIIAB group (Haack et al., 1990) are faster than those determined for IID group of iron meteorites (Yang et al., 1997) which formed in the core of a larger asteroid. This is in good agreement with the Fe isotope data for the Alt Biela (IID) meteorite ($\Delta^{56}Fe_{taen\text{-}kam} = 2.85 \pm 0.74‰$) presented here.

The Nelson County meteorite (IIIF) represents one of the most intensely deformed (pre-terrestrial cold deformation) iron meteorites known (Buchwald, 1975). The kamacite phase in this meteorite shows Neumann lines that are bent and faulted. This is indicative of a violent, plastic deformation event which could have also affected the Fe isotopic exchange between kamacite and taenite, as indicated by the scattered, overlapping isotopic composition (Figs. 12, 13; Table 7).

6.4.2. Non-magmatic groups

Several models have been proposed to describe the origin and trace element composition of the IAB-IIICD iron meteorites. This group has been referred to as non-magmatic since the meteorites appear to have a different segregation/crystallization history compared to the magmatic group. They do not exhibit features of normal fractional crystallization and they have diverse cooling rates. The most accepted model for the formation of the IAB-IIICD group assumes the existence of many discrete small pools or pods of metal, rather than a single metallic core (Goldstein et al., 2009). Wasson and

Kallemeyn (2002) suggested that melting took place because of heating during discrete impact events that occurred either at different locations of a single chondritic body or on different bodies of similar composition. The similarity in tungsten isotopic compositions between the IAB and IIICD irons points to a single impact event dated at 4–7 My after the formation of CAIs, leading to multiple metal pools in a single chondritic parent body. Alternatively, there may have been multiple impacts on multiple chondritic bodies with similar chemical compositions within a narrow time interval of 4–7 My after the formation of CAIs (Qin et al., 2008). Meteorites from such metal pools that have formed independently from each other can have different Fe isotopic fractionation patterns depending on their burial depth or position within the parent body. The Canyon Diablo (IAB) meteorite records slow cooling within its parent body and the Fe isotopic fractionation in this meteorite ($\Delta^{56}Fe_{taen\text{-}kam}$ = 2.07 ± 0.61‰) corresponds to the cooling rates (20-100 °C/My) predicted by Hopfe and Goldstein (2001). The Bohumilitz (IA) meteorite has $\Delta^{56}Fe_{taen\text{-}kam}$ value of 1.40 ± 0.31‰ that also corresponds well to the calculated cooling rates for IAB group (40-70 °C/My; Herpfer et al., 1994).

7. CONCLUSIONS

The study of Fe isotopic variation in iron meteorites can be summarized as follows:

1. The measured Fe isotopic composition of kamacite-taenite pairs in the studied iron meteorites varies significantly within up to ~ 4.5‰ in $\delta^{56}Fe$. The observed isotopic variation is found to be larger compared to the previously reported values. The Fe isotopic composition of the taenite-kamacite pairs shows no correlation with the bulk Ni content of the studied meteorites. Meteorites of the same chemical group IA (Bohumilitz, Canyon Diablo, and Toluca) have distinct iron isotopic composition of their Fe-Ni phases. No relation between the isotopic composition and supposed origin of meteorites from magmatic and non-magmatic members has been found in this study.

2. Differences in spatial resolution of the analytical techniques, combined with small scale isotopic heterogeneities within the meteorite samples, can explain the apparent discrepancy between Fe isotopic composition reported previously in the literature and data reported in this study for the same meteoritic irons. Accordingly, detailed chemical and phase characterization of the samples is critical prior to both bulk and in-situ analysis of iron meteorites.

3. The SIMS analyses have revealed isotopic heterogeneities within the taenite lamellae. Taenite has the heaviest Fe isotopic composition near the taenite-kamacite interface, while the centers of the lamellae are isotopically lighter, similar to the isotopic composition of the adjacent kamacite.

4. The extent of Fe isotopic fractionation $\Delta^{56}Fe_{taen\text{-}kam}$ between co-existing kamacite and taenite correlates with the meteorite cooling rates determined using metallographic methods based on Ni diffusion in taenite. Additional Fe isotopic data for inter-mineral isotopic fractionation in iron meteorites and experimental data for Fe isotopic diffusion are needed before the isotopic diffusion of Fe can be reliably applied to studies of thermal evolution of iron meteorite parent bodies.

Compared to the previous studies of Fe isotopic composition in meteoritic irons, the combination of analytical techniques used in this study provides useful data on samples

with respect to their textural context and inter-mineral relations; this has not been addressed previously. It can be expected that the results presented in this thesis will provide isotopic data that will complement the existing information on the isotopic composition of iron meteorites. Revision of the present-day data on cooling rates of iron meteorites, especially when they are used to estimate the original parent body sizes and collision histories, will be possible on the basis of correlation between Fe isotopic fractionation and meteorite cooling rate. Additional Fe isotopic data for inter-mineral isotopic fractionation in iron meteorites and experimental data for Fe isotopic diffusion are needed before the isotopic diffusion of Fe can be reliably applied to studies of thermal evolution of iron meteorite parent bodies.

8. REFERENCES

Alexander C. M. O'D. and Wang J. (2001) Iron isotopes in chondrules: implications for the role of evaporation during chondrule formation. *Meteorit. Planet. Sci*. **36,** 419–428.

Anbar, A.D., (2004) Iron stable isotopes: beyond biosignatures. *Earth Planet. Sci. Lett.* **217**, 223–236.

Beard B. L., Johnson C. M., Skulan J. L., Nealson K. H., Cox L. and Sun H. (2003) Application of Fe isotopes to tracing the geochemical and biological cycling of Fe. *Chem. Geol.* **195**, 87-117.

Beard, B.L. and Johnson, C.M. (2004a). Fe isotope variations in the modern and ancient earth and other planetary bodies. In: Johnson, C.M., Beard, B.L., Albarede, F. (Eds.), Geochemistry of Non-Traditional Stable Isotopes, Reviews in Mineralogy and Geochemistry, 55. Mineralogical Society of America, Blacksburg, pp. 319–357.

Beard B. L. and Johnson C. M. (2004b) Inter-mineral Fe isotope variations in mantle-derived rocks and implications for the Fe geochemical cycle. *Geochim. Cosmochim. Acta* **68**, 4727-4743.

Bottke, W.F., Nesvorny, D., Grimm, R.E., Morbidelli, A., O'Brien, D.P. (2006) Iron meteorites as remnants of planetesimals formed in the terrestrial planet region. *Nature* **439**, 821–824.

Buchwald V. F. (1975) Handbook of Iron Meteorites, Univ. of California, p.885.

Chabot, N.L., Jones, J.H. (2003) The parameterization of solid metal–liquid metal partitioning of siderophile elements. *Meteorit. Planet. Sci.* **38**, 1425–1436.

Chabot, N.W., Haack, H. (2006) Evolution of asteroidal cores. In: Lauretta, D.S.,McSween, H.Y. (Eds.), Meteorites and the Early Solar System II. University Arizona Press, pp. 747–771.

Cohen B. A., Levasseur S., Zanda B., Hewins R. H. and Halliday A. N. (2006) Kinetic isotope effect during reduction of iron from a silicate melt. *Geochim. Cosmochim. Acta* **70**, 3139-3148.

Cook D. L., Wadhwa M., Clayton R. N., Janney P. E., Dauphas N. and Davis A. M. (2006) Mass-dependent fractionation of nickel isotopes in IIIAB iron meteorites. *Meteorit. Planet. Sci.* **41**:A40.

Dauphas N. (2007) Diffusion-driven kinetic isotope effect of Fe and Ni during formation of the Widmanstätten pattern. *Meteorit. Planet. Sci*. **42**, 1597-1613.

Dauphas N., Pourmand A. and Teng F.Z. (2009) Routine isotopic analysis of iron by HR-MC-ICPMS: How precise and how accurate? *Chem. Geol.* **267**, 175-184.

Dean D. C. and Goldstein J. I. (1986) Determination of interdiffusion coeficients in the Fe-Ni and Fe-Ni-P systems below 900 °C. *Metall. Trans*. **17A**, 1131-1138.

Fantle M.S. and Bullen T.D. (2009) Essentials of iron, chromium, and calcium isotope analysis of natural materials by.thermal ionization mass spectrometry. *Chem. Geol.* **258**, 50-64.

Goldstein, J.I., Ogilvie, R.E. (1965) The growth of the Widmanstätten pattern in metallic meteorites. *Geochim. Cosmochim. Acta* **29**, 893–920.

Goldstein J. J., Scott E. R. D. and Chabot N. L. (2009) Iron meteorites: Crystallization, thermal history, parent bodies, and origin. *Chem. Erde* **69**, 293-325.

Haack H., Rasmussen K. L. and Warren P. H. (1990) Effects of regolith/megaregolith insulation on the cooling histories of differentiated asteroids. *J. Geophys. Res*. **95**, 5111-5124.

Haack H., Scott E. R. D., Love S. G., Brearley A. J. and McCoy T. J. (1996) Thermal histories of IVA stony-iron and iron meteorites: Evidence for asteroid fragmentation and reaccretion. *Geochim. Cosmochim. Acta* **60**, 3103-3113.

Haack, H., McCoy, T.J. (2004) Iron and stony-iron meteorites. In: Davis, A.M., Holland, H.D., Turekian, K.I. (Eds.), Meteorites, Comets, and Planets, Vol. 1. Treatise on Geochemistry. Elsevier-Pergamon,Oxford, pp.325–345.

Herpfer M. A., Larimer J. W. and Goldstein J. I. (1994) A comparison of metallographic cooling rate methods used in meteorites. *Geochim. Cosmochim. Acta* **58**, 1353-1365.

Hezel D.C., Needham A.W., Armytage R., Georg B., Abel R.L., Kurahashi E., Coles B.J., Rehkamper M. and Russell S.S. (2010) A nebula setting as the origin for bulk chondrule Fe isotope variations in CV chondrites. *Earth Planet. Sci. Lett.* **296**, 423-433.

Hopfe W. D. and Goldstein J. I. (2001) The metallographic cooling rate method revised: Application to iron meteorites and mesosiderites. *Meteorit. Planet. Sci* **36**, 135-154.

Horan M. F., Smoliar M. I. and Walker R. J. (1998) ^{182}W and ^{187}Re-^{187}Os systematics of iron meteorites: Chronology for melting, differentiation and crystallization in asteroids. *Geochim. Cosmochim. Acta* **62**, 545-554.

Horn I., von Blanckenburg F., Schoenberg R., Steinhoefel G. and Markl G. (2006) In situ iron isotope ratio determination using UV-femtosecond laser ablation with

application to hydrothermal ore formation processes. *Geochim. Cosmochim. Acta* **70**, 3677-3688.

Kehm K., Hauri E. H., Alexander C. M. O'D. and Carlson R. W. (2003) High precision iron isotope measurements of meteoritic material by cold plasma ICP-MS. *Geochim. Cosmochim. Acta* **67**, 2879–2891.

Koblitz J. (2003) MetBase, version 6.0 (CD-ROM)

Košler J., Pedersen R. B., Kruber C. and Sylvester P. J. (2005) Analysis of Fe isotopes in sulfides and iron meteorites by laser ablation high-mass resolution multi-collector ICP mass spectrometry. *J. Anal. At. Spectrom.* **20**, 192-199.

Košler J., Pedersen R. B., Kruber C. and Sylvester P. J. (2006) Comment on "Analysis of Fe isotopes in sulphides and iron meteorites by laser ablation high-mass resolution multi-collector ICP mass spectrometry" – A reply. *J. Anal. At. Spectrom.* **21**, 214-216.

Kracher A., Willis J., Wasson J. T. (1980) Chemical classification of iron meteorites. IX - A new group (IIF), revision of IAB and IIICD, and data on 57 additional irons. *Geochim. Cosmochim. Acta* **44**, 773-787.

Mittlefehldt D. W., McCoy T. J., Goodrich C. A. and Kracher A. (1998) Non-chondritic meteorites from asteroidal bodies. *Rev. Mineral.* **36**, 51-52.

Mullane E., Russell S. S., Gournelle M. (2005) Nebular and asteroidal modification of the iron isotope composition of chondritic components. *Earth Planet. Sci. Lett.* **239**, 203-218.

Narayan, C., Goldstein, J.I.,(1984a) Nucleation of intragranular ferrite in Fe–Ni–P alloys. *Metall.Trans.* **15A**, 861–865.

Narayan, C., Goldstein, J.I.,(1984b) Growth of intragranular ferrite in Fe–Ni–P alloys. *Metall.Trans.* **15A**, 867–874.

Needham A.W., Porcelli D. and Russell S.S. (2009) An Fe isotope study of ordinary chondrites. *Geochim. Cosmochim. Acta* **73**. 7399-7413.

Nishizawa M., Yamamoto H., Ueno Y., Tsuruoka S., Shibuya T., Sawaki Y., Yamamoto S., Kon Y., Kitajima K., Komiya T., Maruyama S., Hirata T. (2010) Grain-scale iron isotopic distribution of pyrite from Precambrian shallow marine carbonate revealed by a femtosecond laser ablation multicollector ICP-MS technique: Possible proxy for the redox state of ancient seawater. *Geochim. Cosmochim. Acta* **74**, 2760-2778.

Norton R. O. (2002) The Cambridge Encyclopedia of Meteorites. Cambridge University Press, Cambridge, UK, pp. 354.

Poitrasson F., Halliday A. N., Lee D. Ch., Levasseur S. and Teutsch N. (2004) Iron isotope differences between Earth, Moon, Mars and Vesta as possible records of contrasted accretion mechanisms. *Earth Planet. Sci. Lett.* **223**, 253-266.

Poitrasson F., Levasseur S. and Teutsch N. (2005) Significance of iron isotope mineral fractionation in pallasites and iron meteorites for core-mantle differentiation of terrestrial planets. *Earth Planet. Sci. Lett*. **234**, 151-164.

Poitrasson F. (2007) Does planetary differentiation really fractionate iron isotopes? *Earth Planet. Sci. Lett.* **256**, 464-492.

Poitrasson F., Roskosz M. and Corgne A. (2009) No iron isotope fractionation between molten alloys and silicate melt to 2000 °C and 7.7 GPa: Experimental evidence and implications for planetary differentiation and accretion. *Earth Planet. Sci. Lett.* **278**, 376-385.

Polyakov V. B. and Mineev S. D. (2000) The use of Mőssbauer spectroscopy in stable isotope geochemistry. *Geochim. Cosmochim. Acta* **61**, 849-865.

Qin L., Dauphas N., Wadhwa M., Masarik J. and Janney P. E. (2008) Rapid accretion and differentiation of iron meteorite parent bodies inferred from ^{182}Hf–^{182}W chronometry and thermal modeling. *Earth Planet. Sci. Lett.* **273**, 94-104.

Rasmussen, K.L. (1981) The cooling rates of iron meteorites – a new approach. *Icarus* **45**, 564–576.

Rasmussen K. L., Malvin D. J., Wasson J. T. (1988) Trace element partitioning between taenite and kamacite - Relationship to the cooling rates of iron meteorites. *Meteorit. Planet. Sci*. **23**, 107-112.

Rasmussen K. L., Ulff-Moller F. and Haack H. (1995) The thermal evolution of IVA iron meteorites; evidence from metallographic cooling rates. *Geochim. Cosmochim. Acta* **14**, 3049-3059.

Russell S.S., Folco L., Grady M.M., Zolensky M.E., Jones R., Righter K., Zipfel J., Grossman J.N. (2004) The Meteoritical Bulletin, No. 88, 2004 July, *Meteorit. Planet. Sci*. **39**, Supplement, A215-A272.

Schoenberg R. and von Blanckenburg F. (2006) Modes of planetary-scale Fe isotope fractionation. *Earth Planet. Sci. Lett*. **252**, 342-359.

Scott, E.R.D. (1972) Chemical fractionation in iron meteorites and its interpretation. *Geochim. Cosmochim. Acta* **36**, 1205–1236.

Scott E. R. D., Wasson J. T., Buchwald V. F. (1973) The chemical classification of iron meteorites-VII. A reinvestigation of irons with Ge concentrations between 25 and 80 ppm. *Geochim. Cosmochim. Acta* **37**,1957.

Scott E. R. D. and Wasson J. T. (1975) Classification and properties of iron meteorites. *Rev. Geophys. Space Phys*. **13**, 527-546.

Scott E. R. D., Wasson J. T. (1976) Chemical classification of iron meteorites. VIII - Groups IC, IIE, IIIF and 97 other irons. *Geochim. Cosmochim. Acta* **40**, 103-115.

Saikumar V. and Goldstein J. I. (1988) An evaluation of the methods determine the cooling rates of iron meteorites. *Geochim. Cosmochim. Acta* **52**, 715-726.

Short, J.J., Goldstein, J.I. (1967) Rapid methods of determining cooling rates of iron and stony iron meteorites. *Science* **156**, 59–61.

Strelow F. W. E. (1980) Improved separation of iron from copper and other elements by anion-exchange chromatography on a 4% cross-linked resin with high concentrations of hydrochloric acid, *Talanta* **27**, 727-732.

Taylor K.G. and Konhauser K.O. (2011) Iron in earth surface systems. *Elements* **7**, 83-119.

Theis K. J., Burgess R., Lyon I. C. and Sears D. W. (2008) The origin and history of ordinary chondrites: A study by iron isotope measurements of metal grains from ordinary chondrites. *Geochim. Cosmochim. Acta* **72**, 4440-4456.

Voshage H. and Feldmann H. (1979) Investigations on cosmic-ray-produced nuclides in iron meteorites; Exposure ages, meteoroid sizes and sample depths determined by mass spectrometric analyses of potassium and rare gases. *Earth Planet. Sci. Lett.* **45**, 293-308.

Wasson, J.T. (1970) The chemical classification of iron meteorites. IV: Irons with Ge concentrations greater than 190 ppm and other meteorites associated with group I. *Icarus **12***, 407-423.

Wasson, J.T. (1985) Meteorites: Their Record of Early Solar System History. W.H. Freeman, pp. 267.

Wasson, J. T. and Kallemeyn, G. W. (2002) The IAB iron-meteorite complex: a group, five subgroups, numerous grouplets, closely related, mainly formed by crystal segregation in rapidly cooling melts. *Geochim. Cosmochim. Acta* **66**, 2445–2473.

Walter M. J. and Trønnes R. G. (2004) Early Earth differentiation. *Earth Planet. Sci. Lett.* **225**, 253-269.

Weyer S. and Schwieters J. (2003) High precision Fe isotope measurements with high mass resolution MC-ICPMS. *Int. J. Mass Spectrom.* **226**, 355-368.

Weyer S., Münker C., Brey G. P., Woodland A. B., Mezger K. and Anbar A. D. (2005) Iron isotope fractionation during planetary differentiation processes. *Geophys. Res. Abstr.* **7**, 9257.

Williams H. M., Markowski A., Quitté G., Halliday A. N., Teutsch N. and Levasseur S. (2006) Fe isotope fractionation in iron meteorites: New insights into metal-sulphide segregation and planetary accretion. *Earth Planet. Sci. Lett.* **250**, 486-500.

Whitehouse M. J. and Fedo C. M. (2007) Microscale heterogeneity of Fe isotopes in >3.71 Ga banded iron formation from the Isua Greenstone Belt, southwest Greenland. *Geology* **35**, 719-722.

Wood J. A. (1964) The cooling rates and parent planets of several iron meteorites. *Icarus* **3**, 429-459.

Yang C. W., Williams D. B. and Goldstein J. I. (1996) A revision of the Fe-Ni phase diagram at low temperatures (<400 °C). *J. Phase Equilibria* **17**, 522-531.

Yang C. W., Williams D. B. and Goldstein J. I. (1997a) Low-temperature phase decomposition in metal from iron, stony-iron and stony meteorites. *Geochim. Cosmochim. Acta* **61**, 2943-2956.

Yang, C.-W., Williams, D.B., Goldstein, J.I. (1997b) A new empirical cooling rate indicator for meteorites based on the size of the cloudy zone of the metallic phases. *Meteorit. Planet. Sci.* **32**, 423–429.

Yang, J. and Goldstein, J.I. (2005) The formation of the Widmanstätten structure in meteorites. *Meteorit. Planet. Sci.* **40**, 239–253.

Yang C. W. and Goldstein J. I. (2006) Metallographic cooling rates of the IIIAB iron meteorites. *Geochim. Cosmochim. Acta* **70,** 3197-3215.

Yang, J., Goldstein, J.I., Scott, E.R.D. (2008) Metallographic cooling rates of IVA iron meteorites. *Geochim. Cosmochim. Acta* **72**, 3043–3061.

Zhu X. K., Guo Y., O`Nions R. K., Young E. D. and Ash R. D. (2001a) Isotopic homogeneity of iron in the early solar nebula. *Nature* **412**, 311-313.

Zhu X. K., Guo Y., Galy A., O`Nions K., Young E. D. and Ash R. D. (2001b) Iron isotope cosmochemistry: high-precision isotope ratio measurement using MC-ICPMS. *Meteorit. Planet. Sci*. **36**, A231.

Zhu X. K., Guo Y., Williams R. J. P., O`Nions R. K., Matthews A., Belshaw N. S., Canters G. W., de Waal E. C., Weser U., Burgess B. K. and Salvato B. (2002) Mass fractionation processes of transition metal isotopes. *Earth Planet. Sci. Lett.* **200**, 47-62.

CHARLES UNIVERSITY IN PRAGUE

FACULTY OF SCIENCE

ELEMENTAL AND ISOTOPIC STUDY OF DIFFERENTIATED METEORITES AND IMPLICATIONS FOR THE ORIGIN AND EVOLUTION OF THEIR PARENT BODIES

Dissertation thesis

Supplementary material

Published article:

Kohout, T. , Kosterov, A. , Haloda, J. , **Halodová, P**. , Zbořil, R. (2010): Low-temperature magnetic properties of iron-bearing sulfides and their contribution to magnetism of cometary bodies. Icarus 208, 2, 955-962. ISSN 0019-1035. DOI 10.1016/j.icarus.2010.03.021.

Icarus 208 (2010) 955–962

Contents lists available at ScienceDirect

Icarus

journal homepage: www.elsevier.com/locate/icarus

Low-temperature magnetic properties of iron-bearing sulfides and their contribution to magnetism of cometary bodies

Tomáš Kohout [a,b,*], Andrei Kosterov [c], Jakub Haloda [d], Patricie Týcová [d], Radek Zbořil [e]

[a] Institute of Geology, Academy of Sciences, Prague, Czech Republic
[b] Department of Physics, University of Helsinki, 00014 Helsinki, Finland
[c] Institute of Physics, St. Petersburg University, St. Petersburg, Russia
[d] Czech Geological Survey, Prague, Czech Republic
[e] Centre for Nanomaterial Research, Palacky University, Olomouc, Czech Republic

ARTICLE INFO

Article history:
Received 21 December 2009
Revised 15 February 2010
Accepted 15 March 2010
Available online 23 March 2010

Keywords:
Comets
Magnetic fields
Meteorites

ABSTRACT

In this study we present a review of low-temperature magnetic properties of alabandite (Fe, Mn)S, daubreelite $FeCr_2S_4$, pyrrhotite $Fe_{1-x}S$ and troilite FeS updated with new experimental data. The results indicate that besides FeNi alloys mainly daubreelite with its Curie temperature $T_C \sim 150$ K and strong induced and remanent magnetizations may be a significant magnetic mineral in cold environments and may complement that of FeNi or even dominate magnetic properties of sulfide rich bodies at temperatures below T_C.

Comets are known to contain iron-bearing sulfides within dusty fraction and their surfaces are subject to temperature variations in the range of 100–200 K down to the depth of several meters while the cometary interior is thermally stable at several tens of Kelvin which is within the temperature range where alabandite, daubreelite or troilite are "magnetic". Thus not only FeNi alloys, but also sulfides have to be considered in the interpretation of magnetic data from cometary objects such as will be delivered by Rosetta mission. Modeling indicates that magnetic interactions between cometary nucleus containing iron-bearing sulfides and interplanetary magnetic field would be difficult, but not impossible, to detect from orbit. Rosetta's Philae lander present on the surface would provide more reliable signal.

1. Introduction

Iron nickel (FeNi) alloys are dominant magnetic phase in most achondritic and chondritic meteorites and lunar samples (Rochette et al., 2003, 2008, 2009). Review of the magnetic properties of FeNi system can be found for example in Wasilewski (1974).

Additionally, carbides, phosphides and sulfides can be found in some achondritic and chondritic or martian meteorites (Rochette et al., 2003, 2008, 2009). While most of these sulfides (with the exception of ferrimagnetic monoclinic pyrrhotite $Fe_{1-x}S$) are antiferromagnetic or paramagnetic at room temperature, various magnetic transitions occur at lower temperatures enhancing their induced or remanent magnetization, or both. In this study we provide a review of low-temperature magnetic data available for alabandite (Fe, Mn)S, daubreelite $FeCr_2S_4$, pyrrhotite $Fe_{1-x}S$ and troilite FeS and present additional experimental results on these materials.

Such a review is useful for understanding the magnetic properties of primitive extraterrestrial materials at low temperatures typical for their original environment. Possible applications of these data include modeling of the interaction of extraterrestrial bodies with interplanetary magnetic fields in different temperature ranges. For example European Space Agency (ESA) Rosetta mission (launched in 2004) is due to arrive to Comet 67P/Churyumov-Gerasimenko in May 2014 and conduct observations during the approach of the comet to the Sun (Glassmeier et al., 2007a). Both orbiter and Philae cometary lander are equipped with magnetometers (Rosetta Plasma Consortium Magnetometer (RPC-MAG) and Rosetta Magnetometer and Plasma Monitor (ROMAP), respectively). Preliminary studies (Auster et al., 2007; Glassmeier et al., 2007b) take into account only FeNi alloys as the magnetic mineral present in cometary material.

Most stony meteorites and related asteroidal parent bodies are more abundant in FeNi metallic phase than in the iron-bearing sulfide phase. Thus FeNi metal will dominate their magnetic properties (with certain sulfides as daubreelite being significant contributor). In contrast, iron-bearing sulfide phase seems to be more abundant in cometary dust.

Iron-bearing sulfides (mainly troilite, pyrrhotite and FeNi sulfide pentlandite) have been reported in interplanetary dust particles (IDPs) (Dai and Bradley, 2001; Rietmeijer, 2005) and in cometary dust (Brownlee et al., 2006; Lisse et al., 2006; Zolensky

* Corresponding author at: Department of Physics, P.O. Box 64, 00014 Helsinki University, Finland. Fax: +358 919151000.
E-mail address: tomas.kohout@helsinki.fi (T. Kohout).

0019-1035/$ - see front matter © 2010 Elsevier Inc. All rights reserved.
doi:10.1016/j.icarus.2010.03.021

et al., 2006). Moreover, sulfides in these extraterrestrial materials are volumetrically more abundant than a FeNi metallic phase. For this reason the magnetic properties of these sulfides must be considered when interpreting magnetic observations of cometary bodies. Additionally, we consider alabandite and daubreelite as potential compounds present within dusty fraction in our modeling.

2. Instruments and methods

The magnetic measurements were done at the Institute for Rock Magnetism, University of Minnesota (IRM) using Quantum Designs MPMS-5S cryogenic susceptometer (AC/DC). In a previous study (Kohout et al., 2007) the Field Cooled (FC) and Zero Field Cooled (ZFC) induced (in 10 mT field) magnetization curves were shown to be most suitable for the detection of iron-bearing sulfides, particularly daubreelite. Thus, we measured FC and ZFC curves on warming from 5 K to 300 K in 5 K steps for 14 additional enstatite meteorite samples.

The chemical composition of sulfides present in meteorite samples was determined at Czech Geological Survey, Prague, Czech Republic (CGS) using CamScan3200 scanning electron microscope (SEM) equipped with Microspec WDX 3PC Wavelength-dispersive spectrometry (WDS) analyzer. The analyses were performed using an accelerating voltage of 20 kV, 24 nA beam current, 1 μm beam size and ZAF correction procedures. The counting time was 30 s for all analyzed elements. The instrument was calibrated using a combination of natural and synthetic standards.

3. Iron-bearing sulfides in extraterrestrial material

3.1. Alabandite

Alabandite (Fe, Mn)S is a naturally occurring mineral that crystallizes in isometric hexoctahedral (face centered cubic – f.c.c.) NaCl structure. Magnetic properties of synthetic alabandite are summarized in Heikens et al. (1977). Alabandite is paramagnetic at room temperatures and orders antiferromagnetically below the Néel temperature of $T_N \sim 148$ K. At $T_{tr} \sim 130$ K a phase transition occurs interpreted as an abrupt inversion of the rhombohedral distortion of the f.c.c. lattice along [1 1 1] plane accompanied by discontinuous change in the magnetic susceptibility as observed on single crystals.

The magnetic susceptibility and induced magnetization in 10 mT field of antiferromagnetic MnS below T_N remains low, in the range of $\sim 10^{-7}$ m^3/kg and ~0.003–0.004 A m^2/kg, respectively. However, iron free MnS samples slightly enriched in Mn compared to ideal composition show antiferro to ferrimagnetic transition at $T_T \sim 50$ K accompanied with sharp one to two orders of magnitude increase in induced magnetization on cooling through this transition (Petrakovski et al., 2001).

The substitution of Mn ions by Fe has a pronounced effect on the Néel temperature which increases with increasing iron content up to $T_N \sim 185$ K for the $Fe_xMn_{1-x}S$ system of $x = 0.2$ (Petrakovski et al., 2002). Moreover, according to Loseva et al. (1998) and Petrakovski et al. (2002), samples with higher Fe content ($x > 0.25$) exhibit ferrimagnetic behavior above room temperature with Curie temperatures T_C from 730 K ($x \sim 0.27$) to 860 K ($x \sim 0.38$). However, the magnetization of this ferrimagnetic phase is weak, close to that of paramagnetic MnS.

3.2. Troilite

Troilite is an iron sulfide with an ideal stoichiometric composition FeS. It crystallizes into a peculiar lattice (space group $P\bar{6}2c$), which can be thought of as being derived from the NiAs structure. The troilite supercell axes are $a = \sqrt{3}A$ and $c = 2C$, where A and C are NiAs subcell axes (Hägg and Sucksdorff, 1933). Magnetic properties of troilite above room temperature have been studied extensively (Haraldsen, 1937, 1941; Hirahara and Murakami, 1958; Murakami and Hirahara, 1958; Murakami, 1959; Schwarz and Vaughan, 1972; Horwood et al., 1976; Li and Franzen, 1996). Between room temperature and Neél temperature of ~600 K (~325 °C) troilite is antiferromagnetic, with spins parallel to the C-axis of the NiAs subcell below ca. 445 K (Horwood et al., 1976) and orthogonal to it at higher temperatures up to the Neél point at $T_N \sim 600$ K. The low temperature data measured on troilite powderized fraction extracted from the Bruderheim L6 chondrite reveal an existence of a magnetic transition at $T_T \sim 70$ K (Kohout et al., 2007). The nature of this transition is not well understood and is a subject of ongoing research. The magnetic susceptibility remains low at $\sim 10^{-7}$ m^3/kg below the transition with one order of magnitude sharp peak at the transition temperature. The induced magnetization in 10 mT field though increases sharply below the transition, but remains low in the range of ~0.1–0.3 A m^2/kg.

3.3. Pyrrhotite

Pyrrhotite $Fe_{1-x}S$ is an iron sulfide with iron deficiency compared to troilite. Two forms are commonly found in natural samples. While at the room temperature the hexagonal pyrrhotite of stoichiometric compositions Fe_9S_{10} and $Fe_{11}S_{12}$ is antiferromagnetic, the monoclinic form Fe_7S_8 is ferrimagnetic and thus contributes significantly to the bulk rock magnetic properties.

Based on the review by Dunlop and Özdemir (1997, pp. 76–79) the hexagonal pyrrhotite becomes ferrimagnetic in the narrow temperature range between ~475 K (~200 °C) and ~540 K (~265 °C). The Curie point of monoclinic pyrrhotite is higher at ~595 K (~320 °C). The magnetic susceptibility and the saturation remanent magnetization of monoclinic pyrrhotite at room temperature vary with the grain size in range of 1000–7000 × 10^{-8} m^3/kg and 2–6 A m^2/kg, respectively (Dekkers, 1988). The monoclinic pyrrhotite has a low-temperature transition in remanence and coercive force at 30–35 K (most likely isotropic point of the magnetocrystalline anisotropy, Dekkers, 1989; Rochette et al., 1990; Dunlop and Özdemir, 1997, p. 78).

3.4. Daubreelite

Daubreelite ($FeCr_2S_4$) is a naturally occurring mineral that crystallizes in the cubic spinel lattice, Fe^{2+} occupying tetrahedral and Cr^{3+} octahedral sites. Below the Curie temperature $T_C \sim 150$ K Fe^{2+} and Cr^{3+} spins are antiparallel, their inequality producing an overall ferrimagnetic order. Magnetic properties of the natural daubreelite from Coahuila IIAB hexaedrite iron meteorite and of the synthetic $FeCr_2S_4$ are summarized by Kohout et al. (2007) and Tsurkan et al. (2001a,b,c), respectively.

The magnetic susceptibility and induced magnetization in 10 mT are relatively high, in the range of $\sim 10^{-4}$ m^3/kg and ~3.5–5 A m^2/kg, respectively. From the published data, a magnetic transition can be identified as a local magnetization maximum at $T_m \sim 60$ K (Tsurkan et al., 2001a,b,c). Cooling through this transition is accompanied by spin-glass-like features and cubic-to-triclinic symmetry reduction within crystallographic domains (Tsurkan et al., 2001a,b,c; Maurer et al., 2003; Müller et al., 2006).

4. Variations of T_m and T_C in daubreelite-bearing meteorites

In order to get deeper insight into the variation of T_m and T_C in daubreelite we measured FC and ZFC induced magnetization

curves of 14 additional enstatite chondrites covering both enstatite subgroups (EH and EL) and all petrographic types (3–6). Most of these meteorites contain natural daubreelite of various amounts and compositions and thus are suitable natural source of daubreelite for our studies.

The meteorites come from three different collections. Antarctic finds ALH 81 021 (EL6), EET 96 341 (EH4–5), KLE 98 300 (EH3) and MAC 88 136 (EL3) were provided by NASA Johnson Space Center, USA. Meteorites Abee (EH4), Blithfield (EL6), Hvittis (EL6), Indarch (EH4) and Pillistfer (EL6) were provided by the Geological Museum, University of Helsinki, Finland. Meteorites Adhi Khot (Kot) (EH4), Daniel's Kuil (EL6), Jajh Deh Kot Lalu (EL6), St. Mark's (EH5) and Saint-Sauveur (EH5) were provided by Natural History Museum, London. The data of the Neuschwanstein meteorite are from Kohout et al. (2007). The meteorites are listed in Table 1.

A strong contribution of daubreelite to the FC and ZFC induced magnetization is apparent in all EL chondrites while it is weak or missing in EH chondrites (Fig. 1). The kamacite and iron-bearing sulfide abundances and daubreelite compositions were subsequently evaluated on thin sections using SEM–WDS and the results were evaluated with aim to find the relation between the daubreelite compositions and the shift in its T_m and T_C temperatures.

From the results of enstatite meteorites it is apparent that the daubreelite in all samples contain 0.83–3.25 wt.% Mn^{2+} replacing Fe^{2+} ions. However, no obvious correlation was observed between average Mn^{2+} content in daubreelite within the meteorites and variations in its T_m or T_C temperatures (Table 2). Additionally, there was no correlation observed between the homogeneity of daubreelite and the enstatite subgroup, petrographic type, or shock level.

However, it is apparent that daubreelites in all enstatite meteorites have systematically lower T_C by up to 20 K and higher T_m by ~10–15 K, compared to pure synthetic material. Also the natural daubreelite from the Coahuila iron meteorite (with no significant impurities detected) has T_m higher by ~10 K, but T_C close to that of synthetic material.

It seems likely that presence of Mn in daubreelite decreases its T_C. There might be also an increasing effect on T_m. However, this is not supported by Coahuila daubreelite sample. An alternative interpretation (Tsurkan et al., 2001b) explains variations in T_m or T_C temperatures in daubreelite in terms of stress or lattice distortions. With existing data we cannot draw a definite conclusion.

5. Discussion

In Table 3, we compare magnetic susceptibility, induced magnetization and saturation remanent magnetization of alabandite, daubreelite, monoclinic pyrrhotite and troilite to that of FeNi metal (20 wt.% of Ni). We are aware of the fact that the actual values might depend on mineral grain size or composition (i.e. Ni concentration) and thus we present the values as order of magnitude estimates of multi-domain (MD) particles. From Table 3, it is apparent that magnetization of alabandite or troilite in certain temperature regions is still one to three orders of magnitude lower compared to that of FeNi. However, the magnetization values of daubreelite are of the same order of magnitude as those of FeNi. This explains the fact that despite a roughly equal abundance of all of the above mentioned sulfides and kamacite in enstatite chondrites, contributions of daubreelite and kamacite only are apparent in the FC and ZFC induced magnetization curves while signatures of alabandite and troilite are too weak to be detected.

Based on empirical observations as well as on theoretical models (Spencer et al., 1989; Lim et al., 2005), the present surface temperatures of Near Earth Asteroids (NEAs) and asteroids within the main asteroid belt are above temperatures where alabandite, daubreelite or troilite show significant magnetism.

However, modeling of Comet 46P/Wirtanen (Heubner et al., 2006, pp. 197–198) or 67P/Churyumov-Gerasimenko (Heubner et al., 2006, p. 199) shows that the cometary surface is subject to temperature variations in the range of 100–200 K down to the depth of several meters while the cometary interior is thermally stable at several tens Kelvin. This is within the temperature range where alabandite, daubreelite, or troilite are also "magnetic". Thus not only FeNi alloys, but also sulfides have to be considered in the interpretation of magnetic data from cometary objects such as will be delivered by Rosetta mission.

Furthermore, the approach of the comet towards the Sun and the rotation of its nuclei will cause variations in the surface temperature. This may produce detectable changes in the magnetic properties of the comet as various sulfides will change their magnetic ordering states at their characteristic transition temperatures.

To demonstrate and compare magnetic properties of these minerals present within extraterrestrial materials let us model a cold icy cometary body containing dispersed 10 wt.% fine-powder fraction of alabandite, daubreelite, monoclinic pyrrhotite, troilite or FeNi metal. As the magnetic susceptibility of such a body is proportional to the concentration of the magnetic minerals we can estimate from Table 3 the magnetic susceptibility of such a body to be $\sim 10^{-8}$ m^3/kg in the case of either alabandite or troilite (Fig. 2). This is below the magnetic susceptibility of most meteorites (only some HED or SNC meteorites have such low values). Presence of 10 wt.% of monoclinic pyrrhotite will result in susceptibility comparable to these materials while 10 wt.% of daubreelite will result in a magnetic susceptibility $\sim 1000 \times 10^{-8}$ m^3/kg which is comparable to most carbonaceous or LL and L ordinary chondrites or aubrite or ureilite achondrites. Thus, such a cometary body will show similar magnitude of interactions with interplanetary magnetic field (IMF) as with parent bodies of these meteorites. A comet with 10 wt.% of finely dispersed FeNi metal would produce still an order of magnitude higher induced magnetization. As mentioned earlier the magnetic susceptibility of an extraterrestrial body is proportional to the concentration of the magnetic minerals and will vary with the real abundance of those minerals and their mixtures.

The estimate of induced magnetization measured by space probe orbiting a minor Solar System body is discussed in Kohout et al. (2008). This modeling reveals that it will be difficult, but not impossible, to detect such interactions from orbit. Based on Eq. (11) in Kohout et al. (2008), the induced magnetization measured on the orbit around a comet containing 10 wt.% of finely dispersed daubreelite in 10 nT IMF will be in range of 10^{-1}–10^{0} nT. This is within the resolution limit of Rosetta's RPC-MAG instrument (31 pT, Glassmeier et al., 2007b). The ROMAP instrument on the Philae lander (resolution 10 pT, Auster et al., 2007) should

Table 1
List of meteorites subjected to the magnetic measurements.

Meteorite	Group and type	Fall/find	Shock level
Abee	EH4	FA 1953	S2–5
Adhi Khot	EH4	FA 1919	S4
ALH 81 021	EL6	FI	S2
Blithfield	EL6	FA 1910	S2
Daniel's Kuil	EL6	FA 1868	S2
EET 96 341	EH4–5	FI	
Hvittis	EL6	FA 1901	S2
Indarch	EH4	FA 1891	S4
Jajh Deh Kot Lalu	EL6	FA 1926	S2
KLE 98 300	EH3	FI	
MAC 88 136	EL3	FI	S3
Neuschwanstein	EL6	FA 2002	S2
Pillistfer	EL6	FA 1868	S2
Saint-Sauveur	EH5	FA 1914	S4
St. Mark's	EH5	FA 1903	S3

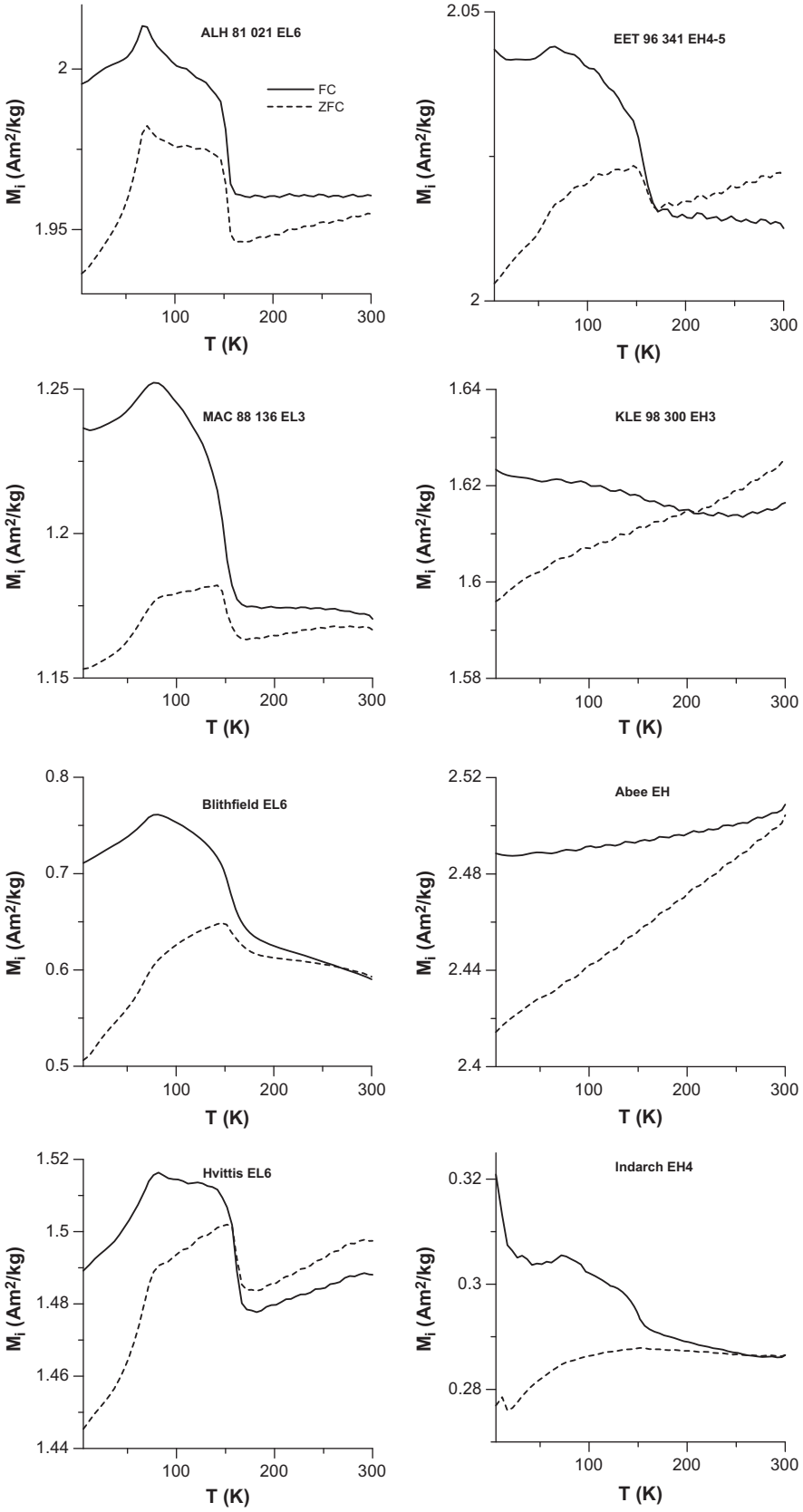

Fig. 1. Field Cooled (FC) and Zero Field Cooled (ZFC) induced (in 10 mT field) magnetization curves of 15 enstatite meteorites.

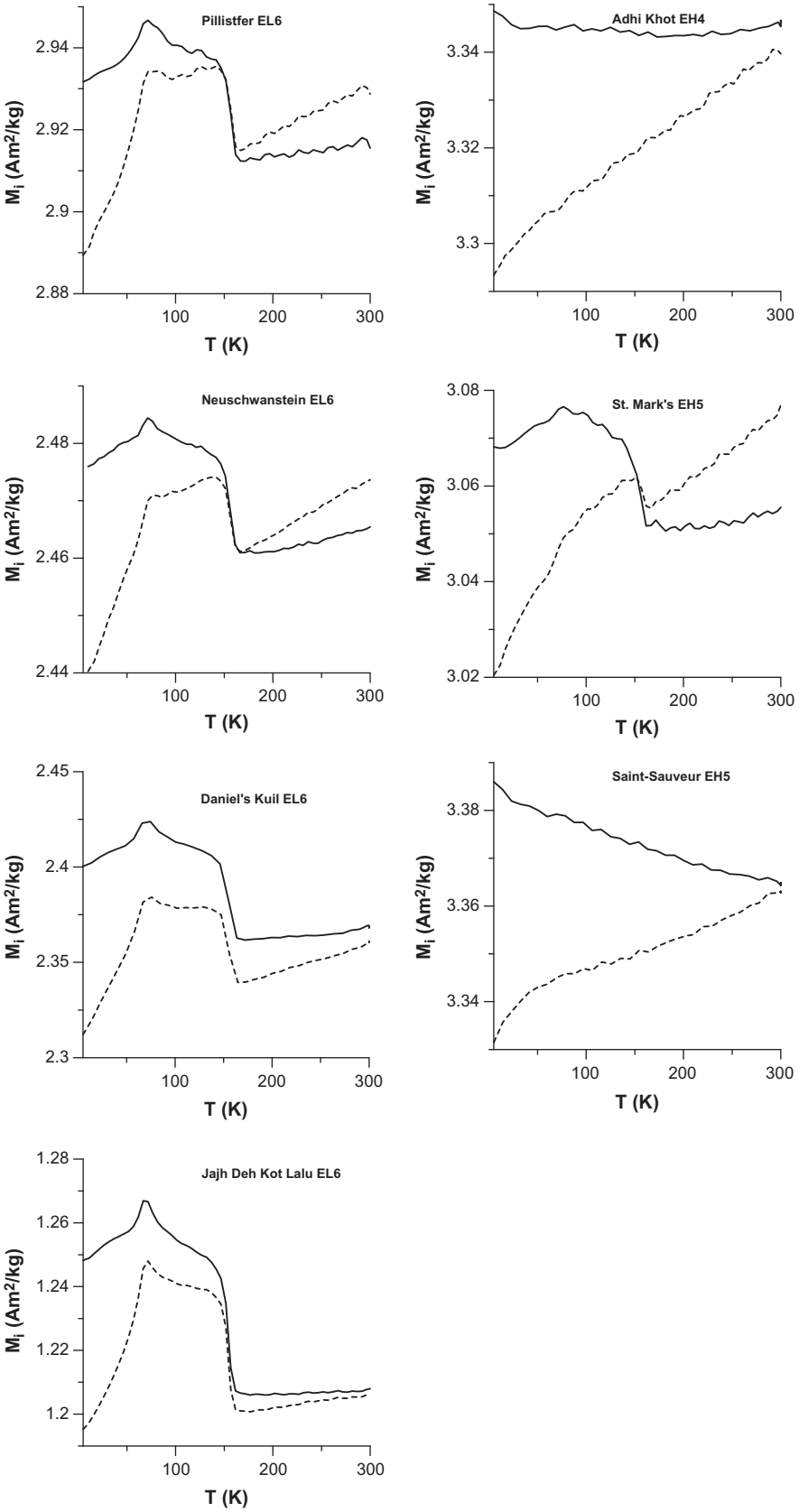

Fig. 1 (*continued*)

Table 2
Magnetic transition (T_m) and Curie (T_C) temperature of daubreelite within enstatite chondrites and daubreelite elemental composition. Included are also data for daubreelite from Coahuila IIAB hexaedrite (Kohout et al., 2007) and for synthetic daubreelite (Tsurkan et al., 2001a).

Meteorite	Group and type	T_m (K)	T_C (K)	Daubreelite composition		
				Mn abundance range (wt.%)	Mn average abundance (wt.%)	Structural formula (atoms per four sulfur formula unit)
Abee	EH4	–	–			
Adhi Khot	EH4	–	–			
ALH 81 021	EL6	69	153	2.63–2.80	2.73	$(Fe_{0.875-0.880}Mn_{0.138-0.148})_{1.018-1.022}\ Cr_{2.031-2.032}S_4$
Blithfield	EL6	80	155	1.58–2.61	2.20	$(Fe_{0.862-0.920}Mn_{0.083-0.138})_{1.000-1.002}\ Cr_{1.997-2.010}S_4$
Daniel's Kuil	EL6	72	155	2.23–2.89	2.57	$(Fe_{0.850-0.886}Mn_{0.116-0.152})_{1.011-1.021}\ Cr_{2.022-2.025}S_4$
EET 96 341	EH4–5	65	156			
Hvittis	EL6	81	160	2.52–2.61	2.56	$(Fe_{0.876-0.883}Mn_{0.135-0.138})_{1.014-1.018}\ Cr_{2.012-2.023}S_4$
Indarch	EH4	74	148	2.35–2.97	2.64	$(Fe_{0.845-0.873}Mn_{0.124-0.157})_{0.998-1.002}\ Cr_{2.014-2.018}S_4$
Jajh Deh Kot Lalu	EL6	69	154	1.74–2.86	2.41	$(Fe_{0.864-0.909}Mn_{0.091-0.150})_{1.001-1.014}\ Cr_{1.980-1.997}S_4$
KLE 98 300	EH3	–	–			
MAC 88 136	EL3	78	148	0.83–2.81	1.84	$(Fe_{0.862-0.974}Mn_{0.044-0.148})_{1.010-1.018}\ Cr_{2.017-2.028}S_4$
Neuschwanstein	EL6	71	155	2.09–3.25	2.89	$(Fe_{0.803-0.878}Mn_{0.125-0.198})_{1.001-1.003}\ Cr_{2.008-2.012}S_4$
Pillistfer	EL6	71	156	0.53–2.11	1.52	$(Fe_{0.892-0.976}Mn_{0.028-0.111})_{1.003-1.004}\ Cr_{1.998-2.018}S_4$
Saint-Sauveur	EH5	–	–			
St. Mark's	EH5	76	155			
Coahuila	Iron	76	164			
Synt. daubreelite		~60	167			

Table 3
The magnetic properties of the sulfides considered in this study. Data are from Dekkers (1988), Kohout et al. (2007), Petrakovski et al. (2001, 2002), Tsurkan et al. (2001a,b,c), and Heikens et al. (1977).

Magnetic mineral	Magnetic susceptibility (10^{-8} m^3/kg)	Induced magnetization in 10 mT field (A m^2/kg)	Saturation remanence imprinted by 1 T (A m^2/kg)
Alabandite (below 150 K)	10	0.003–0.004 0.01–0.1 (below 50 K for MnS slightly enriched in Mn)	
Daubreelite (below 165 K)	10 000	3.5–5	~4–12
Troilite (below 70 K)	10	0.1–0.3	~0.3
Pyrrhotite	1000		2–6
FeNi metal (20 wt.% of Ni)	100 000	~10	~2–3

provide stronger signal and might detect those interactions more reliably.

As the cometary activity increases on its approach to the Sun, dust and volatiles are released to form a coma surrounding the nucleus. Complex solar wind interactions with dust and ionized gas within the coma are expected. Also here a dusty magnetic mineral fraction may contribute to the solar wind driven magnetic interactions. However, it is difficult to quantitatively predict the scale of these interactions.

The magnetic remanence of small dusty grains was recognized as an important factor in the aggregation process (Dominik and Nübold, 2002; Nübold et al., 2003) and may lead to accretional remanence of cometary bodies (Nübold and Glassmeier, 2000). However, such a remanence does not need to be preserved till present time.

Any extraterrestrial body remanence carried by iron-bearing sulfides will be erased while the material warms-up through de-

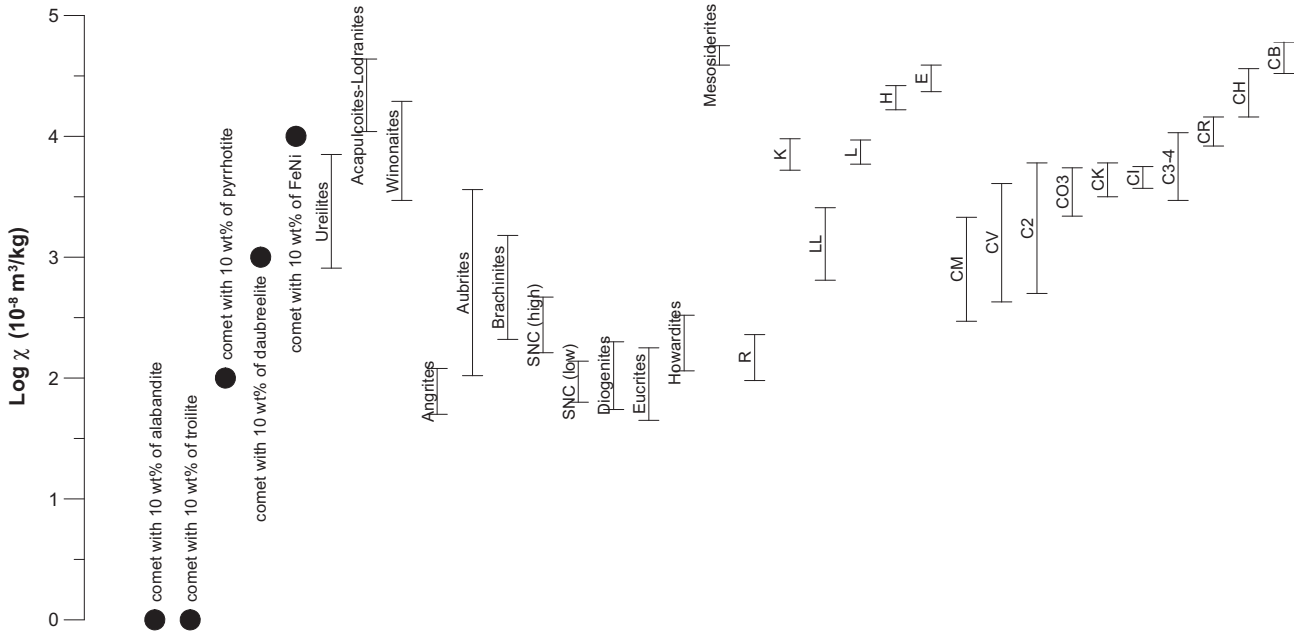

Fig. 2. Model magnetic susceptibility of an icy comet containing dispersed 10 wt.% fine-powder fraction of alabandite, daubreelite, monoclinic pyrrhotite, troilite or FeNi metal and its comparison to susceptibility of meteorites. The temperature of the cometary body with sulfides is supposed to be within the temperature interval specified in Table 3. Meteorite data are from Rochette et al. (2003, 2008, 2009).

scribed sulfide magnetic transitions (Kohout et al., 2007). This can happen periodically to the outer layers of the minor Solar System bodies during their orbital or rotational history (asteroids or periodical comets). Due to this the remanence carried by most iron-bearing sulfides (with exception of monoclinic pyrrhotite) may be partly lost.

The magnetic remanence carried by FeNi grains or monoclinic pyrrhotite may be more stable. While the MD particles are susceptible to viscous magnetic effects, the small single-domain (SD) grains may carry remanent magnetization over a long time and may be carriers of cometary remanent magnetization.

6. Conclusions

Besides FeNi alloys mainly monoclinic pyrrhotite and daubreelite (below its $T_C \sim 150$ K) with strong induced and remanent magnetizations may be a significant magnetic minerals in cold environment. In the case of daubreelite strong induced magnetization below 150 K may complement that of FeNi or even dominate magnetic properties of sulfide rich bodies at these temperatures.

Additionally iron free alabandite samples slightly enriched in Mn compared to ideal composition show antiferro to ferrimagnetic transition at $T_T \sim 50$ K accompanied with sharp one to two orders of magnitude increase in induced magnetization on cooling.

Similar behavior is observed in troilite where magnetic susceptibility shows one order of magnitude sharp peak and induced magnetization increases sharply (but remains low in the range of $\sim$0.1–0.3 A m^2/kg) below a transition at $T_T \sim 70$ K.

Our model of a cometary body with 10 wt.% of alabandite or troilite dusty fraction reveals magnetic interactions an order of magnitude lower than that of the HED or SNC achondritic materials while 10 wt.% of monoclinic pyrrhotite is already within this range. Presence of 10 wt.% of daubreelite results in a magnetic interaction similar to these of aubrite, carbonaceous, L, LL or ureilite meteorite parent bodies and 10 wt.% of FeNi metal produces still an order of magnitude higher induced magnetization. Magnetic interactions between comets containing iron-bearing sulfides and IMF will be difficult, but not impossible, to detect from orbit. The lander present on the surface should provide more reliable signal.

Cometary interiors are kept cold at temperatures of several tens Kelvin while the approach of the comet towards the Sun and the rotation of its nuclei will cause variations in the surface temperature. This may produce detectable changes in the magnetic properties of the comet as various sulfides will change their magnetic ordering states at their characteristic transition temperatures. In future work, other sulfides common in extraterrestrial materials (i.e. pentlandite $(Fe, Ni)_9S_8$) should be magnetically characterized at low temperatures.

Acknowledgments

We would like to thank to Grant Agency of the Czech Academy of Sciences of the Czech Republic (Grant No. KJB300130903), University of Helsinki and IRM visiting fellowship for research and travel funding, to Dr. Cecilia E. Satterwhite, Dr. Caroline Smith and Prof. Martti Lehtinen for loaning the meteorite samples, to Ms. Anne Stine for language corrections and to two anonymous reviewers for constructive comments on the manuscript.

References

Auster, H.U., and 20 colleagues, 2007. ROMAP: Rosetta Magnetometer and Plasma Monitor. Space Sci. Rev. 128, 221–240.

Brownlee D., and 182 colleagues, 2006. Comet 81P/Wild 2 under a microscope. Science 314, 1711–1716.

Dai, Z.R., Bradley, J.P., 2001. Iron–nickel sulfides in anhydrous interplanetary dust particles. Geochim. Cosmochim. Acta 65, 3601–3612.

Dekkers, M.J., 1988. Magnetic properties of natural pyrrhotite. Part I: Behaviour of initial susceptibility and saturation magnetization related rock magnetic parameters in a grain size dependent framework. Phys. Earth Planet. Inter. 52, 376–393.

Dekkers, M.J., 1989. Magnetic properties of natural pyrrhotite. II. High- and low-temperature behaviour of Jrs and TRM as function of grain size. Phys. Earth Planet. Inter. 57, 266–283. doi:10.1016/0031-9201(89)90116-7.

Dominik, C., Nübold, H., 2002. Magnetic aggregation: Dynamics and numerical modeling. Icarus 157, 173–186.

Dunlop, D.J., Özdemir, Ö., 1997. Rock Magnetism Fundamentals and Frontiers. Cambridge Univ. Press, Cambridge, UK, pp. 76–79.

Glassmeier, K.-H., Boehnhardt, H., Koschny, D., Kührt, E., Richter, I., 2007a. The Rosetta mission: Flying towards the origin of the Solar System. Space Sci. Rev. 128, 1–21.

Glassmeier, K.-H., and 13 colleagues, 2007b. RPC-MAG the fluxgate magnetometer in the Rosetta Plasma Consortium. Space Sci. Rev. 128, 649–670.

Hägg, G., Sucksdorff, I., 1933. Die Kristallstruktur von Troilit und Magnetkies. Z. Phys. Chem. B 22, 444–452.

Haraldsen, H., 1937. Magnetochemische Untersuchungen. XXIV. Eine thermomagnetische Untersuchung der Umwandlungen im Troilit–Pyrrhotin–Gebiet des Eisen–Schwefel-Systems. Z. Anorg. Allg. Chem. 231, 78–96.

Haraldsen, H., 1941. Über die Hochtemperaturumwandlungen der Eisen(II)-Sulfidmischkristalle. Z. Anorg. Allg. Chem. 246, 195–226.

Heikens, H.H., Wiegers, G.A., Van Bruggen, C.F., 1977. On the nature of a new phase transition in α-MnS. Solid State Commun. 24, 205–209.

Heubner, W.F., Benkhoff, J., Capria, M.-T., Coradini, A., De Sanctis, C., Orosei, R., Prialnik, D. 2006, Heat and Gas Diffusion in Comet Nuclei. ISSI Scientific Report SR-004. Published for The International Space Science Institute, Bern, Switzerland by ESA Publications Division, Noordwijk, The Netherlands.

Hirahara, E., Murakami, M., 1958. Magnetic and electrical anisotropies of iron sulfide single crystals. J. Phys. Chem. Solids 7, 281–289.

Horwood, L.J., Townsend, M.G., Webster, A.H., 1976. Magnetic susceptibility of single-crystal $Fe_{1-x}S$. J. Solid State Chem. 17, 35–42.

Kohout, T., Kosterov, A., Jackson, M., Pesonen, L.J., Kletetschka, G., Lehtinen, M., 2007. Low-temperature magnetic properties of the Neuschwanstein EL6 meteorite. Earth Planet. Sci. Lett. 261, 143–151. doi:10.1016/j.epsl.2007.06.022.

Kohout, T., Kletetschka, G., Elbra, T., Adachi, T., Mikula, V., Pesonen, L.J., Schnabl, P., Slechta, S., 2008. Physical properties of meteorites – Applications in space missions to asteroids. Meteorit. Planet. Sci. 43, 1009–1020.

Li, F., Franzen, H.F., 1996. Phase transitions in near stoichiometric iron sulfide. J. Alloy. Compd. 238, 73–80.

Lim, L.F., McConnochiea, T.H., Bell, J.F., Hayward, T.L., 2005. Thermal infrared (8–13 μm) spectra of 29 asteroids: The Cornell Mid-Infrared Asteroid Spectroscopy (MIDAS) survey. Icarus 173, 385–408.

Lisse, C.M., and 16 colleagues, 2006. Spitzer spectral observations of the deep impact ejecta. Science 313, 635–640.

Loseva, G.V., Ryabinkina, L.I., Balaev, A.D., 1998. Ferromagnetism and the metal–insulator transition in the magnetic semiconductor system $Fe_xMn_{1-x}S$. Phys. Solid State 40, 250–251 (Translated from Fizika Tverdogo Tela 40, 276–277).

Maurer, D., Tsurkan, V., Horn, S., Tidecks, R., 2003. Ultrasonic study of ferrimagnetic $FeCr_2S_4$: Evidence for low temperature structural transformations. J. Appl. Phys. 93, 9173–9176.

Müller, C., Zestrea, V., Tsurkan, V., Horn, S., Tidecks, R., Wixforth, A., 2006. Spin–lattice coupling in the ferrimagnetic semiconductor $FeCr_2S_4$ probed by surface acoustic waves. J. Appl. Phys. 99, 023906. doi:10.1063/1.2164529.

Murakami, M., 1959. Alpha-transformation mechanism of the antiferromagnetic iron sulfide. Sci. Rep. Tohoku Univ., Ser. 1, 43, 53–61.

Murakami, M., Hirahara, E., 1958. A certain anomalous behavior of iron sulfides. J. Phys. Soc. Jpn. 13, 1407.

Nübold, H., Glassmeier, K.-H., 2000. Accretional remanence of magnetized dust in the Solar Nebula. Icarus 144, 149–159.

Nübold, H., Poppe, T., Rost, M., Dominik, C., Glassmeier, K.-H., 2003. Magnetic aggregation II. Laboratory and microgravity experiments. Icarus 165, 195–214.

Petrakovski, G.A., Ryabinkina, L.I., Abramova, G.M., Velikanov, D.A., Bovina, A.F., 2001. Antiferromagnet–ferromagnet transition in α-Mn_xS manganese sulfides. Phys. Solid State 43, 493–495 (Translated from Fizika Tverdogo Tela 43, 474–476).

Petrakovski, G.A., Ryabinkina, L.I., Abramova, G.M., Balaev, A.D., Romanova, O.B., Makovetski, G.I., 2002. Magnetic properties of $Fe_xMn_{1-x}S$ sulfides exhibiting the magnetoresistive effect. Phys. Solid State 44, 1925–1928 (Translated from Fizika Tverdogo Tela 44, 1836–1839).

Rietmeijer, F.J.M., 2005. Iron–sulfides and layer silicates: A new approach to aqueous processing of organics in interplanetary dust particles, CI and CM meteorites. Adv. Space Res. 36, 201–208.

Rochette, P., Fillion, G., Mattéi, J.-L., Dekkers, M.J., 1990. Magnetic transition at 30–34 Kelvin in pyrrhotite: Insight into a widespread occurrence of this mineral in rocks. Earth Planet. Sci. Lett. 98, 319–328. doi:10.1016/0012-821X(90)90034-U.

Rochette, P., Sagnotti, L., Bourot-Denise, M., Consolmagno, G., Folco, L., Gattacceca, J., Osete, M.L., Pesonen, L.J., 2003. Magnetic classification of stony meteorites: 1. Ordinary chondrites. Meteorit. Planet. Sci. 38, 251–268.

Rochette, P., and 13 colleagues, 2008. Magnetic classification of stony meteorites: 2. Non-ordinary chondrites. Meteorit. Planet. Sci. 43, 959–980.

Rochette, P., Gattacceca, J., Bourot-Denise, M., Consolmagno, G., Folco, L., Kohout, T., Pesonen, L.J., Sagnotti, L., 2009. Magnetic classification of stony meteorites: 3. Achondrites. Meteorit. Planet. Sci. 44, 405–427.

Schwarz, E.J., Vaughan, D.J., 1972. Magnetic phase relations of pyrrhotite. J. Geomagn. Geoelectr. 24, 441–458.
Spencer, J.R., Lebofsky, L.A., Sykes, M.V., 1989. Systematic biases in radiometric diameter determinations. Icarus 78, 337–354.
Tsurkan, V., Baran, M., Szymczak, R., Szymczak, H., Tidecks, R., 2001a. Spin-glass like states in the ferrimagnet $FeCr_2S_4$. Physica B 296, 301–305.
Tsurkan, V., and 10 colleagues, 2001b. Effect of pressure on the magnetic and transport properties of the ferrimagnetic semiconductor $FeCr_2S_4$. J. Appl. Phys. 90, 875–881.
Tsurkan, V., Hemberger, J., Klemm, M., Klimm, S., Loidl, A., Horn, S., Tidecks, R., 2001c. Ac susceptibility studies of ferrimagnetic $FeCr_2S_4$ single crystals. J. Appl. Phys. 90, 4639–4644.
Wasilewski, P.J., 1974. Magnetic remanence mechanisms in iron and iron–nickel alloys, metallographic recognition criteria and implications for lunar sample research. The Moon 9, 335–354.
Zolensky M.E., and 74 colleagues, 2006. Mineralogy and petrology of Comet 81P/Wild 2 nucleus samples. Science 314, 1735–1739.

CHARLES UNIVERSITY IN PRAGUE

FACULTY OF SCIENCE

ELEMENTAL AND ISOTOPIC STUDY OF DIFFERENTIATED METEORITES AND IMPLICATIONS FOR THE ORIGIN AND EVOLUTION OF THEIR PARENT BODIES

Dissertation thesis

Supplementary material

Published article:

Haloda, J. , **Týcová, P.**. , Korotev, R.L. , Fernandes, V.A. , Burgess, R. , Thoeni, M. , Jelenc, M. , Jakeš, P. , Gabzdyl, P. , Košler, J. (2009): Petrology, geochemistry, and age of low-Ti mare-basalt meteorite Northeast Africa 003-A: A possible member of the Apollo 15 mare basaltic suite. Geochimica et Cosmochimica Acta 73, 11, 3450-3470. ISSN 0016-7037. DOI 10.1016/j.gca.2009.03.003.

Available online at www.sciencedirect.com
ScienceDirect
Geochimica et Cosmochimica Acta 73 (2009) 3450–3470
Geochimica et Cosmochimica Acta
www.elsevier.com/locate/gca

Petrology, geochemistry, and age of low-Ti mare-basalt meteorite Northeast Africa 003-A: A possible member of the Apollo 15 mare basaltic suite

Jakub Haloda [a,b,*], Patricie Týcová [a,b], Randy L. Korotev [c], Vera A. Fernandes [d,e,1], Ray Burgess [d], Martin Thöni [f], Monika Jelenc [f], Petr Jakeš [b,2], Pavel Gabzdyl [g], Jan Košler [h]

[a] Department of Rock Geochemistry, Czech Geological Survey, 152 00 Prague, Czech Republic
[b] Institute of Geochemistry, Mineralogy and Mineral Resources, Faculty of Science, Charles University, 128 43 Prague, Czech Republic
[c] Department of Earth and Planetary Sciences, Washington University, C/B 1169, Saint Louis, MO 63130, USA
[d] School of Earth, Atmospheric and Environmental Sciences, University of Manchester, Manchester M13 9PL, UK
[e] Centro de Geofísica, Universidade de Coimbra, Coimbra 3000-134, Portugal
[f] Department of Lithosphere Research, University of Vienna, Althanstraße 14, A-1090 Vienna, Austria
[g] Department of Geological Sciences, Faculty of Science, Masaryk University, 611 37 Brno, Czech Republic
[h] Centre for Geobiology and Department of Earth Science, University of Bergen, Bergen N-5007, Norway

Received 5 November 2008; accepted in revised form 3 March 2009; available online 18 March 2009

Abstract

Northeast Africa 003 (NEA 003) is a lunar meteorite found as a two paired stones (6 and 118 g) in Libya, 2000 and 2001. The main portion (~75 vol%) of the 118 g meteorite, used for this study, (NEA 003-A) consists of mare-basalt and a smaller adjacent portion (~25 vol%) is a basaltic breccia (NEA 003-B). NEA 003-A has a coarse-grained magmatic texture consisting mainly of olivine, pyroxene and plagioclase. The late-stage mineral association is composed mainly of elongated plagioclase, ilmenite, troilite, fayalite, Si–K-rich glass, apatite, and a rare SiO_2 phase. Other accessory minerals include ulvöspinel, chromite, and trace Fe–Ni metal. Olivine and pyroxene contain shock-induced fractures, and plagioclase is completely converted into maskelynite.

The Fe/Mn values of the whole rock, olivines and pyroxenes, and the bulk-rock oxygen isotopic composition provide evidence for the lunar origin of NEA 003-A meteorite. This is further supported by the presence of Fe–Ni metal and the anhydrous mineral association.

NEA 003-A is geochemically and petrographically distinct from previously described mare-basalt meteorites and is not paired with any of them. The petrography and major element composition of NEA 003-A is similar to the composition of low-Ti olivine mare basalts from Apollo 12 and olivine-normative basalts from Apollo 15. The NEA 003-A meteorite shows obvious geochemical similarities in trace elements contents with Apollo 15 olivine-normative basalts and could represent a yet unknown geochemically primitive member of the olivine-normative basalt series. The meteorite is depleted in rare earth elements (REE) and incompatible trace elements indicating a primitive character of the parental magma. The bulk-rock chemical composition demonstrates that the parent melt of NEA 003-A was not contaminated with KREEP components as a result of magma mixing or assimilation processes. Results of crystallization modelling and low minimum cooling rate estimates (~0.07 °C/h) suggest that the parent melt of NEA 003-A crystallized in the lower part of a lava flow containing cumulate olivine (~10%) and was probably derived from more primitive picritic magma by fractional crystallization processes.

* Corresponding author. Address: Department of Rock Geochemistry, Czech Geological Survey, 152 00 Prague, Czech Republic.
E-mail address: jakub.haloda@geology.cz (J. Haloda).
[1] Present address: Berkeley Geochronology Center, Berkeley, CA, USA.
[2] Deceased 29 November 2005.

doi:10.1016/j.gca.2009.03.003

Sm–Nd dating yields an age of 3.09 ± 0.06 Ga which corresponds to the period of lower Eratosthenian lunar volcanic activity, and the near-chondritic ε_{Nd} value of -0.4 ± 0.3 indicates that the meteorite could be derived from a slightly enriched mantle source similar to the Apollo 15 green glasses. Ar–Ar step release results are inconsistent with Sm–Nd ages suggesting that NEA 003-A was exposed to one or more impact events. The most extensive event took place at 1.8 Ga and the shock intensity was likely between 28 and 45 GPa. The absence of solar Ar suggests that NEA 003-A has not been directly exposed at the lunar surface but the cosmic ray exposure age of 209 ± 6 Ma suggests that NEA 003-A resided in the upper regolith for part of its history.

1. INTRODUCTION

The current source of ground-truth information about the geology of the Moon is the approximately 382 kg of rock and regolith samples acquired by Apollo and Luna missions between 1969 and 1976. The Apollo and Luna rocks and regoliths sample the better characterized locations on the Moon, but these rocks are representative only of a small part of the lunar surface (about 16%; Korotev, 2005). Lunar meteorites originated from randomly distributed locations on the surface of the Moon and are likely to come from points distant from the Apollo sites (Korotev, 2005). Many of these meteorites have chemical and mineralogical features different from Apollo and Luna samples. From a total of more than 60 known lunar meteorites, only ten represent unbrecciated mare-basalt samples.

Northeast Africa 003 (NEA 003) is a lunar meteorite find composed of two stones. Both were found by a private collector 12 km NW from Al Qaryah Ash Sharqiyah in Wadi Zamzam area, Libya. The smaller of the two stones (6 g) was found in November 2000. The second stone (118 g) with incomplete fusion crust, which was used for this study, was found nearby in December 2001. All studied samples from this stone are deposited in Department of Rock Geochemistry of Czech Geological Survey. The meteorite contains two adjacent parts, mare-basalt and basaltic breccia. The main portion (~75 vol% of 118 g stone and ~55 vol% of 6 g stone) of the meteorite, designated NEA 003-A (Fig. 1), is an unbrecciated, coarse-grained, low-Ti olivine-rich mare-basalt. The remaining 25 and 45 vol%, respectively, of NEA 003-B, is a basaltic breccia consisting of well-consolidated glassy impact–melt matrix containing scattered mineral fragments with a chemical composition identical to the coarse-grained low-Ti olivine-rich basalt, and two larger clasts of different low-Ti mare-basalt lithologies (Haloda et al., 2006).

In this study we describe the main portion of NEA 003 lunar meteorite, the unbrecciated, low-Ti, olivine-rich mare-basalt designated NEA 003-A, and provide major- and trace-element compositional data along with Sm–Nd and Ar–Ar isotopic data. We show that this basalt is geochemically and petrographically distinct from the previously described mare-basalt meteorites and Apollo mare basalts (see Korotev (2005) for a review of all lunar meteorites known at that time) but that it could have a geological affinity to Apollo 15 olivine-normative basalts.

2. ANALYTICAL METHODS

2.1. Petrography, chemical composition and O isotope composition

Two polished thin sections (21×13 mm and 14×10 mm) and one polished thick section ($16 \times 20 \times 3$ mm) were prepared from different areas of NEA 003-A. Textural and mineralogical characteristics were studied using a LEICA DMLP petrographic microscope.

Backscattered electron (BSE) images and elemental X-ray maps were produced using a CAMSCAN 3200 scanning electron microscope fitted with an Oxford Instruments Energy Dispersive Spectral unit at the Czech Geological Survey in Prague, Czech Republic. Mineral modes were determined using the Area Measurement software (Oxford Instruments) and digital processing of BSE images and elemental X-ray maps.

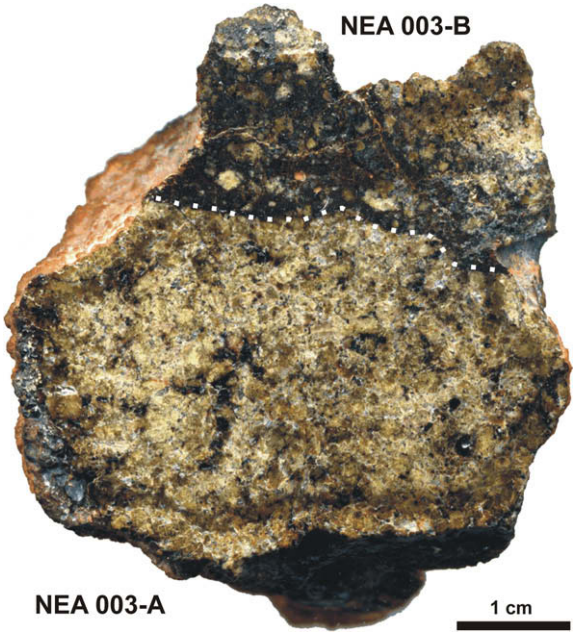

Fig. 1. Incident light image of a polished surface of Northeast Africa 003 lunar meteorite (118 g stone). The main part (~75 vol%) designated as NEA 003-A is an unbrecciated coarse-grained, low-Ti olivine-rich basalt. The adjacent part (NEA 003-B) is a basaltic breccia (~25 vol%).

Mineral compositions were determined using quantitative X-ray wavelength dispersive spectral analysis on an ARL SEMQ electron microprobe at the Naturhistorisches Museum, Vienna, Austria and a CAMECA SX100 electron microprobe at the Natural History Museum, London, UK. The analyses were performed using an accelerating voltage of 15 kV, 20 nA beam current, 1 μm beam size and ZAF correction procedures. The counting times were 20 or 30 s for all analyzed elements. To avoid Na volatilization during the analysis of glass and maskelynite, the beam size was increased to 5 μm. For both instruments a combination of natural and synthetic standards were used for calibration. Quantitative analysis obtained from these two instruments yielded consistent results.

The degree of maskelynitization of plagioclase, SiO_2 structure identification and crystallographic orientation of selected olivine grains were determined by electron backscattered diffraction (EBSD) methods (Schmidt and Olensen, 1989) using HKL Technology Nordlys-II system at Czech Geological Survey, Prague, Czech Republic.

The bulk-rock major and minor element concentrations were determined by XRF analyses. Analyses were performed using a wavelength-dispersive ARL 9400 ADVANT XRF system at Czech Geological Survey, Prague. A split of NEA 003-A with an original mass of 612.28 mg was cleaned in an ultrasonic bath and homogenized by crushing and powdering using an agate mortar and pestle. We analyzed three samples as pressed powder pellets, each sample was prepared from 150 mg of finely grounded sample powder. All XRF analyses were processed to determine measurement precision and average bulk element concentrations. The analytical errors (relative standard deviations) based on the average of 25 BHVO-1 reference standard measurements were better than 3% for Si, Ti, Al, Fe, Mg and Ca. For Cr and Mn the relative standard deviations were better than 7%.

The Na and K concentrations presented in this study were determined on a 50 mg aliquot from a 612.28 mg homogeneous powdered rock sample using ICP-OES. The sample was prepared following the method of Shafer et al. (2004). Analyses were performed using an Iris Advantage Thermo Jarrell Ash ICP-OES system at Czech Geological Survey, Prague. For ICP-OES system calibrations, we used certified reference materials BHVO-1 and BCR-2. Eight analyses were collected from this sample to determine measurement precision and the average element concentrations. The analytical errors (relative standard deviations) based on the average of 25 BHVO-1 reference standard measurements were better than 4% for both measured elements.

The concentration of trace elements including REEs of selected mineral grains from both thin and thick sections was determined using LA-ICP-MS analysis at University of Bergen, Norway. We used the Thermo Finnigan Element ICP-MS coupled to a New Wave UP-213 UV laser. The sample cell was flushed by He gas (99.9999% purity) which was mixed with Ar at the back end of the ICP torch before entering the plasma. The in situ analyses were carried out in a spot-mode, the laser beam of 25 μm diameter allowed us to obtain elemental concentrations of individual mineral grains. The external standards used were synthetic glasses NIST 610 and NIST 612. The relative standard deviations of _30 NIST 610 and 30 NIST 612 measurements were between 1% and 8% for the elements analyzed. Data were reduced using the Glitter software programme. Calcium was used as an internal standard by comparing the LA-ICP-MS CaO wt% abundance with the CaO wt% abundance measured by EMP.

The oxygen isotopic composition of NEA 003-A was determined at the Czech Geological Survey with the GEO 20-20 mass spectrometer using analytical procedures described by Clayton and Mayeda (1963, 1983).

Instrumental neutron activation analysis (INAA) was used to obtain compositional data for minor and trace elements in a 64-mg sample (chip) using the same techniques that have been used by Zeigler et al. (2005) for other lunar meteorites. These analyses were conducted at the Washington University in Saint Louis, USA.

2.2. Sm–Nd dating

Sieved fractions of NEA 003-A were prepared from the crushed bulk sample using conventional techniques. Mineral separates of plagioclase and pyroxene were handpicked in alcohol under a binocular microscope. The handpicked plagioclase (Pl) fraction was $\geqslant$99% pure, clinopyroxene fraction (Cpx) contained insignificant amount of olivine, partly as intergrowths. Impure fractions of plagioclase (Pl-impure), containing opaque phases and minor pyroxene intergrowths), and pyroxene (Cpx-impure), containing olivine and some maskelynite intergrowths, were also prepared. Furthermore, ~2 mg of distinctly black-brown clinopyroxene (Cpx–Fe-rich) grains were carefully handpicked to investigate the potential of within-grain Sm/Nd variation and, possible, age zonation, since clinopyroxene is strongly zoned with respect to major elements (see Section 3.2.2). The black-brown clinopyroxene fragments were identified using EMPA as being Fe-rich, and thus representing outer parts of large pyroxene grains.

Before dissolution the handpicked mineral fractions were rinsed repeatedly in acetone and deionised water in an ultrasonic bath. Sample splits for Sm–Nd analysis were washed for 30 min in warm (~70 °C) 0.8 N HCl to eliminate dust and surface contamination (terrestrial weathering and fluid infiltration, e.g. calcite).

Sample digestion for Sm–Nd isotope analysis was performed in screw-top Savillex® beakers using a mixture of ultrapure HF and $HClO_4$ (5:1 v/v) for 10 days at ~105 °C. After evaporation, the residues were treated with 5.8 N HCl several times. After each cooling, between 5 and 11% of the sample solution was decanted and spiked with a mixed Sm–Nd tracer (^{147}Sm–^{150}Nd) in order to determine Sm and Nd concentrations by isotope dilution (ID). The REE fraction was extracted using Bio-Rad AG® 50 W-X8 resin (200–400 mesh) and 4.0 N HCl. Neodymium and Sm were separated from the REE fraction in a Teflon-coated HdEHP column, and 0.18 N and 0.4 N HCl, respectively, as elution media. Maximum total procedural blanks were <50 pg for Sm and Nd, and thus taken as negligible.

A Finnigan® MAT262 mass spectrometer at the University of Vienna, Austria, was used for the analytical measurements in order to determine Sm and Nd concentrations. Samarium and Nd fractions for ID were loaded as nitrates and measured from Re double filaments. Measurements of Nd isotope compositions were run in static mode on a ThermoFinnigan® Triton TIMS instrument. A $^{143}Nd/^{144}Nd$ ratio of 0.511845 ± 0.000003 ($n = 7$, 2σ) was determined for the La Jolla (Nd) international standard during the period of this study. Within-run mass fractionation of Nd isotopes was corrected using $^{146}Nd/^{144}Nd = 0.7219$ (O'Nions et al., 1977). Uncertainties on the Nd isotope ratios are quoted as $2\sigma m$, uncertainties on the $^{147}Sm/^{144}Nd$ ratios are given as $\pm 1.0\%$, thought to represent maximum errors; the isochron regression calculation is based on these uncertainties. Age errors are given at the 2σ level. Isochron calculation follows Ludwig (2003). Ages are based on decay constants of $6.54 \times 10^{-12}\ y^{-1}$ for ^{147}Sm (Lugmair and Marti, 1978); ε_{Nd} is calculated following the chondritic uniform reservoir (CHUR) parameters of Hamilton et al. (1983).

2.3. Ar–Ar dating

Bulk samples of NEA 003-A were analyzed using both furnace and laser step heating techniques at the University of Manchester. Mineral separates of predominantly pyroxene and predominantly maskelynite were hand-picked from bulk samples after irradiation and step heated using an infra-red (IR)-laser with the aim of further understanding the features observed in age spectra obtained from bulk samples. A total of 23.60 mg of NEA 003-A was positioned between Hb3gr monitors (1072 ± 11 Ma; Turner, 1971) in a silica glass vial and irradiated with a fast neutron fluence of 1.67×10^{18} neutrons cm^{-2}. The irradiation was carried-out in position B2W of the SAFARI-1 reactor at Pelindaba, South Africa. During stepped heating in a resistance furnace, Ar gas was released over the temperature interval of 300–1600 °C using steps of 100 °C or 50 °C and 30 min duration. Argon isotopes were measured using the MS1 mass spectrometer equipped with a Baur-Signer ion source and single Faraday and electron multiplier channeltron detectors. The furnace blank at low temperatures (400–1100 °C) is equivalent to $753 \pm 2 \times 10^{-12}\ cm^3$ STP ^{40}Ar which increases at high temperature (⩾1300 °C) to $3547 \pm 6 \times 10^{-12}\ cm^3$ STP ^{40}Ar. The furnace blanks have an approximately atmospheric Ar isotope composition.

The IR-laser probe employs Nd-YAG continuous wave laser ($\lambda = 1064$ nm). Typical blank is equivalent to $25.7 \pm 0.5 \times 10^{-12}\ cm^3$ STP ^{40}Ar. Argon was extracted using between 13 and 24 heating steps each 1 min duration, with a defocused beam of 3 mm diameter and a maximum of 15 W laser output power. The temperature was controlled by increasing the flashlamp current within the laser output range 2–5 W and analyses continued until the sample was fused. Data for both furnace and IR laser stepped heating have been corrected for blanks, mass discrimination and neutron interference isotopes. Errors on Ar–Ar step ages includes the 1% difference in J value ($J = 0.008808 \pm 0.00013$, including monitor age error) obtained for the monitors and, for total ages, an additional 1.4% uncertainty introduced by the error on the age determination of the Hb3gr monitor. The decay constant value used is $5.543 \times 10^{-10}\ y^{-1}$ (Steiger and Jäger, 1977). Ar–Ar ages are reported at the two standard deviation (2σ) level of uncertainty. Further details of the experimental methods and data reduction procedures are given in Fernandes et al. (2000) and Fernandes and Burgess (2005).

3. RESULTS

3.1. Oxygen isotope composition and confirmation of lunar origin

Several lines of evidence support a lunar origin of NEA 003-A. Fe/Mn atomic ratios of the whole rock (81), olivines (93–110) and pyroxenes (43–89) of NEA 003-A (Haloda et al., 2006) are typical of lunar basalts and distinct from those of other meteorites (Papike et al., 2003). The NEA 003-A bulk-rock oxygen isotope composition of $\delta^{18}O = 5.76 \pm 0.08‰$ (1σ) and $\delta^{17}O = 3.04 \pm 0.05‰$ (1σ) lies on the terrestrial fractionation line (Fig. 2), which is characteristic for lunar rocks (Spicuzza et al., 2007 and references therein) and corresponds to the range of Apollo 12 and Apollo 15 basalts. Additional evidence for the lunar origin of NEA 003-A is the presence of Fe–Ni metal and absence

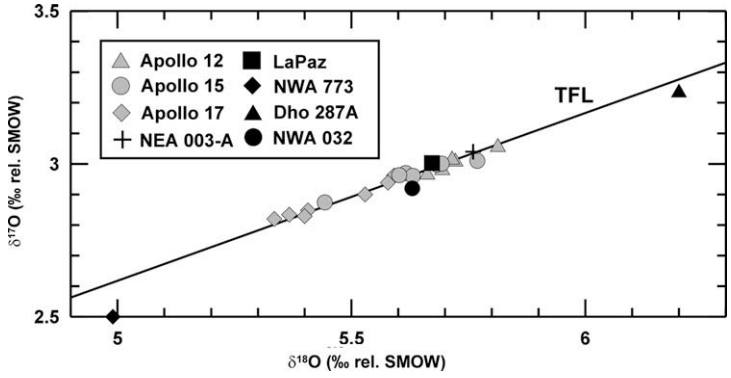

Fig. 2. Oxygen isotopic composition of NEA 003-A plots along the terrestrial fractionation line (TFL) with other basaltic lunar meteorites and Apollo 12, Apollo 15 and Apollo 17 samples. Data sources: NEA 003-A (this study), other lunar samples (Spicuzza et al., 2007).

of water-bearing minerals, which together are indicative of petrogenesis within oxygen fugacities lower than for terrestrial basalts but prevalent in lunar magmatic systems.

3.2. Petrography, textures and mineral chemistry

NEA 003-A has a coarse-grained porphyritic magmatic texture consisting mainly of olivine, pyroxene and plagioclase grains (Fig. 3). Accessory minerals in NEA 003-A include ilmenite, ulvöspinel, chromite, troilite and trace Fe–Ni metal. The distribution of silicate minerals in NEA 003-A is relatively homogeneous. Only small parts of the sample are represented by the late-stage mineral association composed mainly of elongated plagioclase, ilmenite, troilite, fayalite, a rare SiO_2 phase, chlorapatite and Si–K-rich glass (Fig. 3e and f). Other minerals, such as K–Ba-rich glass, K-feldspar, fluorapatite, and REE-merrillite (Jolliff et al., 2006) that are commonly associated with mesostasis in other lunar basalts (Papike et al., 1998) were not found in this sample. Olivine, pyroxene and spinel grains have numerous cracks and fractures that are probably due to shock effects (see Fig. 3). Some of the larger near-surface fractures of the meteorite are filled with the products of terrestrial weathering (mainly secondary Ca-carbonate). Shock event(s) resulted in conversion of all plagioclase into maskelynite. Thin veinlets of melt are present along mineral grain boundaries due to shock metamorphism.

With respect to modal mineralogy, NEA 003-A is most similar to Apollo 12 and Apollo 15 basalts (Table 1). In the following sections, we describe the detailed characteristics of individual minerals and their inter-relationships.

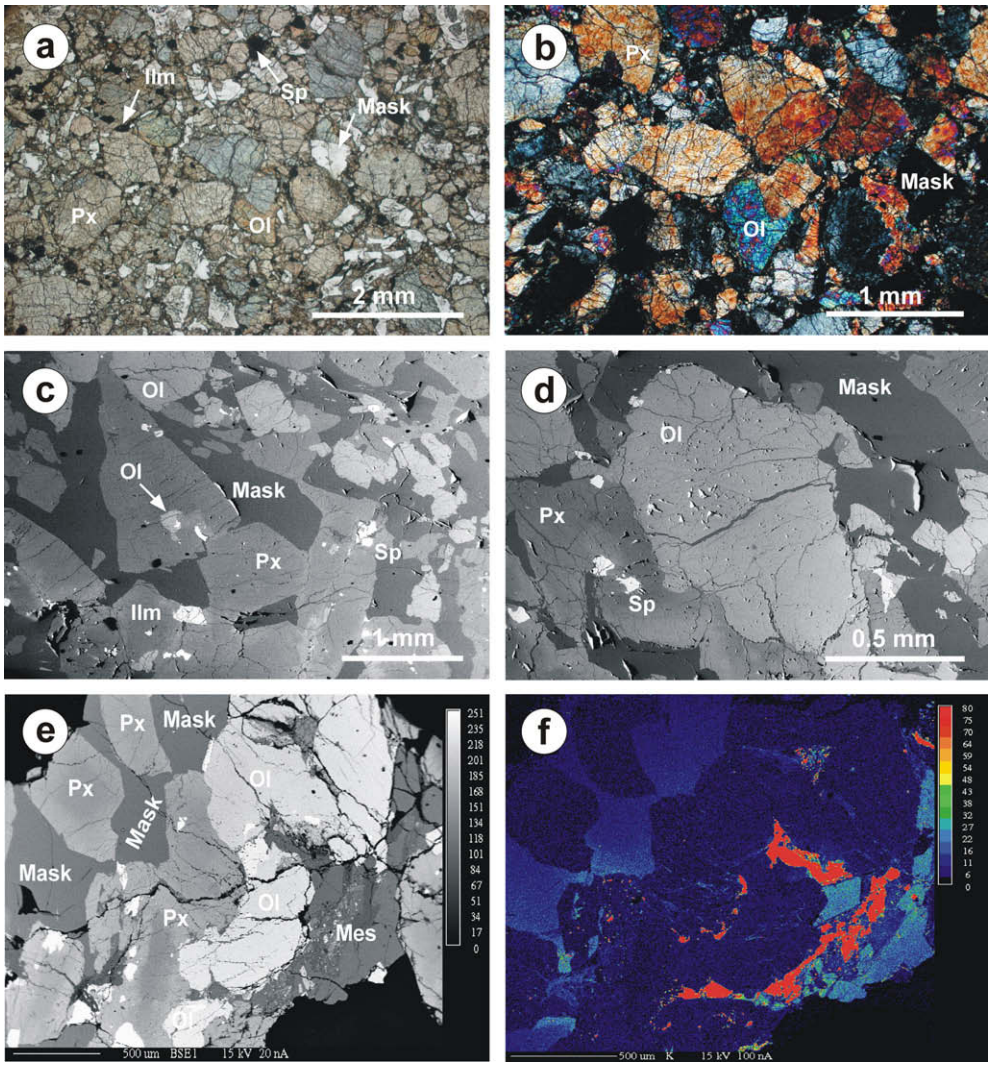

Fig. 3. Photomicrographs, BSE images and element map illustrating the textures and mineralogy of NEA 003-A: (a) coarse-grained olivine-rich low-Ti basalt with typical magmatic texture in plane polarised light; (b) the detail of previous image in polarised light (crossed nicols); (c) BSE image of a part of NEA 003-A lunar meteorite with porphyritic texture, note the olivine grain partially replaced by pigeonitic pyroxene; (d) detailed BSE view of the olivine grain (Ol, olivine; Px, pyroxene; Mask, maskelynite; Sp, spinel; Ilm, ilmenite); (e) BSE image of the porphyritic texture of NEA 003-A with mesostasis region (Mes); and (f) element distribution X-ray map for K showing the K-rich glass in the mesostasis.

Table 1
Modal abundances (vol%) of selected mare-basalt meteorites and similar basalts from Apollo 12 and Apollo 15.

	Mare-basalt meteorites						Apollo 12 and Apollo 15 basalts		
	NEA 003-A	LAP 02205	Dho 287A	NWA 032	Y-793169	A-881757	12040	12012	15555,8
Olivine phenocrysts	17.5	1.2	20.6	11.3	0.0	0.0	22.7	21.6	6.9
Chromite phenocrysts	0.5	0.1	0.4	0.3	0.0	<5	1.2	0.7	0.1
Undifferentiated pyroxene	60.6	56.9	47.4	50.7	56.0	59.0	51.5	53.5	66.8
Feldspar/maskelynite	18.2	33.1	25.9	29.4	42.0	30.0	21.6	19.0	19.7
Silica	tr	2.3	0.2	0.0	0.0	0.0	0.1	0.2	tr
Ulvöspinel	0.3	0.4	0.8	tr	1.0	<5	0.0	0.6	0.4
Ilmenite	1.2	3.3	2.3	4.4	1.0	6.0	2.3	1.9	5.6
Troilite	tr	0.2	0.1	0.7	0.0	<5	0.2	0.4	tr
Fe–Ni metal	tr	tr	tr	tr	0.0	<5	0.0	0.5	tr
Opaque minerals (total)	2.0	4.0	3.6	5.4	2.0	<11	3.7	4.1	6.1
Phosphate	tr	0.3	0.6	—	—	—	—	—	—
Fayalite	tr	1.5	0.2	—	—	—	—	—	—
Shock-melt glass	1.5	0.8	1.4	3.2	0.0	0.0	—	—	—
Volcanic glass/mesostasis	0.2	>4	>3	0.0	0.0	0.0	0.3	1.9	0.3

Data sources: NEA 003-A (this study), LAP 02205 (Anand et al., 2006), Dhofar 287A (Anand et al., 2003), NWA 032 (Fagan et al., 2002), Y-793169 (Takeda et al., 1993), A-881757 (Yanai and Kojima 1991), Apollo 12 basalts: 12,040 and 12,012 (Neal et al., 1994), Apollo 15 basalts: 15555,8 (Rhodes and Hubbard, 1973).

3.2.1. Olivine

Olivines in NEA 003-A are characterized by a great number of euhedral and subhedral grains (0.2–1.4 mm, typically >0.6 mm) with elongate to equant shapes and chemical zonation. The majority of olivines show normal symmetrical zoning with Mg-rich cores and Fe-rich rims, but there are also several olivine grains that show asymmetrical zoning with gradual iron enrichment along their edges. This observation can be best explained by the early-formed olivines being only partially in contact with Fe-enriched melt during crystallization. The early-formed olivine grains often have circular or rounded inclusions of chromite or recrystallized melt-inclusions consisting of fine-grained pyroxene and feldspar. A significant number of Mg-rich olivine ($Fo > 58$) grains are completely enclosed in pigeonitic pyroxene (Fig. 3c). This textural feature is indicative of a reaction between Mg-rich olivines and pyroxenes, where enclosed olivines were partially replaced by pigeonitic pyroxene formed by the reaction olivine + liquid → pigeonite.

Mosaic extinction of olivine grains indicates a deformation of crystal structure and the presence of numerous cracks and fractures suggests an intensive shock process. Based on the barometric classification of Stöffler and Grieve (2007) for basaltic rocks, the shock pressures undergone by this rock are estimated between 28 and 45 GPa (shock stage 2b).

Electron microprobe data for 305 olivine spot analyses were collected to obtain the representative range of Fo components (Fig. 4a and Table 2). CaO concentrations vary from 0.1 to 0.6 wt%, TiO_2 is <0.2 wt%, the Cr_2O_3 range is 0.05–0.5 wt% and the MnO range is 0.2–0.6 wt%. Distribution of the Fo component (in the majority of olivine grains) is in range of $Fo_{73\text{-}19}$ with a mode at about Fo_{53}. The lower frequency in the range of $\sim Fo_{73\text{-}60}$ reflects the partial replacement of Mg-rich olivine by pigeonite. The range of olivine composition is comparable with other mare-basalt meteorites and mare-basalts from Apollo 12 (olivine, pigeonite and ilmenite basalts) and Apollo 15 (olivine-normative basalts), (Fig. 4b). However, the fayalitic olivine typical of mesostasis mineral associations, which has been described for many mare-basalts (e.g. Dhofar 287A, LAP 02205; Basaltic Volcanism Study Project, 1981; Anand et al., 2003; Day et al., 2006) is rare in NEA 003-A (Fig. 4a) because of the lack of mesostasis-rich areas. Variation of the Fo component within several olivine grains was also investigated by collecting electron microprobe data along two orthogonal profiles in each grain (see Section 3.4. for more discussion).

3.2.2. Pyroxenes

Pyroxene is the most abundant phase in NEA 003-A occurring mainly as subhedral grains (0.5–1 mm) and showing similar petrographic features (e.g. shock related) to large olivine crystals (Fig. 3a–e). The grains are generally equant to slightly elongated and are characterized by mosaic extinction and symmetrical chemical zonation. Pyroxenes often contain inclusions of olivine, chromite and ulvöspinel.

The chemical composition of pyroxene shows extreme variations in terms of Mg–Fe–Ca contents following a typical mare-basalt fractionation trend (Fig. 5a). Characteristic zoning of pyroxene is represented by Mg-enriched cores ($En_{69\text{-}47}$, $Wo_{7\text{-}33}$), Ca-Fe-enriched mantles ($En_{55\text{-}40}$, $Wo_{15\text{-}38}$) and Fe-enriched rims ($En_{45\text{-}2}$, $Wo_{35\text{-}12}$). The core-to-mantle Ca-enrichment of pyroxene grains is usually not continuous. This feature reflects a discontinuity in the chemical composition between Mg-rich pigeonite and Ca-rich augite (Fig. 5a). Only a few pyroxene grains at the contact with late-stage minerals show gradual Fe enrichments in their rims towards pyroxferroite composition. Representative compositions of the main types of pyroxene are listed in Table 2.

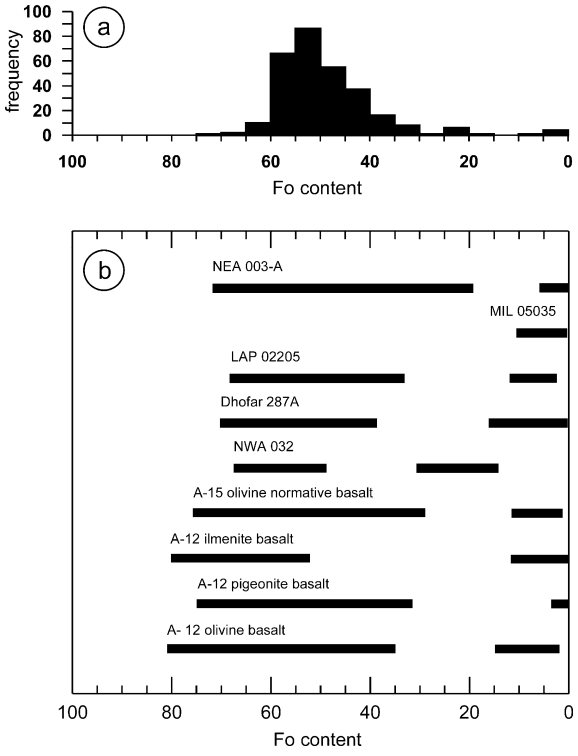

Fig. 4. Composition of olivines in NEA 003-A. (a) A histogram of Fo content in olivine. (b) Comparison of olivine Fo content of NEA 003-A with other selected mare-basalt meteorites and Apollo 12 and Apollo 15 samples. *Data sources:* MIL 05035 (Joy et al., 2008), LAP 02205 (Anand et al., 2006), Dhofar 287A (Anand et al., 2003), NWA 032 (Fagan et al., 2002), Apollo 12 and Apollo 15 basalts (Basaltic Volcanism Study Project, 1981).

Mg-rich cores of pyroxene grains are relatively depleted in high field-strength elements with $\Sigma(Al, Ti, Cr) \approx 0.08$ atoms per formula unit (based on 6-oxygen) in contrast with enrichment in the mantle $\Sigma(Al, Ti, Cr) \approx 0.15$ and in the rim $\Sigma(Al, Ti, Cr) \approx 0.11$ of the grains. The Ti/Al ratios in pyroxene vary depending upon appearance of other liquidus phases during magma crystallization. Aluminium in the cores and mantles of pyroxene enters the pyroxene crystal structure both by Tschermak substitution ($AlAlMg_{-1}Si_{-1}$) and coupled titanian ($TiAl_2Mg_{-1}Si_{-2}$) exchange reactions (Thompson, 1982). The Ti/Al ratios in Mg-rich pyroxene cores vary from 0.25 to 0.3 and reflect initial pigeonite crystallization (Fig. 5b). Ca–Fe-rich pyroxene mantles have typically higher concentrations of Al and Ti due to accommodation of larger amounts of these elements in Ca-rich pyroxene during crystallization compared to Mg-rich pyroxene. However, the initial Ti/Al values (0.25–0.3) sharply increase to 0.5. This change in Ti/Al can be interpreted as being due to the appearance of plagioclase on the liquidus, when the amount of Al uptake into the pyroxene structure was affected by plagioclase crystallization (Fig. 5b). Fe-rich pyroxene rims usually have lower concentration of Al and Ti compared to Ca–Fe-rich pyroxene mantle. The decrease of Ti concentration relates to appearance of ilmenite on the liquidus. Crystallization of ilmenite together with plagioclase and pyroxene leads to the titanium depletion of the residual magma. The Ti/Al values of Fe-rich pyroxene rims vary usually from 0.5 to 0.75. Ti/Al can be close to 1.0 for pyroxene rims with strong Fe-enrichment where they are in contact with late-stage minerals. Small differences in Ti/Al for Fe-rich pyroxene rims indicate that pyroxene, plagioclase and ilmenite crystallized at the same time. The crystallization sequence of major mineral phases of NEA 003-A, derived from variations of Ti and Al contents in pyroxene, is in good agreement with results of crystallization modelling (see Section 3.4). Concentrations of Ti and Al (atoms per 6-oxygen formula unit) of pyroxene cores, mantles and rims, together with a representative profile across one selected pyroxene grain, are shown in Fig. 5b.

3.2.3. Plagioclase feldspar

Plagioclase feldspar of NEA 003-A has the lowest modal abundance (18.2%; Table 1) among all known low-Ti mare-basalt meteorites. The absence of diffraction patterns confirmed by the EBSD method suggests that plagioclase was completely converted into diaplectic glass (maskelynite) during a shock event(s) associated with the impact processes. Total conversion of plagioclase to maskelynite proceeds at a pressure of about 28–45 GPa with a post-shock temperature increase of 200–250 °C (Stöffler and Grieve, 2007). From the total of 10 unbrecciated mare-basalt meteorites only NEA 003-A, Dhofar 287-A (Anand et al., 2003) and Asuka 881757 (Yanai et al., 1993) are showing complete plagioclase to maskelynite conversion. The maskelynite has generally irregular shapes and occasionally occurs as slightly elongate grains (see Fig. 3). Maskelynite compositions fall within the range An_{84-92}, which is typical for the majority of mare-basalts from Apollo 12 and Apollo 15 (Basaltic Volcanism Study Project, 1981; Papike et al., 1998).

3.2.4. Accessory minerals

Accessory minerals of NEA 003-A comprise ilmenite, spinels, Fe–Ni metal, troilite and rare fayalite, Si–K-rich glass, SiO_2 phase and apatite.

Ilmenite is the most abundant opaque phase in this meteorite and forms lath-shaped grains (typically 50–200 μm long) often associated with ulvöspinel. Textures indicating typical subsolidus reduction of ulvöspinel to ilmenite and Fe metal are rarely present (El Goresy, 1976).

Spinel in NEA 003-A occurs as chromite and ulvöspinel. Chromite forms euhedral crystals typically 50–100 μm across, surrounded by other minerals, and is often enclosed in olivine and occasionally in pyroxene. The chemical composition of chromite is near to the chromite end-member of spinel solid solution, with low concentrations of TiO_2, MgO and Al_2O_3 (Table 2 and Fig. 6). Grains composed of a chromite core and rimmed by ulvöspinel are common, occurring mainly at ilmenite–pyroxene–plagioclase grain boundaries. Ulvöspinel rims around chromite were not observed in the case of chromite inclusions within olivine or pyroxene. The boundaries between chromite and ulvöspinel are sharp. The microprobe data for NEA 003-A spinels show a typical fractionation trend (Fig. 6a and b) similar to those observed in A-12 and A-15 basalts (El Goresy et al. 1971; Taylor et al., 1971; El Goresy, 1976).

Table 2
Representative electron microprobe analyses (wt%) of minerals and shock melt glass of NEA 003-A.

Phase	Olivine (core)	Olivine (rim)	Mg-rich pyroxene (core)	Mg–Ca-rich (mantle)	Fe-rich pyroxene (rim)	Fe–pyroxene	Chromite	Ulvöspinel	Ilmenite	Maskelynite	Cl-apatite	Si–K-rich glass
SiO_2	36.84	31.35	52.62	50.80	48.62	44.60	nd	nd	bd	45.67	nd	76.10
TiO_2	0.06	0.07	0.50	1.01	1.27	0.52	6.26	28.93	53.06	nd	nd	0.56
Al_2O_3	0.08	0.11	1.18	2.70	1.57	0.59	11.14	3.06	0.05	33.85	nd	12.80
Cr_2O_3	0.09	0.05	0.68	0.94	0.30	0.04	44.71	10.26	bd	nd	nd	nd
MgO	33.33	9.22	22.81	16.04	9.85	0.04	4.04	1.55	0.29	bd	0.09	0.32
CaO	0.34	0.48	4.50	16.37	15.67	5.00	0.16	0.02	0.17	18.90	52.47	0.45
MnO	0.30	0.53	0.29	0.21	0.34	0.54	0.35	0.43	0.26	nd	nd	0.04
FeO	28.99	58.06	16.90	12.31	22.18	47.94	32.97	55.58	45.51	0.55	1.21	0.62
Na_2O	nd	nd	0.02	0.05	0.05	0.07	nd	nd	nd	0.95	bd	0.67
K_2O	nd	nd	0.003*	0.005*	0.009*	0.010*	nd	nd	nd	0.07	nd	8.67
NiO	bd	bd	bd	bd	0.02	bd	bd	bd	bd	nd	nd	nd
P_2O_5	nd	nd	nd	nd	nd	nd	nd	nd	nd	nd	40.95	nd
Cl	nd	nd	nd	nd	nd	nd	nd	nd	nd	nd	2.94	nd
F	nd	nd	nd	nd	nd	nd	nd	nd	nd	nd	0.68	nd
Total	100.03	99.87	99.49	100.43	99.92	99.26	99.63	99.83	99.34	99.99	98.34	100.23
Oxygen basis	4	4	6	6	6	6	4	4	3	8	24	
Si	0.991	0.991	1.945	1.890	1.907	1.951	—	—	—	2.114	—	—
Ti	0.001	0.002	0.014	0.028	0.037	0.017	0.161	0.789	1.009	—	—	—
Al	0.002	0.004	0.051	0.119	0.073	0.030	0.450	0.131	0.002	1.847	—	—
Cr	0.002	0.001	0.020	0.028	0.009	0.001	1.211	0.294	—	—	—	—
Mg	1.336	0.434	1.257	0.890	0.576	0.002	0.206	0.084	0.011	—	0.014	—
Ca	0.010	0.016	0.178	0.653	0.659	0.234	0.006	0.001	0.005	0.938	9.979	—
Mn	0.007	0.014	0.009	0.007	0.011	0.020	0.010	0.013	0.006	—	—	—
Fe	0.652	1.534	0.522	0.383	0.728	1.753	0.944	1.687	0.962	0.021	0.250	—
Na	—	—	0.001	0.004	0.009	0.001	—	—	—	0.080	—	—
K	—	—	—	—	—	—	—	—	—	0.005	—	—
Ni	—	—	—	—	0.001	—	—	—	—	—	—	—
P											4.756	
Total	3.001	2.996	3.997	4.002	4.010	4.009	2.988	2.999	1.995	5.005	15.000	—
Mg#	67.0	22.1	69.3	69.9	44.2	0.0	—	—	—	—	—	—
Fe/Mn (atom.%)	94.8	107.5	50.1	57.6	66.2	87.7	—	—	—	—	—	—

Nd, not determined; bd, below detection; Fe-pyroxene, pyroxferroite.
* Pyroxene K_2O concentrations were calculated from LA-ICP-MS analyses.

Fe–Ni metal grains are rare, with Ni and Co concentrations in the range of 3–39 and 0.1–1.6 wt%, respectively. Troilite occurs in the form of irregular grains and together with Fe–Ni metal is adjacent to late-stage mineral associations.

A distinctive petrographic feature of NEA 003-A is the low amount of late-stage mesostasis (<0.2 vol%) when compared to other mare basalts. The late-stage mineral association can be found in several interstitial residual melt pockets between the mafic silicate grains and is composed of elongated plagioclase, ilmenite, troilite, fayalite, Si–K-rich glass, a rare SiO_2 phase (which was identified as a glass by EBSD) and apatite (Figs. 3e and f and 7). The typical mesostasis "Swiss-cheese" texture found in Dho 287A and LaPaz Icefield 02205 (Anand et al., 2003, 2006; Day et al., 2006) is not present in NEA 003-A due to low content of these immiscible residual melts.

Shock veins and melt pockets are widely dispersed in the sample, containing small mineral fragments and bubbles. They consist of shock-melted glass with basaltic composition very similar to the composition of the whole-rock meteorite (Table 2).

3.3. Whole-rock chemical composition

The whole-rock major and trace element compositions of NEA 003-A and other similar mare basalts are listed in Table 3. Based on the classification of Neal and Taylor (1992) and the mineral composition of the meteorite, NEA 003-A can be classified as low-Ti, low-Al, low-K, olivine-rich basalt similar to olivine basalts from Apollo 12 and olivine-normative basalts from Apollo 15. The relationship between Al_2O_3 and MgO in NEA 003-A (Fig. 8b) is also consistent with the trend of olivine crystallization in olivine basalts from both Apollo 12 and Apollo 15 (Papike et al., 1998). The TiO_2 to MgO (Fig. 8c) ratio in NEA 003-A is lower than the values observed in Apollo 12 samples, but consistent with Apollo 15 trend. There is a minor difference in the FeO content of NEA 003-A obtained using two different analytical methods: INAA FeO = 18.5–20.1 wt% for

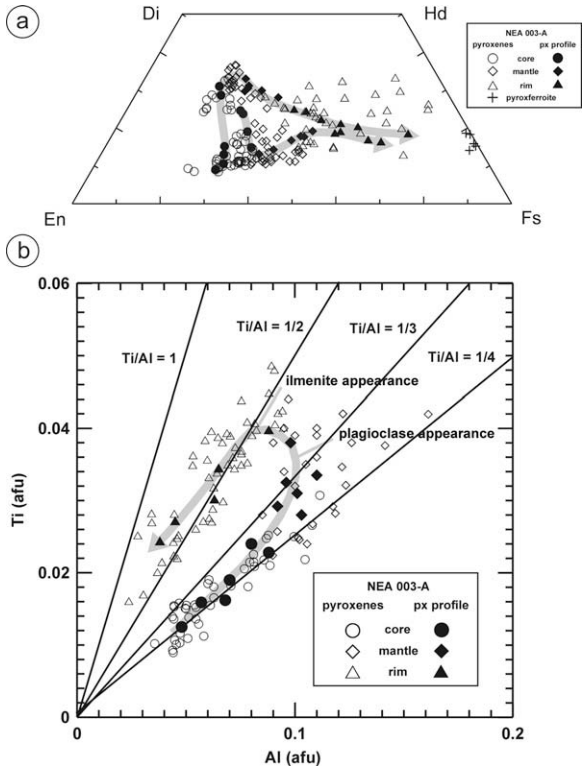

Fig. 5. (a) Pyroxene composition plot for NEA 003-A pyroxenes, two profiles across pyroxene grains (full symbols) show typical trend of composition change during crystallization. (b) Concentration of Al and Ti (atoms per 6-oxygen formula unit) for NEA 003-A pyroxene cores, mantles and rims. The profile across the pyroxene grain (full symbols) show the changes in Al and Ti content during crystallization.

three subsamples, mean value = 19.3 wt%; and XRF FeO = 21.8 wt%. This discrepancy can be explained by the coarse grain size of the meteorite combined with the large difference in sample masses used for analysis (64 mg INAA and 450 mg XRF).

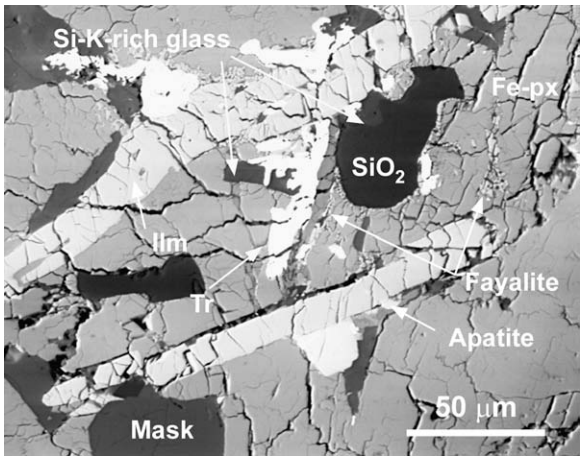

Fig. 7. BSE image of mesostasis area of NEA 003-A with typical late-stage mineral association (Fe–px, Fe-rich pyroxene; Mask, maskelynite; Tr, troilite; Ilm, ilmenite).

The high Co concentration compared to other similar mare basalts (Table 3.) and high Co/Sc ratio reflects the high modal proportions of olivine in the rock. The REE concentrations in NEA 003-A (Table 3 and Figs. 9b–d and 10) are at the low end of the range for Apollo 12 and Apollo 15 basalts. The chondrite-normalized REE pattern of NEA 003-A is flat with small but resolvable Eu depletion a feature typical of many mare basalts (Fig. 10). The low absolute concentration of Eu (0.60 ppm; Table 3) reflects the low modal abundance of plagioclase.

3.4. Crystallization modelling

In order to calculate the Fo content of olivine in equilibrium with a whole rock Mg# (Roeder and Emslie, 1970; Langmuir and Hanson, 1981), we used TiO_2 calibrated K_d (distribution coefficient relating the partitioning of iron and magnesium between olivine and a co-existing low-Ti

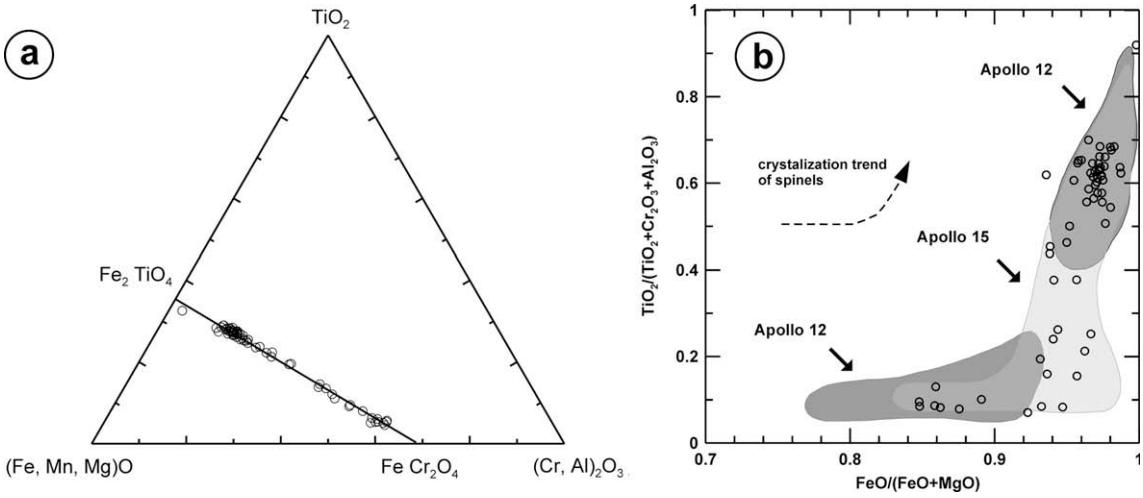

Fig. 6. Composition of spinels from NEA 003-A. (a) Ternary plot (in wt%) after El Goresy (1971) for NEA 003-A spinel composition. (b) FeO/(FeO + MgO) vs. $TiO_2/(TiO_2 + Cr_2O_3 + Al_2O_3)$ in weight percent showing a crystallization trend similar to the trend defined by Apollo 12 and Apollo 15 samples (Papike et al., 1998).

Table 3
Major and trace element composition of NEA 003-A and other mare-basalt meteorites and similar Apollo 12 olivine basalts and Apollo 15 olivine-normative basalts.

	Mare-basalt meteorites								Apollo 12 and 15 basalts					
	NEA 003-A CGS	NEA 003-A WUSL	NEA 003-A (−10%)	LAP 02205	Dho 287A	NWA 032	Y-793169	A-881757	12012,15	12040,36	12015,9–11	12,009	15016,195	15555,807
wt%														
SiO_2^*	44.72		45.54	45.2	43.2	44.7	46	47.1	44.17	43.89	44.98	45	44.6	45
TiO_2^*	1.34		1.49	2.72	2.76	3.08	2.19	2.45	2.64	2.74	2.86	2.9	2.24	2.02
$Al_2O_3^*$	8.02		8.93	10	8.35	8.74	11.1	10	7.71	7.41	8.57	8.59	8.54	9.16
$Cr_2O_3^*$	0.52	0.59	0.58	0.19	0.65	0.4	0.24	0.29	0.69	0.74	0.68	0.76	0.84	0.74
FeO^*	21.83	19.3	21.56	23.2	22.1	23	21.2	22.5	20.69	20.83	20.18	21	21.74	21.49
MnO^*	0.27		0.3	0.23	0.29	0.33	0.32	0.34	0.3	0.26	0.29	0.28	0.28	0.28
MgO^*	13.59		10.97	5.99	13.2	8.45	5.75	6.3	14.37	16.1	11.88	11.6	11.22	11.32
CaO^*	9.16		10.19	11.2	8.74	10.9	12	11.8	8.47	7.87	9.21	9.42	9.37	9.47
Na_2O^{**}	0.31	0.262	0.34	0.33	0.53	0.37	0.27	0.25	0.21	0.2	0.23	0.23	0.22	0.23
K_2O^{**}	0.08	<0.3	0.09	0.11	0.19	0.11	0.06	0.04	0.06	0.04	0.06	0.06	0.04	0.05
Total	99.84		99.99	99.83	100.01	100.08	99.13	101.07	99.31	100.08	98.94	99.84	99.09	99.76
Mg#	52.6		47.6	31.4	51.5	39.6	32.6	33.3	55.3	57.9	51.2	49.6	47.9	48.4
μg/g														
Sc		50.8		58.6	35.2	56	93.7	99.4	41.9	42.6	48.4	46	40.7	39.1
Co		50.5		37.3	42.3	42	29.8	27.9	56	59.5	47.8	50.1	54.6	55.4
Ni		84		27.6	20	50	53	52	60	101	62	55	72	67
Sr		117		135.3	530	142	78	115	89	94	84	86.4	90	90
Ba		252		164.7	200	242	34	27	56	54	65	55.5	57	39
La		3.0		13.4	12.9	11.2	4.72	3.69	—	4.3	6.2	5.62	5.22	3.88
Ce		8.5		37.31	30.3	29.7	14.8	10.9	13.8	12.5	16	16.1	15.2	11.6
Nd		4.5		25.12	20.4	21	11.9	8.31	—	8.8	14.4	12.7	8	8
Sm		1.69		7.56	6.31	6.61	4.3	2.88	4.02	3.1	4.3	3.91	3.67	2.78
Eu		0.6		1.24	1.18	1.1	1.31	1.1	0.76	0.79	0.98	0.89	0.82	0.78
Tb		0.46		1.93	1.22	1.56	1.02	0.76	1.17	0.92	1.16	0.9	0.82	0.6
Yb		1.94		6.37	3.35	5.79	4.59	3.26	3.4	2.9	3.6	3.05	2.18	1.77
Lu		0.28		0.88	0.51	0.8	0.66	0.52	0.47	0.37	0.52	0.45	0.31	0.25
Hf		1.1		5.39	2.64	5	3.01	2.2	3.4	2.4	3.3	—	2.49	2.03
Ta		0.15		0.77	0.71	0.62	0.31	0.22	—	0.3	0.38	0.3	0.37	0.29
Th		0.43		2.33	0.9	1.9	0.68	0.42	0.67	0.47	0.74	0.85	0.41	0.29
U		0.29		0.55	—	0.45	0.09	0.16	—	—	—	0.23	—	—

Analytical data of NEA 003-A were acquired by using XRF (∗) and ICP-OES (∗∗) in Czech Geological Survey (CGS) and by INAA in Washington University, St. Louis (WUSL). NEA 003-A (−10%) is recalculated bulk-composition after 10% olivine removal for crystallization modelling.

Other data sources: LAP 02205 (Anand et al., 2006), Dhofar 287A (Anand et al., 2003), NWA 032 (Fagan et al., 2002), Yamato 793169 (Warren and Kallemeyn, 1993; Koeberl et al., 1993), Asuka 881757 (Warren and Kallemeyn, 1993; Koeberl et al., 1993), Apollo 12 olivine basalts: 12012,15, 12015,9–11 (Rhodes et al., 1977), 12040,36 (Neal et al., 1994) and 12009 (Snyder et al., 1997), Apollo 15 olivine normative basalts: 15555,807 and 15016,195 (Ryder and Schuraytz, 2001).

liquid) of Delano (1980). The calculated TiO_2 K_d for NEA 003-A is 0.33 and the Fo content of olivine in NEA 003-A with Mg# = 52.6 (Table 3) is calculated to be Fo_{77}. However, the highest observed Fo content in the cores of the earliest formed olivines (Fo_{73}) is lower than the calculated Fo content. This discrepancy, combined with other geochemical features (high MgO and low Al_2O_3 concentrations, and high Co/Sc ratio), is indicative of the presence of cumulate olivine and its accumulation in the parental magma. Thus, prior to modelling the crystallization sequence, the proportion of cumulate olivine was calculated (equilibrium Fo content = measured Fo content) and corresponds to a value of 10%. This olivine portion was removed, and the bulk composition of NEA 003-A was recalculated (see Table 3). The recalculated bulk-rock composition was used for crystallisation modelling using the PELE software (Boudreau, 1999) based on the algorithms and database of Ghiorso (1985) and Ghiorso and Sack (1994).

The results of low-pressure (1-bar) models of the crystallization sequence for equilibrium and fractional crystallization provide consistent datasets. Modelling started with a liquidus temperature of 1334 °C and an oxygen fugacity equivalent to the iron–wüstite buffer. When comparing both models, fractional crystallization yields better fit between predicted and observed compositional ranges for most mineral phases. This is consistent with other lines of evidence for fractional crystallization of this rock (e.g. type of chemical zonation for olivine, pyroxene and plagioclase—see Sections 3.2.1–3.2.3, strong REE variations be-

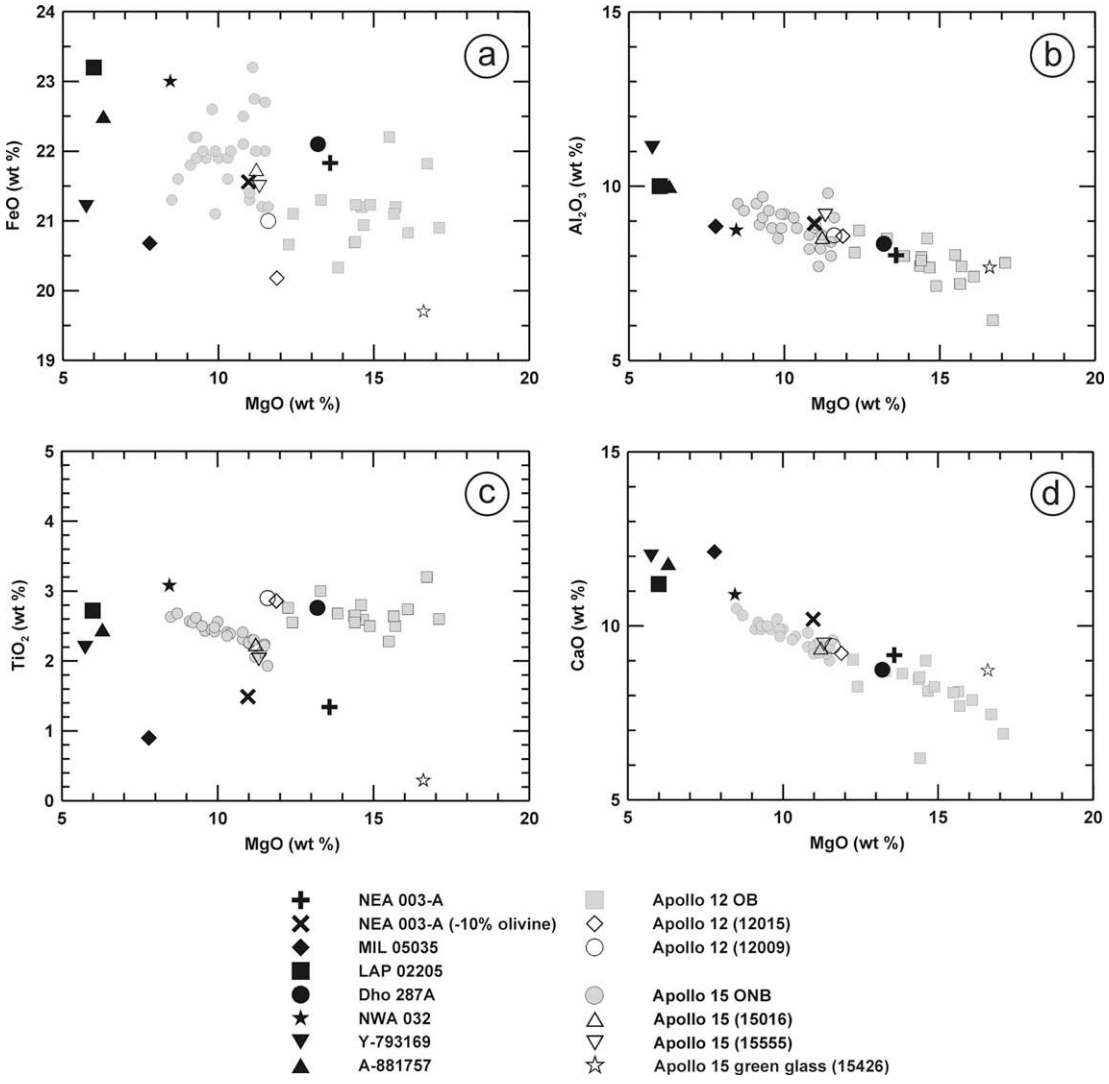

Fig. 8. Major element chemistry of NEA 003-A compared with selected unbrecciated mare-basalt meteorites and Apollo 12 olivine basalts and Apollo 15 olivine-normative basalts. Data sources: NEA 003-A (this study), Miller Range (MIL) 05035 (Joy et al., 2008), LAP 02205 (Anand et al., 2006), Dhofar 287A (Anand et al., 2003), NWA 032 (Fagan et al., 2002), Yamato 793169 (Warren and Kallemeyn, 1993), Asuka 881757 (Warren and Kallemeyn, 1993), Apollo 12 olivine basalts (Rhodes et al., 1977; Neal et al., 1994), Apollo 15 olivine-normative basalts (Ryder and Schuraytz, 2001) and Apollo 15 green glass: 15426 (Taylor et al., 1973).

tween core and rim for pyroxene and plagioclase grains—see Section 3.5.1). The low-pressure model of fractional crystallization for the recalculated bulk composition of NEA 003-A (Fig. 11) predicts that chromian-spinel crystallized as the first phase from the cooling liquid at 1334 °C, followed by olivine (Fo_{73}) at 1241 °C, pigeonite (En_{71}, Wo_6) at 1171 °C, plagioclase (An_{87}) at 1148 °C, clinopyroxene (En_{63}, Wo_{26}) at 1130 °C and ilmenite at 1032 °C. The predicted and observed compositional ranges of mineral phases are in good agreement, with the exception of plagioclase where the compositional range is more scattered (observed An_{84-92}, predicted An_{86-88}). This difference may be a result of compositional zoning in plagioclase however it is not significant for the interpretation of crystallization history. In addition, the difference between the observed and predicted chemical compositions of plagioclase cannot be a result of total conversion to maskelynite during shock process(es) because plagioclase grains show normal magmatic zoning without any homogenization of chemical composition.

The results of crystallization modelling of NEA 003-A described above confirms the presence of cumulate olivine and its accumulation in parental magma and is also consistent with the crystallization sequence derived from Ti and Al variations in pyroxenes (Section 3.2.2 and Fig. 5b).

The chemical zoning preserved in olivine crystals provides information about the cooling-rate during crystallization. The variations of Fo content in 12 olivine grains, measured along mutually orthogonal profiles across the grains, were used to estimate the minimum cooling rates. The effects of crystallographic orientation on Mg–Fe diffusion in the olivine grains was taken into account in the calculation (Taylor et al., 1977). Minimum cooling rate estimates based on the variation of Fo content in olivine crystals require iterative

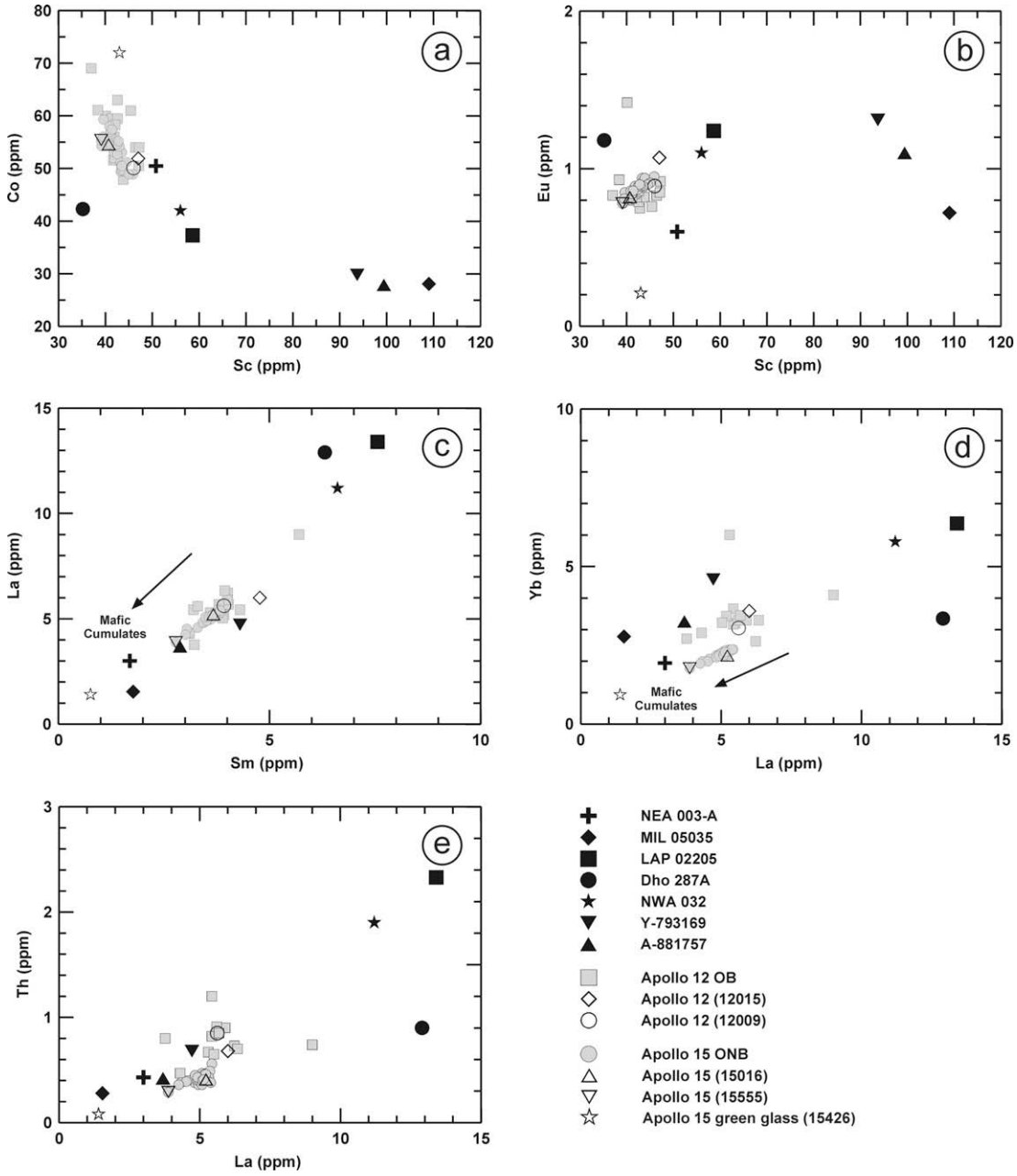

Fig. 9. Trace element chemistry of NEA 003-A compared with selected unbrecciated mare-basalt meteorites and Apollo 12 olivine basalts and Apollo 15 olivine-normative basalts. Data sources: NEA 003-A (this study), Miller Range (MIL) 05035 (Joy et al., 2008), LAP 02205 (Anand et al., 2006), Dhofar 287A (Anand et al., 2003), NWA 032 (Fagan et al., 2002), Yamato 793169 (Koeberl et al., 1993), Asuka 881757 (Koeberl et al., 1993), Apollo 12 olivine basalts (Rhodes et al., 1977; Neal et al., 1994), Apollo 15 olivine-normative basalts (Ryder and Schuraytz, 2001) and Apollo 15 green glass: 15426 (Taylor et al., 1973).

calculations (Taylor et al., 1977). Based on this procedure, the calculated minimal cooling rate for the randomly oriented olivine crystals was ~0.07 °C/h.

3.5. Age determination

3.5.1. Sm–Nd results

We have analyzed five mineral fractions for their Sm–Nd isotope compositions. The analytical results are listed in Table 4a and plotted in an isochron diagram in Fig. 12.

Samarium and Nd concentrations and Sm/Nd ratios are generally well within the range expected from REE distribution coefficients and fractionation models for plagioclase–clinopyroxene pairs (e.g. Jacobsen and Wasserburg, 1979, and references therein), as well as experimentally determined values in Ca-feldspar–pyroxene pairs of terrestrial mafic systems, or ancient lunar samples (Nyquist et al., 1989; Nyquist and Shih, 1992; Premo and Tatsumoto, 1992), with slight variations among the clinopyroxene fractions.

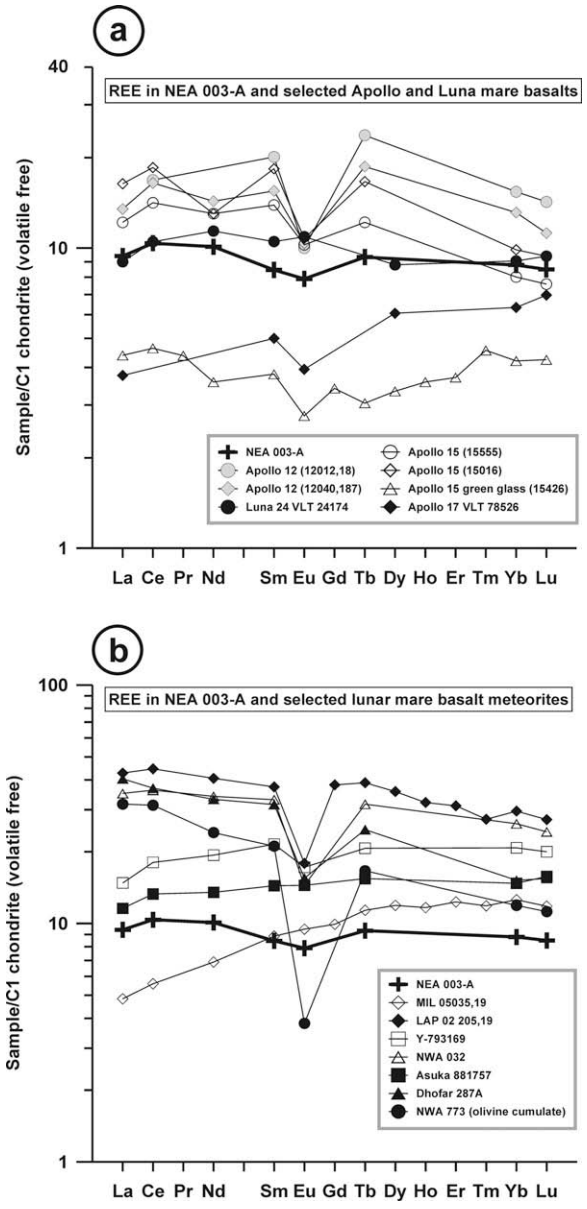

Fig. 10. (a) Volatile-free, chondrite-normalized plot of REEs in NEA 003-A and selected Apollo and Luna mare basalts. (b) Volatile-free, chondrite-normalized plot of REEs in NEA 003-A and selected mare-basalt meteorites. Normalization values are from Anders and Grevesse (1989). *Data sources:* Apollo 12 basalts: 12012,18 (Rhodes et al., 1977) and 12040,187 (Neal et al., 1994), Apollo 15 basalts: 15555 and 15016 (Ryder and Schuraytz, 2001), Apollo 15 green glass: 15426 (Taylor et al., 1973), Apollo 17 (Wentworth et al., 1979), Luna 24 (Ma et al., 1978), Asuka 881757 (Koeberl et al., 1993), Yamato 793169 (Koeberl et al., 1993), LAP 02205 (Anand et al., 2006), Dhofar 287A (Anand et al., 2003), NWA 032 (Fagan et al., 2002), Miller Range 05035 (Joy et al., 2008) and NWA 773 (Jolliff et al., 2003).

The $^{147}Sm/^{144}Nd$ ratios determined in our study for pure plagioclase (Pl) and clinopyroxene (Cpx) are 0.169 and 0.321, respectively (Table 4a). The relatively low Nd and Sm concentrations in the Cpx fraction (Table 4a) are due to a considerable amount of admixed olivine. As expected

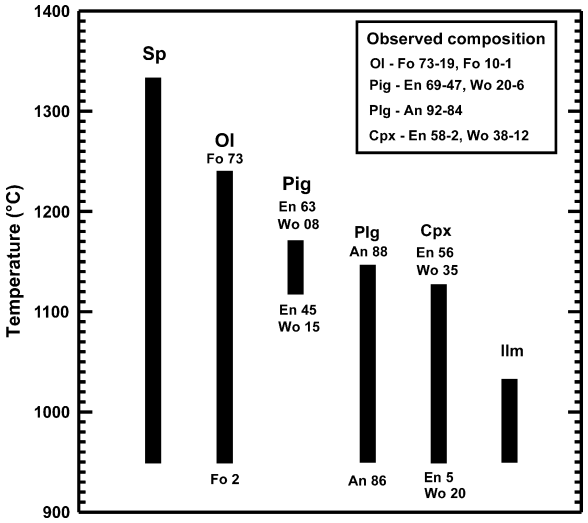

Fig. 11. Results of fractional crystallization modelling of the NEA 003-A recalculated bulk-rock composition (Table 3). The figure also shows predicted and observed compositional ranges of the most abundant phases of NEA 003-A (Sp, spinel; Ol, olivine; Pig, pigeonite; Plg, plagioclase; Cpx, clinopyroxene; Ilm, ilmenite).

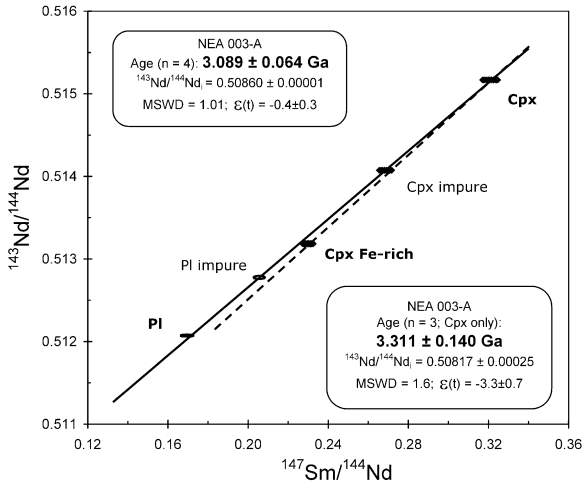

Fig. 12. Sm–Nd isotopic data for mineral fractions of NEA 003-A shown as an isochron diagram. Note that symbol sizes exceed analytical errors. See text for data interpretation. The 3.089 ± 0.064 Ga Sm–Nd regression age (continuous line) is interpreted to be the primary crystallization age of the rock.

from the modal composition, and because plagioclase and clinopyroxene are the major REE-bearing phases, the two impure mineral fractions have an intermediate composition between the pure Pl and Cpx fractions as is evident in the isochron diagram (Fig. 12; and Table 4a). However, the fraction "Cpx impure" may also include a REE-rich accessory phase with a lower Sm/Nd (likely ilmenite or apatite, since its Nd concentration of 5 ppm is considerably higher compared to the "pure" Cpx, Nd = 1.69 ppm; Table 4a). The fraction "Cpx–Fe-rich" has a lower $^{147}Sm/^{144}Nd$ of 0.23 (Table 4a) compared to the "pure" Cpx fraction, which also suggests that clinopyroxene must be strongly zoned with respect to trace elements (REE).

The LA-ICP-MS was used to document the suggested REE zonation of minerals, used for age determination. The REE concentrations were measured for core and rim of selected clinopyroxene and plagioclase grains. The results are presented in Table 5. Clinopyroxene and plagioclase show significant variations: clinopyroxene core and rim have 0.5–5.8 ppm Nd and 0.4–1.7 ppm Sm whereas plagioclase core and rim have 0.3–2.0 ppm Nd and 0.2–0.5 ppm Sm, respectively. The high trace element variations in pyroxene and plagioclase can be attributed to a relatively long period of crystallization for both phases. In addition, trace element enrichment from core to rim of pyroxene and plagioclase indicates fractional crystallization of NEA 003-A from parent melt.

Fig. 12 shows that four out of five data points (Cpx, Cpx impure, Pl impure, Pl) plot on a linear array (solid line). If pooled together in one single regression calculation the age obtained is $t = 3.089 \pm 0.064$ Ga, with $(^{143}Nd/^{144}Nd)_i = 0.508610 \pm 0.000095$ and $\varepsilon_{Nd3089} = -0.4 \pm 0.3$ (MSWD = 1.01). Within the limits of analytical uncertainties, this age corresponds to an isochron. A separate regression of the "pure" Pl and Cpx fractions yields an identical, two-point isochron result of $t = 3.096 \pm 0.073$ Ga, $(^{143}Nd/^{144}Nd)_i = 0.50861 \pm 0.00010$ corresponding to $\varepsilon_{Nd3096} = -0.1 \pm 0.3$. The two low-Sm/Nd fractions (Pl–Pl impure) yield a younger apparent age of 2.94 ± 0.22 Ga. This value is, however, indistinguishable within the uncertainty from the more precise age. Interestingly, Cpx–Fe-rich plots clearly off the 3.1 Ga "mean" trend line. If Cpx–Fe-rich fraction is regressed with the Cpx fraction, it defines an age of 3.30 ± 0.14 Ga and an initial $^{143}Nd/^{144}Nd$ of 0.50817 ± 0.00025, corresponding to a significantly more negative $\varepsilon_{Nd3.3}$ of -3.4 ± 0.7. If the fraction "Cpx impure" is also included (dashed line), the result is identical: $t = 3.31 \pm 0.14$ Ga, $(^{143}Nd/^{144}Nd)_i = 0.50817 \pm 25$ ($\varepsilon_{Nd3.31} = -3.3 \pm 0.7$; MSWD = 1.6). Inclusion of all five data points in one single regression, yields $t = 3.107 \pm 0.240$ Ga ($\varepsilon_{Nd3.1} = -0.9 \pm 1$), with considerable excess scatter (MSWD = 6.3).

For reasons discussed later in Section 4.2, we consider the age of 3.089 ± 0.064 Ga, $(^{143}Nd/^{144}Nd)_i = 0.508610 \pm 0.000095$, $\varepsilon_{Nd3089} = -0.4 \pm 0.3$, and MSWD = 1.01 to best represent the crystallization age of NEA 003-A.

3.5.2. Ar–Ar results

The Ar–Ar data for bulk samples and plagioclase and pyroxene separates are given in Table 4b and the age and Ca/K spectra are shown in Fig. 13a and 13b. The $^{38}Ar/^{36}Ar$ ratios range from ~0.19 at low temperature to 1.6 at high temperature suggesting that Ar is a mixture of trapped and cosmogenic components. At low temperature, the lack of ^{39}Ar release associated with high $^{40}Ar/^{36}Ar$ ratios indicates that that trapped Ar is more likely to be terrestrial atmosphere associated with weathering rather than solar Ar. The absence of solar Ar suggests that NEA 003-A was not directly exposed at the lunar surface throughout its history.

Age spectra for the two bulk samples (Fig. 13a) do not overlap probably because the relatively coarse-grain size of this basalt means that the smaller sample used for laser-heating is unlikely to be representative of the bulk meteorite. However, the similarity in the age pattern between the laser-heated bulk-rock and the pyroxene separates (Fig. 13b) is consistent with pyroxene being the most abundant mineral phase in this sample. The age spectra of the two bulk samples (in particular the laser step heated sample) and the pyroxene separate are similar showing increasing apparent ages over the initial 15–30% of ^{39}Ar release, reaching a maximum value of 2.781 ± 0.058 Ga at 950 °C (the maximum age for the laser step heating of the bulk sample is 3.052 ± 0.588 Ga), followed by a decrease in apparent age over the remaining ^{39}Ar release to <2 Ga. At high temperature, the apparent ages decrease markedly to ~1.2 Ga. The pattern of Ca/K values shows the opposite pattern to the apparent ages, steadily increasing with temperature (Fig. 13a and b). The pyroxene is chemically zoned for Ca and K (Table 2). Thus, most of the variation in Ca/K value may be attributed to the chemical zonation as

Table 4
(a) Sm–Nd analytical results of NEA 003-A mineral separates. (b) Summary of ^{40}Ar–^{39}Ar age data for bulk, breccia and basalt fragments of NEA 003-A.

Material	Sample wt. (mg)	Sm (ppm)	Nd (ppm)	$^{147}Sm/^{144}Nd$	$^{143}Nd/^{144}Nd$	$\pm 2s_m$
(a) Sm–Nd results						
PI	22.6	0.188	0.671	0.1695	0.512073	0.0000087
PI impure	34.2	0.564	1.663	0.2057	0.512777	0.0000170
Cpx	32.06	0.897	1.692	0.3208	0.515168	0.0000040
Cpx impure	36.62	2.238	5.039	0.2686	0.514074	0.0000040
Cpx–Fe-rich	2.3	2.870	7.548	0.2299	0.513185	0.0000060

Material	Sample wt. (mg)	K (ppm)[a]	Ca (%)[a]	Total age (GA)	CRA age (Ma)
(b) Ar–Ar results					
Bulk-IR	2.11	160	4.8	1.744 ± 0.070	212.3 ± 7.5
Bulk-furnace	17.65	327	7.6	2.314 ± 0.040	206.0 ± 6.3
Maskelynite-separates	3.86	112	4.2	2.418 ± 0.044	202.8 ± 3.1
Pyroxene-separates	0.98	90	2.8	1.745 ± 0.060	209.0 ± 4.9

The ^{40}Ar–^{39}Ar age data were obtained by IR-stepped heating. Calculated ages show error in 2σ which includes error for *J*-value determination.

[a] K and Ca content reported were calculated based on the ^{39}Ar and ^{37}Ar released during laser heating.

Table 5
REE concentrations of selected pyroxene and plagioclase grains.

Phases	Pyroxene (En_{61} Wo_{13})		Pyroxene (En_{48} Wo_{35})		Pyroxene (En_{29} Wo_{22})		Pyroxene (En_{8} Wo_{26})		Plagioclase (An_{91})		Plagioclase (An_{89})		Plagioclase (An_{86})	
ppm		±1σ		±1σ		±1σ		±1σ		±1σ		±1σ		±1σ
La	0.11	0.02	0.10	0.02	0.36	0.06	1.86	0.10	0.32	0.02	0.36	0.02	1.31	0.05
Ce	0.33	0.03	0.49	0.04	1.48	0.14	6.08	0.26	0.70	0.03	0.86	0.03	3.15	0.10
Pr	0.04	0.01	0.10	0.02	0.36	0.06	1.01	0.04	0.08	0.01	0.11	0.01	0.43	0.02
Nd	0.54	0.09	0.87	0.12	2.17	0.38	5.78	0.21	0.33	0.03	0.52	0.04	2.01	0.09
Sm	0.38	0.09	0.70	0.13	0.67	0.27	1.65	0.19	0.20	0.08	0.24	0.09	0.54	0.09
Eu	0.03	0.01	0.05	0.02	0.17	0.07	0.45	0.03	1.29	0.05	1.44	0.06	1.44	0.06
Gd	0.50	0.15	1.19	0.22	2.32	0.61	2.70	0.15	0.12	0.03	0.11	0.04	0.73	0.07
Tb	0.16	0.02	0.23	0.03	0.49	0.08	0.53	0.02	0.02	<0.01	0.04	0.01	0.11	0.01
Dy	0.98	0.11	2.09	0.19	3.22	0.36	4.12	0.16	0.07	0.01	0.08	0.02	0.88	0.05
Ho	0.25	0.03	0.55	0.05	0.72	0.10	0.93	0.03	0.02	<0.01	0.01	<0.01	0.16	0.01
Er	0.74	0.09	1.56	0.14	2.23	0.29	2.80	0.10	0.02	<0.01	0.06	0.01	0.48	0.03
Tm	0.11	0.02	0.24	0.03	0.37	0.08	0.44	0.03	0.03	0.01	0.04	0.01	0.06	0.02
Yb	0.81	0.10	1.69	0.18	2.51	0.39	3.17	0.13	0.03	0.01	0.06	0.01	0.38	0.03
Lu	0.13	0.02	0.26	0.03	0.41	0.08	0.50	0.02	0.01	<0.01	0.01	<0.01	0.04	0.01

opposed to release from different mineral phases. In contrast to pyroxene, the apparent age and Ca/K spectra for maskelynite (Fig. 13b) are relatively flat with apparent ages of between 2.0 and 2.5 Ga. The complexities of shock on the Ar system in NEA 003-A are unknown but different minerals may have experienced both Ar loss by diffusion during shock heating and Ar gain by shock implantation. For this reason we consider only total ages obtained by integrating Ar released by all the temperature steps. Total ages are reported in Table 4b and range between 1.8 (pyroxene) to 2.4 Ga (maskelynite, bulk).

Cosmic ray exposure (CRE) age spectra are relatively flat for 84–94% of the $^{37}Ar_{Ca}$ release (Fig. 13c). Using the equations of Eugster and Michel (1995) and taking into account the contribution from Ca, Fe, Ti, Cr, Mn, K and Ni (from Table 3), a ^{38}Ar production rate of 1.013×10^{-8} cc/g/Ma is obtained for a 2π exposure (i.e. exposure on the lunar surface only). This production rate gives CRE plateau ages between 206 and 212 Ma, with a weighted average of 209 ± 6 Ma (Fig. 13c, Table 4b). The lack of trapped solar Ar in NEA 003-A means that the CRE ages should be regarded as the minimum period of residence in the upper regolith of this meteorite.

4. DISCUSSION

4.1. Comparison with other lunar basalts

4.1.1. Apollo and Luna basalts

NEA 003-A, classified as low-Ti, low-Al, low-K olivine mare-basalt, has a major element composition close to low-Ti olivine mare basalts from Apollo 12 and low-Ti olivine-normative basalts from Apollo 15 (Fig. 8). However, the majority of Apollo 12 olivine basalts and Apollo 15 olivine-normative basalts are richer in TiO_2 (Fig. 8c) compared to NEA 003-A. Furthermore, Apollo 12 basalts often contain cumulate olivine (Walker et al.,1976) with higher MgO and lower Al_2O_3 and CaO concentrations (Fig. 8b, d) than those in NEA 003-A.

As demonstrated by crystallisation modelling (Section 3.4), a portion of the olivine in NEA 003-A is of cumulate origin and its highest Fo content is not in equilibrium with whole rock Mg#. For the comparison with other lunar basalts we removed the corresponding portion (~10%, see Section 3.4) of olivine cumulate content from the meteorite bulk-rock composition. The recalculated NEA 003-A bulk composition (Table 3) therefore reflects the character of the parental magma without any influence from the cumulate component. Most Apollo 12 olivine basalts show a similar discrepancy between measured Fo content of olivine cores and calculated equilibrium Fo content, indicating that a portion of the olivine in these rocks is also of cumulate origin (Rhodes et al., 1977; Neal et al., 1994). Ryder and Schuraytz (2001) calculated the amount of olivine separation or addition that dominates the chemical differences among most of the Apollo 15 olivine-normative mare basalts to be 15%. However, they conclude that none of the analyzed rocks in their study show any evidence of significant olivine accumulation.

Comparing the recalculated bulk composition of NEA 003-A (Table 3) with the compositions of similar Apollo 12—12,009 and 12,015 olivine basalts (without cumulate component; Rhodes et al., 1977; Lindstrom and Haskin, 1978) show that there are some similarities but the TiO_2 concentration and Mg# value for 12,009 and 12,015 basalts are higher (Table 3 and Fig. 8c). Moreover, the different trace element compositions (discussed below) reveal that there is not much evidence for a possible connection with the evolution of Apollo 12 olivine basalts. The recalculated bulk composition of NEA 003-A shows a better match to Apollo 15 samples 15,016 and 15,555 olivine-normative basalts, where TiO_2 concentrations and Mg# values are close to NEA 003-A (Table 3 and Fig. 8c). We propose that NEA 003-A bears a close similarity to Apollo 15 olivine-normative basalts with respect to their major element compositions.

The whole-rock trace-element composition of NEA 003-A is characterized by lower REE concentrations (Table 3) and a less pronounced Eu anomaly than Apollo 12 and Apollo 15 basalts (Fig. 10a). NEA 003-A is depleted in light REE (LREE) and plots of La vs. Yb and Sm vs. La (Fig. 9c and d) show that concentrations of LREE approach the

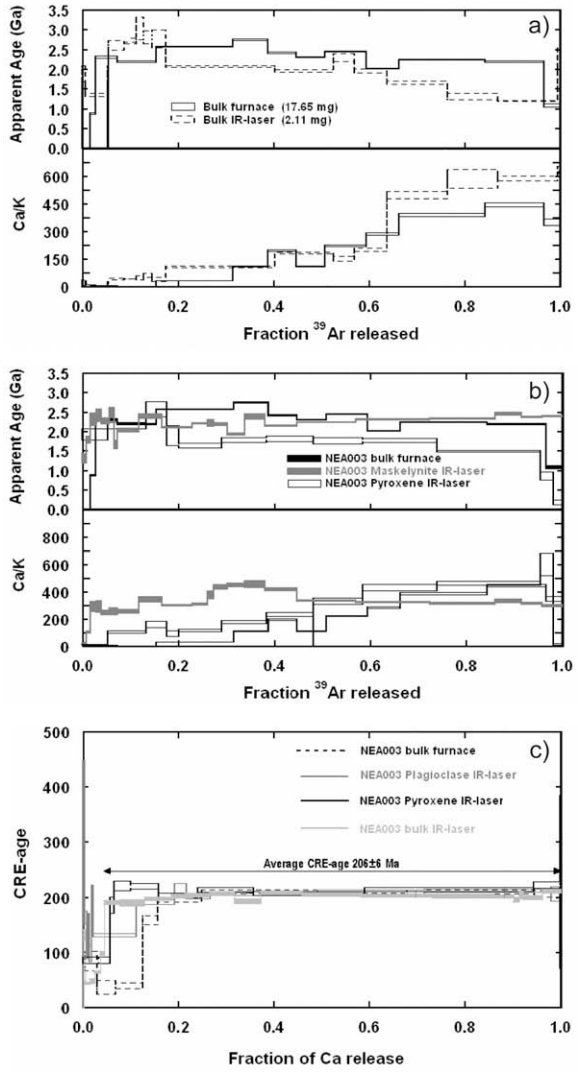

Fig. 13. Apparent age and Ca/K vs. fraction of ^{39}Ar released during step heating for NEA 003-A: (a) bulk samples; and (b) pyroxene and maskelynite separates. (c) Cosmic ray exposure (CRE) age vs fraction of Ca released for bulk, pyroxene and maskelynite samples.

composition of Apollo 15 olivine-normative basalts following the trend of mafic cumulates (Neal and Taylor, 1992). The LREE concentrations of Apollo 12 olivine basalts follow the same trend (Fig. 9c and d), but are obviously higher than for NEA 003-A and Apollo 15 olivine-normative basalts (Neal et al., 1994). The low incompatible trace element concentration of NEA 003-A (Table 3) indicates an absence of a significant KREEP component and also that NEA 003-A is generally more geochemically primitive than Apollo 15 olivine-normative basalts and Apollo 12 olivine basalts, but with a closer relationship with the former. It is therefore possible that NEA 003-A represents an unknown geochemically primitive member of the Apollo 15 olivine-normative basalt series.

We suggest that NEA 003-A parent melt was derived from primitive picritic magma by magmatic differentiation processes. The evidence of a primitive chemical composition of NEA 003-A with low REE concentration, near chondritic initial Nd isotopic ratios very similar to Apollo 15 green glasses (see Section 4.2 for more discussion), with no geochemical evidence for hybridization of the parent melt by magma mixing and assimilation processes supports this hypothesis.

4.1.2. Mare-basalt meteorites

Among unbrecciated low-Ti mare-basalt meteorites, NEA 003-A has a similar modal mineralogy and major element composition to Dhofar 287A. Dhofar 287A also contains a significant portion of cumulate olivine. However, the alkali content and trace element geochemistry (Th and REE concentration) of both meteorites are different due to the presence of a KREEP component in Dhofar 287A (Anand et al., 2003).

NEA 003-A has the highest concentration of Co and the lowest concentration of Eu among the unbrecciated low-Ti mare-basalt meteorites (Fig. 9a and b and Table 3) due to its high modal abundance of olivine and the lowest modal abundance of plagioclase (Table 1). The REE concentrations of NEA 003-A are different from all mare-basalt meteorites with the exception of Kalahari 009. However, Kalahari 009 is a very low-Ti mare-basalt breccia with completely different composition, origin and evolution (Schulz et. al., 2007; Terada et al., 2007; Sokol et al. 2008).

On the basis of its geochemistry, mineralogy and petrology, crystallization age and cosmic ray exposure age, NEA 003-A represents a new type of mare-basalt which is not paired with any other previously described lunar meteorites. We conclude that NEA 003-A represents a previously unknown type of low-Ti mare-basalt that was probably derived from a chemically similar magma source to Apollo 15 olivine-normative basalts.

4.2. Crystallization and shock ages

The apparent four-point Sm–Nd regression age of 3.089 ± 0.064 Ga calculated for different mineral separates, has a good fit (MSWD = 1.01) indicating that the age has chronological significance (Fig. 12). This 3.09 ± 0.06 Ga age is at the lower end of the age range for low-Ti and/or aluminous lunar basalts from Apollo missions (e.g. Shih et al., 1987; Nyquist and Shih, 1992). However, the "Cpx–Fe-rich" fraction is slightly outside analytical uncertainties of this age and could also bear important chronological information. The 3.3 ± 0.14 Ga age (calculated for the clinopyroxene fractions alone; Fig. 12) would suggest that Cpx may have retained its primary, or at least a more pristine, Sm–Nd age. The discrepancy in Sm–Nd age could then be explained by partial disturbance or re-setting of the Sm–Nd system during the shock processes which converted plagioclase into maskelynite. However, a recent study of Gaffney et al. (2007) suggests no or very little effect of shock metamorphism on the Sm–Nd systematics of Apollo basalt samples even at shock pressures of up to 55 GPa. Furthermore, the shock event(s) forming maskelynite was fast with little heating, since there is no petrographic evidence of recrystallization. The supposed post-shock temperature of

200–250 °C (Stöffler and Grieve, 2007) would have been insufficient to cause Sm–Nd diffusion since the closure temperatures for pyroxene and plagioclase are much higher. The olivines, pyroxenes and plagioclases/maskelynites retained their normal (igneous) zoning and thus the chemical equilibration of divalent major cations was not achieved during the shock metamorphism. It is unlikely that, under these conditions, diffusion of trivalent Sm and Nd took place, and thus ions were not re-distributed and the Sm–Nd system remained closed.

Alternatively, the Sm–Nd system could be influenced by terrestrial contamination due to weathering processes taking place in the hot desert environment where the meteorite was found. Detailed study of individual mineral phases under SEM and using EMPA revealed the presence of large numbers of shock fractures within olivine and pyroxene grains. BSE images show that these fractures are filled with secondary weathering products (mainly calcite), particularly in the outer part of olivine and pyroxene grains (Fig. 3). This is in contrast to maskelynite where the fractures are almost absent. It is likely that during preparation of mineral separates these contamination products were not completely eliminated by acid washing. The Fe-rich pyroxene rims represent the most affected region of the pyroxene grains and slight disturbance in Sm–Nd data can be explained by the presence of terrestrial contamination in this separate.

Overall, the low-Ti mare basalts sampled by Apollo and Luna missions on the Moon range in age from 3.08 to 3.37 Ma (Taylor, 1982; Heiken et al., 1991; Shearer et al., 2006). However, some basaltic lunar meteorites (NWA 032/479, LAP 02205 and paired stones, NWA 773 and paired stones) are younger than Apollo and Luna samples (Fagan et al., 2002; Fernandes et al. 2003; Borg et al., 2004; Rankenburg et al., 2007). Their ages together with Sm–Nd age of NEA 003-A (3.09 ± 0.06 Ga) are within the period of lower Eratosthenian lunar volcanic activity (Stöffler and Ryder, 2001).

The low concentration of incompatible elements and low normalized REE content of NEA 003-A would suggest that the chemical composition of the primary melt was not significantly modified by mixing and assimilation processes. The near-chondritic ε_{Nd} value of -0.4 ± 0.3 (or -0.1 ± 0.3, if only the Pl–Cpx pair is considered) suggests that the basaltic melt of NEA 003-A originated from a slightly enriched source (Fig. 14), less fractionated than most depleted Apollo mare basalts. Lunar rocks with ε_{Nd} values similar to NEA 003-A include mare-basalt meteorite Dhofar 287-A (Shih et al., 2002) and Apollo feldspathic basalt 12038 (Nyquist et al., 1981), (Fig. 14). Unlike NEA 003-A, the composition of these latter basalts (high concentrations of incompatible elements, REEs and high alkali content), (Compston et al., 1971; Nyquist et al., 1981; Anand et al., 2003) indicates that the primary rock melts underwent KREEP assimilation processes. Initial Nd isotopic compositions (ε_{Nd} values) of lunar meteorites younger than NEA 003-A (NWA 032/479, LAP 02205 and paired stones, NWA 773 and paired rocks) are distinct from NEA 003-A (Fig. 14).

The chondritic initial Nd isotopic composition together with other geochemical features of NEA 003-A preclude a common origin with Apollo 12 olivine basalts, as was also concluded previously for the low-Ti mare-basalt meteorite LaPaz Icefield 02205 (Rankenburg et al., 2007). However, there is a strong geochemical affinity of NEA 003-A to Apollo 15 olivine-normative basalts and we can assume that a slightly more evolved source magma of Apollo 15 olivine-normative basalts could be derived by fractional crystallisation from a magma source having a similar composition to NEA 003-A. In contrast, the geochemically similar olivine-normative basalts 15555 and 15016 from Apollo 15 suite were derived from isotopically more depleted source than the near-chondritic NEA 003-A (Fig. 14). Most likely the magma source of these rocks evolved separately in isolated geochemically similar reservoirs. These isotopically distinct magma sources with various initial Nd isoto-

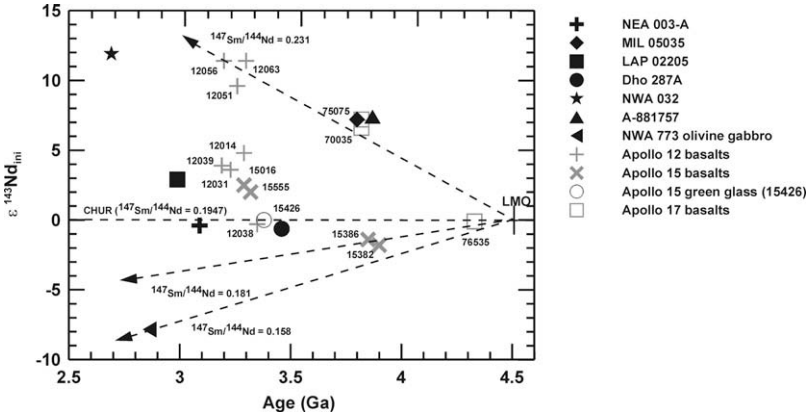

Fig. 14. Initial Nd isotopic composition ε_{Nd} vs age plot for NEA 003-A, mare-basalt meteorites and selected Apollo 12, Apollo 15, and Apollo 17 basalts. The plot indicates that the basaltic melt of NEA 003-A was derived from a very slightly enriched source having $^{147}Sm/^{144}Nd$ ratio very close to CHUR $^{147}Sm/^{144}Nd$ ratio, whereas most of Apollo 12, Apollo 15, and Apollo 17 basalts were derived from a strongly depleted basaltic melt (higher $^{147}Sm/^{144}Nd$ ratio). *Data sources:* NEA 003-A (this study), MIL 05035 (Nyquist et al., 2007), LAP 02205 (Rankenburg et al., 2007), Dhofar 287A (Shih et al., 2002), NWA 032 (Borg et al., 2007), A-881757 (Misawa et al., 1992), NWA 733 olivine gabbro (Borg et al., 2004), Apollo 12, 15 and 17 basalts (Nyquist et al., 1979; Nyquist and Shih, 1992; Nyquist et al., 1995), Apollo 15 green glass: 15426 (Lugmair and Marti, 1978).

pic compositions within Apollo 15 suite were discussed by Nyquist and Shih (1992). The crystallization ages of NEA 003-A (3.09 ± 0.06 Ga) and olivine-normative Apollo 15 basalts ($\sim 3.3 \pm 0.02$ Ga) (Stöffler et al., 2006) are different, but an origin of NEA 003-A during a younger magmatic phase of low-Ti mare-basalt volcanism within the Apollo 15 olivine-normative basalt suite could be envisaged. The near-chondritic ε_{Nd} value of -0.4 ± 0.3 indicates that NEA 003-A could also be derived from a mantle source similar to the Apollo 15 green glass which is also characterized by very low and unfractionated REE abundances (Fig. 10) and near-chondritic Sm/Nd evolution (Lugmair and Marti, 1978). Apollo 15 green glasses are also older (3.38 Ga; Spangler et al., 1984) than NEA 003-A however the basaltic equivalent to these picritic glasses is unknown.

The discordant Ar–Ar and Sm–Nd ages suggest that the K–Ar system was re-set by an impact event at ~1.8 Ga ago. Impact shock was followed by a period of heating sufficient to permit loss of radiogenic ^{40}Ar, but not hot enough to melt plagioclase (<900 °C, e.g. hot ejecta blanket). The Ar–Ar ages from the maskelynite and pyroxene separates are in reverse of what would be expected based upon closure temperature. A tentative explanation for this discrepancy involves an impact event that caused all the minerals to be degassed of their radiogenic ^{40}Ar and re-setting the K–Ar system. During impact the shock features observed in olivine, pyroxene, spinels and the conversion of plagioclase to diaplectic plagioclase glass (maskelynite) developed. This event took place 1.745 ± 0.060 Ga the age obtained from the pyroxene separates), and the shock intensity was of ~28–45 GPa (Stöffler and Grieve, 2007). During the shock event some of the ^{40}Ar released from pyroxene and plagioclase was re-implanted or diffused into maskelynite. This "excess" ^{40}Ar results in relatively old ages (2.418 ± 0.044 Ga) observed for the maskelynite separates as well as those seen for the bulk sample step heated in the Ta-furnace. The process of Ar implantation has been well investigated e.g. Davis (1977), Jessberger and Ostertag (1982), Bogard et al. (1986 and 1989), Wiens and Pepin (1988) and Stephan and Jessberger (1992). These authors suggest that Ar can be implanted at shock pressures as low as 10 GPa due to gas diffusion from pores/cracks into silicates.

It is interesting to note two further observations relevant to the low Ar–Ar ages. Firstly, NEA 003-A and Kalahari 009 are the only two mare-basalt meteorites currently known, in which the K–Ar system has been reset during impact (Sokol et al., 2008); and second that the presence of maskelynite is not incontrovertible evidence that the K–Ar age has been reset. For example, Asuka 881757 shows the presence of maskelynite, however, the Ar–Ar age is within error of the crystallization age obtained by other isotope dating methods (e.g. Sm/Nd, Rb/Sr, U–Th/Pb; Misawa et al., 1992).

5. CONCLUSIONS

1. Crystallization age, cosmic ray exposure age and geochemical and petrological features of NEA 003-A indicate that this meteorite is not paired with any other previously described lunar meteorite. NEA 003-A is a unique low-Ti mare-basalt that is different from Apollo and Luna samples and low-Ti mare-basalt meteorites.

2. The mineralogy, bulk-rock major and trace element composition of NEA 003-A shows similarities with the Apollo 15 olivine-normative basalts. The depletion of REE is indicative of the mafic-cumulate evolution of this rock. It is possible that NEA 003-A represents a previously unknown geochemically primitive type of the Apollo 15 olivine-normative basalt series.

3. Geochemical characteristics (e.g. high Mg#, low concentration of K_2O and Al_2O_3, low concentration of incompatible elements) together with results of crystallization modelling demonstrate the presence of a significant portion of cumulate olivine and suggest that NEA 003-A parent melt was not contaminated by KREEP components during magma mixing and assimilation processes. Low concentrations of incompatible elements also reveal the primitive nature of the parent melt. This parent melt was itself probably derived from a primitive picritic magma by magmatic differentiation processes.

4. Crystallization modelling, the crystallization sequence derived from Ti and Al variations in pyroxenes, and the presence of strong REE variations between core and rim of pyroxene and plagioclase grains, all confirm formation of this rock by fractional crystallization processes. Low minimum cooling rate estimates (~0.07 °C/h) based on the variation of Fo content in olivine suggests that NEA 003-A crystallized in the deeper part of a lava flow in the presence of cumulate olivine.

5. The Sm–Nd crystallization age (3.089 ± 0.064 Ga) corresponds to the period of lower Eratosthenian lunar volcanic activity. Older crystallization ages of geochemically similar Apollo 15 olivine-normative basalts ($\sim 3.3 \pm 0.02$ Ga) indicate that it is possible that NEA 003-A represents a product of younger low-Ti mare-basalt volcanism within the Apollo 15 olivine-normative basalt suite.

6. The initial Nd isotopic composition and near-chondritic ε_{Nd} value (-0.4 ± 0.3) indicate that NEA 003-A could have been derived from a primitive, slightly enriched mantle source that was less fractionated compared to most depleted Apollo mare basalts. The primitive character of NEA 003-A mantle source indicates is similar to that of the Apollo 15 green glass.

7. The discordant Ar–Ar and Sm–Nd ages suggest that the K–Ar system was reset by an impact event at ~1.8 Ga ago with the shock pressures of ~28–45 GPa, that also caused complete conversion of plagioclase to maskelynite. The absence of solar Ar suggests that this impact event did not expose NEA 003-A at the lunar surface and that it remained shielded from galactic cosmic rays and solar wind particles during its lunar history. However, the cosmic ray exposure age of 209 ± 6 Ma implies that NEA 003-A resided in the upper regolith for at least a part of its history.

ACKNOWLEDGMENTS

Franz Brandstätter (Naturhistorisches Museum, Vienna, Austria) and Anton Kearsley (Natural History Museum, London, UK) are thanked for help with EMPA analyses. V.A.F. was funded

by the Fundação para a Ciência e a Tecnologia, Portugal. V.A.F. and R.B. were additionally funded by Particle Physics and Astronomy Research Council and the Royal Society, UK. Tomas Magna (Czech Geological Survey, Prague, Czech Republic) is thanked for critical review of the manuscript. We thank Mahesh Anand (The Open University, Milton Keynes, UK), an anonymous reviewer and Associate Editor Christian Koeberl (University of Vienna, Austria) for constructive comments and suggestions which significantly improved the quality of the paper.

REFERENCES

Anand M., Taylor L. A., Misra K. C., Demidova S. I. and Nazarov M. A. (2003) KREEPy lunar meteorite Dhofar 287A: a new lunar basalt. *Meteorit. Planet. Sci.* **38**, 485–499.

Anand M., Taylor L. A., Floss CH., Neal C. R., Terada K. and Tanikawa S. (2006) Petrology and geochemistry of LaPaz Icefield 02205: a new unique low-Ti mare-basalt meteorite. *Geochim. Cosmochim. Acta* **70**, 246–264.

Anders E. and Grevesse N. (1989) Abundances of the elements: meteoritic and solar. *Geochim. Cosmochim. Acta* **53**, 197–214.

Basaltic Volcanism Study Project (1981) In *Basaltic Volcanism on the Terrestrial Planets*. Chapter 1.2.9: Lunar Mare Basalts. Pergamon Press, Inc., New York, pp. 236–266.

Bogard D., Hörz F. and Johnson P. (1986) Shock-implanted noble gases II: an experimental study with implications for the origin of Martian gases in shergottite meteorites. *J. Geophys. Res.* **91**, E99–E114.

Bogard D., Hörz F. and Johnson P. (1989) Shock-implanted noble gases II: additional experimental studies and recognition in naturally shocked terrestrial materials. *Meteorit. Planet. Sci.* **24**, 113–123.

Borg L. E., Shearer C. K., Asmerom Y. and Papike J. J. (2004) Prolonged KREEP magmatism on the Moon indicated by the youngest dated lunar igneous rock. *Science* **432**, 209–211.

Borg L., Gaffney A. and De Paolo D. (2007) Rb–Sr and Sm–Nd isotopic systematics of NWA 032. *70th Annual Meeting of the Meteoritical Society*, Lunar and Planetary Institute, Houston. #5232 (abstr.).

Boudreau A. E. (1999) A version of the MELTS software program for the PC platform. *Comput. Geosci.* **25**, 21–203.

Clayton R. N. and Mayeda T. K. (1963) The use of bromine pentafluoride in the extraction of oxygen from oxides and silicates for isotopic analysis. *Geochim. Cosmochim. Acta* **27**, 43–52.

Clayton R. N. and Mayeda T. K. (1983) Oxygen isotopes in eucrites, shergottites, nakhlites and chassignites. *Earth Planet. Sci. Lett.* **62**, 1–6.

Compston W., Berry H., Vernon M. J., Chappell B. W. and Kay M. J. (1971) Rubidium-strontium chronology and chemistry of lunar material from the Ocean of Storms. In *Proc. 2nd Lunar Sci. Conf.*, Lunar Planet. Inst., Houston, pp. 1471–1485.

Davis P. K. (1977) Effects of shock pressure on ^{40}Ar–^{39}Ar radiometric age determinations. *Geochim. Cosmochim. Acta* **41**, 195–205.

Day J. M. D., Taylor L. A., Floss C., Patchen A. D., Schnare D. W. and Pearson D. G. (2006) Comparative petrology, geochemistry and petrogenesis of evolved, low-Ti lunar mare basalt meteorites from the LaPaz Icefield, Antarctica. *Geochim. Cosmochim. Acta* **70**, 1581–1600.

Delano J. W. (1980) Chemistry and liquid phase Apollo 15 red glass. Implications for the deep lunar interior. In *Proc. 11th Lunar Sci. Conf.*, Lunar Planet. Inst., Houston, pp. 251–288.

El Goresy A., Ramdohr P. and Taylor L. A. (1971) The opaque minerals in the lunar rocks from Oceanus Procellarum. In *Proc. 2nd Lunar Sci. Conf.*, Lunar Planet. Inst., Houstan, pp. 219–235.

El Goresy A. (1976) Oxide minerals in lunar rocks. In *Oxide minerals* (ed. D. Rumble). Mineralogical Society of America, Washington, DC, pp. EG1–EG43.

Eugster O. and Michel Th. (1995) Common asteroid break-up events of eucrites, diogenites, and howardites and cosmic-ray production rates for noble gases in chondrites. *Geochim. Cosmochim. Acta* **59**, 177–199.

Fagan T. J., Taylor G. J., Keil K., Bunch T. E., Wittke J. H., Korotev R. L., Jolliff B. L., Gillis J. J., Haskin L. A., Jarosewich E., Clayton R. N., Mayeda T., Fernandes V. A., Burgess R., Turner G., Eugster O. and Lorenzetti S. (2002) Northwest Africa 032: product of lunar volcanism. *Meteorit. Planet. Sci.* **37**, 371–394.

Fernandes V. A., Burgess R. and Turner G. (2000) Laser ^{40}Ar–^{39}Ar studies of Dar al Gani 262 lunar meteorite. *Meteorit. Planet. Sci.* **35**, 1355–1364.

Fernandes V. A., Burgess R. and Turner G. (2003) ^{40}Ar–^{39}Ar chronology of lunar meteorites Northwest Africa 032 and 773. *Meteorit. Planet. Sci.* **38**, 555–564.

Fernandes V. A. and Burgess R. (2005) Volcanism in Mare Fecunditatis and Mare Crisium: Ar–Ar studies. *Geochim. Cosmochim. Acta* **69**, 4919–4934.

Gaffney A. M., Borg L. E. and Asmerom Y. (2007) Disturbance of Sm–Nd, Rb–Sr and U–Pb isochrons during shock and thermal metamorphism—an experimental approach. *Lunar Planet. Sci. XXXVIII*. Lunar Planet. Inst., Houston. #1424 (abstr.).

Ghiorso M. S. (1985) Chemical mass transfer in magmatic processes. I. Thermodynamic relations and numerical algorithms. *Contrib. Miner. Petrol.* **90**, 107–120.

Ghiorso M. S. and Sack R. O. (1994) Chemical mass transfer in magmatic processes. IV. A revised and internally consistent thermodynamic model for the interpolation and extrapolation of liquid–solid equilibria in magmatic systems at elevated temperatures and pressures. *Contrib. Miner. Petrol.* **119**, 197–212.

Haloda J., Korotev R. L., Tycova P., Jakes P. and Gabzdyl P. (2006) Lunar meteorite Northeast Africa 003-A: a new lunar mare basalt. *Lunar Planet. Sci. XXXVII*. Lunar Planet. Inst., Houston. #2269 (abstr.).

Hamilton P. J., O'nions R. K., Bridgewater D. and Nutman A. (1983) Sm–Nd studies of Archean metasediments and metavolcanics from West Greenland and their implications for the Earth's early history. *Earth Planet. Sci. Lett.* **62**, 263–272.

Heiken G., Vaniman D. and French B. M., 1991. Lunar Sourcebook. A User's Guide to the Moon. Cambridge University Press, Berlin.

Jacobsen S. B. and Wasserburg G. J. (1979) Nd and Sr isotopic study of the Bay of Islands Ophiolite complex and the evolution of the source of Midocean Ridge Basalts. *J. Geophys. Res.* **84** (B3), 7429–7445.

Jessberger E. K. and Ostertag R. (1982) Shock-effects on the K–Ar system of plagioclase feldspar and the age of anorthosite inclusions from North-Eastern Minnesota. *Geochim. Cosmochim. Acta* **46**, 1465–1471.

Jolliff B. L., Korotev R. L., Zeigler R. A., Floss C. and Haskin L. A. (2003) Northwest Africa 773: lunar mare breccia with a shallow-formed olivine-cumulate component, very-low-Ti (VLT) heritage, and a KREEP connection. *Geochim. Cosmochim. Acta* **67**, 4857–4879.

Jolliff B. L., Hughes J. M., Freeman J. J. and Zeigler R. A. (2006) Crystal chemistry of lunar merrillite and comparison to other meteoritic and planetary suites of whitlockite and merrillite. *Am. Mineral.* **91**, 1583–1595.

Joy K. H., Crawford I. A., Anand M., Greenwood R. C., Franchi I. A. and Russell S. S. (2008) The petrology and geochemistry of Miller Range 05035: a new lunar gabbroic meteorite. *Geochim. Cosmochim. Acta* **72**, 387–402.

Koeberl C., Kurat G. and Brandstätter F. (1993) Gabbroic lunar mare meteorites Asuka-881757 (Asuka-31) and Yamato-793169: geochemical and mineralogical study. In. *Proc. NIPR Symp. Antarct. Meteorites*, vol. **6.** Nat. Inst. Polar Res., Tokyo, pp. 14–34.

Korotev R. L. (2005) Lunar geochemistry as told by lunar meteorites. *Chemie der Erde* **65**, 297–346.

Langmuir C. H. and Hanson G. N. (1981) Calculating mineral–melt equilibria with stoichiometry, mass balance, and single-component distribution coefficients. In *Thermodynamics of Minerals, Melts, Advances in Physical Geochemistry* (eds. R. C. Newton, A. Navrotsky and B. J. Wood). Springer-Verlag, New York, pp. 247–271, vol. 1.

Lindstrom M. M. and Haskin L. A. (1978) Causes of compositional variations within mare basalt suites. In *Proc. 9th Lunar Sci. Conf.*, Lunar Planet. Inst., Houstan, pp. 465–486.

Ludwig K. R. (2003) User's manual for Isoplot 3.00. In *Berkley Geochronology Center Special Publication*, 74 pp.

Lugmair G. W. and Marti K. (1978) Lunar initial $^{143}Nd/^{144}Nd$: differential evolution of the lunar crust and mantle. *Earth Planet. Sci. Lett.* **39**, 3349–3357.

Ma M. S., Schmitt R. A., Taylor G. J., Warner D., Lange D. E. and Keil K. (1978) Chemistry and petrology of Luna 24 lithic fragments and <250 μm soils: constraints on the origin of the VLT mare basalt. In *Mare Crisium: The view from Luna 24* (eds. R. B. Merill and J. J. Papike). Pergamon Press, New York, pp. 569–592.

Misawa K., Tatsumoto M., Dalrymple G. B. and Yanai K. (1992) An extremely low U/Pb source in the Moon: U–Th-Pb, Sm–Nd, Rb–Sr and $^{40}Ar/^{39}Ar$ isotopic systematics and age of lunar meteorite Asuka 881757. *Geochim. Cosmochim. Acta* **57**, 4687–4702.

Neal C. R. and Taylor L. A. (1992) Petrogenesis of mare-basalts: a record of lunar volcanism. *Geochim. Cosmochim. Acta* **56**, 2177–2211.

Neal C. R., Hacker M. D., Snyder G. A., Taylor L. A., Liu Y. G. and Schmitt R. A. (1994) Basalt generation at the Apollo 12 site. Part 1: new data, classification, and re-evaluation. *Meteorit. Planet. Sci.* **29**, 334–348.

Nyquist L. E., Shih C. Y., Wooden J. L., Bansal B. and Wiesmann H. (1979) The Sr and Nd isotopic record of Apollo 12 basalts: Implication for lunar geochemical evolution. *Proc. 10th Lunar Sci. Conf.*, 77–114.

Nyquist L. E., Wooden J. L., Shih C. Y., Wiesmann H. and Bansal B. (1981) Isotopic and REE studies of lunar basalt 12038: Implications for the petrogenesis of aluminous mare basalts. *Earth Planet. Sci. Lett.* **55**, 335–355.

Nyquist L. E., Lindstrom M., Bansal B., Mittlefeldt D., Shih C. Y. and Wiesmann H. (1989) Chemical and isotopic constraints on the petrogenesis of the Large Mare Basalt Clast in Breccia 15459. In *Proc. 19th Lunar Sci. Conf.*, Lunar Planet. Inst., Houstan, pp. 163–174.

Nyquist L. E. and Shih C. Y. (1992) The isotopic record of lunar volcanism. *Geochim. Cosmochim. Acta* **56**, 2213–2234.

Nyquist L. E., Wiesmann H., Bansal B., Shih C. Y., Keith J. E. and Harper C. L. (1995) ^{146}Sm–^{142}Nd formation interval for the lunar mantle. *Geochim. Cosmochim. Acta* **59**, 2817–2837.

Nyquist L. E., Shih C. Y. and Reese Y. D. (2007) Sm–Nd and Rb–Sr ages for MIL 05035: implications for surface and mantle sources. *Lunar Planet. Sci. XXXVIII*. Lunar Planet. Inst., Houston. #2103 (abstr.).

O'nions R. K., Hamilton P. J. and Evensen M. N. (1977) Variations in $^{143}Nd/^{144}Nd$ and $^{87}Sr/^{86}Sr$ in oceanic basalts. *Earth Planet. Sci. Lett.* **34**, 13–22.

Papike J. J., Ryder G. and Shearer C. K. (1998) Lunar samples. In *Planetary Materials* (ed. J. J. Papike). Mineralogical Society of America, Washington, DC, pp. 5-1–5-234.

Papike J. J., Karner J. M. and Shearer C. K. (2003) Determination of planetary basalt parentage: A simple technique using the electron microprobe. *Am. Mineral.* **88**(2–3), 469–472.

Premo W. R. and Tatsumoto M. (1992) U–Th–Pb, Rb–Sr, and Sm–Nd isotopic systematics of lunar Troctolitic Cumulate 76535: implications on the age and origin of this early lunar, deep-seated cumulate. In *Proc. 22th Lunar Sci. Conf.*, Lunar Planet. Inst., Houstan, pp. 381–397.

Rankenburg K., Brandon A. D. and Norman M. D. (2007) A Rb–Sr and Sm–Nd isotope geochronology and trace element study of lunar meteorite LaPaz Icefield 02205. *Geochim. Cosmochim. Acta* **71**, 2120–2135.

Rhodes J. M. and Hubbard N. J. (1973) Chemistry, classification, and petrogenesis of Apollo 15 mare-basalts. In *Proc. 4th Lunar Sci. Conf.*, Lunar Planet. Inst., Houstan, pp. 1127–1148.

Rhodes J. M., Blanchard D. P., Dungan M. A., Brannon J. C. and Rodgers K. V. (1977) Chemistry of Apollo 12 mare basalts: magma types and fractionation processes. In *Proc. 8th Lunar Sci. Conf.*, Lunar Planet. Inst., Houstan, pp. 1305–1338.

Roeder P. L. and Emslie R. F. (1970) Olivine–liquid equilibrium. *Contrib. Miner. Petrol.* **29**, 275–289.

Ryder G. and Schuraytz B. C. (2001) Chemical variation of the large Apollo 15 olivine-normative basalt rock samples. *J. Geophys. Res.* **106**, 1435–1451.

Schmidt N. H. and Olensen N. O. (1989) Computer-aided determination of crystal-lattice orientation from electron-channelling patterns in the SEM. *Can. Mineral.* **28**, 15–22.

Schulz T., Sokol A., Palme H., Weckwerth G., Münker C. and Bischoff A. (2007) Chemical composition and Lu-Hf age of the lunar mare basalt meteorite Kalahari 009. *70th Annu. Meeting Meteor. Soc.,* Lunar and Planetary Institute, Houston. #5151 (abstr.).

Shafer J., Neal C. R. and Castillo P. (2004) Compositional variability in lavas from the Ontong Java Plateau: results from basalt clasts within the volcaniclastic sequence of Ocean Drilling Program Leg 192 Site 1184. In *Origin and Evolution of the Ontong Java Plateau* (eds.J. G. Fitton, J. J. Mahoney, P. J. Wallace and A. D. Saunders), vol. 229. J. Geol. Soc. London Spec. Pub. pp. 333–351.

Shearer C. K., Hess P. C., Wieczorek M. A., Pritchard M. E., Parmentier E. M., Borg L. E., Longhi J., Elkins-Tanton L. T., Neal C. R., Antonenko I., Canup R. M., Halliday A. N., Grove T. L., Hager B. H., Lee D. C. and Wiechert U. (2006) Thermal and magmatic evolution of the moon. In *New views of the Moon* (eds. B. L. Jolliff, M. A. Wieczorek, C. K. Shearer and C. R. Neal). Mineralogical Society of America and Geochemical Society, Washington, DC, pp. 365–518.

Shih C. Y., Nyquist L. E., Bogard D. D., Dasch E. J., Bansal B. M. and Wiesmann H. (1987) Geochronology of high-K aluminous mare basalt clasts from Apollo 14 breccia 14304. *Geochim. Cosmochim. Acta* **51**, 3255–3271.

Shih C. Y., Nyquist L. E., Reese Y., Wiesmann H., Nazarov M. A. and Taylor L. A. (2002) The chronology and petrogenesis of the mare basalt clast from lunarmeteorite Dhofar 287: Rb–Sr and Sm–Nd isotopic studies. *Lunar Planet. Sci. XXXII*. Lunar Planet. Inst., Houston. #1344 (abstr.).

Snyder G. A., Neal C. R., Taylor L. A. and Halliday A. N. (1997) Anataxis of lunar cumulate mantle in time and space. Clues from trace-element, strontium and neodymium isotopic chem-

istry of parental Apollo 12 basalts. *Geochim. Cosmochim. Acta* **61**, 2731–2747.

Sokol A. K., Fernandes V. A., Schulz T., Bischoff A., Burgess R., Clayton R. N., Münker C., Nishiizumi K., Palme H., Schultz L., Weckwerth G. and Mezger K. (2008) Geochemistry, petrology and ages of the lunar meteorites Kalahari 008 and 009: new constraints on early lunar evolution. *Geochim. Cosmochim. Acta* **72**, 4845–4873.

Spangler R. R., Warasila R. and Delano J. W. (1984) ^{39}Ar–^{40}Ar ages for the Apollo 15 green and yellow volcanic glasses. *Proc. 14th Lunar Sci. Conf. J. Geophys. Res* **89**, B487–B497.

Spicuzza M. J., Day J. M. D., Taylor L. A. and Valley J. W. (2007) Oxygen isotope constraints on the origin and differentiation of the Moon. *Earth Planet. Sci. Lett.* **253**, 254–265.

Steiger R. H. and Jäger E. (1977) Subcommission on geochronology: convention on the use of decay constants in geochronology and cosmochronology. *Earth Planet. Sci. Lett.* **36**, 359–362.

Stephan T. and Jessberger E. K. (1992) Isotope systematics and shock-wave metamorphism: III. K–Ar in experimentally and naturally shocked rocks; the Haughton impact structure, Canada. *Geochim. Cosmochim. Acta* **56**, 1591–1605.

Stöffler D. and Ryder G. (2001) Stratigraphy and isotope ages of lunar geologic units: chronological standard for the inner solar system. *Space Sci. Rev.* **96**, 9–54.

Stöffler D., Ryder G., Ivanov B. A., Artemieva N. A., Cintala M. J. and Grieve R. A. F. (2006) Cratering History and lunar Chronology. In *New views of the Moon* (eds. B. L. Jolliff, M. A. Wieczorek, C. K. Shearer and C. R. Neal). Mineralogical Society of America and Geochemical Society, Washington, DC, pp. 519–596.

Stöffler D. and Grieve R. A. F. (2007) Impactites. In *Metamorphic Rocks—A Classification, Glossary of Terms* (eds. D. Fettes and J. Desmons). Cambridge University Press, Cambridge, UK, pp. 82–92.

Takeda H., Arai T. and Saiki K. (1993) Mineralogical studies of lunar meteorite Yamato-793169. In. *Proc. NIPR Symp. Antarct. Meteorites*, vol. **6.** Nat. Inst. Polar Res., Tokyo, pp. 3–13.

Taylor L. A., Kullerud G. and Bryan W. B. (1971) Opaque mineralogy and textural features of Apollo 12 samples and a comparison with Apollo 11 rocks. In *Proc. 2nd Lunar Sci. Conf.*, Lunar Planet. Inst., Houstan, pp. 855–871.

Taylor L. A., Onorato P. I. K. and Uhlmann D. R. (1977) Cooling rate estimations based on kinetic modeling of Fe–Mg diffusion in olivine. In *Proc. 8th Lunar Sci. Conf.*, Lunar Planet. Inst., Houstan, pp. 1581–1592.

Taylor S. R., Gorton M. P., Muir P., Nance W., Rudowski R., Ware N. (1973) Lunar highlands composition: Apennine front. In *Proc. 4th Lunar Sci. Conf.*, Lunar Planet. Inst., Houstan, pp. 1445–1459.

Taylor S. R. (1982) *Planetary Science. A Lunar Perspective*. Lunar and Planetary Institute, Houston.

Terada K., Anand M., Sokol A. K., Bischoff A. and Sano Y. (2007) Cryptomare magmatism 4.35 Gyr ago recorded in lunar meteorite Kalahari 009. *Nature* **450**, 849–853.

Thompson, Jr., J. B. (1982) Composition space. An algebraic and Geometric approach. In *Characterization of Metamorphism Through Mineral Equilibria* (ed. J. M. Ferry). Mineralogical Society of America, Washington, DC, pp. 1–31.

Turner G. (1971) ^{40}Ar–^{39}Ar dating: the optimization of irradiation parameters. *Earth Planet. Sci. Lett.* **10**, 227–234.

Walker D., Longhi J. and Hays J. F. (1976) Heterogeneity in titaniferous lunar basalts. *Earth Planet. Sci. Lett.* **30**, 27–36.

Warren P. H. and Kallemeyn G. W. (1993) Geochemical investigation of two lunar mare meteorites: Yamato-793169 and Asuka-881757. In *Proc. NIPR Symp. Antarct. Meteorites*, vol. **6.** Nat. Inst. Polar Res., Tokyo, pp. 35–57.

Wentworth S., Taylor G. J., Warner R. D. and Keil K. (1979) The unique nature of Apollo 17 VLT mare basalt. *Proc. 10th Lunar Sci. Conf.*, vol. 2. Lunar Planet. Inst., Houston, pp. 207–223.

Wiens R. C. and Pepin R. O. (1988) Laboratory shock experiments of noble gases, nitrogen, and carbon dioxide into basalt, and implications for trapped gases in shergottite EETA 79001. *Geochim. Cosmochim. Acta* **52**, 295–307.

Yanai K. and Kojima H. (1991) Varieties of lunar meteorites recovered from Antarctica. In *Proc. NIPR Symp. Antarct. Meteorites*, vol. **4.** Nat. Inst. Polar Res., Tokyo, pp. 70–90.

Yanai K., Kojima H. and Naraoka H. (1993) The Asuka-87 and Asuka-88 collections of Antarctic meteorites; Search, discoveries, initial processing, and preliminary identification and classification. In *Proc. NIPR Symp. Antarct. Meteorites*, vol. **6.** Nat. Inst. Polar Res., Tokyo, pp. 137–147.

Zeigler R. A., Korotev R. L., Jolliff B. L. and Haskin L. A. (2005) Petrography and geochemistry of the LaPaz Icefield basaltic lunar meteorite and source crater pairing with Northwest Africa 032. *Meteorit. Planet. Sci.* **40**, 1073–1101.

Associate editor: Christian Koeberl

CHARLES UNIVERSITY IN PRAGUE

FACULTY OF SCIENCE

ELEMENTAL AND ISOTOPIC STUDY OF DIFFERENTIATED METEORITES AND IMPLICATIONS FOR THE ORIGIN AND EVOLUTION OF THEIR PARENT BODIES

Dissertation thesis

Supplementary material

Peer-reviewed articles published during PhD study (first pages):

Verner, K. , Žák, J. , Pertoldová, J. , Trubač, J. , **Týcová, P.** (2010): Reply to the comments on Magmatic history and geophysical signature of a post-collisional intrusive center emplaced near a crustal-scale shear zone: the Plechý granite pluton (Moldanubian batholith, Bohemian Massif). International Journal of Earth Sciences, 1-2. ISSN 1437-3254. DOI 10.1007/s00531-010-0519-0.

Haloda, J., Rapprich, V., Holub, F. V., **Halodová P.**, Vaculovi T. (2010): Crystallization history of Oligocéne ijolitic rocks from the Doupovské hory Volcanic Komplex (Czech Republic). Journal of Geosciences 55, 279-297. ISSN 1802-6222. DOI 10.3190/jgeosci.076.

Chadima, M. , Cajz, V. , **Týcová, P.** (2009): On the interpretation of normal and inverse magnetic fabric in dikes: Examples from the Eger Graben, NW Bohemian Massif. Tectonophysics 466, 1-2, 47-63. ISSN 0040-1951. DOI 10.1016/j.tecto.2008.09.005.

Verner, K. , Žák, J. , Pertoldová, J. , Šrámek, J. , Sedlák, J. , Trubač, J. , **Týcová, P.**. (2009): Magmatic history and geophysical signature of a post-collisional intrusive center emplaced nearby a crustal-scale shear zone: the Plechý granite pluton (Moldanubian batholith, Bohemian Massif). International Journal of Earth Sciences 98, březen, 517-532. ISSN 1437-3254. DOI 10.1007/s00531-007-0285-9.

Závada, P. , Schulmann, K. , Lexa, O. , Hrouda, F. , Haloda, J. , **Týcová, P.** (2009): The mechanism of flow and fabric development in mechanically anisotropic trachyte lava. Journal of Structural Geology 31, 11, 1295-1307. ISSN 0191-8141. DOI 10.1016/j.jsg.2009.04.002.

Pertoldová, J. , **Týcová, P.** , Verner, K. , Košuličová, M. , Pertold, Z. , Košler, J. , Konopásek, J. , Pudilová, M. (2009): Metamorphic history of skarns, origin of their protolith and implication for genetic interpretation; an example from three units of the Bohemian Massif. Journal of Geosciences 54, 2, 101-134. ISSN 1802-6222. DOI 10,3190/jgeosci,044.

Hasalová, P. , Schulmann, K. , Lexa, O. , Hrouda, F. , Ulrich, S. , Haloda, J. , **Týcová, P.** (2008): Origin of migmatites by deformation-enhanced melt infiltration of orthogneiss: a new model based on quantitative microstructural analysis. Journal of Metamorphic Geology 26, 1, 29-53. ISSN 0263-4929. DOI 10.1111/j.1525-1314.2007.00743.x.

Žák, J. , Verner, K. , **Týcová, P.** (2008): Grain-scale processes in actively deforming magma mushes: new insights from electron backscatter diffraction (EBSD) analysis of biotite schlieren in the Jizera granite, Bohemian Massif. Lithos 106, 3-4, 309-322. ISSN 0024-4937. DOI 10.1016/j.lithos.2008.08.006.

Žák, J. , Verner, K. , **Týcová, P.** (2008): Multiple magmatic fabrics in plutons: an overlooked tool for exploring interactions between magmatic processes and regional deformation?. Geological Magazine 145, 4, 537-551. ISSN 0016-7568. DOI 10.1007/S0016756808004573.

Borovička, J. , Weber, H. , Jopek, T. , Jakeš, P. , Randa, Z. , Brown, P.G. , ReVelle, D.O. , Kalenda, P. , Schultz, L. , Kučera, J. , Haloda, J. , **Týcová, P.** , Frýda, J. , Brandstatter, F. (2003): The Morávka meteorite fall: 3. Meteoroid initial size, history, structure and composition. Meteoritics and Planetary Science 38, 7, 1005-1021. ISSN 1086-9379.

Int J Earth Sci (Geol Rundsch) (2011) 100:893–894
DOI 10.1007/s00531-010-0519-0

REPLY

Reply to the comments on "Magmatic history and geophysical signature of a post-collisional intrusive center emplaced near a crustal-scale shear zone: the Plechý granite pluton (Moldanubian batholith, Bohemian Massif)"

Kryštof Verner · Jiří Žák · Jaroslava Pertoldová · Jakub Trubač · Patricie Týcová

Received: 19 November 2009 / Accepted: 19 December 2009 / Published online: 29 January 2010

On the basis of geochemical data and single zircon evaporation ages, K. Breiter made an attempt to challenge our model for the synkinematic emplacement of the Plechý pluton (Verner et al. 2009). Before we address his main comments point by point, we emphasize that we would rather prefer to receive a process-oriented discussion on more general issues of pluton construction, and not on local geology, as it would be appropriate for a first-class venue such as International Journal of Earth Sciences. In general, we also find inadequate to discuss the internal structure and emplacement of plutons solely from the standpoint of geochemical and geochronologic data.

(1) Definition of geologic units in the Plechý pluton. The geologic map published by Verner et al. (2009; fig. 2) is a compilation of new detailed mapping of the Czech part of the area at the scale of 1:25,000 (Pertoldová 2010; Pertoldová et al. 2010) and reconnaissance mapping of the adjacent German and Austrian parts. The differences between our map and previously published maps of Ott (1988, 1992), including the definition, interpretation, and uncertainties regarding the disputable Dreisessel and Steinberg granites, were clearly explained and discussed in detail in Verner et al. (2009). We may thus only suspect that K. Breiter was in a hurry when reading our paper, as many of his comments just repeat in other words what we said in the section "Plechý pluton and its host rock", p. 520, last two paragraphs.

(2) The inferred emplacement sequence. The existing $^{207}Pb/^{206}Pb$ single zircon ages (Siebel et al. 2008) overlap within errors and indicate a rather narrow time span for crystallization of the Steinberg (328.1 ± 1.7 Ma), Dreisessel (327.1 ± 1.9 Ma), and Plöckenstein (324.1 ± 3.4 Ma) granites. The Steinberg and Dreisessel granites yield very similar single zircon ages, which is a particularly troublesome fact for K. Breiter's interpretation that these granite varieties represent two separate intrusions. Hence, the $^{207}Pb/^{206}Pb$ single zircon data constrain the age of the Plechý pluton as a whole, but provide no rigorous information on the relative emplacement sequence of its component intrusions. Instead, the emplacement sequence should be inferred from field relations, nature and geometry of contacts, and internal fabric patterns of individual units as presented in our paper (Verner et al. 2009).

(3) The insignificance of the garnet-bearing Marginal granite. Again, we guess that K. Breiter did not read our paper carefully because we clearly expressed the uncertainties regarding the interpretation of the Marginal granite (see the last paragraph of the Discussion section on p. 529 and note the question mark in fig. 10 in Verner et al. 2009). The Marginal granite, regardless of its petrogenesis, forms a small, poorly exposed unit which is totally unimportant to our general model for the emplacement of the Plechý pluton in relation to the late-Variscan paleostress field (the main topic of our paper).

K. Verner · J. Žák · J. Pertoldová
Czech Geological Survey, Klárov 3,
11821 Prague, Czech Republic

K. Verner
Institute of Petrology and Structural Geology,
Faculty of Science, Charles University,
Albertov 6, 12843 Prague, Czech Republic

J. Žák (✉) · J. Trubač
Institute of Geology and Paleontology,
Faculty of Science, Charles University,
Albertov 6, 12843 Prague, Czech Republic
e-mail: jirizak@natur.cuni.cz

P. Týcová
Czech Geological Survey, Geologická 6,
15500 Praha, Czech Republic

Journal of Geosciences, 55 (2010), 279–297 DOI: 10.3190/jgeosci.076

Original paper

Crystallization history of Oligocene ijolitic rocks from the Doupovské hory Volcanic Complex (Czech Republic)

Jakub HALODA[1*], Vladislav RAPPRICH[1], František V. HOLUB[2], Patricie HALODOVÁ[1], Tomáš VACULOVIČ[3]

[1] *Czech Geological Survey, Klárov 3, 118 21 Prague 1, Czech Republic; jakub.haloda@geology.cz*
[2] *Institute of Petrology and Structural Geology, Faculty of Science, Charles University, Albertov 6, 128 43 Prague 2, Czech Republic*
[3] *Institute of Chemistry, Faculty of Science, Masaryk University, Kotlářská 2, 611 37 Brno, Czech Republic*
[*] *Corresponding author*

Ijolitic rocks of the Flurbühl Composite Intrusion rank to the most primitive intrusive rocks found within the Doupovské hory Volcanic Complex. Studies of mineral chemistry together with crystallization modelling of melteigite and ijolite brought new information about the evolution of ijolitic magmas and their ascent. Crystallization modelling affirms the absence of accumulated minerals and confirms that the recalculated major-element bulk-rock analyses reflect the compositions of their original parental magmas accurately. Melteigite developed by early equilibrium crystallization under pressure of approximately 4 kbar (estimated minimum cooling rate is ~0.02 °C/hr) and subsequent fractional crystallization under much lower pressure (~0.2 kbar). Ijolite originated by fractional crystallization of a slightly more evolved magma batch under lower pressures probably at the final emplacement level. The results of crystallization modelling and estimates of REE contents in parental melts suggest a close genetic relationship between both rock suites. The olivine-bearing melteigite was postulated as a possible parental magma composition for derivation of the olivine-free ijolite.

Keywords: Nephelinolite, melteigite, ijolite, crystallization modelling, fractional crystallization, Doupovské hory Mts.
Received: 16 April 2010; accepted: 19 September 2010; handling editor: D. Dolejš

1. Introduction

High-level intrusions are rather common in mafic alkaline volcanic complexes. However, they are mostly hidden and even where they crop out thanks to advanced erosion of the volcanic edifices, their original features are frequently obscured by alteration processes. Therefore, detailed research and models of magmatic evolution in such intrusions are rather scarce.

We have investigated intrusive rocks from the central part of the Doupovské hory Volcanic Complex (the Flurbühl Composite Intrusion) that provide the possibility to study the sub-surface magmatic processes related to formation and evolution of the still preserved superficial volcanic complex. The petrology and bulk-rock chemistry of the entire subvolcanic suite with two observed differentiation trends is described by Holub et al. (this volume). From the whole association of alkaline rocks we selected for detailed examination of mineral chemistry and crystallization history the very fresh ijolitic rocks with nearly anhydrous mineral assemblages.

The major aims of this contribution are to unravel the crystallization history of these intrusive rocks rich in mafic minerals, to evaluate a possible role of mafic mineral accumulation in the genesis of the melteigite, and to decipher its relationship to ijolites with lower abundances of the mafic phases.

2. Geological setting

The Doupovské hory Volcanic Complex (DHVC) occupies the western part of the northeast-southwest-trending Eger (Ohře) Graben (EG) in northwestern Bohemia (Czech Republic; Fig. 1). The EG belongs to the system of Cenozoic rifts in central and western Europe (European Cenozoic Rift System *sensu* Dèzes et al. 2004 – ECRIS). The EG follows the older Variscan suture between the Saxothuringian and Teplá–Barrandian domains (Babuška et al. 2010; Mlčoch and Konopásek 2010) in the northwestern part of the Bohemian Massif. It is interpreted as an incipient rift structure formed during two distinct phases of extension (Rajchl et al. 2009). The first phase lasted from the late Eocene until the early Miocene. It was characterised by the NNE–SSW to N–S oriented horizontal extension, oblique to the rift axis. The palaeostress field of the oblique extension most probably reflected lithospheric doming due to thermal perturbation of the lithosphere (Dèzes et al. 2004), which resulted also in extensive OIB-like magmatism within the EG. The later, orthogonal extensional phase is explained by stretching along the crest of a growing regional-scale anticlinal feature, which supports the recent hypothesis of the lithospheric folding in the Alpine–Carpathian foreland (Dèzes et al. 2004; Bourgeois et al. 2007; Rajchl et al. 2009).

Tectonophysics 466 (2009) 47–63

Contents lists available at ScienceDirect

Tectonophysics

journal homepage: www.elsevier.com/locate/tecto

On the interpretation of normal and inverse magnetic fabric in dikes: Examples from the Eger Graben, NW Bohemian Massif

Martin Chadima [a,b,*], Vladimír Cajz [a,c], Patricie Týcová [d]

[a] Institute of Geology, Academy of Sciences of the Czech Republic, Rozvojová 269, CZ-16500 Prague, Czech Republic
[b] Agico, Inc., Ječná 29a, Box 90, CZ-62100 Brno, Czech Republic
[c] Faculty of Science, J. E. Purkyně University, České mládeže 8, CZ-40096 Ústí nad Labem, Czech Republic
[d] Czech Geological Survey, Geologická 6, CZ-15200 Prague, Czech Republic

ARTICLE INFO

Article history:
Received 3 March 2008
Received in revised form 24 July 2008
Accepted 7 September 2008
Available online 16 September 2008

Keywords:
Anisotropy of magnetic susceptibility
Anisotropy of magnetic remanence
Lattice preferred orientation
Sanidine
EBSD
Multi-function Kappabridge

ABSTRACT

Recent studies of igneous rocks indicate that the predominant occurrence of normal/inverse fabric in dikes may either reflect the presence of multi-domain (MD)/single-domain (SD) grains or it may result from different orientation mechanisms of magnetic minerals in magmas of different viscosities. The ambiguity in physical vs. geological cause of normal/inverse magnetic fabric must be answered before any successful geological interpretation of magnetic fabric can be made. In order to address this problem, we studied magnetic fabric of selected dikes associated with the SW–NE trending Eger Graben (NW Bohemian Massif). The studied area offered very extensive collection of rock types: basanite, bostonite, camptonite, tinguaite, and trachybasalt. Magnetic susceptibility varies according to rock type and reflects the relative contents of magnetic minerals. In most cases, titanomagnetite with variable Ti content was identified as main magnetic carrier. The degree of anisotropy is relatively low, in most cases less than 10%, the shape of anisotropy ellipsoid ranges from slightly prolate to neutral and oblate. Several different types of magnetic fabric (using anisotropy of low-field magnetic susceptibility, AMS) were observed in studied dikes: so-called normal and inverse magnetic fabrics and anomalous magnetic fabric. Comparing all studied sites it seems that the type of magnetic fabric is lithology-dependent. Normal magnetic fabric with magnetic foliations and subhorizontal magnetic lineations both parallel to the dike margins was found in bostonite and trachybasalt dikes. Inverse magnetic fabric with magnetic lineations and magnetic foliations perpendicular to the dike margins was found in camptonite dikes. Anisotropy of anhysteretic remanent magnetization (AMR) indicate that the observed inverse magnetic fabric may be caused by the presence of SD magnetic grains; AMR fabric being normal with respect to dike margins. In contrast to that no single-domain particles were revealed using frequency dependence and anhysteretic susceptibility measurements. The AMS measured in variable weak magnetic fields is field dependent for camptonite dike and field independent for other rock types, i.e. bostonite, basanite, tinguaite, and trachybasalt. For further flow direction and tectonic interpretations of magnetic fabric in dikes it is suggested to use preferably the AMR fabric (at least for dikes which demonstrate significant field dependence of AMS) as it reflects the 'true' rock fabric more accurately than AMS fabric.

1. Introduction

Rock magnetic techniques can significantly contribute to the studies of the evolution of volcanic regions. Paleomagnetism can provide a relative dating tool (e.g., Cox et al., 1963) or a means of documenting block rotations and tilts (e.g., Schreiber and Rotsch, 1998; Riley et al., 1999); magnetic anisotropy can be used as a magma flow-direction indicator (e.g., Knight and Waker, 1988). Assuming a direct relationship between rock fabric and magnetic fabric, magnetic anisotropy can be employed for assessment of rock fabric in igneous rocks where foliation and lineation is often difficult to observe and measure. Indeed, since the pioneer work of Khan (1962), the anisotropy of magnetic susceptibility (AMS) has become widely used method to infer the mineral fabric of dikes, lava flows and other tabular bodies of igneous rocks (review in Cañón-Tapia, 2004, and references therein) with important implications for volcanism (Knight and Waker, 1988; Porreca et al., 2006), or regional tectonics (Callot et al., 2001). Despite of its extensive use, the interpretation of the AMS in igneous rocks is not, in many cases, straightforward and may be complicated by several factors (e.g., Rochette et al., 1999).

In volcanic rocks, the magnetic anisotropy is caused by the preferred orientation of strongly magnetic grains, in most cases titanomagnetites. A simple model for a volcanic dike assumes the so-

* Corresponding author. Institute of Geology, Academy of Sciences of the Czech Republic, Rozvojová 269, CZ-16500 Prague, Czech Republic. Tel.: +420 511 116 302.
E-mail address: chadima@sci.muni.cz (M. Chadima).

0040-1951/$ – see front matter © 2008 Elsevier B.V. All rights reserved.
doi:10.1016/j.tecto.2008.09.005

Int J Earth Sci (Geol Rundsch) (2009) 98:517–532
DOI 10.1007/s00531-007-0285-9

ORIGINAL PAPER

Magmatic history and geophysical signature of a post-collisional intrusive center emplaced near a crustal-scale shear zone: the Plechý granite pluton (Moldanubian batholith, Bohemian Massif)

Kryštof Verner · Jiří Žák · Jaroslava Pertoldová · Josef Šrámek · Jiří Sedlák · Jakub Trubač · Patricie Týcová

Received: 21 May 2007 / Accepted: 10 November 2007 / Published online: 13 December 2007

Abstract The Plechý pluton, southwestern Bohemian Massif, represents a late-Variscan, complexly zoned intrusive center emplaced near the crustal-scale Pfahl shear zone; the pluton thus provides an opportunity to examine the interplay among successive emplacement of large magma batches, magmatic fabric acquisition, and the late-Variscan stress field associated with strike-slip shearing. The magmatic history of the pluton started with the emplacement of the porphyritic Plechý and Haidmühler granites. Based on gravity and structural data, we interpret that the Plechý and Haidmühler granites were emplaced as a deeply rooted, ~NE–SW elongated body; its gross shape and internal fabric (steep ~NE–SW magmatic foliation) may have been controlled by the late-Variscan stress field. The steep magmatic foliation changes into flat-lying foliation (particularly recorded by AMS) presumably as a result of divergent flow. Magnetic lineations correspond to a sub-horizontal ~NE–SW finite stretch associated with the divergent flow. Subsequently, the Třístoličník granite, characterized by steep margin-parallel magmatic foliation, was emplaced as a crescent-shaped body in the central part of the pluton. The otherwise inward-younging intrusive sequence was completed by the emplacement of the outermost and the most evolved garnet-bearing granite (the Marginal granite) along the southeastern margin of the pluton.

Keywords Anisotropy of magnetic susceptibility (AMS) · Bohemian Massif · Emplacement · Granite · Pluton

Electronic supplementary material The online version of this article (doi:10.1007/s00531-007-0285-9) contains supplementary material, which is available to authorized users.

K. Verner · J. Žák (✉) · J. Pertoldová
Czech Geological Survey, Klárov 3,
Prague 11821, Czech Republic
e-mail: jirizak@natur.cuni.cz

K. Verner
Institute of Petrology and Structural Geology,
Faculty of Science, Charles University, Albertov 6,
Prague 12843, Czech Republic

J. Žák · J. Trubač
Institute of Geology and Paleontology, Faculty of Science,
Charles University, Albertov 6, Prague 12843, Czech Republic

J. Šrámek
Czech Geological Survey, Ječná 29, Brno 62100,
Czech Republic

J. Sedlák
Miligal Ltd, Axmanova 531, Brno 62300, Czech Republic

P. Týcová
Czech Geological Survey, Geologická 6,
Prague 15500, Czech Republic

Introduction

In the Bohemian Massif (Central European Variscides), formed by accretion of several Gondwana-derived microplates to the Old Red (Laurussia) Continent during the Devonian to Carboniferous (Pharaoh 1999; Winchester 2002 and references therein), the entire Variscan orogenic history was accompanied by episodic magmatic activity which reveals the following general relations between granitoid petrogenesis and the geodynamic setting (see Finger et al. 1997 and Schaltegger 1997 for reviews). (1) The syn-collisional Late Devonian–Early Carboniferous (~370–340 Ma) crustal thickening broadly overlaps with the emplacement of metaluminous, calc-alkaline and high-K, I-type plutons. (2) Rapid exhumation of the lower- to

Journal of Structural Geology 31 (2009) 1295–1307

Contents lists available at ScienceDirect

Journal of Structural Geology

journal homepage: www.elsevier.com/locate/jsg

The mechanism of flow and fabric development in mechanically anisotropic trachyte lava

Prokop Závada [a,*], Karel Schulmann [b], Ondrej Lexa [c], František Hrouda [d], Jakub Haloda [e], Patricie Týcová [e]

[a] Department of Tectonics and Geodynamics, Institute of Geophysics AS CR, v.v.i., Boční II/1401, 141 31 Prague 4, Czech Republic
[b] Centre de Géochimie de la Surface, EOST, Université Louis Pasteur, Strasbourg Cedex, France
[c] Institute of Petrology and Structural Geology, Charles University, Prague, Czech Republic
[d] Agico Inc., Brno, Czech Republic
[e] Czech Geological Survey, Klárov 3, Prague, Czech Republic

ARTICLE INFO

Article history:
Received 18 August 2008
Received in revised form
23 March 2009
Accepted 12 April 2009
Available online 18 April 2009

Keywords:
Trachyte
Lava dome
Fibre-slip mechanism
Mechanical anisotropy
Sanidine
Anisotropy of magnetic susceptibility

ABSTRACT

Anisotropy of magnetic susceptibility (AMS) and Electron back-scattered diffraction (EBSD) of magnetite and sanidine fabrics throughout an eroded trachyte lava dome in Tertiary volcanic province of the NW Czech Republic revealed two fabric types. The high degree of AMS fabric is associated with sanidine textural domains similar to normal kink bands (Type I fabric) and occupies the whole body except the SW margin. Folded fabric and low anisotropy of AMS also in the SW margin reveals sanidine alignment domains resembling reverse kink-bands (Type II fabric). The flow of trachyte lava occurred via simultaneous slip of sanidine crystals along their (010) planes and also by readjustment of the textural domain boundaries according to the fibre-slip theory. This microfabric study suggests that the Type II fabrics resulted from collapse of vertically anisotropic trachyte crystal mush above the feeding conduit. Type I fabric is interpreted to originate from Type II fabrics by further stretching of highly attenuated fold limbs. Asymmetric Type I fabrics along margins of the dome are related to outflow of trachyte lava away from the conduit region due to divergent flow. The trachyte fabric zonality is interpreted to reflect the process of successive emplacement of progressively rotated trachyte lava lobes within a lava dome that locally preserves the collapsed and folded vertical fabrics.

1. Introduction

The investigation of fabrics generated by lava flows requires structural, microstructural and quantitative fabric analyses (Smith, 2002). However, the small size of fabric elements makes microstructural studies difficult, so that analysis of anisotropy of magnetic susceptibility (AMS) is often employed (for review see Tarling and Hrouda, 1993).

Studies regarding fabrics in lavas focused mainly on basalts forming dykes or lava flows (Kolofíková, 1976; Raposo and Ernesto, 1995; Herrero-Bervera et al., 2001), or small aspect-ratio (height to width) rhyolitic domes (Fink, 1983; Smith and Houston, 1995; Merle, 1998; Buisson and Merle, 2002, 2004; Castro et al., 2002; Cañón Tapia and Castro, 2004; Maeno and Taniguchi, 2006). In contrast, systematic investigations of flow fabrics in crystal-rich volcanic extrusions that form large aspect-ratio domes or laccoliths are less common. Growth of these domes is typically by successive emplacement of "lobes" or "spines" of lava, which emerge and are transported sideways by newer lava lobes (Nakada et al., 1995; Melnik and Sparks, 1999; Sparks et al., 2000).

The internal fabric patterns of solidified phonolite or trachyte cupola-like bodies, which show high crystal content, were previously examined by the methods of structural analysis of macroscopic fluidality and jointing, X-ray diffraction and universal-stage (Cloos and Cloos, 1927; Varet, 1971; Jančušková et al., 1992). Introduction of the AMS technique allowed even more complex microstructural investigation of these cupolas (Arbaret et al., 1993). Utilisation of electron back-scattered diffraction (EBSD) and quantitative image analysis methods together with AMS can overcome the issues related to small grain size of fabric elements. The deformation/flow mechanism deciphered from trachyte fabrics using these methods is the focus of this paper.

In this study, a partly exposed trachyte body in the České středohoří Mountains is examined to determine the mechanisms of

* Corresponding author. Tel.: +420 267 103 074; fax: +420 272 761 549.
E-mail address: zavada@ig.cas.cz (P. Závada).

0191-8141/$ – see front matter © 2009 Elsevier Ltd. All rights reserved.
doi:10.1016/j.jsg.2009.04.002

Original paper

Metamorphic history of skarns, origin of their protolith and implications for genetic interpretation; an example from three units of the Bohemian Massif

Jaroslava PERTOLDOVÁ[1*], Patricie TÝCOVÁ[1], Kryštof VERNER[1], Monika KOŠULIČOVÁ[1], Zdeněk PERTOLD[2], Jan KOŠLER[3], Jiří KONOPÁSEK[1], Marta PUDILOVÁ[2]

[1] *Czech Geological Survey, Klárov 3, 118 21 Prague 1, Czech Republic;* jaroslava.pertoldova@geology.cz
[2] *Institute of Geochemistry, Mineralogy and Mineral Resources, Charles University, Albertov 6, Prague 2, 128 43, Czech Republic*
[3] *Centre for Geobiology and Department of Earth Science, University of Bergen, Allegaten 41, N-5007 Bergen, Norway*
[*] *Corresponding author*

Skarns in the Svratka Unit, in the neighbouring part of the Moldanubian Zone and in the Kutná Hora Complex were studied with respect to their metamorphic evolution, major- and trace-element geochemistry, oxygen isotopic composition and zircon ages. Skarns form competent lenses and layers in metamorphosed siliciclastic rocks and preserve some early deformation structures and several equilibrium assemblages representing the products of successive metamorphic reactions. The main rock-forming minerals, garnet and clinopyroxene, are accompanied by less abundant magnetite, amphibole, plagioclase, epidote ± quartz. In the **Svratka Unit** the early prograde M_1, prograde/peak M_2, and retrograde M_3 metamorphic stages have been distinguished. Metamorphic conditions in skarns of the **Moldanubian Zone** are limited to a relatively narrow interval of amphibolite facies. The prograde and retrograde events in the **Kutná Hora Complex** skarns probably took place under amphibolite-facies conditions. The presence of magnetite and the increasing proportion of the andradite component in the garnet indicate locally increased oxygen fugacity.

Skarn geochemistry does not show systematic differences in the skarn composition among the three units. The regional variations are exceeded by differences among samples from individual localities. The Al_2O_3/TiO_2, Al_2O_3/Zr, TiO_2/Nb ratios point to the variable proportion of the detrital material, combined in skarn protoliths with CaO and FeO, the major non-detrital components. The skarns exhibit elevated abundances of Cu, Zn, Sn and As. The Eu/Eu* ratio varies in the range of 0.5–8.6, the total REE contents vary from 8 to 345 ppm. The lowest ΣREE values (< 100 ppm) occur in skarns with magnetite mineralization. The wide intervals of ΣREE and Eu/Eu* values are interpreted to indicate variations in the temperature and redox conditions among layers of the same locality and at various localities.

The oxygen isotope compositions of garnets, pyroxenes and amphiboles from skarns of the Svratka Unit exhibit a range of $\delta^{18}O$ = 0.1 to 4.1 ‰. *In situ* (laser-ablation ICP-MS) U-Pb dating of zircon from one of the Svratka Unit skarn bodies yielded a wide range of ages (0.5–2.6 Ga), supporting the detrital origin of this zircon population.

The skarn protoliths were probably rocks of mixed detrital-exhalative origin deposited on the sea floor.

The geological position of skarns, with their structural and metamorphic record, probably reflect tectono-metamorphic evolution shared with that of their host rocks. The geochemical characteristics, including oxygen isotopic compositions and the presence of detrital zircons with a wide range of ages exclude metasomatic, and point to a sedimentary-exhalative mode of origin for the studied skarns.

Keywords: skarn, Bohemian Massif, petrology, geochemistry, oxygen isotopes, detrital zircon age
Received: 1 April 2009; accepted 11 June 2009; handling editor: W. S. Faryad
The online version of this article (http://dx.doi.org/10.3190/jgeosci.044) contains supplementary electronic material.

1. Introduction

Detailed modern contributions dealing with the nature and genesis of skarns were published by many geologists during the past few decades from different geological environments all over the world, for instance Jamtveit et al. (1993), Nicolescu et al. (1998), Meinert et al. (2003) or Gaspar et al. (2008).

The review of world skarn deposits has been presented by Einaudi et al. (1981), Burt (1982), Meinert (1998) and Meinert et al. (2005). These publications and reviews are devoted to skarns with mostly contact metamorphic and metasomatic history accompanied by igneous-related hydrothermal input. Several authors have studied the mineralogy/petrology and genetic aspects of various skarn bodies in the Bohemian Massif, partly with emphasis on the pre-metamorphic history and open- *vs.* closed-system conditions of formation.

Formation under the open-system conditions implies a metasomatic mode of formation (i.e., metasomatism

J. metamorphic Geol., 2008, **26,** 29–53 doi:10.1111/j.1525-1314.2007.00743.x

Origin of migmatites by deformation-enhanced melt infiltration of orthogneiss: a new model based on quantitative microstructural analysis

P. HASALOVÁ,[1,2] K. SCHULMANN,[1] O. LEXA,[1,2] P. ŠTÍPSKÁ,[1] F. HROUDA,[2,3] S. ULRICH,[2,4] J. HALODA[5] AND P. TÝCOVÁ[5]
[1]*Université Louis Pasteur, CGS/EOST, UMR 7517, 1 rue Blessig, Strasbourg 67084, France (hasalovap@seznam.cz)*
[2]*Institute of Petrology and Structural Geology, Charles University, Albertov 6, 12843 Prague, Czech Republic*
[3]*AGICO, Ječná 29a, 621 00 Brno, Czech Republic*
[4]*Institute of Geophysics, Czech Academy of Sciences, Boční II/1401, 14131 Praha 4, Czech Republic*
[5]*Czech Geological Survey, Klárov 3, 118 21 Prague 1, Czech Republic*

ABSTRACT A detailed field study reveals a gradual transition from high-grade solid-state banded orthogneiss via stromatic migmatite and schlieren migmatite to irregular, foliation-parallel bodies of nebulitic migmatite within the eastern part of the Gföhl Unit (Moldanubian domain, Bohemian Massif). The orthogneiss to nebulitic migmatite sequence is characterized by progressive destruction of well-equilibrated banded microstructure by crystallization of new interstitial phases (Kfs, Pl and Qtz) along feldspar boundaries and by resorption of relict feldspar and biotite. The grain size of all felsic phases decreases continuously, whereas the population density of new phases increases. The new phases preferentially nucleate along high-energy like–like boundaries causing the development of a regular distribution of individual phases. This evolutionary trend is accompanied by a decrease in grain shape preferred orientation of all felsic phases. To explain these data, a new petrogenetic model is proposed for the origin of felsic migmatites by melt infiltration from an external source into banded orthogneiss during deformation. In this model, infiltrating melt passes pervasively along grain boundaries through the whole-rock volume and changes completely its macro- and microscopic appearance. It is suggested that the individual migmatite types represent different degrees of equilibration between the host rock and migrating melt during exhumation. The melt topology mimicked by feldspar in banded orthogneiss forms elongate pockets oriented at a high angle to the compositional banding, indicating that the melt distribution was controlled by the deformation of the solid framework. The microstructure exhibits features compatible with a combination of dislocation creep and grain boundary sliding deformation mechanisms. The migmatite microstructures developed by granular flow accompanied by melt-enhanced diffusion and/or melt flow. However, an AMS study and quartz microfabrics suggest that the amount of melt present did not exceed a critical threshold during the deformation to allow free movements of grains.

Key words: crystal size distribution; melt infiltration; melt topology; migmatites; quantitative textural analysis.

INTRODUCTION

Movement of a large volume of granitic melt is an important factor in the compositional differentiation of the continental crust (Fyfe, 1973; Collins & Sawyer, 1996; Brown & Rushmer, 2006) and the presence of melt in rocks profoundly influences their rheology (Arzi, 1978). The migration of melt through the crust is controlled by melt buoyancy and pressure gradients resulting from the combination of gravity forces and deformation (Wickham, 1987; Sawyer, 1994). There are three major mechanisms controlling melt migration through the continental crust: (i) diapirism resulting in upward motion of low-density magma through higher density rocks (Chandrasekhar, 1961; Ramberg, 1981); (ii) dyking that describes melt migration by hydrofracturing of the host rock and transport of melt through narrow dykes (Lister & Kerr, 1991; Petford, 1995); (iii) and migration of a melt through a network of interconnected pores during deformation or compaction of solid matrix (McKenzie, 1984; Wickham, 1987).

Brown & Solar (1998a) and Weinberg & Searle (1998) proposed that during active deformation melt moves by pervasive flow and it is essentially pumped through the system parallel to the principal finite elongation in the form of foliation-parallel veins. Based on a number of field studies, pervasive melt migration at outcrop scale controlled by regional deformation has been suggested by various authors (Collins & Sawyer, 1996; Brown & Solar, 1998b; Vanderhaeghe, 1999; Marchildon & Brown, 2003).

Lithos 106 (2008) 309–322

Contents lists available at ScienceDirect

Lithos

journal homepage: www.elsevier.com/locate/lithos

Grain-scale processes in actively deforming magma mushes: New insights from electron backscatter diffraction (EBSD) analysis of biotite schlieren in the Jizera granite, Bohemian Massif

Jiří Žák [a,b,*], Kryštof Verner [b,c], Patricie Týcová [d]

[a] Institute of Geology and Paleontology, Faculty of Science, Charles University, Albertov 6, Prague, 12843, Czech Republic
[b] Czech Geological Survey, Klárov 3, Prague, 11821, Czech Republic
[c] Institute of Petrology and Structural Geology, Faculty of Science, Charles University, Albertov 6, Prague, 12843, Czech Republic
[d] Czech Geological Survey, Geologická 6, Prague, 15200, Czech Republic

ARTICLE INFO

Article history:
Received 2 April 2008
Accepted 19 August 2008
Available online 5 September 2008

Keywords:
Electron backscatter diffraction (EBSD)
Granite
Magnetic susceptibility anisotropy
Pluton
Schlieren

ABSTRACT

In the porphyritic Jizera granite, Bohemian Massif, three distinct types of lattice-preferred orientations of biotite grains were revealed in schlieren-delineated magmatic structures using the electron backscatter diffraction (EBSD) method. (1) Biotite basal planes (001) reorient from schlieren-subparallel near the schlieren base to schlieren-perpendicular in the upper part of the schlieren. Both orientations share subhorizontal ~N–S to ~NNE–SSW-trending *a* axes. (2) In some domains, the *a* axes are steep and at a high angle to the schlieren plane while the *c* axes plunge shallowly and rotate around an ill-defined *a* axis. (3) In other domains, the EBSD coincides with background magnetic fabric of the host granite revealed using the anisotropy of magnetic susceptibility (AMS) method: that is, the *a* axes plunge shallowly to the SE or NW while the *c* axes are subhorizontal and cluster around the ~NE–SW trend.

These multiple biotite orientations in the schlieren are interpreted to reflect (1) velocity-gradient in laminar magma flow along channel-like conduits, localized within the high-strength host phenocryst framework, (2) grain-scale gravity-driven constrictional deformation of the magma mush, and (3) overprinting background (tectonic?) deformation transmitted across large parts of the magma chamber prior to its final crystallization. The grain-scale mechanisms of biotite fabric acquisition in the schlieren presumably involved rotation of biotite crystals during flow, with the biotite alignment reflecting the flow geometry and kinematics, replaced after flow cessation by melt-aided grain-boundary sliding of those biotite crystals still enclosed in melt pockets within otherwise static, highly crystallized magma mush. The latter process was sufficient to reorient biotite grains but not to cause destruction of the schlieren.

Using the Jizera granite as a case example, we argue that the lattice-preferred orientation of mineral grains in mafic schlieren is highly sensitive to reorient in response to processes both associated with the schlieren formation (e.g., localized magma flow) and those that occur later and are superimposed onto the effectively solid, high-strength magma mush.

1. Introduction

Mafic schlieren are variously-shaped modal concentrations of mafic minerals that occur as small-scale structures in granitoid plutons and diatexites. In many cases, schlieren have one sharp contact against the host rock while the other margin is gradational (e.g., Weinberg et al., 2001; Milord and Sawyer, 2003). Despite their negligible size with respect to the host plutons, schlieren are important markers of the rheological state of the magma and of a wide variety of physical processes in magma chambers, such as convection, magma flow, or gravitational differentiation (e.g., Cloos, 1925; Barriére, 1981; Clarke and Clarke, 1998; Weinberg et al., 2001; Milord and Sawyer, 2003; Pons et al., 2006; Wiebe et al., 2007; Barbey et al., 2008).

Unlike most studies, which have dealt with mafic schlieren in terms of their field relationships, overall geometry, or chemical composition, we focus here on their internal fabric, i.e., the preferred orientation of mafic minerals inside the schlieren. In an attempt to understand the grain-scale processes and hypersolidus finite strain recorded by schlieren, the electron backscatter diffraction (EBSD) method was employed to analyze the lattice-preferred orientation of biotite in variously-shaped schlieren in the porphyritic Jizera granite of the Krkonoše–Jizera Plutonic Complex, Bohemian Massif. This granite is unusual in that it hosts some complex schlieren-bounded

* Corresponding author. Institute of Geology and Paleontology, Faculty of Science, Charles University, Albertov 6, Prague, 12843, Czech Republic.
E-mail address: jirizak@natur.cuni.cz (J. Žák).

0024-4937/$ – see front matter © 2008 Elsevier B.V. All rights reserved.
doi:10.1016/j.lithos.2008.08.006

Geol. Mag. **145** (*4*), *2008, pp. 537–551. © 2008 Cambridge University Press*
doi:10.1017/S0016756808004573 *Printed in the United Kingdom*

Multiple magmatic fabrics in plutons: an overlooked tool for exploring interactions between magmatic processes and regional deformation?

JIŘÍ ŽÁK*†, KRYŠTOF VERNER†‡ & PATRICIE TÝCOVÁ§

*Institute of Geology and Paleontology, Faculty of Science, Charles University, Albertov 6, Prague, 12843, Czech Republic
†Czech Geological Survey, Klárov 3, Prague, 11821, Czech Republic
‡Institute of Petrology and Structural Geology, Faculty of Science, Charles University, Albertov 6, Prague, 12843, Czech Republic
§Czech Geological Survey, Geologická 6, Prague, 152 00, Czech Republic

(*Received* 17 April 2007; *accepted* 25 July 2007; First published online 11 April 2008)

Abstract – This paper elaborates on the concept of multiple magmatic fabrics in plutons. After a general overview of various types of multiple fabrics that may develop in magmatic rocks, two case examples of porphyritic granite and melasyenite plutons in the Bohemian Massif are examined. In the Jizera granite, complex variations in K-feldspar phenocryst shape-fabric revealed by image analysis of a 200 m long section of an underground tunnel are in contrast with homogeneously oriented magnetic (AMS) fabric carried by coaxial contributions of biotite, magnetite and maghemite. In the Knížecí Stolec melasyenite pluton, emplacement-related margin-parallel feldspar foliation was overprinted by flat-lying foliation; the latter is interpreted to record regional tectonic strain. At the two stations examined in detail, the crystallographic-preferred orientation of biotite and amphibole in the inter-phenocryst matrix (measured using electron back-scatter diffraction – EBSD) differed from both feldspar fabric and also from the AMS principal directions. Multiple magmatic fabrics in these two plutons are interpreted in terms of fabric superposition, where late weak strain is superposed onto a high-strength phenocryst framework, but is accommodated preferentially by small mineral grains (biotite, magnetite) in the melt-bearing matrix. This mechanism may explain the discrepancy between mesoscopic feldspar fabric and AMS. We conclude that multiple magmatic fabrics in plutons may thus result from accumulated strain caused by different processes during final crystallization and, as such, may serve as a sensitive indicator of the evolving interactions between magmatic and tectonic processes in the Earth's crust.

Keywords: deformation, fabric, granite, magnetic susceptibility anisotropy, pluton.

1. Introduction

Since the innovative and seminal work of Hans Cloos (Cloos, 1925), magmatic fabrics in plutons, that is, shape-preferred orientations of magmatic minerals acquired in melt-present conditions (Paterson, Vernon & Tobisch, 1989; Paterson *et al.* 1998; Vernon, 2000), have been extensively employed to infer a wide range of magmatic and tectonic processes in the Earth's crust (see Paterson *et al.* 1998 for review). For instance, fabric patterns and structural relations around plutons in conjunction with radiometric ages may provide rigorous, and in many cases the only available, constraints on dating regional tectonic deformation and plate kinematics in magmatic arcs and orogenic belts (e.g. Gleizes *et al.* 1998; Paterson *et al.* 1998; Benn *et al.* 2001; Archanjo *et al.* 2002; Callahan & Markley, 2003).

A vast majority of fabric studies have documented a single magmatic fabric in a single pluton and, logically, have inferred a single fabric-forming process. The fabric formation thus has been traditionally thought to result either from internal magmatic processes or regional tectonics, depending on the temporal evolution of mechanical coupling of the pluton/host rock system (Paterson *et al.* 1998; Barros, Barbey & Boullier, 2001). This approach has also been adopted in numerous anisotropy of magnetic susceptibility (AMS) studies of granitoid plutons, as the AMS provides a fast and efficient method for analysis and quantification of magnetic fabric controlled by the orientation of ferromagnetic and paramagnetic minerals (for reviews and principles of the AMS method see, e.g. Hrouda, 1982; Jackson & Tauxe, 1991; Rochette, Jackson & Aubourg, 1992; Tarling & Hrouda, 1993; Borradaile & Henry, 1997; Bouchez, 1997; Borradaile, 2003, pp. 297–326).

These seemingly straightforward views on the significance of magmatic (macroscopic) fabric and magnetic fabric (revealed using AMS) have been somewhat complicated by the recent discovery of multiple fabrics

*Author for correspondence: jirizak@natur.cuni.cz

Meteoritics & Planetary Science 38, Nr 7, 1005–1021 (2003)
Abstract available online at http://meteoritics.org

The Morávka meteorite fall: 3. Meteoroid initial size, history, structure, and composition

J. BOROVIČKA,[1*] H. W. WEBER,[2] T. JOPEK,[3] P. JAKEŠ,[4] Z. RANDA,[5] P. G. BROWN,[6] D. O. REVELLE,[7] P. KALENDA,[8] L. SCHULTZ,[2] J. KUCERA,[5] J. HALODA,[4] P. TÝCOVÁ,[4] J. FRÝDA,[9] and F. BRANDSTÄTTER[10]

[1]Astronomical Institute of the Academy of Sciences, 25165 Ondrejov, The Czech Republic
[2]Max-Plank-Institut für Chemie, Joh. J.-Becher-Weg 27, D–55128 Mainz, Germany
[3]Astronomical Observatory of A.Mickiewicz University, Sloneczna 36, 60286 Poznan, Poland
[4]Institute of Geochemistry, Mineralogy and Mineral Resources, Faculty of Science, Charles University, Albertov 6, 12843 Prague 2, The Czech Republic
[5]Nuclear Physics Institute, Academy of Sciences, 25068 Rez near Prague, The Czech Republic
[6]Department of Physics and Astronomy, University of Western Ontario, London, Ontario N6A 3K7, Canada
[7]Los Alamos National Laboratory, P. O. Box 1663, MS J557, Los Alamos, New Mexico 87545, USA
[8]CoalExp, Kosmonautu 2, 70030 Ostrava 3, The Czech Republic
[9]Czech Geological Survey, Geologická 6, 15200 Prague 5, The Czech Republic
[10]Department of Mineralogy and Petrography, Museum of Natural History, Burgring 7, A–1010 Vienna, Austria
[*]Corresponding author. E-mail: borovic@asu.cas.cz

(Received 06 September 2002; revision accepted 25 June 2003)

Abstract–The properties and history of the parent meteoroid of the Morávka H5–6 ordinary chondrites have been studied by a combination of various methods. The pre-atmospheric mass of the meteoroid was computed from fireball radiation, infrasound, seismic signal, and the content of noble gases in the meteorites. All methods gave consistent results. The best estimate of the pre-atmospheric mass is 1500 ± 500 kg. The fireball integral bolometric luminous efficiency was 9%, and the acoustic efficiency was 0.14%. The meteoroid cosmic ray exposure age was determined to be $(6.7 \pm 1.0) \times 10^6$ yr. The meteorite shows a clear deficit of helium, both ^{3}He and ^{4}He. This deficit can be explained by solar heating. Numerical backward integration of the meteoroid orbit (determined in a previous paper from video records of the fireball) shows that the perihelion distance was probably lower than 0.5 AU and possibly as low as 0.1 AU 5 Ma ago. The collision which excavated Morávka probably occurred while the parent body was on a near-Earth orbit, as opposed to being confined entirely to the main asteroid belt. An overview of meteorite macroscopic properties, petrology, mineralogy, and chemical composition is given. The meteorites show all mineralogical features of H chondrites. The shock level is S2. Minor deviations from other H chondrites in abundances of trace elements La, Ce, Cs, and Rb were found. The ablation crust is enriched with siderophile elements.

INTRODUCTION

The fall of the Morávka H5–6 ordinary chondrites in the Czech Republic on May 6, 2000 became one of the best documented meteorite falls in history. The corresponding fireball was videotaped by 3 casual witnesses and sonic booms were recorded by 16 seismic stations in the Czech Republic and Poland and by 1 infrasonic station in Germany. Satellites in Earth orbit detected part of the fireball light curve. Six meteorites with a total mass of 1.4 kg have been recovered up to May 2003. Borovička et al. (2003) gave an overview of the events associated with the fall, determined the fireball trajectory and orbit from the video records, and presented the satellite observed light curve. Brown et al. (2003) described and interpreted in detail the infrasonic and seismic data.

In this paper, we concentrate on the pre-atmospheric properties and history of the meteoroid. Various methods, which are usually used separately, are employed to determine the meteoroid initial mass. Cosmic ray exposure age and gas retention age are then determined from the concentration of noble gases in the meteorites, and a helium deficit is revealed.

CHARLES UNIVERSITY IN PRAGUE

FACULTY OF SCIENCE

ELEMENTAL AND ISOTOPIC STUDY OF DIFFERENTIATED METEORITES AND IMPLICATIONS FOR THE ORIGIN AND EVOLUTION OF THEIR PARENT BODIES

Dissertation thesis

Supplementary material

Conference abstracts presented during my PhD study:

Haloda J., **Týcová P**., Thöni M., and Jelenc M. (2009) The petrogenesis and chronology of lunar meteorite Northeast Africa 003-A: Sm-Nd and Rb-Sr isotopic studies (abstract). In Lunar and Planetary Science XL, abstract no. 1247, 40th Lunar and Planetary Science Conference, Houston.

Haloda, J., Gabzdyl, P., **Týcová, P**., Fernandes, V.A. (2007): Lunar meteorite Northeast Africa 003-A: Microstructures, crystallization modeling and possible lunar source areas. In -: Lunar and Planetary Science XXXVIII, s. 1768-1769. Lunar and Planetary Institute. Houston.

Haloda, J., **Týcová, P**., Jakes, P. (2006): Lunar meteorite Northeast Africa 003-B: A new lunar mare basaltic breccia. Lunar and Planetary Science - Contributions, s. 2311. LPI. USA.

Haloda, J., Korotev, R., **Týcová, P.** (2006): Lunar meteorite Northeast Africa 003-A: A new lunar mare basalt. Lunar and Planetary Science - Contributions, s. 2269. LPI. USA.

Týcová P. and Košler J. (2006) Laser ablation MC ICP-MS analyses of Fe isotopes in iron meteorites. ICP Information Newsletter, vol. 31, p. 317-318.

Košler, J. , **Týcová, P.** (2006): Fe isotopic fractionation in iron meteorites - A potential thermometer?. Geochimica et Cosmochimica Acta, 70 (18): Suppl. S, s. A331. Elsevier. Oxford. ISBN 0016-7037.

Haloda J., Irving A. J., and **Týcová P.** (2005) Lunar meteorite Northeast Africa 001: An anorthositic regolith breccia with mixed highland/mare components (abstract). In Lunar and Planetary Science XXXVI, no. 1487, Lunar and Planetary Institute, Houston.

Týcová P. and Košler J. (2005) Fe isotopic variations in iron meteorites and implications for parent-body thermal histories. International Assoc. of Geochemistry, AIG6 Abstract, 243-244.

Košler J. and **Týcová P.** (2005) In-situ analysis of Fe isotopes by laser ablation multicollector ICP-MS: Limits and applications. International Assoc. of Geochemistry, AIG6 Abstract, 124-125.

THE PETROGENESIS AND CHRONOLOGY OF LUNAR METEORITE NORTHEAST AFRICA 003-A: Sm-Nd AND Rb-Sr ISOTOPIC STUDIES. Jakub Haloda[1,2], Patricie Tycova[1,2], Martin Thöni[3] and Monika Jelenc[3], [1]Institute of Geochemistry, Charles University, 128 43 Prague 2, Czech Republic, [2]Czech Geological Survey, Barrandov, 150 00 Prague 5, Czech Republic (jakub.haloda@geology.cz; patricie.tycova@geology.cz), [3]Department of Litosphere Research, University of Vienna, Vienna, A-1090, Austria (martin.thoeni@univie.ac.at; monika.jelenc@univie.ac.at).

Introduction: NEA 003-A is a lunar mare basalt, previously described by [1,2]. The younger ages 2.315 ± 0.04 Ga and 1.762 ± 0.054 Ga, which were obtained by Ar-Ar dating [3], are discordant to our Sm-Nd age, suggesting the resetting of K-Ar system during single or multiple impact event(s). Here we present the Sm-Nd and Rb-Sr data in order to address the problem of meteorite origin and age of crystallization.

Sample preparation: Five mineral separates were prepared for Sm-Nd isotopic measurements - the pure plagioclase (Pl) fraction, clinopyroxene fraction (Cpx), impure fractions of plagioclase (Pl-impure), pyroxene (Cpx-impure), containing olivine and some maskelynite intergrowths, and Fe-rich clinopyroxene (Cpx-Fe-rich). The duplicate mineral separates for Rb-Sr inculed fractions Pl, Pl impure, Cpx, and Cpx impure. Before dissolution the handpicked mineral fractions were rinsed repeatedly in acetone and deionised water in an ultrasonic bath. Sample splits for Sm-Nd analysis were washed for 30 minutes in warm (~70 °C) 0.8 N HCl to eliminate dust and surface contamination (terrestrial weathering and fluid infiltration, e.g. calcite). Splits for Rb-Sr analysis were washed for 20 min at room temperature, using 0.24 N HCl.

Neodymium and Sm were separated from the REE fraction in a Teflon-coated HdEHP column, and 0.18 N and 0.4 N HCl, respectively, as elution media. Maximum total procedural blanks were < 50 pg for Sm and Nd, and thus taken as negligible. Samples for Rb-Sr analysis were spiked directly and subsequently dissolved in ultrapure HF-HNO_3 (4:1 v/v). Elemental separation followed conventional techniques, using Bio-Rad AG® 50W-X8 (200-400 mesh) resin and 2.5 N and 1.0 N HCl as eluants.

Measurements of Nd and Sr isotope compositions and ID fractions were run in static mode on a ThermoFinnigan® Triton TIMS instrument at the University of Vienna, Austria.

Sm-Nd results: The Sm-Nd analytical data are plotted in an isochron diagrams in Figure 1, which shows that four out of five data points (Cpx, Cpx impure, Pl impure, Pl) plot on a linear array (solid line). If pooled together in one single regression calculation the age obtained is t = 3.089±0.064 Ga, with $(^{143}Nd/^{144}Nd)_i$ = 0.508610±0.000095 and $\varepsilon_{Nd3.089}$ = -0.4±0.3 (MSWD = 1.01). Interestingly, Cpx Fe-rich plots clearly off the 3.1 Ga "mean" trend line. If Cpx Fe-rich fraction is regressed with the Cpx and Cpx impure fractions (dashed line), it defines an age of 3.31±0.14 Ga and an initial $^{143}Nd/^{144}Nd$ of 0.50817±0.00025, corresponding to a significantly more negative $\varepsilon_{Nd3.31}$ of -3.3±0.7; MSWD = 1.6.

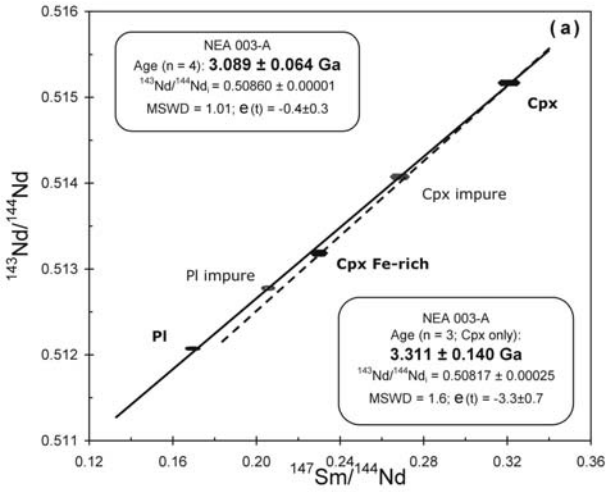

Fig. 1.: Sm-Nd isotopic data for mineral fractions of NEA 003-A shown as an isochron diagram.

Rb-Sr results: The Rb-Sr analytical data are plotted as an isochron diagram, Fig. 2. The measured $^{87}Sr/^{86}Sr$ ratios for Pl fractions are very low, ranging from 0.6999 (for Pl) to 0.7007 (for Pl impure 2). In the isochron plot, however, the data points show extreme scatter, and no obvious correlation between Sr isotope composition and Rb/Sr is observed. This prevents any reliable age information to be drawn from this data set. It is evident that high $^{87}Sr/^{86}Sr$ ratios and low $^{87}Rb/^{86}Sr$ ratios, mainly for clinopyroxene fractions, are tending towards the present seawater value of $^{87}Sr/^{86}Sr$~0.7090, strongly suggesting that the hot-desert environment alteration processes has affected the Rb-Sr isochron system of the meteorite. If we construct the reference isochron for the least altered mineral fraction Pl impure2 (Fig. 2) and for Sm-Nd age 3.089±0.064, we can estimate an initial $^{87}Sr/^{86}Sr_i$ of ~ 0.69949.

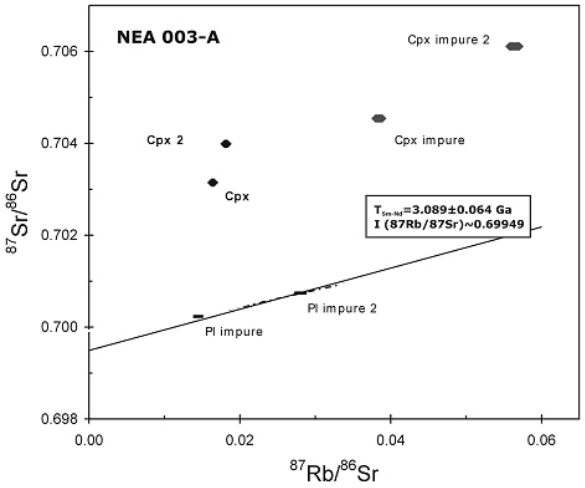

Fig. 2.: Rb-Sr isotopic data for mineral fractions of NEA 003-A shown as an isochron diagram.

Isotopic constrains on petrogenesis: The discrepancy in Sm-Nd age could be explained by partial disturbance or re-setting of the Sm-Nd system during the shock processes which converted plagioclase into maskelynite. However, a recent study of [4] suggests no or very little effect of shock metamorphism on the Sm-Nd systematics of lunar basalt samples. Furthermore, the shock event(s) forming maskelynite was fast with little heating, since there is no petrographic evidence of recrystallization. The supposed post-shock temperature of 200–250˚C [5] would have been insufficient to cause Sm-Nd diffusion since the closure temperatures for pyroxene and plagioclase are much higher.

Alternatively, the Sm-Nd system could be influenced by terrestrial contamination due to weathering processes taking place in the hot desert environment where the meteorite was found [1]. Study of individual mineral phases under SEM and using EMPA revealed the presence of large numbers of shock fractures filled with secondary weathering products, particularly in the outer part of olivine and pyroxene grains. This is in contrast to maskelynite where the fractures are almost absent. The Fe-rich pyroxene rims represent the most affected region of the pyroxene grains and slight disturbance in Sm-Nd data can be explained by the presence of terrestrial contamination in this separate. Therefore we consider the age of 3.089±0.064 Ga, $(^{143}Nd/^{144}Nd)_i$ = 0.50861±0.000095, ε_{Nd3089} = -0.4±0.3, and MSWD = 1.01 to best represent the crystallization age of NEA003-A.

Previous studies [1,2] shows that there is a strong geochemical affinity of NEA 003-A to Apollo 15 olivine-normative basalts and we can assume that a slightly more evolved source magma of Apollo 15 olivine-normative basalts could be derived by fractional crystallisation from a magma source having a similar composition to NEA 003-A. In contrast, the geochemically similar olivine-normative basalts 15555 and 15016 from Apollo 15 suite were derived from isotopically more depleted source than the near-chondritic NEA 003-A (Fig. 3). Most likely, the magma source of these rocks evolved separately in isolated geochemically similar reservoirs [6].

The Sm-Nd crystallization age (3.089±0.064 Ga) corresponds to the period of lower Eratosthenian lunar volcanic activity. Older crystallization ages of geochemically similar Apollo 15 olivine-normative basalts (~ 3.3±0.02 Ga) suggest that NEA 003-A can be a product of younger low-Ti mare basalt volcanism within the Apollo 15 olivine-normative basalt suite. The near-chondritic ε_{Nd} value of –0.4±0.3 indicates that NEA 003-A could also be derived from a mantle source similar to the Apollo 15 green glass which is also characterized by very low and unfractionated REE abundances and near-chondritic Sm/Nd evolution [7].

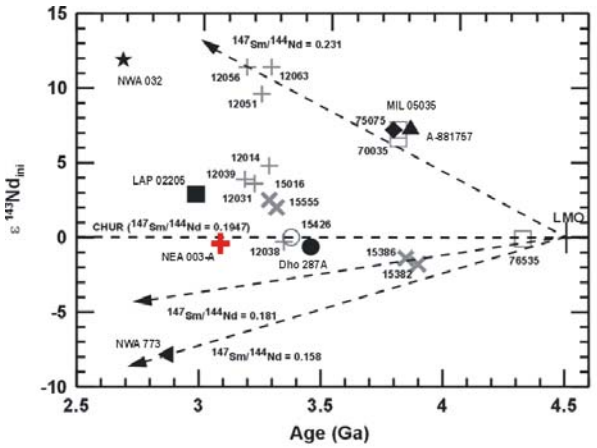

Fig. 3.: Initial Nd isotopic composition ε_{Nd} vs age plot for NEA 003-A, lunar mare basalt meteorites and selected Apollo 12, Apollo 15 and Apollo 17 basalts.

References: [1] Haloda J. et al. (2006) *LPS XXXVII,* Abstract #2269. [2] Haloda J. et al. (2007) *LPS XXXVIII,* Abstract #1768. [3] Haloda J. et al. (2007) *Eos Trans. AGU 88,* Abstract #V23B-1440. [4] Gaffney A. M. et al. (2007) *LPS XXXVIII,* Abstract #1424. [5] Stöffler D. and Grieve R. A. F. (2007) Impactites. In *Metamorphic rocks - a classification and glossary of terms* (editors: Fettes D. and Desmons J.). [6] Nyquist L. E. and Shih C. Y. (1992) *GCA* 56, 2213-2234. [7] Lugmair, G. W. and Marti, K. (1978) *EPSL* 39, 3349-3357.

LUNAR METEORITE NORTHEAST AFRICA 003-A: MICROSTRUCTURES, CRYSTALLIZATION MODELING AND POSSIBLE LUNAR SOURCE AREAS.

Jakub Haloda[1,2], Pavel Gabzdyl[3], Patricie Tycova[1,2], Vera Assis Fernandes[4, 5, 6] [1]Institute of Geochemistry, Charles University, 128 43 Prague 2, Czech Republic, [2]Czech Geological Survey, Barrandov, 150 00 Prague 5, Czech Republic (haloda@cgu.cz), [3]Department of Geological Sciences, Masaryk University, 611 37 Brno, Czech Republic (gabzdyl@hvezdarna.cz), [4]Univ. Coimbra, Portugal; [5]Univ. Manchester, UK, [6]Univ. College London, UK (veraafernandes@yahoo.com).

Introduction: The Apollo and Luna rocks and regolith samples are coming from the known locations on the Moon, but these rocks represent only small part of the lunar surface. Samples from other unsampled parts of the Moon are represented by increasing group of lunar meteorites. These meteorites come from unknown locations on the Moon and were ejected by meteoroid impacts. Many of these meteorites have features different from Apollo samples and they were probably derived from so far unexplored areas of the Moon.

Northeast Africa 003 (NEA 003) is a mare basalt and basaltic breccia [1]. The lithology we designate Northeast Africa 003-A (NEA 003-A), which comprises the main portion (~75 vol.%) of the meteorite, is an unbrecciated mare basalt. Adjacent part, Northeast Africa 003-B (NEA 003-B), is a basaltic breccia (~25 vol%) [2].

Petrography, Mineral and Bulk Chemical Composition - Summary: NEA 003-A is a coarse-grained low-Ti olivine-rich basalt. The rock is showing porphyritic texture of olivine (Fo_{73-19}), zoned pyroxene ($En_{5-71}Wo_{6-38}$) and plagioclase (An_{84-92}),. Undulatory to mosaic extinction of olivine and pyroxene crystals indicate that these crystals have been deformed and presence of the numerous crack and fractures indicate the intensive shock processes. All plagioclase is totally converted to maskelynite. High Mg# (52.6) together with low concentration of Al_2O_3, CaO, Na_2O and K_2O of this sample can be an indicator of primitive character of the source magma and presence of cumulate olivine. The presence of cumulate olivine is in good agreement with petrographic observation, olivine mineral chemistry and modal composition of NEA 003-A with high abundance of Mg-Fe enriched phases and low plagioclase content.

NEA 003-A has the lowest and flattest chondrite-normalized REE pattern among all known mare-basalt meteorites. Concentrations of incompatible trace elements of NEA 003-A are very low in comparison with majority of other lunar basalts. The only known lunar basalts with comparably low ITE concentrations are the VLT basalts of Apollo 17 and Luna 24.

Detail petrography, mineral and bulk chemistry have been previously described in [1].

Microstructures: Microstructure relations among NEA 003-A mineral phases can provide crucial information for understanding the magma evolution and crystallization with the purpose to define the mode of magma flow and degree of shock metamorphism. For this study we used the method of image analysis and electron backscatter difraction (EBSD). EBSD data for determining the crystallographic preffered orientation (CPO) of olivine, pyroxene and ilmenite were collected. The data were collected in manual mode for quantification of inter-mineral angular relations and in linescan automatic mode for specification of misorientations of selected mineral grains.

Image processing collected with optical microscope show a homogenous distribution of minerals within the sample with no preferred orientation of grains. Misorientations of selected olivine, pyroxene and ilmenite grains were studied in two orthogonal misorientation profiles for each grain. Acquired misorientation data (Fig. 1) reveal a small angular deviations within the internal structure of grains which could be ascribed to the shock process.

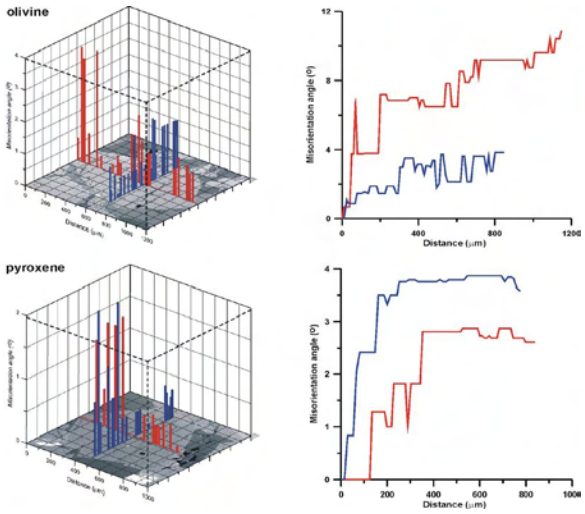

Figure 1.: (left) Orthogonal misorientation profiles for selected grains of olivine and pyroxene. 3D plots show change in misorientation along profile relative to the previous measurement. (right) Distance (μm) versus misorientation angle (°) plot show change in misorientation along profile relative to the first measurement.

CPO data for olivine, pyroxene and ilmenite show no significant preferred orientation typical for many volcanic rock from Earth. This fact together with coarse grained texture of the sample could be an evidence for relatively stable magma crystallization conditions and obviously low influence of a magma flow. CPO data for each phase are represented in stereographic projection of main crystalographic plains in Figure 2.

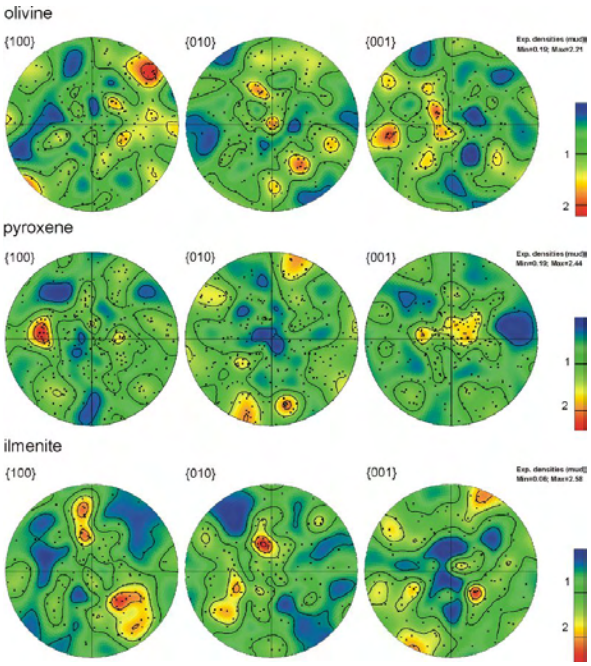

Figure 2.: CPO data for olivine (189 points), pyroxene (251 points) and ilmenite (124 points) are presented in stereographic projection of main crystalographic plains on lower hemisphere.

Crystallization Modeling: For calculation of Fo content of olivine in equilibrium with a whole rock Mg# [3] we used the TiO_2 calibrated Kd [4], where NEA 003-A has a Kd=0,33. Calculated Fo content of olivine for NEA 003-A Mg#=52,6 is about Fo_{77}. However, the highest measured Fo content in the cores of the earliest formed NEA 003-A olivines (Fo_{72}) is lower than the calculated Fo content. This fact together with unusually high modal portion of olivine and some above mentioned geochemical features indicate the presence of cumulate olivine and his accumulation in the parental magma.

Before crystallization modeling we had calculated the portion of cumulate olivine (equiliblium Fo content=measured Fo content). This olivine portion (10%) was removed and the bulk composition of NEA 003-A was recalculated. The recalculated bulk-rock composition was modeled using the PELE software based on the algorithms and database of [5,6]

The results of low-pressure (1bar) models of crystallization sequence for equilibrium and fractional crystallization provide good and consistent datasets. Modeling started with a liquidus temperature of 1327 ^{o}C and oxygen fugacity equivalent to Iron-Wustite buffer. Comparing both models, fractional crystallization provides better results which with conspicuous agreement between predicted and observed compositional ranges of majority of mineral phases. The low-presure model of fractional crystallization for recalculated NEA 003-A bulk-composition predict that chromian-spinel crystallized as a first phase from a cooling liquid at 1327 ^{o}C, followed by olivine (Fo_{73}) at 1241 ^{o}C, pigeonite (En_{71}, Wo_6) at 1171 ^{o}C, clinopyroxene (En_{63}, Wo_{26}) at 1130 ^{o}C and plagioclase (An_{87}) at 1148 ^{o}C.

Predicted and observed compositional ranges of mineral phases are very similar, excluding the plagioclase where bigger difference can be registered (observed An_{84-92}, predicted An_{86-88}). This difference is possible subsequence of the shock processes and complete conversion of plagioclase to maskelynite.

Possible lunar source areas: Using global remote sensing data from Lunar Prospector gamma ray spectrometer [7] and from Clementine spectral reflectance [8], these data can indicate several possible source areas for NEA 003 A. Most recently determined Ar/Ar age for NEA 003-A described in [9] is 2.377±0.04 Ga (2σ). NEA 003-A thus represents a very young lunar low-Ti olivine rich basalt. In respect to the young age of the meteorite we can specify the possible source areas: Oceanus Procellarum, Mare Imbrium and central (younger) part of Mare Serenitatis, where the longer active volcanic activity is considered [10].

References: [1] Haloda J. et al. (2006) *LPSC XXXVII*, abst. #2269; [2] Haloda J., et al. (2006) *LPSC XXXVII*, abst. #2270; [3] Roeder P. L. et al. (1970) *Contrib. Mineral. Petrol.* 29, 275-289; [4] Delano J. W. et al. (1980) *Proc. Lunar Sci. Conf.* 11, 251-288; [5] Ghioroso M. S. (1985) *Contrib. Mineral. Petrol.* 90, 107-120; [6] Ghioroso M. S. et al. (1994) *Contrib. Mineral. Petrol.* 119, 197-212; [7] Lawrence D. J. et al. (2000) *J. Geophys Res.* 105, 20, 307-20,331; [8] Giguere T. et al. (2000) *Meteoritics and Planetary Science* 35, 193-200; [9] Fernandes V. A. et al. (2007) *LPSC XXXVIII*, in this volume; [10] Hiesinger H. et al. (1998) *LPSC XXIX*, abs. #1243.

LUNAR METEORITE NORTHEAST AFRICA 003-B: A NEW LUNAR MARE BASALTIC BRECCIA.

Jakub Haloda[1,2], Patricie Tycova[1,2], Petr Jakes[1], Pavel Gabzdyl[3], Jan Kosler[4] [1]Institute of Geochemistry, Charles University, 128 43 Prague 2, Czech Republic, [2]Czech Geological Survey, Barrandov, 150 00 Prague 5, Czech Republic (haloda@cgu.cz), [3]Department of Geological Sciences, Masaryk University, 611 37 Brno, Czech Republic (gabzdyl@hvezdarna.cz), [4]Department of Earth Science, University of Bergen, Bergen, N-5007 Norway (Jan.Kosler@geo.uib.no).

Introduction: Northeast Africa 003-B (NEA 003-B) is the brecciated lithology of a new, 124 g lunar meteorite Northeast Africa 003 (NEA 003) found in November 2000 (6 g stone) and in December 2001 (118 g stone) in northern Libya in wadi Zam Zam area [1]. Approximately 25% of the larger stone consists of the NEA 003-B lithology, which is basaltic breccia consisting of well consolidated glassy impact-melt matrix that contains scattered mineral fragments of the NEA 003-A lithology (low-Ti olivine-rich basalt) and two larger lithic clasts of low-Ti mare basalt lithologies. The present study is directed at the breccia portion of the meteorite.

Petrography and Mineral Chemistry: The brecciated portion of NEA 003 meteorite has a very sharp contact with the attached low-Ti olivine-rich basalt NEA 003-A. Weathering grade is low, calcite and gypsum veinlets are present.

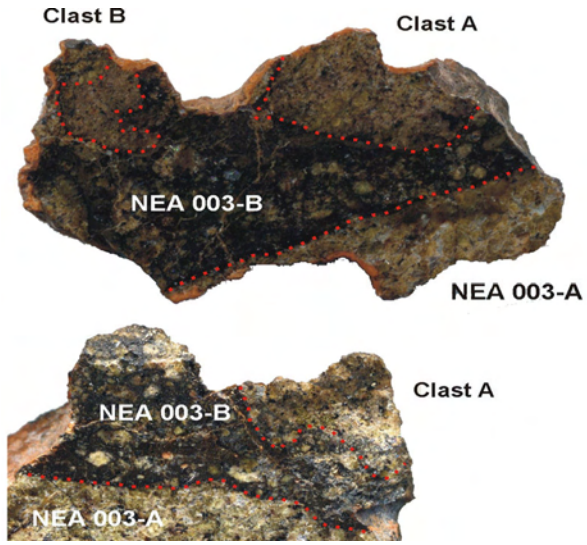

Figure 1. Photograph of two sections of specimen Northeast Africa 003-B lunar basaltic breccia.

The rock consists of two low-Ti basalt clast (clast A and clast B) and glassy impact melt matrix (Fig. 1).

Impact melt matrix contains scattered mineral fragments with chemical composition identical to minerals in NEA 003-A. The impact melt surrounds the sharp clast boundaries as well as fills the space between the scattered mineral clasts. It commonly includes vesicles and schlieren. The representative chemical composition of impact melt is shown in Table 1. No regolith component was found in the matrix.

Clast A. Clast A is a low-Ti olivine mare basalt with porphyritic texture of olivine (Fo_{71-40}), zoned pyroxene ($En_{6-57}Wo_{9-39}$) and plagioclase (An_{85-92}), (Fig. 3.). Olivine an pyroxene show extensive symetrical zoning with gradual iron enrichment. All plagioclase is totally converted to maskelynite. The Clast A contains late-stage mesostasis composed of silica, Fe-rich pyroxene and pyroxferroite, plagioclase, ilmenite, troilite, apatite, whitlockite and fayalitic olivine with Si-K-rich glass and pockets of K-Ba-rich glass. Opaque phases include predominatly ilmenite, ulvöspinel, chromite, troilite and trace Fe-Ni metal. Shock veins and impact melt pockets are present throughout the sample.

Mineral modes, determined by image analysis from X-ray maps and BSE images, are (vol%): olivine = 10.6; pyroxene = 56.7; plagioclase = 28.1; ilmenite = 1.5; spinel = 0.5; mesostasis+impact melt = 2.6.

The Fe/Mn atomic ratios in pyroxenes are (Fe/Mn = 42-93 atom%) and olivines (Fe/Mn = 91-119 atom%). Undulatory to mosaic extinction of olivine and pyroxene crystals, presence of numerous cracks and fractures indicate the intensive shock processes.

Clast B. The smaller clast shows similar porphyritic texture to Clast A. Typical composition of main minerals is: olivine (Fo_{48-32}), zoned pyroxene (En_{18-51} Wo_{9-41}) and plagioclase (An_{85-94}). Olivine crystals show only week zonation. Zoning in pyroxenes is clear and symmetrical. Identically with Clast A, olivine and pyroxene were affected by intensive shock processes and all plagioclase was converted to maskelynite. The presence of late-stage mesostasis is rare and it is composed of silica, Fe-rich pyroxene, plagioclase, ilmenite and troilite. Opaque phases include ilmenite, ulvöspinel, troilite and trace Fe-Ni metal. Impact melt pockets and veins are common.

Mineral modes, determined by image analysis from X-ray maps and BSE images, are (vol%): olivine = 12.2; pyroxene = 59.5; plagioclase = 24.3; ilmenite = 1.4; spinel = 0.5; mesostasis+impact melt = 2.1.

The Fe/Mn atomic ratios in pyroxenes are (Fe/Mn = 42-93 atom%) and olivines (Fe/Mn = 91-119 atom%).

Chemical Composition: The concentrations of major elements were estimated using EMPA analyses of mineral phases and mineral modes determined by image analysis from X-ray maps and BSE images. REEs concentrations of Clast A were estimated from LA-ICP-MS analysis done for individual minerals and mineral modes. These calculated whole-rock compositions and REEs concentrations may have large errors, but this technique can yield the reasonable approximations of whole-rock composition of the lithic clast. The estimated whole-rock major and rare earth element concentrations are presented in Table 1 and Fig. 2.

Majors	wt%			REEs	ppm
	Clast A	Clast B	impact melt		Clast A
SiO2	44.6	45.0	43.6	La	9.2
TiO2	1.9	1.8	2.1	Ce	23.6
Cr2O3	0.4	0.6	0.6	Nd	15.6
Al2O3	9.7	10.1	8.6	Sm	4.8
FeO	21.0	20.9	22.8	Eu	1.2
MnO	0.3	0,3	0.3	Gd	6.6
MgO	10.9	9.9	12.9	Tb	1.2
CaO	10.5	10.7	8.5	Dy	8.6
Na2O	0,4	0.2	0,2	Ho	1.9
K2O	0,2	0.1	0,1	Er	5.6
Total	**99.9**	**99.6**	**99.7**	Tm	0.9
				Yb	6
				Lu	0.8

Table 1. Chemical composition of major (Clast A, B and impact melt) and REE elements (Clast A) of Northeast Africa 003-B lunar meteorite.

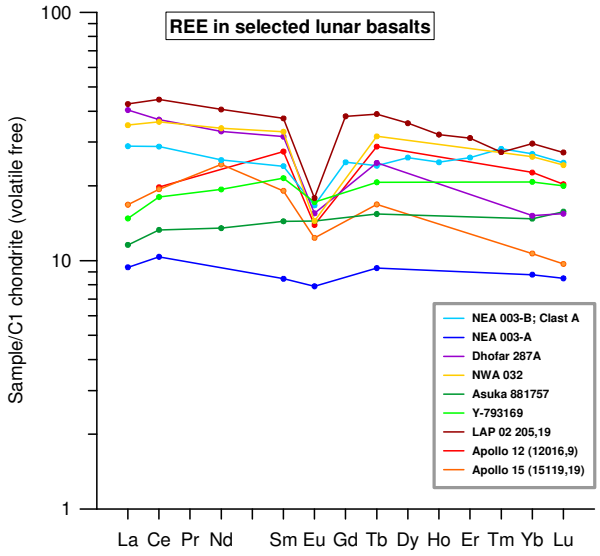

Figure 2. Volatile-free, chondrite-normalized plots of estimated REEs in NEA 003-B; Clast A and selected lunar basalts. REE concentrations are normalized to values of [3] multiplied by the factor 1.36. Data source for other selected lunar basalts is [4] and [6].

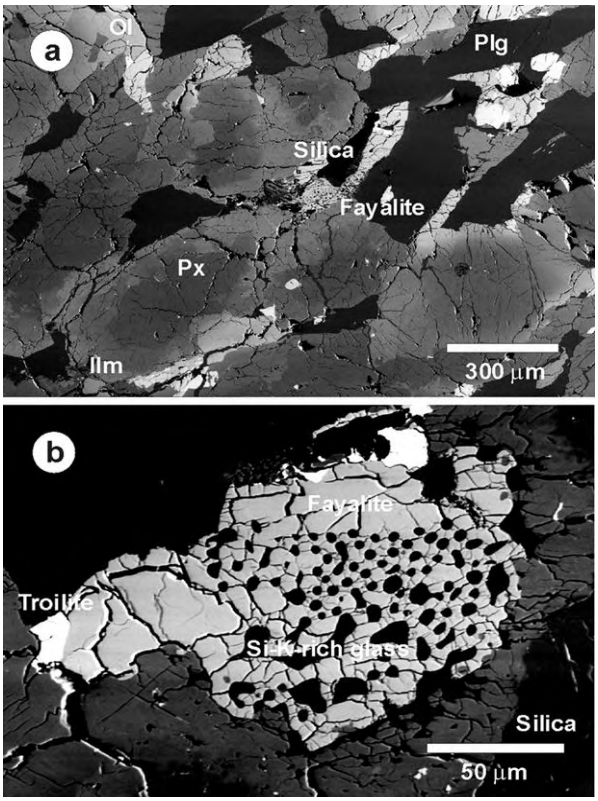

Figure 3. (a) BSE image of the texture of basaltic Clast A-olivine (Ol), extremely zoned pyroxene (Px), plagioclase (Plg), ilmenite (Ilm), silica (Silica) and fayalite (Fayalite). (b) BSE image of fayalite contains inclusions of Si-K-rich glass.

Discussion: NEA 003-B is a brecciated part of the new lunar meteorite, dominated by different mare-basalt lithologies. Both lithic clasts present in the impact melt matrix correspond to olivine-rich low-Ti mare basalt suite with more evolved chemical composition when compared to NEA 003-A mare basalt. When compared to Dhofar 287B breccia, NEA 003-B contains no VLT lithologies, glasses or regolith components. The lithic clasts are similar in texture, mineralogy, chemistry and REE pattern to Apollo 12 and Apollo 15 low-Ti mare basalts [2]. The presence of low-Ti basaltic rocks in NEA 003 meteorite could be related to the progressive fractionation of single parent low-Ti melt. The subsequent impact could expose the basalts from different depths and cause the cementation of the basalt ic fragments.

References: [1] Haloda J. et al. (this volume); [2] Papike J.J. (1998) in Planetary Materials, *Reviews in Mineralogy, 36*, ch. 5, M.S.A.; [3] Anders E. and Grevessen N. (1989) *Geochimica et Cosmochimica Acta* 53:197-214; [4] Fagan T. J. et al. (2002) *Meteoritics & Planetary Science* 37: 371-394; [5] Anand M. et al. (2003) *Meteoritics & Planetary Science* 38: 485-499.; [6] Anand M. et al. (2004) LPSC XXXVI: 1626.

LUNAR METEORITE NORTHEAST AFRICA 003-A: A NEW LUNAR MARE BASALT.

Jakub Haloda[1,2], Randy L. Korotev[3], Patricie Tycova[1,2], Petr Jakes[1], Pavel Gabzdyl[4] [1]Institute of Geochemistry, Charles University, 128 43 Prague 2, Czech Republic, [2]Czech Geological Survey, Barrandov, 150 00 Prague 5, Czech Republic (haloda@cgu.cz), [3]Department of Earth and Space Sciences, Washington University, C/B 1169, Saint Louis, MO 63130 (korotev@wustl.edu), [4]Department of Geological Sciences, Masaryk University, 611 37 Brno, Czech Republic (gabzdyl@hvezdarna.cz).

Introduction: Northeast Africa 003 (NEA 003) is a 124 g lunar meteorite found in November 2000 (6 g stone) and in December 2001 (118 g stone) in northern Libya in wadi Zam Zam area. This rock is a mare basalt and basaltic breccia. The lithology we designate Northeast Africa 003-A (NEA 003-A), which comprises the main portion (~75 vol.%) of the meteorite, is an unbrecciated mare basalt. Adjacent part, Northeast Africa 003-B (NEA 003-B), is basaltic breccia (~25 vol%) consisting of well consolidated glassy impact-melt matrix which contains scattered mineral fragments of chemical composition identical with composition of NEA 003-A and two larger clasts of low-Ti mare basalt lithologies.

Petrography and Mineral Chemistry: NEA 003-A is a coarse-grained low-Ti olivine-rich basalt (Fig. 1). Weathering grade is low, calcite and gypsum veinlets are present.

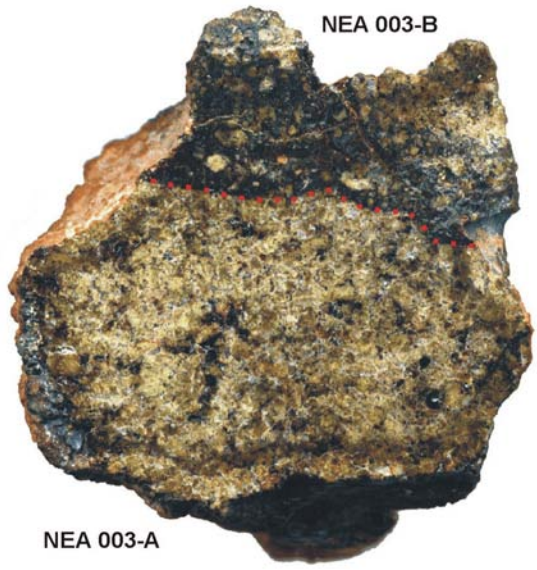

Figure 1. Photograph of 118 g specimen of Northeast Africa 003 lunar meteorite.

The rock is showing porphyritic texture of olivine (Fo_{73-19}), zoned pyroxene ($En_{5-71}Wo_{6-38}$) and plagioclase (An_{84-92}), (Fig. 4.). Majority of olivine crystals show normal symetrical zoning but number of olivine crystals show asymmetrical zoning with gradual iron enrichment. Pyroxene grains are often enclosing inclusions of olivine, chromite and ulvöspinel. Undulatory to mosaic extinction of olivine and pyroxene crystals indicate that these crystals have been deformed and presence of the numerous crack and fractures indicate the intensive shock processes. All plagioclase is totally converted to maskelynite.

The Fe/Mn atomic ratios in pyroxenes (Fe/Mn = 43-89 atom%) and olivines (Fe/Mn = 93-108 atom%) within the sample affirms the lunar origin. The Fe and Mn concentrations and composition of pyroxene and olivine are plotted in Fig. 2, after [1].

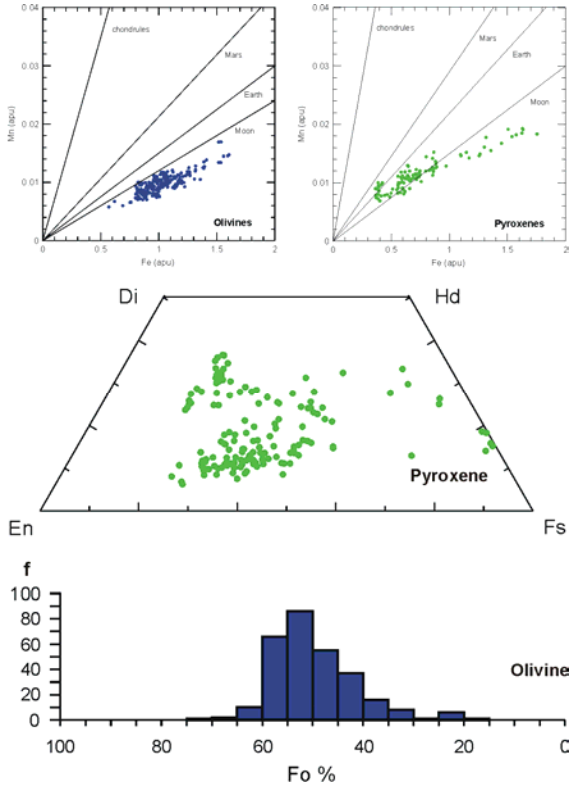

Figure 2. Olivine and pyroxene compositions of Northeast Africa 003-A.

The meteorite contains late-stage mesostasis composed of silica, Fe-rich pyroxene and pyroxferroite, plagioclase, ilmenite, troilite and apatite. Opaque phases include chromite, Ti-rich chromite, ulvöspinel, ilmenite, troilite and trace Fe-Ni metal. Shock veins and impact

melt pockets are present throughout the sample. Mineral modes, determined by data processing from X-ray maps and BSE images, are (vol%): olivine = 17.5; pyroxene = 60.6; plagioclase = 18.2; ilmenite = 1.2; spinel = 0.8; mesostasis+impact melt = 1.8.

Chemical Composition

The selected whole-rock major, trace and rare earth elements are presented in Table 1. The concentrations of major elements were obtained using XRF and ICP-MS analyses. Trace elements and REEs were analyzed using INAA. The Fe/Mn ratios: (6 g stone, Fe/Mn= 85, 118 g stone, Fe/Mn=81).

Majors	wt%	Traces+REEs	ppm
SiO2	44.72	Sc	50.8
TiO2	1.34	Co	50.5
Cr2O3	0.52	Ni	84
Al2O3	8.02	Sr	117
FeO	21.83	Ba	252
MnO	0.27	La	3.0
MgO	13.59	Ce	8.5
CaO	9.16	Nd	4.5
Na2O	0.31	Sm	1.69
K2O	0.1	Eu	0.60
Total	**99.86**	Tb	0.46
		Yb	1.94
		Lu	0.28
		Hf	1.1
		Ta	0.15
		Th	0.43
		U	0.29

Table 1. Chemical composition of major and trace elements of Northeast Africa 003-A lunar meteorite.

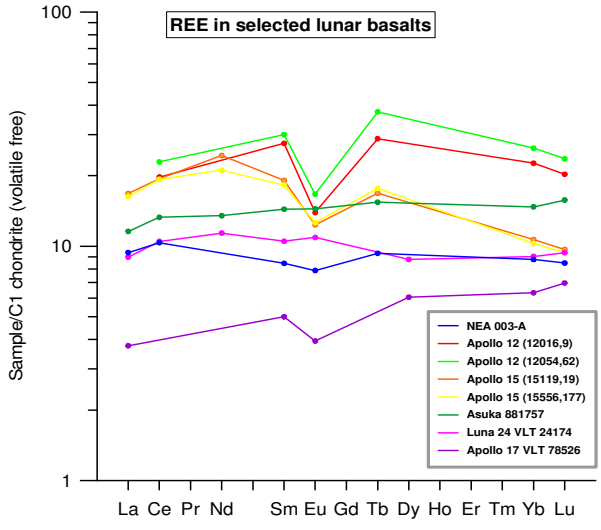

Figure 3. Volatile-free, chondrite-normalized plots of REEs in Northeast Africa 003-A and selected lunar basalts. REE concentrations are normalized to values of [2] multiplied by the factor 1.36. Data source for other selected lunar basalts is [3].

Discussion

When we compare NEA 003-A with other crystalline lunar basaltic meteorites, NEA 003-A is different in terms of texture, high modal abundance of olivine (17.5 vol.%) and mineral chemistry. The only lunar basaltic meteorite that have comparable amount of olivine is Dhofar 287A (20.6 vol%) [4]. Petrographically, NEA 003-A has similarities to Apollo 12 and 15 olivine basalts. Compositionally, however, is NEA 003-A different from the other basaltic lunar meteorites and Apollo and Luna mare basalts. The whole-rock MgO of NEA 003-A is the highest and TiO_2 content is the lowest among lunar unbrecciated basaltic meteorites [5]. In terms of REE contents, NEA 003-A has the lowest and flattest chondrite-normalized REE pattern among all known mare-basalt meteorites. These features suggests that NEA 003-A represents a previously unsampled lithology with no exact match to any so far described lunar basaltic meteorite.

References: [1] Papike J.J. (1998) in Planetary Materials, *Reviews in Mineralogy, 36*, ch. 5, M.S.A.; [2] Anders E. and Grevessen N. (1989) *Geochimica et Cosmochimica Acta* 53:197-214; [3] Fagan T. J. et al. (2002) *Meteoritics & Planetary Science* 37: 371-394; [4] Anand M. et al. (2003) *Meteoritics & Planetary Science* 38: 485-499; [5] Korotev R. L. (2005) *Chemie der Erde* 65: 297-346.

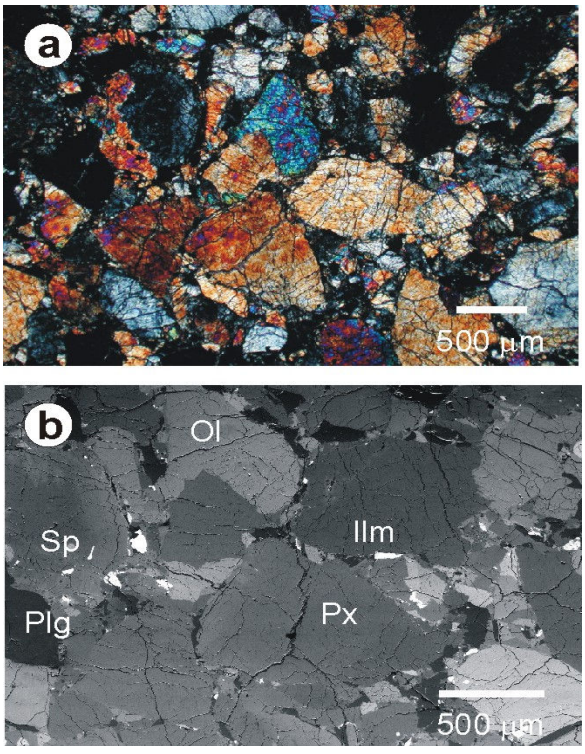

Figure 4. (a) Microscopic image in transmitted light (crossed nicols) showing a typical porphyritic texture of the rock, (b) BSE image of the meteorite`s texture - olivine (Ol), pyroxene (Px), plagioclase (Plg), ilmenite (Ilm) and spinel (Sp).

extraction and analysis.

[1] M. Moldovan, E.M. Krupp, A.E. Holliday and O.F.X. Donard, *J. Anal. At. Spectrom.*, **19**, 815-822 (2004).
[2] Freddy C. Adams, *J. Anal. At Spectrom.*, **16**, 926-930 (2001).
[3] Hakan Gürleyük and Dirk Wallschläger, *J. Anal. At. Spectrom.*, **16**, 926-930 (2001).
[4] Bruce R. James, John C. Petura, Rock J. Vitale, and George R. Mussoline, *Environ. Sci Technol.*, **29**, 2377-2381 (1995).
[5] Dengwei Huo and H. M. "Skip" Kingston, *Anal. Chem.*, **72**, 5047-5054 (2000).

F08 IMPROVEMENTS IN TRACE ELEMENT ANALYSIS WHEN USING A NEW ION-OPTICS DESIGN ICP-MS WITH LASER ABLATION ICP-MS FOR BASALTIC AND ANDESITIC NATURAL GLASSES. **Susan C. Woods**, Harvard University, Department of Earth and Planetary Sciences, 20 Oxford St., Cambridge, MA, 02138; Fergus Keenan, Thermo Electron Corporation, 265 Davidson Ave, Suite 10, Somerset, NJ, 08873; Phil Shaw, Thermo Electron Corporation, Ion Path, Road Three, Winsford Cheshire, CW10 0PE, United Kingdom, and Charles H. Langmuir, Harvard University, Department of Earth and Planetary Sciences; swoods@fas.harvard.edu

Ultratrace element analysis with ICP-MS is very dependent on the blank levels measured with elevated instrument blanks being the major cause of inaccuracy and poor detection limits. This is especially true for the determination of Group I and II elements and the transition metals. Much of the instrumental blank in the transition metal region in ICP-MS is due to polyatomic species. In laser ablation ICP-MS, the essentially dry plasma has much reduced levels of polyatomic species formation, so that instrumental blanks are more often derived from sputtered materials from depositions on the interface. This is the primary cause of instrument blanks for elements such as Li and Na. This work will describe the use of a new ion optics design with significantly lower instrumental blanks from the interface and how these improvements benefit this analytical technique's precision and detection limits. Basaltic and andesitic natural glasses will be used to demonstrate the performance of the traditional ion optic design of the Thermo Electron X Series and the new design of the X SeriesII ICP-MS, in conjunction with a New Wave 213 nm laser ablation system.

F09 LASER ABLATION MC ICP-MS ANALYSES OF Fe ISOTOPES IN IRON METEORITES. Patricie Tycova, Czech Geological Survey, Klarov 3, Prague 1, 118 21, Czech Republic, and **Jan Kosler**, Department of Earth Science, University of Bergen, Allegaten 41, N-5007 Bergen, Norway; tycova@cgu.cz

Iron is one of the most abundant rock-forming elements in our solar system. It occurs in meteorites in metallic form, as well as in silicates and sulfides. The natural mass-dependent isotopic variation of Fe is in the range of ~4 per mil (‰, $^{56}Fe/^{54}Fe$ ratios). Iron isotopic composition is potentially a powerful tracer of planetary formation and differentiation processes. However, the mechanisms that produce iron isotopic fractionation in extraterrestrial materials remain poorly understood. Iron meteorites, that are believed to represent material from the metallic cores of differentiated parent bodies, appear to be homogenous in Fe isotopic composition on a bulk-meteorite scale with an average bulk-rock $\delta^{56}Fe$ of –0.03 ± 0.04‰ (2 sigma) [1 and references therein]. Only a few attempts have been made to study the variations in Fe isotopic composition in meteorites on the scale of individual mineral grains. Zhu *et al.* [2] and Poitrasson *et al.* [3] found isotopic differences between Fe metal and coexisting silicates in pallasites that experienced a significant high-temperature inter-mineral isotopic fractionation during plan-

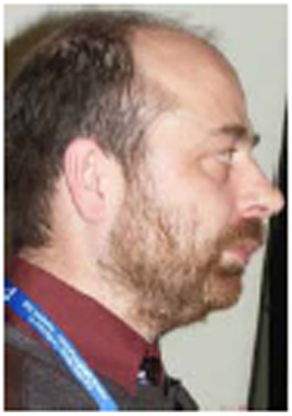

etary core-mantle differentiation. Large fractionations (~0.5‰ in δ^{56}Fe) were also observed between different pallasite metal separates. These variations are interpreted to reflect Fe isotope fractionation during exsolution of coexisting phases, rather than during silicate-metal separation [4]. Poitrasson *et al.* [3] found small differences in Fe isotopic composition of Fe-Ni phases in iron meteorites (up to 0.2‰ in δ^{56}Fe), suggesting that heterogeneities of Fe isotopes on the scale of individual minerals may exist. By using in situ Fe isotopic analyses, Košler *et al.* [5] reported larger Fe isotopic variations between kamacite and taenite (~ 3‰ in δ^{56}Fe) in two iron meteorites.

We have used laser ablation multicollector ICP mass spectrometry (MC ICP-MS) to measure Fe isotopic composition of five iron meteorite groups with different textural and mineral components. Despite a somewhat lower precision compared to solution MC ICP-MS analysis of Fe isotopes, this technique provides useful information on the isotopic composition of Fe on the mineral-scale.

Iron isotope analyses were performed using a Thermo Finnigan Neptune high-mass resolution MC ICP-MS coupled to a New Wave UP-213 UV laser at the University of Bergen. To suppress the isotopic fractionation and to improve the reproducibility of Fe isotopic measurements, the analyses were obtained from linear laser rasters in adjacent kamacite and taenite lamellae. The ICP source of MC ICP-MS was operated at hot plasma conditions. A mass resolving power of 6450 (5, 95% definition) was required to resolve the Fe peaks from interfering molecules present in the ICP. Four Fe isotopes (54, 56, 57 and 58) were measured simultaneously and the contributions of Cr and Ni to masses 54 and 58 were monitored using masses 53 and 60, respectively. The measured isotopic ratios were corrected for mass discrimination from measurements of IRMM-014 iron metal isotopic reference material before and after each analysis (standard-sample-standard bracketing). Laser ablation analyses of synthetic FeNi alloys with known Fe isotopic composition and variable Ni-content suggest that, for the analytical conditions used in this study, there was no significant matrix effects on the measured Fe isotopic composition of kamacite and taenite. The reproducibility of measurements achieved on homogenous Fe metal standard was *ca.* 0.2‰ (δ^{56}Fe, 2 sigma).

The natural variability of Fe isotopic composition in iron meteorites revealed by this *in-situ* laser ablation MC ICP-MS study suggests that the assumption of Fe isotopic homogeneity of meteorites should be re-evaluated, at least on a mineral scale. The metallic phases of the studied meteorites show Widmanstätten patterns that result from oriented intergrowth of low-nickel kamacite and high-nickel areas consisting of a complex mixture of several phases, generally referred to as taenite. The isotopic composition of taenite is heavier compared to the co-existing kamacite in all studied samples; the extent of variation in the Fe isotopic composition differs significantly for meteorites from different chemical groups. Mass differences between iron isotopes can lead to preferential concentration of the heavy isotope in the phase with stronger chemical bonds. This isotopic partitioning can result in fractionation of Fe isotopes between the FeNi phases present in iron meteorites during the meteorite cooling and transformation of taenite into kamacite. Additional isotopic effects are most likely caused by solid-state isotopic diffusion in both alloys. Differences in diffusion rates of ^{57}Fe and ^{56}Fe in kamacite and taenite are expected to contribute to the observed Fe isotopic variability. Rapid cooling rates would produce less fractionation of Fe isotopes compared to slow meteorite cooling. This is in good agreement with our data that show a systematic relation between independently calculated cooling rates (based on Ni diffusion in taenite) and the Fe isotopic fractionation between kamacite and taenite for individual iron meteorite groups. Further quantification of the Fe isotopic diffusion will have to await experimental measurement of diffusion parameters for ^{56}Fe and ^{57}Fe in the FeNi alloys. The availability of precise and accurate Fe isotopic diffusion data will help to lower the temperature range that can be currently determined in iron meteorites using Ni-diffusion thermometery (*ca.* 500°C). Provided that the Fe isotopic composition preserves a record of thermal history of iron meteorites, it may help us in understanding the evolution of planetary bodies.

[1] B.L. Beard and C.M. Johnson, *Rev. Mineral. Geochem.*, **55**, 319-357 (2004).
[2] X.K. Zhu, Y. Guo, R.J.P. Williams, R.K. O'Nions, A. Matthews, N.S. Belshaw, G.W. Canters, E.C.

de Waal, U. Weser, B.K. Burgess, and B. Salvato, *Earth Planet. Sci. Lett.*, **200**, 47-62 (2002).
[3] F. Poitrasson, S. Levasseur, and N. Teutsch, *Earth Planet. Sci. Lett.*, **234**, 151-164 (2005).
[4] S. Weyer, C. Münker, G.P. Brey, A.B. Woodland, K. Mezger, and A.D. Anbar, *Geophys. Res. Abstr.*, **7**, 9257 (2005).
[5] J. Košler, R.B. Pedersen, C. Kruber, and P.J. Sylvester, *J. Anal. At. Spectrom.*, **20**, 192-199 (2005).

F10 CALCIUM ISOTOPE RATIO ANALYSIS OF QUEEN CONCH (*STROMBUS GIGAS*). Neal Julien, Midwest Research Institute - Florida Division, 1470 Treeland Blvd SE, Palm Bay, FL 32909; njulien@mriresearch.org; Ashley Spring, Florida Institute of Technology, 150 W. University Blvd., Melbourne, FL 32901; aspring@fit.edu

Overfishing in Florida and the Caribbean has depleted the stocks of wild queen conch (*Strombus gigas*). Attempts to increase these stocks through aquaculture have had limited success due to low survival rates when released, which is believed to be due, at least in part, to lower shell strength compared to wild conch. Research aimed at increasing shell strength to improve survival of cultured stock in the wild is on-going. The objectives of this research are to determine (1) whether juvenile queen conch absorb calcium for shell production from the water, substrate, and/or food, and (2) whether juvenile queen conch absorb calcium for shell production through the stomach lining, gills, or mantle. There are at least two ways to determine the source of calcium and the body part used to absorb calcium for shell production. One method is to rear juvenile queen conch in systems where one or more calcium sources are removed. A second method is to rear conch under the known successful techniques and compare calcium isotope ratios of source material and possible absorption points. With the first method it proved difficult to remove calcium without affecting other processes and adding additional unwanted factors into the experiment. The isotopic ratio method does not alter the rearing conditions or growth and was chosen for further evaluation.

Isotopic analysis of calcium by quadrupole inductively coupled plasma mass spectrometry (qICPMS) has been difficult because of isobaric and molecular interferences, with the most problematic being direct overlap of ^{40}Ca by ^{40}Ar. The use of collision and reaction cells prior to mass analysis has resulted in a significant reduction in this interference, and ^{40}Ar can virtually be completely removed from the sample spectrum using hydrogen as the cell gas. The wide distribution of isotopic abundances of the element (from ^{40}Ca at 96.941% to ^{46}Ca at 0.004%) also poses a problem for accurate isotope ratio measurements, but the use of dual mode detectors capable of pulse and analog operation permit monitoring of low and high ion counts in the sample simultaneously. Measurement precision was improved compared to the conventional instrument configuration using an enhanced stability sample introduction system.

In May 2005, 19 conch were sacrificed and the stomach lining, gills, mantle, and shell removed for analysis. The substrate, feed and water samples from the growth tanks were also collected for analysis. Soft tissue samples (stomach lining, gills, mantle and feed) were dried at 60°C for 3 days, then 100 mg of each sample was solubilized with tetramethylammonium hydroxide (TMAH) and digested with a mixture of nitric and hydrochloric acids for analysis, then diluted to 50 mL . Hard samples (shell and substrate) were digested with a mixture of nitric and hydrochloric acids for analysis, and diluted to 50 mL.

The analysis was performed with an 7500c ICPMS (Agilent Technologies, Palo Alto, CA) using a PC^3-SSI sample introduction system (Elemental Scientific, Inc., Omaha, NE). The analytical isotopes were ^{40}Ca, ^{42}Ca, ^{43}Ca, ^{44}Ca, and ^{48}Ca. Signals at m/z 80, 84, 86, and 88 were also monitored for evaluation of interference from doubly charged ions of these masses. A 5 mg/L solution of gallium was added on-line and measured at ^{69}Ga and ^{71}Ga as the internal standard. Mass bias correction factors were determined with a 5 mg/L solution prepared from National Institute of Standards and

Natural tracer profile in a deep claystone formation (Opalinus Clay of Mont Russelin, Switzerland)

M. Koroleva[1], M. Mazurek[1], A. Gautschi[2], T. Bigler[3]

[1]Institute of Geological Sciences, University of Bern Baltzerstrasse 3, CH-3012 Bern, Switzerland (koroleva@geo.unibe.ch; mazurek@geo.unibe.ch)
[2]Nagra, Hardstr. 70, CH-5430 Wettingen, Switzerland (andreas.gautschi@nagra.ch)
[3]Physics Institute, University of Bern Sidlerstrasse 5, CH-3012 Bern, Switzerland (tbig@climate.unibe.ch)

Natural tracers in pore water of Opalinus Clay, a 180 Ma old shale formation, were studied in cores drilled from a tunnel penetrating an anticline of the Jura Mountains in NW Switzerland. This thin-skinned mountain belt was folded between 10 and 3 Ma in the late stages of the Alpine collision. Six 4 m deep boreholes were drilled to cover a profile from the core of the anticline to its SE limb.

In the core of the anticline, a water with Cl^- content similar to that of modern sea water was collected from an extensometer borehole in the underlying Liassic claystone close to the contact with the Opalinus Clay. Water seepages into the tunnel containing fresh water were collected in the Dogger limestone overlying Opalinus Clay in the SE limb of the anticline. The horizontal distance between the locations where the saline and the fresh water samples were taken is ca. 400 m and is largely constituted of Opalinus Clay. In order to identify and quantify the large-scale transport process(es) in Opalinus Clay and to assess the long-term-evolution of pore water, the contents of Cl^-, Br^-, $\delta^{18}O$, δ^2H and helium were analysed using dedicated techniques.

The Cl^- distribution in pore water shows a regular and well defined profile from Liassic claystones with the highest values (about 450 mmol/kgH_2O), decreasing across Opalinus Clay and reaching approximately 140 mmol/kgH_2O in the Dogger limestone in the southern limb of the anticline. The distribution of stable water isotopes and helium also shows systematic variations. Both δ^2H and $\delta^{18}O$ are highest in the centre of the anticline (about $-38‰$ and $-4.6‰$, respectively) and decrease to $-59‰$ and $-8.3‰$, respectively, in the Dogger in the limb. Similarly, helium contents decrease from 4.19×10^{-4} to 1.74×10^{-4} ccSTP/gH_2O. In contrast to Cl^-, both water isotopes and helium show an anomaly related to a major fault zone close to the contact between Opalinus Clay and a tectonic slice of underlying Toarcian rock.

The available data are consistent with a model considering very old, possibly connate pore water in the centre of the anticline, which evolves towards fresh water in the limb. Calculations testing the hypothesis that the spatial distribution of tracers can be explained as due to diffusion are under way, and the mechanisms that resulted in the geochemical anomaly in the fault are evaluated.

doi:10.1016/j.gca.2006.06.668

Fe isotopic fractionation in iron meteorites—A potential thermometer?

J. Kosler[1], P. Tycova[2]

[1]Department of Earth Science, University of Bergen, Norway (jan.kosler@geo.uib.no)
[2]Czech Geological Survey, Prague, Czech Republic (tycova@cgu.cz)

Fe isotopic differences between coexisting taenite and kamacite in meteoritic irons have been recently reported by several studies. They all consistently show that the lamellae of Ni-rich mixture of phases (generally referred to as taenite) are isotopically heavier than the adjacent Ni-poor phase (kamacite). The extent of isotopic variation in individual meteorites varies from a fraction of permil to several permil and the $\delta^{57}Fe$ and $\delta^{56}Fe$ compositions suggest a mass dependent fractionation. The heavier Fe isotopic composition of taenite can be explained by its predominantly FCC structure with stronger Fe–Fe and Fe–Ni bonds compared to the predominantly BCC structure of kamacite. The spectroscopic data that could be used to predict the Fe isotopic fractionation in the meteoritic Fe–Ni alloys are not available but equilibrium isotopic fractionation of $\sim 0.7‰$ $\delta^{57}Fe$ at 750 °C (typical kamacite–taenite unmixing temperature) can be expected from the analogy with Fe metal (Polyakov and Mineev, 2000).

Laser ablation MC ICP-MS study of meteoritic irons from different meteorite chemical groups revealed a systematic correlation between the kamacite–taenite Fe isotopic offset ($\Delta^{56,57}Fe_{kamacite-taenite}$) and the meteorite cooling rates (5–500 °C/My) calculated independently using metallographic methods based on Ni diffusion in taenite. This correlation is interpreted as resulting from Fe isotopic diffusion between kamacite and taenite lamellae and variable meteorite cooling rates.

Diffusion of Ni in taenite can normally be used to estimate the meteorite cooling rates between the kamacite–taenite unmixing temperature (~750 °C) and the temperature when Ni diffusion in Fe–Ni alloys effectively ceases (~450 °C). The low temperature histories of iron meteorites have so far been extrapolated from the Ni diffusion data. In contrast, the isotopic diffusion of Fe is effective even at lower temperatures and it can provide us with an important tool for deciphering the complete thermal histories of iron meteorites and their planetary parent bodies.

Reference

Polyakov, V.B., Mineev, S.D., 2000. *Geochim. Cosmochim. Acta* **64**, 849–865.

doi:10.1016/j.gca.2006.06.669

LUNAR METEORITE NORTHEAST AFRICA 001: AN ANORTHOSITIC REGOLITH BRECCIA WITH MIXED HIGHLAND/MARE COMPONENTS. Jakub Haloda[1,2], Anthony J. Irving[3] and Patricie Tycova[1,2], [1]Institute of Geochemistry, Charles University, 128 43 Prague 2, Czech Republic, [2]Czech Geological Survey, Barrandov, 150 00 Prague 5, Czech Republic (haloda@cgu.cz), [3]Department of Earth and Space Sciences, University of Washington, Seattle, WA 98195, USA (irving@ess.washington.edu).

Introduction: Northeast Africa 001 (NEA 001) is a 262 g lunar meteorite found in 2002 in northern Sudan. This rock is a clast-rich anorthositic regolith breccia with minor mare basalt component.

Petrography: NEA 001 is a polymict regolith breccia composed of various types of lithic clasts (up to 1 cm in size), isolated mineral fragments, glass fragments and spherules embedded in a well-consolidated microcrystalline impact melt matrix (Fig. 1). The rock is heavily fractured as a result of multiple shock events, but it remains coherent due to the presence of impact-melt matrix. Typical composition of the impact-melt matrix is (wt%): SiO_2 = 45.7, Al_2O_3 = 24.1, FeO = 7.2, MgO = 7.4, CaO = 14.6, Na_2O = 0.5, TiO_2 = 0.5.

Figure 1. Photograph of 120 g specimen of NEA 001.

Mineral fragments are in most cases smaller than 100 μm in size, including plagioclase, pyroxene and olivine, with minor Mg-Al spinel, chromite, ilmenite, troilite, FeNi metal and silica. Plagioclase compositions vary in range $An_{92-99}Or_{<0.2}$. Pyroxene mineral fragments show a wide range of compositions Wo_{2-39} En_{13-80} (Fig.2). Several pyroxene fragments possess exsolution lamellae up to 10 μm wide, some of the pyroxene grains have marginal symplectitic intergrowths of fayalite+hedenbergite+silica after former pyroxferroite. Olivine fragments (Fig. 2) vary from Fo_{48} to Fo_{82}, with rare Fe-rich grains falling outside that range (Fo_{9-22}). Analyses of the Fe/Mn atomic ratio in pyroxenes (Fe/Mn = 43-86 atom%) and olivines (Fe/Mn = 93-100 atom%) within the sample affirms the lunar origin. The Fe and Mn concentrations of pyroxene are plotted in Fig. 3, after [1]. We have observed regolith components such as glass spherules and fragments set within the matrix. Some glasses are partially devitrified, containing plagioclase and pyroxene crystals (Fig. 4). The matrix glass and glass fragments have largely anorthositic compositions (<6 wt% FeO), however some glass fragments are relatively high in Fe and Ca/Al ratio.

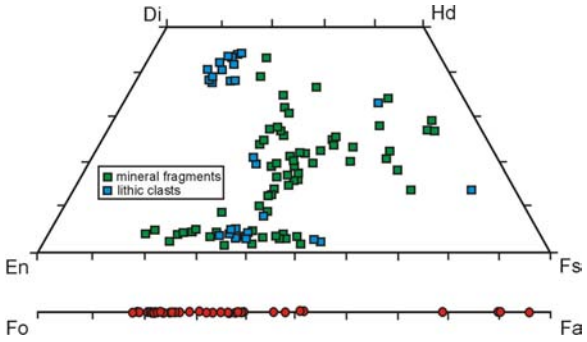

Figure 2. Pyroxene and olivine compositions in NEA 001. Note that some pyroxene grains fall within the field for mare basalts [2], suggesting that they were not derived from highland lithologies.

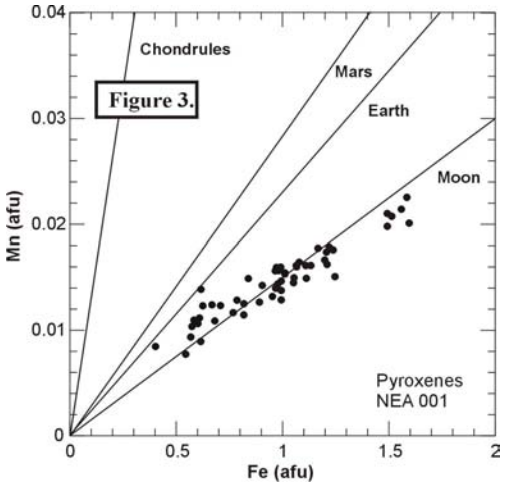

Highland clasts: Lithic clasts are mainly of anorthositic lithologies and the most abundant are impact-melt breccias, plagioclase/glass intergrowths and regolith breccias (mixture of glass and mineral fragments) commonly showing breccia-in-breccia textures. Fragments of primary igneous rocks of anorthositic to gabbroic composition are common, containing plagioclase

An_{95-97}, low-Ca pyroxene $En_{46-65}Wo_{2-5}$ and high-Ca pyroxene $En_{35-48}Wo_{37-44}$ and rare olivine Fo_{79}.

Mare basalt clasts: Sparse clasts of mare basalts of VLT-mare affinities are present (Fig. 4). These clasts show commonly porphyritic to ophitic textures with plagioclase (An_{91-96}), pyroxene (pigeonite to augite), olivine and accessory ilmenite. One small basaltic clast (0.1 x 0.1 mm in size), with porphyritic texture is composed of strongly zoned pyroxene, plagioclase (An_{86}), ilmenite laths, accesory apatite, FeNi metal and troilite. The presence of ilmenite in the basaltic clast suggests this may not be a VLT composition, however the small sample size precludes any definitive conclusions.

Discussion: The major lithologies present in NEA 001 correspond in chemistry to the ferroan anorthosite suite in lunar highland rocks. The regolithic nature of the meteorite is proven by the presence of glass spherules and fragments, but we have not observed agglutinates in the studied sample. There is also evidence of contribution of mare basaltic material in NEA 001 – fragments of Fe-rich augites and pigeonites, breakdown products of pyroxferroite, Fe-rich olivine and the presence of a few pristine basaltic clasts.

Regolith breccias are very common among lunar meteorites [3]. The presence of VLT basalts or mare basaltic component as clasts and fragments in lunar-highlands meteorites was reported earlier [4-8]. The distinctive coarse grainsize and specific mafic mineral compositions of NEA 001, together with the absence of agglutinates and KREEP materials, indicate that this specimen is different from other known lunar meteorites and probably represents an independent fall (see also bulk compositional data given by [9]). We conclude that the lunar source area for NEA 001 is a terrain of highlands rich in ferroan lithologies, with minor mare basalt components.

References: [1] Papike J.J. et al. (2003) *Am. Min., 88*, 469-472; [2] Papike J.J. (1998) in Planetary Materials, *Reviews in Mineralogy, 36*, ch. 5, M.S.A.; [3] Korotev R.L. et al. (2003) *GCA, 67*, 24, 4895-4923; [4] Taylor L.A. et al. (2004) *LPS XXXV*, CD-ROM #1755; [5] Nazarov M.A. et al. (2002) *LPS XXXIII*, CD-ROM #1293; [6] Semenova S. et al. (2000) *LPS XXXI,* CD-ROM #1252; [7] Arai T. et al. (2004) *LPS XXXV,* CD-ROM #2155; [8] Neal C.R. et al. (1990) *LPSC XXI*, 861-862. [9] Korotev R. L. and Irving A. J. (2005) *LPS XXXVI, this volume*.

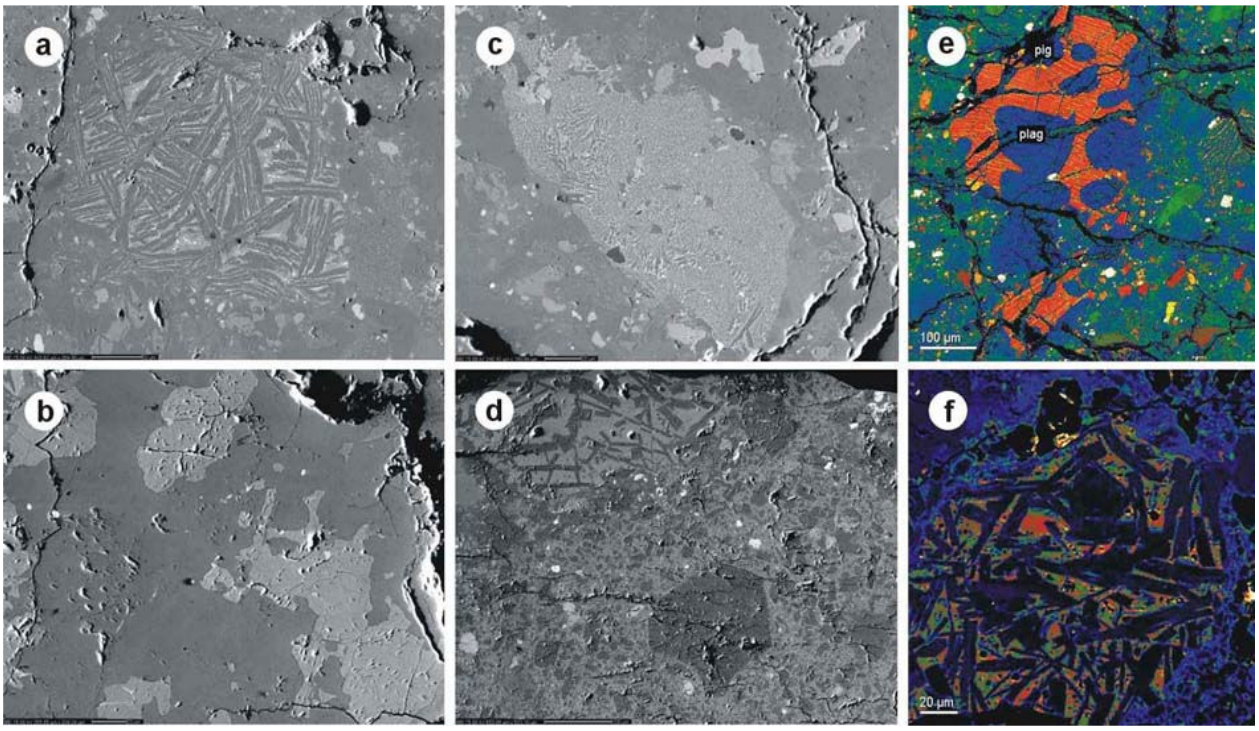

Figure 4. (a) Back scattered electron (BSE) image of a plagioclase/glass lithic clast (200 µm in longest dimension). (b) BSE image of anorthositic lithic clast (230 µm). (c) BSE image of devitrified glass fragment within regolith breccia. (d) BSE image of impact-melt breccia partially enclosing lithic clast of plagioclase+glass composition. (e) False-color BSE image showing primary igneous gabbroic clast of the ferroan highlands suite. (f) False-color BSE image of basaltic clast.

Fe isotopic variations in iron meteorites and implications for parent-body thermal histories

PATRICIE TÝCOVÁ[1,2] *AND JAN KOŠLER*[3]

[1] Czech Geological Survey, Geologická 6, 152 00 Praha 5, Czech Republic; e-mail: tycova@cgu.cz
[2] Dept. of Geochemistry, Charles University, Prague, Czech Republic
[3] Dept. of Earth Science, University of Bergen, N-5007 Bergen, Norway; e-mail: kosler@natur.cuni.cz

Iron isotopic variations in extraterrestrial materials

The largest terrestrial variations in Fe isotopic composition (~ 4 per mil in $^{56}Fe/^{54}Fe$ ratios) in natural samples have been described from low temperature sedimentary environments (Beard et al., 2003). However, the Fe isotopic variations are not limited to terrestrial rocks. Chondritic meteorites, in particular individual chondrules, define a spread of $^{56}Fe/^{54}Fe$ ratios of ~ 2.5 ‰ (Zhu et al., 2001; Kehm et al., 2003; Mullane et al., 2003). In contrast, the bulk-rock analyses of achondrite meteorites (including iron and lunar meteorites) and terrestrial igneous rocks have a relative narrow range of ± 0.05 ‰ (Beard and Johnson, 2004) of Fe isotopic composition ($\delta^{56}Fe$ relative to IRMM-014 isotopic standard). The reported variations in extraterrestrial samples were most likely produced by mass-dependent low temperature fractionation processes, and it appears that the solar nebula was well homogenized with respect to the Fe isotopes (Zhu et al., 2001; Kehm et al., 2003). It has been suggested that variations in Fe isotopic composition may exist on the scale of individual minerals that form the iron meteorites (Košler et al., 2005). Six iron meteorites-octahedrites: Canyon Diablo (IA), Horh Uul (IIIAB), Alt Biela (IID), Nelson County (IIIF), Gibeon (IVA) and Joe Wright Mountain (IIIB); each representing a different chemical group, were analyzed in this study.

Experimental

Isotopic measurements were performed on a Finnigan Neptune high-mass resolution MC-ICP-MS (University of Bergen) coupled to a New Wave UP-213 UV laser. The sample-standard bracketing technique using IRMM-014 iron metal standard was used to correct for instrumental mass-bias of Fe isotopes. The analytical procedure and data reduction are detailed in Košler et al. (2005).

Results and discussion

The Fe isotopic composition of the coexisting FeNi phases taenite (Ni-rich) and kamacite (Ni-poor), and of cohenite $(FeNi)_3C$ in the studied meteorites varies significantly, showing a good correlation that corresponds to the mass dependent isotopic fractionation in the three isotope plot ($\delta^{56}Fe$ vs. $\delta^{57}Fe$; Fig. 1). The composition of Fe in taenite is isotopically heavier compared to kamacite in all studied meteorites, and the range of the Fe isotopic composition in the meteorites straddles the narrow band of Fe isotopic composition previously reported for terrestrial igneous rocks (Fig. 2). The extent of variation in the Fe isotopic composition differs significantly for individual meteorite samples. Previous studies (Beard and Johnson, 2004; Zhu et al., 2002) reported on inter-mineral isotopic fractionation in terrestrial metamorphic rocks and in pallasites as a result of high-temperature isotopic equilibration. The fractionation of Fe isotopes between cohenite – taenite – kamacite is most likely controlled by solid-state diffusion during the transformation of taenite into kamacite, in which Ni and Fe can migrate into the crystal structures of both alloys. Differences in the relative diffusion rates of Fe isotopes in kamacite and taenite may produce the observed Fe isotopic variability (up to ~4 ‰ $^{56}Fe/^{54}Fe$) in iron meteorites. Diffusion is more rapid at high temperatures and becomes less efficient as the metal cools down; thus rapid cooling rates would only produce a minimum fractionation of Fe isotopes. Cooling rates play a key role in studying the size of meteorite parent bodies and their thermal evolution. The relative differences ($\Delta^{56}Fe$) between the iron isotopic composition of coexisting taenite and kamacite pairs in the studied samples could have resulted from several factors: burial depth, degree of parent-body differentiation, initial composition and cooling rate. Our data suggest a close relation between the calculated cooling rates and the Fe

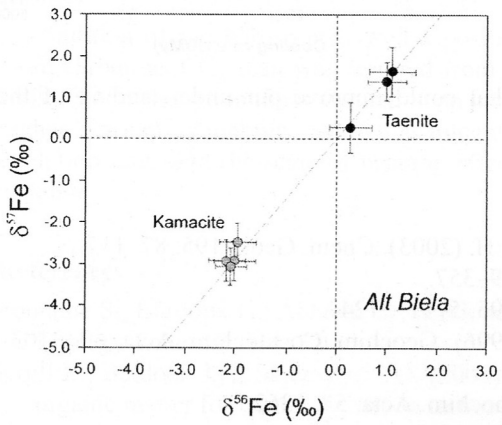

Figure 1. Three isotope plot showing the composition of taenite and kamacite from Alt Biela iron meteorite (the uncertainties are ± 2 sigma). The dashed line is the theoretical mass fractionation line for Fe isotopes (see Beard and Johnson, 2004).

isotope fractionation between kamacite and taenite (Fig. 3). The Horh Uul and Joe Wright Mountain meteorites represent a core of relatively small differentiated asteroid that was disrupted by a single impact event. The calculated cooling rates for IIIAB group (Haack et al., 1990) are faster than those determined for IID group of iron meteorites (Yang et al., 1997), which were formed in the core of a larger asteroid. The Canyon Diablo meteorite was derived from a slowly cooled parent body with a radius >50 km (Herpfer et al., 1994). The Fe isotopic fractionation in these meteorites corresponds to the predicted cooling rates (Hopfe and Goldstein, 2001). Recent data suggest that the Gibeon meteorite was formed in the core of a small, differentiated asteroid that was disrupted by a major impact shortly after its formation (Haack et al., 1996). The asteroid was subsequently re-accreted and underwent a rapid cooling (Rasmussen et al., 1995). This thermal history is also recorded in its Fe isotopic composition. The Nelson County meteorite is the most intensely deformed (pre-terrestrial, cold-worked) iron meteorite known. The kamacite phase in this meteorite shows Neumann lines that are bent and faulted. This is indicative of a violent, plastic deformation event, which could have affected also the Fe isotopic exchange between kamacite and taenite as seen from their overlapping isotopic composition in Fig. 2.

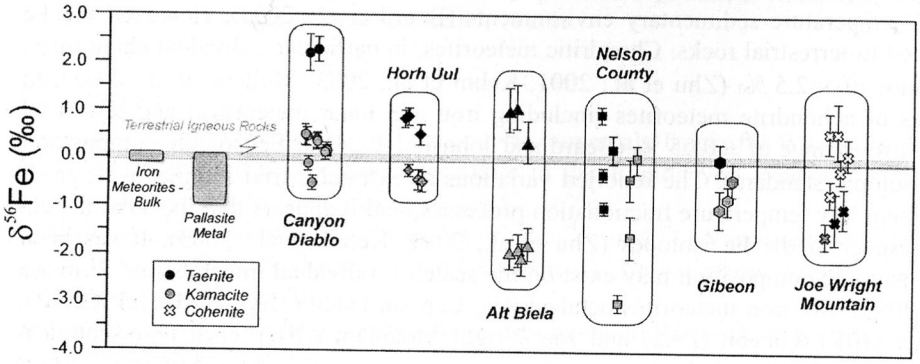

Figure 2. Summary of Fe isotopic data for iron meteorite samples, all values are relative to IRMM-014 standard. Data from bulk iron meteorites are from Kehm et al. (2003), the pallasite metal data are from Beard and Johnson (2004). Data for Canyon Diablo and Horh Uul (with the ± 2 sigma uncertainties) were taken from Košler et al. (2005).

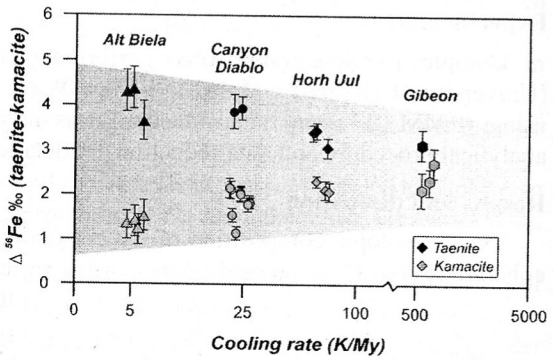

Figure 3. Variation of calculated meteorite cooling rates with the relative difference in isotopic composition of taenite-kamacite pairs $\Delta^{56}Fe$ ‰ = $\delta^{56}Fe_{taenite}$ - $\delta^{56}Fe_{kamacite}$. Data for cooling rates are from Haack et al., 1990; Yang et al., 1997; Herpfer et al., 1994; Hopfe and Goldstein, 2001.

In summary, the Fe isotopic variations in individual constituents of iron meteorites can provide useful information that could improve our understanding of the thermal histories of planetary bodies.

References

Beard B.L., Johnson C.M., Skulan J.L., Nealson K.H., Cox L., Sun H. (2003): Chem. Geol., 195, 87–117.

Beard B.L., Johnson C.M. (2004): Rev. Mineral. Geochem., 55, 319–357.

Haack H., Rasmussen K.L. Warren P.H. (1990): J. Geophys. Res., 95, 5111–5124.

Haack H., Scott E.R.D., Love S.G., Brearley A.J., McCoy T.J. (1996): Geochim. Cosmochim. Acta, 60, 3103–3113.

Herpfer M.A., Larimer J.W., Goldstein J.I. (1994): Geochim. Cosmochim. Acta, 58, 1362.

Hopfe W.D., Goldstein J.I. (2001): Meteoritics Planet. Sci., 36, 135–154.

Kehm K., Hauri E.H., Alexander C.M.O`D., Carlson R.W. (2003): Geochim. Cosmochim. Acta, 67, 2879–2897.

Košler J., Pedersen R.B., Kruber C., Sylvester P.J. (2005): J. Anal. At. Spectrom., 20, 192–199.

Mullane E., Russell S.S., Gournelle M., Mason T.F.D. (2003): Geophysical Research Abstracts, #6830.

Rasmussen K.L., Ulff-Moller F., Haack H. (1995): Geochim. Cosmochim. Acta, 14, 3049–3059.

Yang C.W., Williams D.B. Goldstein J.I. (1997): Meteoritics Planet. Sci., 32, 423–429.

Zhu X.K., Guo Y., O`Nions R.K., Young E.D., Ash R.D. (2001): Nature, 412, 311–313.

Zhu X.K., Guo Y., Williams R.J.P., O`Nions R.K., Matthews A., Belshaw N.S., Canters G.W., de Waal E.C., Weser U., Burgess B.K., Salvato B. (2002): Earth Planet. Sci. Lett., 200, 47–62.

In-situ analysis of Fe isotopes by laser ablation multicollector ICP-MS: Limits and applications

JAN KOŠLER[1,2], *PATRICIE TÝCOVÁ*[2]

[1] Department of Earth Science, University of Bergen, N-5007 Norway; e-mail: jan.kosler@geo.uib.no
[2] Czech Geological Survey, Klárov 3, 118 21 Praha 1, Czech Republic; e-mail: tycova@cgu.cz

Introduction

Iron isotopes can potentially provide us with a powerful tool for tracing rock formation and differentiation processes. The isotopic composition of Fe in nature varies from ca –2.5 to +1.5 ‰ (δ^{56}Fe relative to IRMM-014 isotopic standard); however data from terrestrial igneous and metamorphic rocks and meteorites suggest that the "initial" (primary) isotopic composition of Fe for terrestrial biotic and abiotic processes falls within a much narrower range of ± 0.05 ‰ (Beard et al. 2003). Most of the natural variability in Fe isotopic composition can be related to low temperature abiotic processes and possibly also to microbial fractionation (Johnson et al. 2004 and references therein). The majority of existing Fe isotopic data comes from bulk analyses of geological samples. Only a few attempts have been made to study the variations in Fe isotopic composition on a small (e.g. mineral grain) scale. Graham et al. (2004) found differences in the Fe isotopic composition of pyrite and chalcopyrite from the Grasberg porphyry deposit in Indonesia, suggesting an Fe isotopic fractionation of up to 4 ‰ (δ^{56}Fe) between the coexisting sulphides. Beard and Johnson (2004) reported variations of up to 0.5 ‰ between individual minerals in metamorphic rocks, and Williams et al. (2005) reported high-temperature inter-mineral Fe isotopic fractionation from mantle rocks of up to 1 ‰. In iron meteorites, Košler at al. (2005) and Poitrasson et al. (2005) found isotopic differences between Fe-Ni phases (kamacite and taenite) of up to 2.9 and 0.2 ‰, respectively, suggesting that natural heterogeneities of Fe isotopes on a mineral scale might be larger than previously thought.

Despite the growing field of applications of isotope geochemistry of transitional metals, the mechanisms of Fe isotopic fractionation are still poorly understood and there still are some analytical difficulties with both bulk and in situ methods. For bulk analyses, problems are related to the fractionation of isotopes during ion exchange chromatographic separation and isotopic fractionation of metals between different chemical species in the laboratory. For in situ methods, problems include proper control of instrumental mass bias, spectral interferences and time-dependent isotopic fractionation produced at the microbeam-sample interface and in the ICP source of the mass spectrometer.

Here we explore the limits and possibilities of in situ Fe isotopic analyses of small samples using laser ablation multicollector ICP mass spectrometry (MC ICP-MS). Despite a somewhat lower precision and accuracy compared to solution MC ICP-MS of Fe separated from bulk samples, this technique may provide geologically useful information on the isotopic composition of Fe on a small scale of individual mineral grains or their parts.

Experimental

In this study we have used a Finnigan Neptune high-mass resolution MC ICP-MS coupled to a New Wave UP-213 UV laser at University of Bergen to analyse Fe isotopes in the IRMM-014 metallic Fe isotopic reference material, synthetic and natural Fe sulphides, and iron meteorites. The technique followed the procedure described in Košler et al. 2005. Briefly, the samples were mounted in 1 inch epoxy resin blocks and polished to achieve a flat and smooth surface suitable for laser ablation analysis. The laser was fired at 10 Hz repetition rate using an energy density of 1 – 7 J/cm^2 and a laser beam diameter of 40 – 80 μm, depending on the concentration of Fe in the analysed sample. Single laser spot analyses were used to study the phenomena of time-dependent Fe isotopic fractionation during ablation but most of the analyses during this study were obtained from traverses (linear rasters) of the laser beam across the sample surface. The ICP source of MC ICP-MS was operated at hot plasma conditions. A mass resolving power of 6450 (5,95% definition) was used, and the Fe peak intensities were measured on the ca. 15 mili a.m.u. wide flat-top plateau on the lower mass side of the Fe peaks. Data were acquired in a static mode using six detectors from an array of nine faraday cups mounted in the MC ICP-MS. Typically, a single analysis consisted of measurement of the instrument baseline, 120 isotopic ratios obtained during 40 seconds of gas blank measurement, followed by 200 seconds of acquisition corresponding to the laser ablation sampling. The measured isotopic ratios were corrected for mass discrimination from measurements of the IRMM-014 isotopic reference material or the synthetic FeS, before and after each analysis.

Results

Laser-induced fractionation of Fe isotopes was more pronounced during the single laser spot analyses. The results of ablation experiments suggest that the isotopic composition of aerosol produced by ablation of Fe alloys

and Fe sulphides was not homogeneous; the nm-sized amorphous particles were by several ‰ lighter compared to the μm-sized crystalline particles. The fractionation trend produced by the laser was similar to that observed in natural samples. In order to limit the effects of laser-induced fractionation of Fe isotopes, all subsequent analyses were carried out in laser-raster mode. The reproducibility of measurements achieved on homogeneous Fe metal standard was ca. 0.2 ‰ (δ^{56}Fe).

Analyses of kamacite and taenite phases in several iron meteorites revealed isotopic differences of up to several ‰, similar to those described in Košler et al. 2005. However, the extent of fractionation between kamacite and taenite varies significantly between individual meteorites. It appears that the observed kamacite-taenite Fe isotopic fractionation can be correlated with the thermal histories of the studied meteorites and that it could possibly be used to constrain the cooling rates and hence the sizes of parent bodies of iron meteorites.

Iron isotopic composition of natural hydrothermal pyrite precipitated deep in the upflow zone of the Mohns Ridge, N. Atlantic, is heavier by 2–4 per mil compared to the isotopic composition of vent-fluid pyrite precipitated at the seafloor. The isotopic composition of the later overlaps with the known Fe isotopic composition of vent fluids from the Atlantic and Pacific oceans (-0.78 to -0.30 ‰ δ^{56}Fe). On average, hydrothermal vent fluids have a slightly lighter iron isotopic composition than the oceanic crust, suggesting that seafloor hydrothermal systems fractionate iron isotopes. However, the overlap between the vent fluids and the pyrites of the chimney fragment shows that precipitation of pyrite from supersaturated fluids at the seafloor does not significantly fractionate the iron isotopes. The heavy iron isotopic composition in the pyrite precipitated deep in the upflow zone suggests that a significant fractionation may take place in the deeper parts of the upflow zone, and that this could explain the shift towards lighter iron (compared to oceanic crust) seen in vent fluids on the ocean floor.

In summary, despite the limitations of laser ablation analysis of Fe isotopes in sulphides and metal alloys as described above, the laser ablation MC ICP-MS technique can provide useful information on small-scale Fe isotopic variations that could not be resolved by conventional solution analysis, even when combined with micro-sampling. The somewhat lower precision of laser ablation analyses of Fe isotopes (ca. 0.2 ‰) compared to the conventional solution measurements (ca. 0.1 ‰ or better) does not preclude the technique from being useful for studying natural Fe isotopic variations in a number of geological applications, especially where analyses of small samples or the textural context of analysed objects are important for the interpretation of Fe isotopic data.

References

Beard B.L., Johnson C.M., Skulan J.L., Nealson K.H., Cox L., Sun H. (2003): Application of Fe isotopes to tracing the geochemical and biological cycling of Fe. Chem.Geol. 195, 87–117.

Beard B.L., Johnson C.M. (2004): Inter-mineral Fe isotope variations in mantle-derived rocks and implications for the Fe geochemical cycle. Geochim. Cosmochim. Acta 68, 4727–4743.

Graham S., Pearson N., Jackson S., Griffin W., O'Reilly S.Y. (2004): Tracing Cu and Fe from source to porphyry: in situ determination of Cu and Fe isotope ratios in sulfides from the Grasberg Cu-Au deposit. Chem. Geol. 207, 147–169.

Johnson C.M., Beard B.L., Roden E.E., Newman D.K., Nealson K.H (2004): Isotopic constraints on biogeochemical cycling of Fe. Rev. Mineral. Geochem. 55, 359–408.

Košler J., Pedersen R.B., Kruber C., Sylvester P.J. (2005): Analysis of Fe isotopes in sulfides and iron meteorites by laser ablation high-mass resolution multi-collector ICP mass spectrometry. J. Analyt. Atom. Spectrom. 20, 192–199.

Poitrasson F., Levasseur S., Teutsch N. (2005): Significance of iron isotope mineral fractionation in pallasites and iron meteorites for the core–mantle differentiation of terrestrial planets. Earth Planet. Sci. Lett. 234, 151–164.

Williams H.M., Peslier A.H., McCammon C., Halliday A.N., Levasseur S., Teutsch N., Burg J.-P. (2005): Systematic iron isotope variations in mantle rocks and minerals: The effects of partial melting and oxygen fugacity. Earth Planet. Sci. Lett. 235, 435–452.